UNIVERSITY OF LIEGE
Faculty of Applied Sciences

EXPERIMENTAL AND NUMERICAL STUDY OF CRACKING DURING THE DRYING OF POROUS MATERIALS: APPLICATION TO THE FIELDS OF CHEMICAL ENGINEERING AND GEOMECHANICS

Thesis submitted to obtain the degree of
Doctor of Philosophy in Applied Sciences

Presented by

Julien HUBERT

Director :   Frédéric COLLIN, Chargé de cours à l'Université de Liège
Jury :   M. Robert CHARLIER (Président), Professeur à l'Université de Liège
               Mme. Angélique LÉONARD, Professeur à l'Université de Liège
               M. Lyesse LALOUI, Professeur à l'École polytechnique fédérale de Lausanne
               M. Frédéric DEBASTE, Chargé de Cours à l'Université Libre de Bruxelles
               M. Pierre GERARD, Chargé de Cours à l'Université Libre de Bruxelles
               Mme. Séverine LEVASSEUR, Ondraf/Niras

December 2018

Remerciements

Une thèse de doctorat, ce n'est pas une destination, c'est un voyage. La route est longue et semée d'embûches mais lorsqu'elle s'arrête, c'est avec le sourire qu'on regarde le chemin parcouru. Néanmoins, ce périple je n'aurais pu le mener à bien sans l'aide d'un certain nombre de personnes à qui je voudrais dédier ce travail.

Tout d'abord, je souhaiterais remercier Frédéric Collin d'avoir cru en moi et de m'avoir proposé cette aventure. Il a été le guide sans lequel je me serais perdu en chemin. Sa patience, son aide, son attention de tous les instants, ses questions toujours pertinentes (bien que parfois dérangeantes) mais aussi la pression qu'il a sue, à juste titre, me mettre ont été le moteur qui m'a permis d'avancer. J'exprime aussi toute ma gratitude envers Robert Charlier pour m'avoir laisser rejoindre son équipe ainsi que pour le suivi de mon travail.

Je voudrais également remercier tous les membres de l'équipe pour l'environnement stimulant et jovial dans lequel ils m'ont permis d'évoluer durant ces quatre années (et des poussières...) : Benjamin, Benoît, Anne-Catherine, Georgia, Marc, Simon, Elnaz, Gwendal, Liliana, Albert, Gilles, Sanae, Kien, Giulio et François. J'ai une pensée particulière pour François qui a su supporter mes élucubrations et autres bavardages intempestifs (même s'il a essayé de fuir au pays des kangourous). Je souhaite aussi le remercier pour son écoute et ses remarques qui m'ont toujours permis d'aller de l'avant.

Je remercie pareillement Angélique Léonard et Erwan Plougonven pour leur contribution. Leurs remarques et leur suivi de mon travail m'ont été d'une grande aide. Plus spécifiquement, merci à Erwan pour son aide dans le traitement des images tomographiques d'argile de Boom qui m'ont permis d'obtenir des résultats d'une grande précision.

Je me dois aussi de mentionner mes amis que je remercie de ne pas m'en vouloir de les avoir délaissés pendant l'année écoulée. Ce n'est pas faute de m'avoir invectivé pour mes absences répétées et mon manque de réactivité mais je sais que tout cela part d'un bon sentiment.

Ce n'est pas très original mais je souhaiterais néanmoins remercier mes parents. A mon père, pour son soutient infaillible quelque soit la situation et pour son regard critique mais toujours pertinent sur mon état d'avancement, merci Papa. A ma mère, pour son attitude bienveillante, sa tendresse dans les instants de doute (et les bons petits plats les soirs où j'étais débordé), merci Maman.

Enfin, je remercie Julie. Elle a été, tout au long de ces quatre années, mais plus encore ces derniers mois, la garante de mon équilibre et le phare qui m'a permis de rester sur le droit

chemin durant les longues soirées de rédaction. A elle qui a accepté cet ingrat second rôle dans mon esprit. A elle qui a su maintenir le navire à flot (quand je ne faisais plus rien !). Je n'y serais pas arrivé sans toi, merci.

Abstract

Porous material drying is a process used in many engineering fields such as food (conversation), plastic (polymer), chemical, pharmaceutical and wood (paper paste, composite beam for construction) industries as well as any manufactured process based on paste or powder. It is also of importance in civil engineering because of its impact on soil properties and soil-structure interaction. Given, the number and the importance of these applications, it is a thoroughly studied phenomenon and this PhD work aims at furthering our understanding of the mechanisms behind it as well as those controlling desiccation cracking.

This PhD work is part of a F.R.S-FNRS project revolving around unsaturated porous material desiccation cracking and supported by the collaboration of research groups from the geomechanical team (GEO3) and the chemical engineering team (LGC) of the University of Liège which is the principal strength of this work : it combines the experimental expertise of the LGC team with the numerical knowledge of the GEO3 team. This allow to collect a vast amount of data which are used to validate the numerical models. Sensitivity studies are also conducted to get a better understanding of the influence of each individual process.

Shrinkage   For the geomechanical research group of the University of Liège, the study of the drying behavior is conducted under the scope of deep geological storage of nuclear wastes. This follows previous works of the team carried on nuclear wastes disposal. This concept is based on the multi-barrier principle : wastes isolation is guaranteed by the combination of natural and engineered barriers. During the operation phase, these tunnels are ventilated to allow for people circulation which may lead to desiccation of the host rock at the surface of the tunnel and to cracking.

Given the importance of ensuring good sealing conditions, understanding the drying behavior of the host rock is essential. In Belgium, the considered potential host rock is Boom clay which is thus the material studied throughout the first part of this PhD work. On a geological timescale, this formation belongs to the Rupelian (from 36 to 30 million years ago). This formation is located in the Mol area in the north of Belgium. It is constituted of an alternation of silty clay layer and more clayey layer. This clay structure leads to a material presenting a strong orthotropy. Boom clay has been chosen as a potential host rock because of a series of properties making it a suitable candidate :

- Very low hydraulic conductivity ;

- Good radionucleide retention capacity ;

- Has been stable for millions of years ;

- Self healing capacity.

An experimental convective drying campaign is conducted to gather the data required for the validation of our numerical model. This campaign used the infrastructure of the LGC team of the University of Liège. More specifically, the use of an X-ray microtomograph and the expertise of the LGC in terms of image analysis has been instrumental in quantifying very accurately the variation of volume of the samples. Based on those data, thermo-hydro-mechanical simulations have been performed using the finite element code LAGAMINE (developed by the GEO3 team) to reproduce the experimental observations. A comprehensive step by step approach is followed highlighting the influence of each mechanism on the overall process. Overall, the simulations lead to a excellent fit of the experimental results.

Cracking   The second part of this PhD thesis uses the expertise acquired during the first one as a stepping stone to go further and focuses on the modeling of desiccation cracking. With this goal, a tensile failure constitutive law has been implemented in Liège finite element code LAGAMINE. This law needs to be written in effective stress and to be verifiable for the high suction range observed during drying experiments. Several material point simulations are performed to test the behavior of the implemented constitutive law. Finally, convective drying experiments are simulated using the described framework. This part of the thesis was done on a second material because cracking in Boom clay samples always occured along the bedding planes of the material. It was thus not appropriate to validate the isotropic tensile failure criterion implemented. Resorcinol Formaldehyde hydrogels were chosen because of previous interest of the team from the chemical engineering department (LGC) in its drying behavior and cracking conditions and because it is a synthetic material meaning that it is mostly istropic and homogeneous. The LGC is interested in the drying behavior of this material because, after cure, it can be submitted to pyrolysis to obtain high specific surface carbonate porous structures which have many industrial applications as alternatives to activated carbon. But depending on the curing conditions, the material may suffer desiccation cracking which is detrimental to the end goal where a monolithic structure is required. Previous works of the LGC on the hydrogels have made available a important quantity of data on the drying kinetics and shrinkage behavior of the material as well as a few mechanical and textural properties. Nonetheless, these properties were insufficient to carry numerical simulations and experiments were conducted to obtain the undocumented properties of the material. The simulations performed using the implemented tensile failure criterion in combination with the pre-existent thermo-hydro-mechanical framework allowed to successfully predict crack initiation.

Résumé

Le séchage des matériaux poreux est un procédé essentiel dans de nombreux domaines industriels tel que l'industrie alimentaire (conservation des produits), la plasturgie (polymère et dérivés), l'industrie chimique et pharmaceutique, les filières de transformation du bois (éléments composites pour la construction, pâte de papier, etc.), les procédés de manufactures impliquant des pâtes, poudres ou granulé et le génie civil (mécanique des sols, retrait lors de la prise du béton, etc.). Le nombre et l'importance de ces applications en ont fait un phénomène fortement étudié. Les principaux enjeux liés aux problèmes de séchage sont le retrait et la fissuration qui peut en découler si celui-ci est empêché. Ce projet vise donc à améliorer la connaissance des mécanismes gouvernant la fissuration lors du séchage convectif de matériaux poreux déformables. La principale force de ce projet est qu'il combine à la fois une approche expérimentale et une approche numérique. Ces deux aspects permettent d'obtenir des données expérimentales précieuses à la validation de tout model numérique et de conduire, une fois le modèle validé, de nombreuses analyses de sensibilités afin d'obtenir une meilleure compréhension des phénomènes à l'oeuvre. Ce travail repose également sur la collaboration d'équipes issues du génie chimique (LGC) et de géomécanique (GEO3).

Retrait L'une des applications du séchage pour l'ingénieur civil est son influence sur les intéractions sol-structure. Le laboratoire de géomécanique de l'Université de Liège (GEO3) travaille depuis plusieurs années sur un problème de ce type : l'enfouissement des déchets nucléaire en couche géologique profonde. Ce concept est basé sur une méthode de confinement des déchets en suivant le principe de multi-barrières : une succession de couches jouant chacune un rôle spécifique dans le but de prévenir la migration des radio-nucléides et la contamination de l'environnement. Durant les phases de maintenance précédant le stockage des déchets, les galeries sont ventilées pour permettre la circulation des personnes ce qui peut mener au séchage de la roche en parois et à l'apparition de fissures. Une bonne compréhension du comportement de la roche hôte lors du séchage est donc nécessaire pour assurer l'étanchéité du système. En Belgique, la roche étudiée est l'argile de Boom. Il s'agit d'une formation rocheuse du Rupélien (de 36 à 30 millions d'années) située dans la région de Mol. En terme géologique, cette formation rocheuse est constituée d'une alternance de plans d'argile limoneuse et de plans plus argileux. Cette structure mène à la formation d'un matériau présentant une forte orthotropie. Cette roche a été choisie en raison d'une série de propriétés qui en font un bon candidat pour le stockage des déchets nucléaire :

- Très faible perméabilité à l'eau ;

- Bonne capacité de rétention des radionucléides ;

- Bonne stabilité pendant des millions d'années ;

- Une capacité d'auto régénération (fermeture des fissures).

Une campagne expérimentale de séchage a été menée sur l'argile de Boom afin d'obtenir autant de données que possible en termes de cinétique de séchage, de retrait et de potentielle fissuration. Cette campagne a été réalisée en utilisant les infrastructures du Laboratoire de Génie Chimique et a permis, grâce à l'utilisation d'un microtomographe à rayon X et de l'expertise du LGC en termes de traitement d'image, d'obtenir une quantification très précise des variations de volume des échantillons. Sur base de ces données, des modélisations numériques ont été réalisées en utilisant le logiciel éléments finis LAGAMINE (développé par le service de géomécanique de l'ULiège). Afin de pouvoir reproduire le comportement expérimentalement observé, un modèle Thermo-hydro-mécanique orthotrope avec élasticité non-linéaire a été utilisé. La correspondance entre les résultats expérimentaux et numérique est excellente. Des études de sensibilités ont été réalisées sur différents paramètres hydro-mécaniques clés afin de parfaire la compréhension des mécanismes à l'oeuvre. Cette première phase du projet a donc été consacrée à la compréhension et à la maîtrise des cinétiques de séchage et de retrait afin d'être capable de reproduire numériquement et avec grande précision le phénomène de retrait.

Fissuration   Le second enjeu de ce projet est la capacité à prédire l'apparition de fissure lors du séchage. Dans ce cadre, une loi de comportement a été implémentée dans le code éléments finis LAGAMINE afin de pouvoir prédire une rupture en traction pour un matériau poreux non saturé. Cette loi a été spécifiquement prévue en contrainte effective afin de pouvoir tenir compte de l'influence de la succion (la variable dominante dans les problèmes de séchage) sur la résistance en traction du matériau. Cette loi a été validée dans des conditions simples (traction uni-axiale) avant d'être appliquée à des problèmes de séchage convectif. Bien que les échantillons d'argile de Boom testés présentes des fissures suite au séchage, celles-ci se développent systématiquement selon une direction préférentielle correspondant aux plans de litage du matériau. L'argile de Boom n'est donc pas un matériau adéquat pour valider un modèle de fissuration homogène isotrope. Un second matériau a donc dû être choisi : une résine de Résorcinol-Formaldéhyde. Ce matériau a été choisi car il s'agit d'un matériau de synthèse dont les propriétés sont homogènes et isotrope ce qui en fait un meilleur candidat pour la validation de notre modèle numérique. De plus, le laboratoire de génie chimique s'intéresse depuis plusieurs années au comportement de ce matériau car, après séchage, ces résines peuvent être soumises à une pyrolyse afin d'obtenir des matériaux carbonés à très hautes surface spécifique dont les applications industrielles sont nombreuses (alternative au charbon actif). Il est donc primordial d'être en mesure de prévenir l'apparition de fissures afin de conserver un matériau monolithique. Les travaux antérieurs du laboratoire de génie chimique ont fournis une quantité de données relative à la cinétique de séchage et de retrait du matériau ainsi que certaines de ses propriétés mécaniques. Néanmoins, ces données étaient insuffisantes pour pouvoir modéliser le comportement du matériau. Une campagne de caractérisation hydro-mécanique a donc été menée afin de déterminer les paramètres nécessaires (module de Young, résistance en traction uniaxiale, perméabilité à l'eau, courbe de rétention d'eau) ainsi que leur évolution en fonction de la succion. Sur base de ces mesures, des simulations numériques ont été réalisée et ont permis de prédire l'apparition de fissure en fonction des conditions de séchage.

4

Contents

Chapter 1

Introduction

Contents

1.1 Scope of the Study

Desiccation cracking is a phenomenon related to the tensile failure of material during drying. The most famous example is the crack pattern observable in dry mud as visible on Fig. 1.1. Such occurrences may seen harmless but porous material drying is a process involved in

Figure 1.1: Soil crusting developed in a drying soil under field conditions (Sánchez et al. (2014))

many engineering fields where drying and its most direct consequences, shrinkage, and in certain conditions, desiccation cracking can can have dramatic economic, environmental or safety consequences.

For example, one of the oldest application of drying is age-old : food drying (Hayashi (1989)). It was used for the conservation of aliments (fruits, meat, etc.) to preserve them over long period of time. More recently food has been dried for health or economic reason (Chen and Mujumdar (2009)). Indeed, decreasing the water content helps preventing the proliferation of bacteria but it also decreases the volume and mass of aliments reducing transport costs. In all

these cases, though, the work of the engineer is to formulate a controlled drying environment which will lead to an un-warped crack-free final product so it can be distributed and sold.

In the wood industry, drying is also a very important process (Dincer (1998)). *Every* wooden element is dried before use whatever its final application. Dried timber is stronger, lighter and more resistant to decay and mold development. Composite beams for construction and particleboard for furniture also require dried wooden particle because those are easier to handle and glue together much better. Avoiding cracking in any of those applications is essential for obvious reasons (who would want to buy a cracked Ikea bookshelf?).

In many other fields such as the paper, chemical, pharmaceutical, concrete industries, materials engineers are faced with shrinkage and sometimes desiccation cracking problems and have had to either adapt the production conditions or change the formulations of the product to avoid these issues.

For the civil engineer, drying and desiccation cracking mostly manifest in soils and soil-structure interactions. In some cases it can be a critical phenomenon leading to major damage to soil supported structures or earthen structures. Desiccation cracking is a major problem in slope stability since it alters the properties of the soil at the top of the slope and the water pressure distribution inside sometimes leading to landslides. In the case of earthen dykes or dams, desiccation cracking creates preferential flow paths which enable the formation of erosion tunnels and the overall failure of the retaining structure with catastrophic consequences. It can also be a major concern for waste management. The compacted clay liner at the bottom of landfills can crack when it is left exposed to air prior to the landfill filling (cf. Fig. 1.2). The liner is supposed to act as a low permeability barrier to prevent contamination of the bio-

Figure 1.2: Desiccation cracks in clay liner at the bottom of futur municipal solid waste landfill Rowe and Hosney (2010)

sphere by leachate from the municipal solid wastes. If the liner is cracked then its permeability increases by several orders of magnitude preventing it from playing its confinement role. A similar problem can occur for deep geological storage of nuclear waste where the host rock of the storage tunnels may crack during the operation phase. The galleries are ventilated to allow for the circulation of the operational personnel which cause a desaturation of the host rock at the surface of the tunnel. If cracks occur, they modify the properties of the host rock preventing it from playing its confinement role which may lead to severe environmental repercussions.

Drying in itself can also be detrimental because it is directly responsible for subsidence phenomena. The soil under a building is protected from seasonal change in atmosphere relative

humidity and thus its volume remains mostly constant. On the other hand, soil near the facades of a building is submitted to important moisture gradient and volume changes due to shrinkage. This leads to differential settlements which can cause fracturing of the structure near the facades, rupture of pipes, etc. and have been responsible for billions in structural damages (see Fig. 1.3)

Figure 1.3: Example of subsidence caused damage to a house facade.

These are a few examples in a very long list of shrinkage and desiccation cracking related problems. Getting a better understanding of the mechanisms at play and being able to predict the amplitude of shrinkage and/or the conditions in which cracking occurs would go a long way in improving many engineering processes.

During this PhD work, desiccation cracking is studied in the scope of two of the many application described earlier : polymer production in the chemical industry and deep geological storage of nuclear waste. This PhD work is a part of a F.R.S-FNRS project supported by the collaboration of research groups from the geomechanical team (GEO3) and the chemical engineering team (LGC) of the University of Liège. As such this work is separated in two interconnected parts related to materials of interest in the scope of each research group's ongoing work.

For the geomechanical research group, the context of this research is the deep geological storage of nuclear wastes. This concept aims at preventing any contamination of the environment by radionucleides. Wastes isolation is provided by the combination of a series of natural and engineered barriers. This method is referred to as the multi-barriers principle (cf. Fig. 1.4). The wastes are placed in super-containers formed of different layers that all have a specific role with the goal of decreasing the *risk* of biosphere contamination. The host rock is the last and one of the most important barrier. Its study is thus of the utmost importance to be sure that it can withstand the thermo-hydro-mechanical loading induced by the nuclear wastes storage. One of the load applied to the host rock is the ventilation needed to allow for people circulation during the operation period of the galleries. This exposure to air may lead to a desiccation of the host rock at the surface of the tunnel and to possible desiccation cracks. If cracks occur, they may cause an important increase of the hydraulic permeability of the geological barrier in the damaged zone partially preventing it from playing its containment role. It is therefore
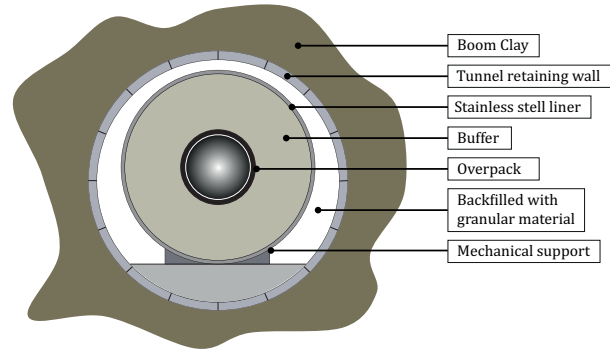
Figure 1.4: Multi-barriers principle Craeye et al. (2009)

important to closely study the drying behavior of the host rock. In Belgium, the considered host rock is Boom clay which is thus the material studied for the geomechanical application part of this PhD thesis.

For the chemical engineering team, the material studied is a Resorcinol Formaldehyde hydrogel. It is an interresting material for drying behavior study because after drying this material can be submitted to pyrolisis to obtain high specific surface area carbon structures which have many industrial applications as activated carbon alternatives. Nonetheless the convective drying of the gels can, depending of the synthesis and drying conditions lead to desiccation cracking (Job (2005)). Since crack-free monoliths are required, investigating the drying behavior of the RF hydrogels is an important issue.

1.2 Objectives

This work aims to improve our understanding of the mechanisms behind cracking/fracturing of unsaturated porous deformable materials during convective (using a warm humid air flow) drying. To do so a good understanding of the drying process is required. This works relies on both an experimental and a modeling approach. More specifically, the objectives are :

- constituting a comprehensive knowledge base about convective drying, shrinkage and desiccation cracking to be able to identify the key features to be considered for the constitutive modeling of the phenomena. This requires a considerable amount of bibliographic and experimental work. Fortunately, this work can count on the expertise of the geomechanical research group (GEO3) in multi-physics coupled modeling (Collin (2003)), porous medium - atmosphere interactions (Gerard (2011)) as well as the expertise of the chemical engineering team (LGC) for drying behavior experimental investigation ;

- the accurate simulation of a drying experiment as a thermo-hydro-mechanical phenomenon. Previous works conducted in the GEO3 team mainly focused of the hydraulic aspect of the problem and fully coupled simulations have yet to be performed ;

- the choice of a constitutive law for tensile failure modeling. The selected criterion will need to be able to account for the high suction range reached during a drying process ;

- the implementation of the chosen model into the finite element code LAGAMINE as well as its validation on simple problems ;

- the application of the suggested framework to convective drying experiments presenting desiccation cracking to try to reproduce the observed behavior.

1.3   Outline of the thesis

This thesis is composed of 8 chapters covering the literature review and developments achieved during the PhD research. The chapters are organized in a logical sequence, starting with the description of the notions required to investigate the drying behavior of unsaturated porous media and then moving on to the modeling of the drying phenomenon and of desiccation cracking.

Chapter 2   aims to present the general framework adopted to model the thermo-hydro-mechanical processes. The governing equations, including the balance equations, constitutive equations and equilibrium restrictions are expressed in the usual differential local form.

Chapter 3   follows the same trend as chapter 2 but for the notions related to the drying phenomenon. The different methods of drying are presented and more specifically convective drying which will be used throughout this PhD work. The drying kinetics are analyzed as a mean to understand the different processes going on during a convective drying experiment. Shrinkage is also introduced.

Chapter 4   is the final part of the comprehensive knowledge base required to investigate drying experiments. Here, the general formulation of 2D coupled finite elements is presented. The governing balance equations introduced in chapter 2 are expressed in weak form to be able to solve the problem over large domains. Said system of non-linear equations is then solved and the global solution of the problem is presented.

Chapter 5   starts by introducing the nuclear waste disposal problem as well as the envisioned solution : deep-geological storage. In this framework, Boom clay is studied as a potential host material. Its drying behavior is of interest because desiccation cracking may occur in storage galleries during the operation phase. Its properties and composition are presented. Then, an experimental convective drying campaign was conducted to gather data for numerical modeling. Its procedure and result analysis are detailed. Finally, numerical simulations are performed to reproduce the observed experimental behavior.

Chapter 6   focuses on desiccation cracking and starts by defining the notion of crack. Desiccation cracking is a mode I failure which means it is controlled by a material tensile strength. The different methods to measure that strength are presented. Finally, a review of the models found in the literature to predict desiccation cracking initiation and crack depth is presented.

Chapter 7   starts by detailing the constitutive law chosen to simulate tensile failure. Then the complete mechanical framework is presented as well as its implementation into the in house built finite element code LAGAMINE. Several material point simulations are conducted to validate the behavior of the selected constitutive law.

Chapter 8   is where all the tools presented throughout this PhD work are combined to predict desiccation cracking. It starts by introducing the material used for validation as well as the scope under which it is studied. The new material is a Resorcinol-Formaldehyde hydrogel whose drying behavior is of interest because after drying it can be submitted to pyrolysis to obtain high specific surface carbon structures which are interesting alternatives to activated carbon. A short review of its documented properties is presented as well as the experiments conducted to investigate undocumented ones. Finally, convective drying experiments are simulated using the framework developed and desiccation cracking is successfully predicted.

Chapter 9   concludes with a summary and outlooks for future works.

This thesis start with by presenting the complete framework used to model the thermo-hydro-mechanical processes at play during a drying experiment of a deformable porous medium. The first step is to introduce the notion of deformable porous media as well as the mathematical tools used to describe it. This is the objective of the next chapter.

Chapter 2

Introduction to the porous media

Contents

2.1   Introduction

The modeling of the drying process as a Thermo (**T**)-Hydro (**H**)-Mechanical (**M**) problem requires the definition of a rigorous framework. The goal of this chapter is thus to lay a comprehensive basis for the developments presented in the next chapters.

Both materials considered throughout this work can be considered as porous media. Hence, the first chapter of this thesis starts by introducing the concept of porous medium as well as the different quantities characterizing it. In this work, a porous medium is composed of a solid, a

liquid and a gas phase. Before detailing the equations governing the different phenomena, it is necessary to define the referential in which they will be expressed. An updated Lagrangian formulation is used, which is common in large deformation problems. The balance equations governing the **T-H-M** problem can then be considered. They are developed in the usual local differential form. In order to link the balance equations to the principal variables of the problem, constitutive laws are presented. In particular, the water retention model is presented to account for water distribution and capillary effects. A multiphasic flow model is used to describe the fluid mass flows and since drying is an anisothermal problem, a heat diffusion model is included as well. A mechanical framework is also detailed. In this work, the different phases of the porous medium are assumed to be in thermodynamic equilibrium and the equilibrium restrictions are expressed. Finally, emphasis is placed on the different couplings encountered throughout the chapter and linking the different aspects of the **T-H-M** problem.

2.2 Theory of porous media

First, let us define the notion of porous medium. It is a material containing pores. The skeletal part of the material is called the "matrix" and constitutes the "solid phase". The volume inbetween the solid grains forms the pores. A porous medium is often characterized by its porosity, n. It is defined as the ratio of the pore volume, V_v, to the total volume of the medium, V (Verruijt and Van Baars (2007)):

$$n = \frac{V_v}{V} \tag{2.1}$$

A porous medium can be defined as "saturated" or "unsaturated" (cf. Fig 2.6). In a saturated porous medium, only one fluid fills the porosity whereas in an unsaturated porous medium the pore volume is filled by two fluids. One is a wetting fluid and constitutes the liquid phase and the other is a non-wetting fluid and forms the gas phase. Classically, in the field of geomaterials, the liquid phase is composed of water and dissolved air and the gas phase of dry air and water vapor.
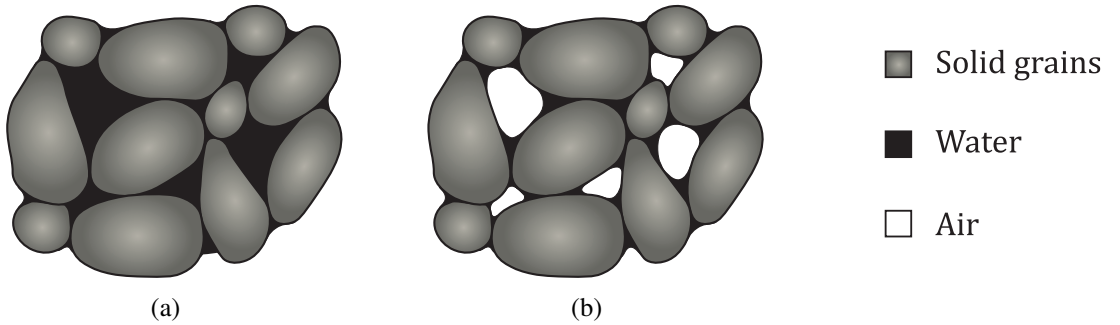
Figure 2.1: Saturated (a) and unsaturated (b) porous medium

In the case of an unsaturated medium, it is useful to define the portion of the pore volume occupied by each fluid phase. This quantity is called the *saturation degree*, S_r. In the following, $S_{r,l}$ and $S_{r,g}$ represent the saturation degree of liquid and gas respectively.

Since the accurate description of such a complex system can prove difficult, different approaches have been suggested to describe it in a simplified manner and build an idealized homogeneous continuum (Dieudonné (2016)):

Macroscopic theories   Macroscopic theories are based on the consolidation theory proposed by Terzaghi (1944), and later extended by Biot (1941, 1956, 1962); Biot and Temple (1972). In these theories, the porous medium is studied at the macroscopic scale. Accordingly, stresses and other related concepts are macroscopic concepts. In addition, the different phases are not treated separately, and the balance equations are written for the whole porous medium, without any distinction between the different phases and species (or constituents). Further extensions of Biot's work include the contributions of Coussy (1995) and Dormieux et al. (1995).

Averaging theories   In averaging theories (Hassanizadeh and Gray (1979a,b)), two structural levels are defined, namely a microscopic scale, corresponding to the pore level, and a macroscopic scale, which corresponds to the representative elementary volume (REV). At the microscopic level, the system is viewed as the overlap of interpenetrating continua. In opposition to the mixture theory, each continuum occupies only a part of the space. The different continua are separated by interfaces, which have their own thermodynamic properties. Balance equations (and sometimes constitutive laws) are introduced at this scale. Averaging techniques are then used to obtain averaged (over the REV) macroscopic field equations. Different averaging methods may be used, ranging from analytical to numerical (e.g. Finite Element Square method). Special care should be taken to select the size of the REV (see Bear (2013); Hassanizadeh and Gray (1979a); Bachmat and Bear (1986); De Marsily (1986)).

Theories of mixtures   In the theories of mixtures, the porous medium is also studied at the macroscopic scale but the balance equations are expressed for each phase separately (Bowen (1980)). All phases are assumed to occupy the same region of space simultaneously as the overlapping of different continua (cf. Fig.2.2) and thus every point of the idealized system consists of a mixture of phases :
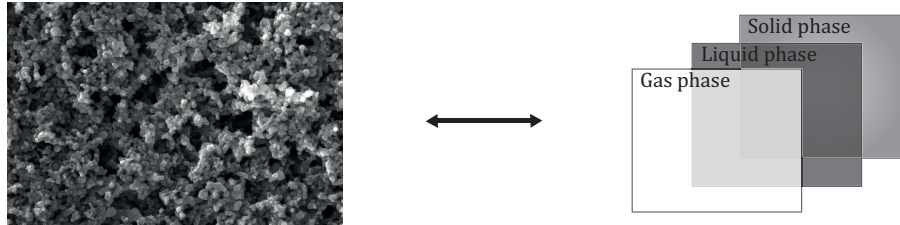
Figure 2.2: Definition of equivalent continua

This supposes the definition of volume fractions to create homogenized continua so that the methods of continuum mechanics can be applied :

$$\eta_i = \frac{V_i}{V} \tag{2.2}$$

where V_i is the volume of the phase i. The following volume fractions can be defined :

$$\eta_s = 1 - n \tag{2.3}$$

$$\eta_l = S_{r,l}\, n \tag{2.4}$$

$$\eta_g = S_{r,g}\, n = (1 - S_{r,l})\, n \tag{2.5}$$

where s, l, g correspond respectively to the solid, liquid and gas phase. The sum of all volume fractions must be equal to 1. The real density, ρ_i of a given phase, i, is classically expressed as :

$$\rho_i = \frac{m_i}{V_i} \tag{2.6}$$

where m_i is the mass of the phase i. In mixture theory, homogenized continua related to each phase are established. It is possible to define the reduced density of the homogenized continuum corresponding to a chosen phase, ρ^i, as the product of the real density, ρ_i, and the volume fraction, η_i, of that phase :

$$\rho^i = \eta_i \rho_i = \frac{V_i}{V} \frac{m_i}{V_i} = \frac{m_i}{V} \tag{2.7}$$

In this work, the approach of mixture theories is chosen because it allows for the description of deformation of the porous medium, of fluid flows and heat transfer as well as coupled phenomena. The averaging theories are also able to do so but require experimental investigation at the micro scale, which is not the usual scale in geomechanics laboratory experiments.

2.3   Referential definition

Before presenting any of the equations expressing the kinematics behind the coupled phenomena at work during desiccation processes, it is necessary to define the reference configuration used. Considering the initial and final configurations as identical is acceptable as long as the deformations are infinitesimal. For large deformation problems, a distinction is made between the deformed and the initial configurations. In large deformation continuum mechanics, two approaches are commonly used :

- **Eulerian description** The problem is stated with regard to the deformed configuration while the motion of material through a stationary control volume is considered, i.e. the movement of the particle is described with respect to a fixed referential frame(cf. Fig. 2.3(a)).

- **Lagrangian description** The problem is stated with regard to the reference configuration while we track the movement of all particles of the body, i.e. the referential frame moves with the material points (cf. Fig. 2.3(b)).

(a)   (b)
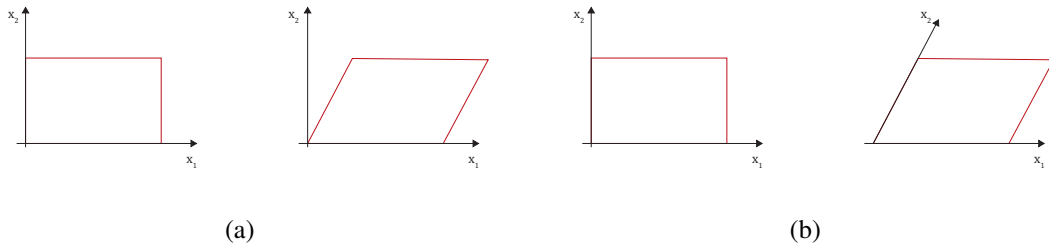
Figure 2.3: Schematic representation of (a) Eulerian (b) Lagrangian referential

In this work, an updated Lagrangian formulation is used to describe the kinematics of the deformable porous medium. An updated Lagrangian referential differs from a total Lagrangian

one because in the former the variables of the problem are expressed with respect to an updated referential frame, (X_1, X_2), whereas the latter expresses the variables with respect to the initial configuration, (X_1^0, X_2^0). The deformation gradient for the current configuration, x_i, with
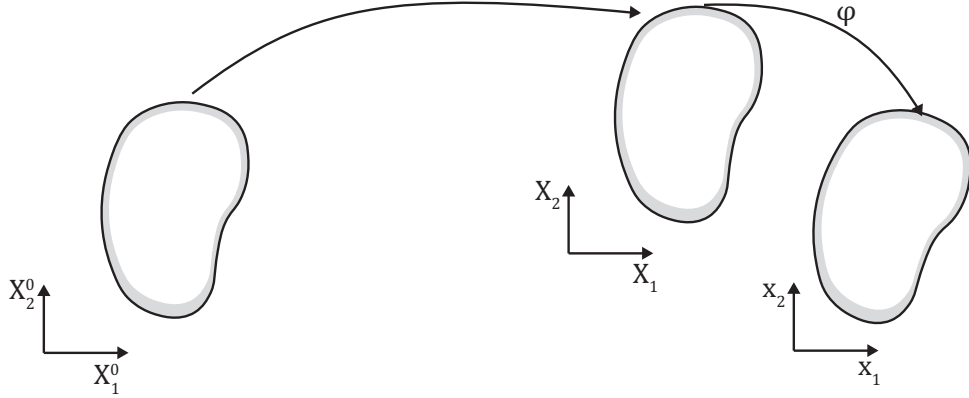
Figure 2.4: Updated Lagrangian formulation with initial configuration in the referential frame (X_1^0, X_2^0), the updated reference configuration in the updated referential frame (X_1, X_2) and the deformed configuration in the current referential frame (x_1, x_2). φ is the mapping that associates a material point of the reference configuration with the current one, $x_i = \phi(X_i)$.

respect to the reference configuration, X_i (cf. Fig.2.4), is characterized through the definition of the transformation tensor F_{ij} which links the coordinate systems in reference and deformed configuration:

$$F_{ij} = \frac{\partial x_i}{\partial X_j} \tag{2.8}$$

The velocity of a material point is given by :

$$v_i = \frac{dx_i}{dt} = \dot{x}_i \tag{2.9}$$

where t is the time. The velocity gradient tensor is expressed as :

$$L_{ij} = \frac{\partial v_i}{\partial x_j} \tag{2.10}$$

which can be split into symmetrical and anti-symmetrical parts :

$$L_{ij} = \frac{1}{2}(L_{ij} + L_{ji}) + \frac{1}{2}(L_{ij} - L_{ji}) \tag{2.11}$$

The Cauchy strain tensor is given by the symmetrical part :

$$\dot{\varepsilon}_{ij} = \frac{1}{2}(L_{ij} + L_{ji}) \tag{2.12}$$

Whereas the spin tensor is defined by the anti-symmetrical part :

$$\omega_{ij} = \frac{1}{2}(L_{ij} - L_{ji}) \tag{2.13}$$

11

The total Cauchy stress tensor, σ_{ij}, is associated with the Cauchy strain rate. The tensor consists of nine components that completely define the state of stress at a point inside a material in the deformed configuration. The Cauchy stress tensor is used for stress analysis of material bodies experiencing small deformations. However, for large deformation problems, the incremental formulation requires the definition of an objective derivative of the stress field, independent of rigid body rotation. The Jaumann derivative (Jaumann (1911)) is thus introduced to describe large strains and rotations:

$$\overline{\sigma}_{ij} = \dot{\sigma}_{ij} - \omega_{ij}\sigma_{ij} + \sigma_{ij}\,\omega_{ij} \tag{2.14}$$

In this work, the geomechanics sign convention is adopted, i.e. stresses and strains are positive in compression.

2.4 Balance equations

The balance equations are obtained for a mixture composed of three phases : solid, liquid and gas. The solid phase is composed of an assembly of solid grains, the liquid phase is composed of water and dissolved air. The gas phase is made of two constituents, dry air and water vapor. Fig. 2.5 presents a summary of the different phases and species :
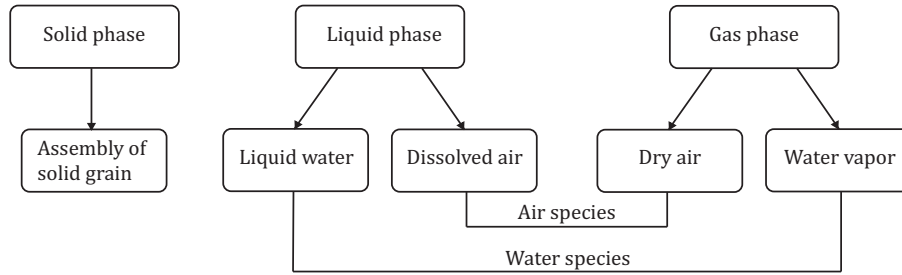
Figure 2.5: Definition of phases and species (modification based on Collin (2003)

In the following, the different balance equations of the thermo-hydro-mechanical problem are developed in the usual differential local form. These equations consist of the balance of momentum of the mixture, the solid's mass balance equation, the fluids' mass balance equations both for water and air and since drying is an anisothermal problem an energy balance equation is also expressed.

2.4.1 Momentum balance equation

The mixture momentum balance equation corresponds to the equilibrium equation of the continuous medium (Malvern (1969)) composed of the three phases (solid, liquid, and gas). Let us consider a given deformable porous medium loaded by volume forces, F_i and surface forces, T_i. Any chosen control volume inside that porous medium is subjected to the same volume forces and to surface forces, t_i. This configuration is shown in Fig.2.6(a).
Let's consider a small tetrahedral volume $OABC$ (cf. Fig. 2.6(b)) such that the ABC side is a part of the external surface of the medium. The outward normal vector to that side is n_i. The

12
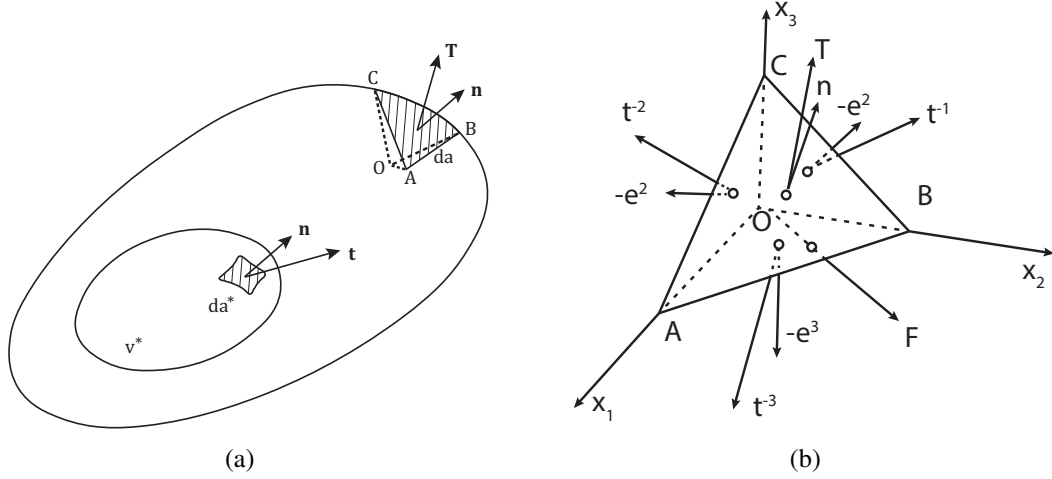
Figure 2.6: (a) Porous medium configuration (b) Tetrahedron OABC

other sides of the tetrahedron are defined so that their normal vector is parallel (and of opposite direction) to one of the reference frame axis. The tetrahedron volume, v, is arbitrarily chosen. If the medium is at equilibrium, we know that this chosen volume is at equilibrium too which is expressed as:

$$da\, T_i + da^1 t_i^{-1} + da^2 t_i^{-2} + da^3 t_i^{-3} + dv F_i = 0 \tag{2.15}$$

$$\Longleftrightarrow da T_i + da^k t_i^{-k} + dv F_i = 0 \tag{2.16}$$

where t_i^{-k} is the stress vector acting on the side of the tetrahedron of area da^k whose normal vector is parallel and of direction opposite to the kth axis of the reference frame, e_i^k. By Newton's third law of motion,

$$t_i^{-k} = -t_i^k \tag{2.17}$$

And Eq. 2.16 becomes :

$$da\, T_i - da^k t_i^k + dv F_i = 0 \tag{2.18}$$

If the tetrahedral volume, v, is chosen infinitesimal then dv is negligible and it comes :

$$da\, T_i - da^k t_i^k = 0 \tag{2.19}$$

The area of the other sides can be expressed in function of the area of the ABC side :

$$da^k = da\, cos(n_i e_i^k) = da\, n^k \tag{2.20}$$

where n^k is the scalar component of vector n_i in the direction of the kth axis of the reference frame, e_i^k. Eq. 2.19 becomes :

$$da T_i - da\, n^k t_i^k = 0 \tag{2.21}$$

$$\Longleftrightarrow T_i - n^k t_i^k = 0 \tag{2.22}$$

The stress vectors, t_i^k can be expressed in the global referential frame as :

$$t_i^k = \sigma_{ij} e_j^k \tag{2.23}$$

13

where σ_{ij} is the Cauchy total stress tensor introduced in section 2.3. Using Eq. 2.23, Eq. 2.22 becomes :

$$T_i - n^k \sigma_{ij} e_j^k = 0 \tag{2.24}$$

$$\Longleftrightarrow T_i - \sigma_{ij} n_j = 0 \tag{2.25}$$

which is the surface balance equation of the considered porous medium.

Let us, now, consider an arbitrary control volume, v^*, delimited by a surface, a^*, in the porous medium. If this control volume is at equilibrium, we get :

$$\int_{v^*} F_i \, \mathrm{d}v^* + \int_{a^*} t_i \, \mathrm{d}a^* = 0 \tag{2.26}$$

Eq. 2.25 gives :

$$t_i = \sigma_{ij} n_j \tag{2.27}$$

And thus :

$$\int_{v^*} F_i \, \mathrm{d}v^* + \int_{a^*} \sigma_{ij} n_j \, \mathrm{d}a^* = 0 \tag{2.28}$$

Using Gauss' theorem, we can change the integral over the boundary to an integral over a volume. It comes :

$$\int_{v^*} F_i \, \mathrm{d}v^* + \int_{v^*} \frac{\partial \sigma_{ij}}{\partial x_j} \, \mathrm{d}v^* = 0 \tag{2.29}$$

This equation is true whatever the control volume chosen. It is thus independent from the volume and we therefore obtain the differential form of the general momentum balance equation.

$$\frac{\partial \sigma_{ij}}{\partial x_j} + F_i = 0 \tag{2.30}$$

In our case, the only volume force is gravity and Eq. 2.30 becomes :

$$\frac{\partial \sigma_{ij}}{\partial x_j} + \rho g_i = 0 \tag{2.31}$$

where g_i is the gravitational acceleration vector and ρ is the density of the mixture :

$$\rho = \rho_s(1-n) + \rho_l S_{r,l} n + \rho_g(1 - S_{r,l})n \tag{2.32}$$

where ρ_l, ρ_g are respectively the densities of the liquid and gas phases.

2.4.2   Mass balance equations

The compositional approach (Panday and Corapcioglu (1989); Olivella et al. (1994); Collin (2003)) is used to establish the mass balance equations. This approach balances species rather than phases and has the advantage of canceling out the phase exchange terms. As described in section 2.3, an updated Lagrangian description is used so that the referential follows the deformable solid phase. The description of the fluid phases is Eulerian in the sense that we compute the fluid flows with respect to the solid phase.

Using the same approach as the one described for the balance of momentum, we consider a chosen control volume, v, delimited by a surface, a. The outward unit normal vector to the surface is n_i. At the surface, a flux, q, of a chosen quantity (such as the mass), $S(t)$, is injected. The first relation that can be expressed is the surface balance equation that states the equilibrium between the normal component of the outflows through the surface, f_i, and the flux imposed at the surface, q :

$$n_i f_i + q = 0 \tag{2.33}$$

A second relationship can be defined and it expresses that the storage term of the chosen quantity, $\frac{\partial S}{\partial t}$, must be equal to the sum of the source/sink term inside the control volume, Q, and the flows through the surface, q. For the chosen quantity $S(t)$, we can write :

$$S(t) = \int_v s(x, t) \, \mathrm{d}v \tag{2.34}$$

And thus the storage term is:

$$\frac{\partial S}{\partial t} = \int_v \frac{\partial s}{\partial t} \, \mathrm{d}v \tag{2.35}$$

The equilibrium equation writes :

$$\int_v \frac{\partial s}{\partial t} \, \mathrm{d}v = \int_a q \, \mathrm{d}a + \int_v Q \, \mathrm{d}v \tag{2.36}$$

integrating Eq. 2.33 in Eq. 2.36 gives :

$$\int_v \frac{\partial s}{\partial t} \, \mathrm{d}v = \int_a -(n_i f_i) \, \mathrm{d}a + \int_v Q \, \mathrm{d}v \tag{2.37}$$

Using Gauss' theorem, we can change the integral over the boundary to an integral over a volume. It comes :

$$\int_v \frac{\partial s}{\partial t} + \frac{\partial f_i}{\partial x_i} - Q \, \mathrm{d}v = 0 \tag{2.38}$$

This equation holds regardless of the chosen control volume. It is thus independent from the volume and we therefore obtain the differential form of the general balance equation of a chosen quantity $S(t)$.

$$\frac{\partial s}{\partial t} + \frac{\partial f_i}{\partial x_i} - Q = 0 \tag{2.39}$$

2.4.2.1   Solid mass balance equations

Because of the definition of the reference system, conservation of the solid mass is always met. The solid mass balance equation reads :

$$\frac{\partial m_s}{\partial t} = \frac{\partial}{\partial t} \left(\rho_s (1 - n) V \right) = 0 \tag{2.40}$$

where m_s is the mass and ρ_s is the density of the solid respectively. If the solid particles are supposed incompressible then Eq. 2.40 reduces to :

$$\frac{\dot{V}}{V} = \frac{\dot{n}}{1 - n} \tag{2.41}$$

and thus the variation of the porosity is given by :

$$\dot{n} = (1 - n)\frac{\dot{V}}{V} \tag{2.42}$$

2.4.2.2 Water mass balance equations

The balance equation for water in the liquid and gas phases can be written using the expression obtain in Eq. 2.39 and substituting the chosen quantity, S, by the mass, m_j^i of the species (in exponent), i, in the considered phase (in subscript), j :

$$\frac{\partial}{\partial t}(m_l^w) + \frac{\partial}{\partial x_i}(f_{l,i}^w) + \dot{E}_{H_2O}^{w-v} = Q_l^w \tag{2.43}$$

$$\frac{\partial}{\partial t}\left(m_g^w\right) + \frac{\partial}{\partial x_i}(f_{g,i}^w) - \dot{E}_{H_2O}^{w-v} = Q_g^w \tag{2.44}$$

where m_l^w, m_g^w are the masses of liquid water and vapor respectively and $f_{l,i}^w$, $f_{g,i}^w$ are the liquid water and water vapor mass flows. Q_l^w, Q_g^w are the liquid water and water vapor source/sink terms. $\dot{E}_{H_2O}^{w-v}$ is the mass of liquid water transformed into vapor. Given the compositional approach, we can express a mass balance equation for the whole water species rather than for each phase and the phase exchange terms are thus canceling each other out. This combined balance equation thus accounts for the liquid water as well as the water vapor and is given by :

$$\underbrace{\frac{\partial}{\partial t}(m_l^w) + \frac{\partial}{\partial x_i}(f_{l,i}^w)}_{\text{Liquid water}} + \underbrace{\frac{\partial}{\partial t}\left(m_g^w\right) + \frac{\partial}{\partial x_i}(f_{g,i}^w)}_{\text{Water vapor}} = Q_w \tag{2.45}$$

2.4.2.3 Air mass balance equations

The same can be done for the air species and the balance equation obtained writes as :

$$\underbrace{\frac{\partial}{\partial t}\left(m_g^a\right) + \frac{\partial}{\partial x_i}(f_{g,i}^a)}_{\text{Dry air}} + \underbrace{\frac{\partial}{\partial t}(m_l^a) + \frac{\partial}{\partial x_i}(f_{l,i}^a)}_{\text{Dissolved air}} = Q_a \tag{2.46}$$

where m_g^a, m_l^a are the masses of dry and dissolved air respectively and $f_{g,i}^a$, $f_{l,i}^a$ are the dry and dissolved air mass flows. Q_a is the air source term.

2.4.3 Energy balance equation

All the phases are supposed to be at the same temperature so that a single energy balance equation is required to describe the thermal aspects. For this single equation, the general form of the mass balance equation (cf. Eq. 2.39) is also applicable even though it is a different phenomenon (Charlier (1987)). The energy balance equation is expressed in enthalpic form. Only the energies linked to the heat transfer and the energy required for the change of phase from liquid water to vapor are considered in the balance equation and all the terms linked to the work of mechanical forces, kinetic energy, etc. are neglected. Heat transfer only includes conduction and convection through the different phases because radiation is neglected.

$$\dot{S}_T + \frac{\partial V_{T,i}}{\partial x_i} + \dot{E}_{H_2O}^{w-v} . L - Q_T = 0 \tag{2.47}$$

where S_T is the enthalpy of the system, V_T is the heat flux, Q_T is the heat production term and L is the water evaporation latent heat.

2.5 Constitutive equations

The balance equations presented introduce a number of variables, such as the total stress tensor, the degree of saturation, the fluid fluxes and the heat flux. These variables are linked to the displacement field, the liquid pressure field, the gas pressure field and the temperature field through relations called constitutive equations. In the case of a thermo-hydro-mechanical problem, the required constitutive equations are : the water retention model, the multiphasic flow model, the mechanical model and the heat diffusion model.

2.5.1 Water retention model

Capillary forces develop between the material solid grains if it is unsaturated and affect the fluid transfers. These forces are related to the quantity of water filling the porous space; they increase when the porous material desaturates. The material retention behavior is generally represented by a water retention curve linking the suction to the degree of water saturation.

2.5.1.1 Capillarity

When two non-miscible fluids are in contact, an interface appears in between them and within which surface tensions exist. Those tensions are the result of the difference in inter-molecular forces between the particle in the fluid and those at the interface as shown on Fig. 2.7.
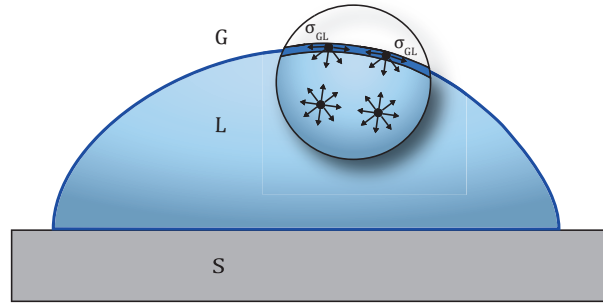
Figure 2.7: Molecular forces on a particle of water Collin (2003)

Particles within the fluid are at equilibrium whereas those in the interface are not and thus surface tensions, σ_{GL}, appear to restore the force equilibrium.

If we now consider two fluids, L and G, in contact with a perfectly plane solid surface S (cf Fig. 2.8), the surface tensions σ_{GL}, σ_{SG} and σ_{SL} exist at the interface. The equilibrium is expressed with Young-Dupré's formula (Dupré and Dupré (1869)) :

$$\sigma_{SG} = \sigma_{SL} + \sigma_{GL} \cos \theta \tag{2.48}$$

17

where θ is the angle between the interface of the two fluids and the solid surface.
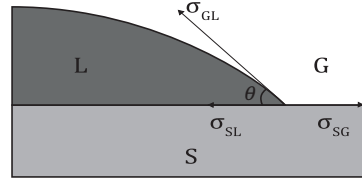
Figure 2.8: Surface tensions (modification based on Collin (2003))

In the general case, the liquid surface makes an angle θ with the particle surface. This angle is called the contact angle and depends on the affinity of the fluids-solid surface affinity. For the contact to be possible between the fluid and the solid surface, the following condition has to be verified :

$$cos\theta = \frac{\sigma_{SG} - \sigma_{SL}}{\sigma_{GL}} < 1 \tag{2.49}$$

This means that for the contact to be possible, the contact angle must be lower than $90°$. Such a fluid is said to be a *wetting fluid*. On the contrary, if $\theta > 90°$, as is the case for fluid G in Fig. 2.8, than such a fluid is called a *non-wetting fluid*. The surface tensions appearing are responsible for the so-called *capillary effect*. This effect is well exhibited in the experiment visible at Fig.2.9. In this experiment, when the capillary tube is plunged into the bask of water, the water level rises into the tube until a certain height is reached, this level is given by Jurin's law which expresses the vertical equilibrium :

$$p_c = p_g - p_l = \rho_w gh = \frac{2\sigma_{GL}cos\,\theta}{r} \tag{2.50}$$

where p_c is the capillary pressure expressed as the difference between the gas pressure, p_g, and the liquid pressure, p_l and r is the radius of the tube. The smaller the radius of the tube the greater the capillary effect. This concept explains the phenomena taking place in an unsaturated

Figure 2.9: Experimental configuration (modification based on Collin (2003))

porous medium with two fluids (Delage (1987)). There is a relation linking the capillary pressure and the relative quantity of each fluid in the pore volume. This relation usually links the capillary pressure with the saturation degree of the liquid phase. Experiments have shown that

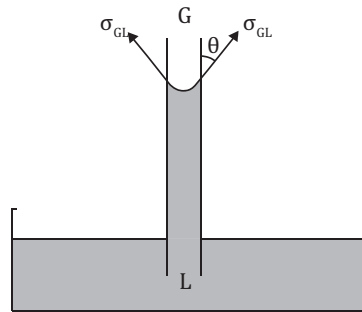the contact angle is not the same depending on which phase is pushing the other out (Bear and Verruijt (1987)). For this reason, it is necessary to define this relation depending on whether the liquid phase is pushed out or the opposite. Also, considering the pores as simple tubes with constant radius is an oversimplified view since it is clear pores have variable radii and are interconnected which means the capillary pressure can be different, for a same saturation degree, depending on the path followed by the liquid phase (Delage et al. (2001)).

2.5.1.2 Concept of suction

In soil mechanics, suction is often used with a similar meaning to capillary pressure. Suction is a concept including capillary effect but also other phenomena. Water total potential in an unsaturated porous medium can be defined as the energy needed to extract the water from the medium and is expressed as (Collin (2003)) :

$$\psi = \psi_g + \psi_p + \psi_m + \psi_o \tag{2.51}$$

where ψ_g, ψ_p, ψ_m and ψ_o are respectively the gravitational potential, the external pressure potential, the matric potential and the osmotic potential. The total suction can be defined as a negative potential. It has two contributions : the matric suction and the osmotic suction. Matric suction is associated with the interactions between liquid and solid while the osmotic suction is related to the difference of concentration in solutions and corresponds to the osmotic pressure. The matric suction is equivalent to the capillary pressure and is thus associated with the capillary phenomena just explained. In this work, the total suction is defined as :

$$s = p_g - p_l \tag{2.52}$$

which corresponds to the definition of the capillary suction in Eq. 2.50. "*However, essentially for historical reasons, it is used to express the degree of attachment of the liquid phase onto the solid phase, regardless of the attraction mechanism. Therefore, the suction as defined reflects interactions between water and solid and should be differentiated from capillary phenomena*" (Gens (2010)). The relation between the total suction and the quantity of water stored in a porous medium is called the water retention curve. The quantity of water can be expressed in terms of water content or saturation degree. Since the saturation degree appears explicitly in the mass balance equation (cf. Eq. 2.45), it is preferred. A typical water retention curve can be seen in Fig. 2.10.

Four main domains can be distinguished :

- When the suction is lower than the air-entry pressure, the medium is fully saturated. The air entry pressure is the suction at which the pores start to be invaded by air.

- After the air entry pressure, the funicular state is reached. In this domain, the liquid phase is continuous while the gas phase is composed of bubbles.

- Then comes the pendular state in which neither phase is continuous. The liquid phase forms bonds between grains.

- The last domain is the residual state in which the saturation of the sample is equal to the residual saturation degree, S_{res} which corresponds to the quantity of water that cannot be extracted from the medium.
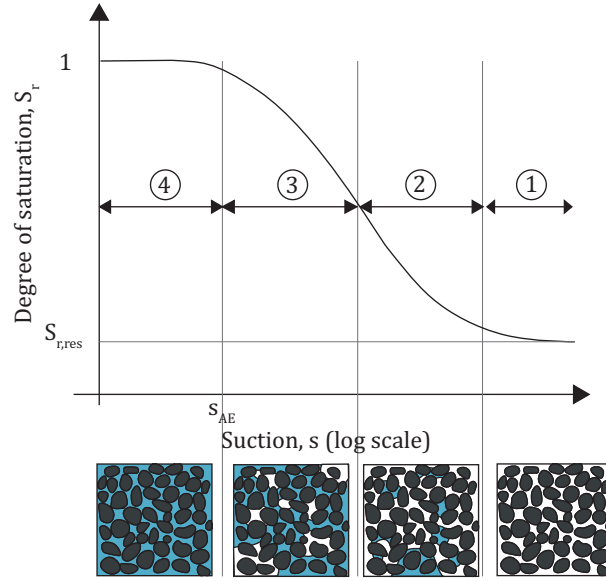
Figure 2.10: Water retention curve and the different domain of saturation in porous media (based on Dieudonné (2016) after Nuth and Laloui (2008))

In granular materials, the water retention behavior is directly controlled by the pore size distribution of the material. Under the hypothesis that the pores can be represented as a bundle of different size cylindrical tubes (Millington and Quirk (1959)), the pores start filling from the smallest to the biggest. The degree of saturation can thus be defined as :

$$S_{r,w}(X) = \int_{X_{min}}^{X} f(x) \, dx \tag{2.53}$$

where X_{min} is the smallest pore size and X is the biggest pore size currently filled with water. $f(x)$ expresses the pore size distribution. Jurin's law allows to associate a value of suction (because in this case, its definition is equivalent to the capillary pressure) to each pore size x. It is expressed as :

$$s(x) = \frac{2\sigma_{GL}cos\theta}{x} \tag{2.54}$$

where σ_{GL} is the surface tension of water and θ is the contact angle between water and solid phases. Inserting Eq. 2.53 in Eq. 2.54, it comes :

$$S_{r,w}(X) = \int_{X_{min}}^{X} f(\frac{2\sigma_{GL}cos\theta}{s}) \, dx = S_{r,w}(s) \tag{2.55}$$

where $S_{r,w}(s)$ is the water retention model. This curve can be drawn theoretically based on Jurin's law and the assumed pore size distribution but experimental curves often differ from theoretical ones. Empirical formulations have been suggested based on observations and experimental measurements. A large number of constitutive models have been developed to represent the water retention behavior of porous media. The most famous is the formulation suggested by Van Genuchten (1980) :

$$S_{r,w} = S_{res} + (S_{sat} - S_{res})(1 + (\frac{s}{\alpha_{vG}})^{n_{vG}})^{-m_{vG}} \tag{2.56}$$

in which $n_{vG} [-]$, $m_{vG} [-]$ are model parameters. n_{vG} is associated with the rate of desaturation of the soil while m_{vG} is linked to the curvature of the water retention curve for high suctions. $\alpha_{vG} [Pa]$ is a model parameter related to the air entry pressure, $S_{res} [-]$ is the water residual saturation, $S_{sat} [-]$ is the water maximum saturation and $s [Pa]$ is the suction.

2.5.2 Multiphasic flows in unsaturated porous media

Here, we introduce the description of the different fluids' transports in unsaturated porous media using a biphasic flow model. The mass flows introduced in Eq. 2.45 and Eq. 2.46 take into account the advection of each phase using Darcy's generalized law and the diffusion of the species within each phase using Fick's law. Due to the small amount of dissolved air in the liquid phase, the dissolved air's influence on the liquid phase properties is neglected. For the same reason, the liquid water diffusion within the liquid phase is also neglected.

2.5.2.1 Fluid internal transfers

The mass flows are expressed as :

$$f_{l,i}^{w} = \rho_w q_{l,i} \tag{2.57}$$

$$f_{g,i}^{w} = \rho_v q_{g,i} + i_{v,i} \tag{2.58}$$

$$f_{l,i}^{a} = \rho_{da} q_{l,i} + i_{da,i} \tag{2.59}$$

$$f_{g,i}^{a} = \rho_a q_{g,i} + i_{a,i} \tag{2.60}$$

where ρ_w, ρ_v, ρ_{da}, ρ_a are respectively the densities of the liquid water, the water vapor, the dissolved air and the dry air. $q_{l,i}$, $q_{g,i}$ are the advective fluxes of the liquid and of the gas phases with respect to the solid phase and $i_{v,i}$, $i_{da,i}$, $i_{a,i}$, are the non-advective fluxes (diffusion) of water vapor, dissolved air and dry air respectively. The water mass balance equation then becomes Richard's equation :

$$\underbrace{\frac{\partial}{\partial t} \left(\rho_w S_{r,w} n V \right) + \frac{\partial}{\partial x_i}(\rho_w q_{l,i})}_{\text{Liquid water}} + \underbrace{\frac{\partial}{\partial t} \left(\rho_v (1 - S_{r,w}) n V \right) + \frac{\partial}{\partial x_i}(\rho_v q_{g,i} + i_{v,i})}_{\text{Water vapor}} = Q_w \tag{2.61}$$

And the air balance equation is given by :

$$\underbrace{\frac{\partial}{\partial t} \left(\rho_a (1 - S_{r,w}) n V \right) + \frac{\partial}{\partial x_i}(\rho_a q_{g,i} + i_{a,i})}_{\text{Dry air}} + \underbrace{\frac{\partial}{\partial t} \left(\rho_{da} S_{r,w} n V \right) + \frac{\partial}{\partial x_i}(\rho_{da} q_{l,i} + i_{da,i})}_{\text{Dissolved air}} = Q_a$$
$$\tag{2.62}$$

where Q_w, Q_a are the injected water and air fluxes respectively.

Advective Flows Liquid water and gas advective fluxes are given by the generalization of Darcy's law for unsaturated cases. They correspond to the macroscopic velocity of each phase with respect to the solid phase (Eulerian description):

$$q_{l,i} = -\frac{k_{rel,w}(S_{r,w})k_{sat,ij}}{\mu_w}\left(\frac{\partial p_w}{\partial x_j} + \rho_w g_j\right) \tag{2.63}$$

$$q_{g,i} = -\frac{k_{rel,g}(S_{r,g})k_{sat,ij}}{\mu_g}\left(\frac{\partial p_g}{\partial x_j} + \rho_g g_j\right) \tag{2.64}$$

in which p_w, p_g are the water and gas pressures, μ_w, μ_g are the water and gas dynamic viscosities, $k_{rel,w}$ and $k_{rel,g}$ are the water and gas relative permeabilities and $k_{sat,ij}$ is the intrinsic saturated permeability. The intrinsic permeability depends exclusively on the material and is independent of the considered fluid, in contrast to the hydraulic conductivity which depends on the fluid characteristics:

$$K_{sat,ij} = \frac{k_{sat,ij}\rho_w g}{\mu_w} \tag{2.65}$$

The relative permeabilities take into account the change in cross section responsible for the fluid flows with the amount of liquid in the porous material. For a given degree of saturation, the water relative permeability is defined as the ratio between the unsaturated water permeability and the saturated water permeability. It takes a value of 0 in theoretically completely dry conditions and 1 in saturated conditions. The gas relative permeability is just the ratio of the unsaturated gas permeability to the gas permeability for dry conditions. The water relative permeability $k_{rel,w}$ can be determined based on the degree of water saturation and the formulation proposed by van Genuchten is chosen :

$$k_{rel,w} = \sqrt{S_{r,w}}\left(1 - \left(1 - S_{r,w}^{\frac{1}{m_{vG}}}\right)^{m_{vG}}\right)^2 \tag{2.66}$$

where $m_{vG}\,[-]$ is a model parameter.

The properties of the gas phase are defined based on the assumption that the gas phase is an *ideal mixture* of dry air and water vapor (Pollock, 1986; Gawin et al., 1996):

$$\mu_g = \left(\frac{\rho_a}{\rho_g \mu_a} + \frac{\rho_v}{\rho_g \mu_v}\right)^{-1} \tag{2.67}$$

$$\rho_g = \rho_a + \rho_v \tag{2.68}$$

Anisotropic intrinsic permeability   For anisotropic materials, the general form of the intrinsic permeability tensor requires nine components for the description of the flow characteristics. This number reduces to six by the symmetric property of the tensor. However most materials present limited forms of anisotropy and stratified materials require only two parameters for the description of the water flow: one parallel and another perpendicular to the stratification direction. For vertical layering (cf. Fig. 2.11), the intrinsic hydraulic permeability tensor is defined by :

$$\underline{\underline{k}}_{sat} = \begin{pmatrix} k_{sat,\parallel} & 0 & 0 \\ 0 & k_{sat,\perp} & 0 \\ 0 & 0 & k_{sat,\parallel} \end{pmatrix} \tag{2.69}$$

where $k_{sat,/\!/}$ and $k_{sat,\perp}$ are the intrinsic permeabilities parallel and perpendicular to the stratification, respectively.
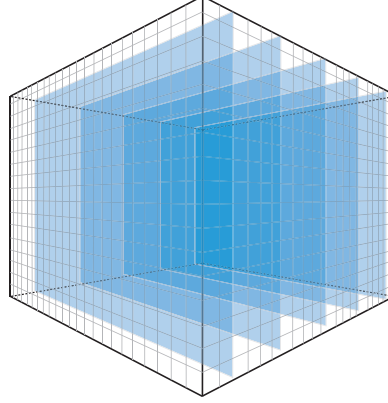

Figure 2.11: Vertical bedding planes for transverse istotropy

Diffusion   The diffusion of the species within each phase are assumed to follow Fick's law of diffusion in a tortuous medium. The diffusion of vapor in the gas phase and of dissolved air in the liquid phase are linked to vapor and dissolved air density gradients respectively:

$$i_{v,i} = -D_{v-a}\tau_v n S_{r,g}\rho_g \frac{\partial}{\partial x_i}\left(\frac{\rho_v}{\rho_g}\right) = -i_{a,i} \tag{2.70}$$

$$i_{da,i} = -D_{da-w}\tau_v n S_{r,w}\rho_w \frac{\partial}{\partial x_i}\left(\frac{\rho_{da}}{\rho_w}\right) \tag{2.71}$$

where D_{v-a}, D_{da-w} are the molecular diffusion coefficients of the vapor in the gas phase and of the dissolved air in the liquid water. τ_v $[-]$ is the tortuosity of the porous medium.

2.5.2.2   Liquid density variation

The liquid water density ρ_w is a function of the water pressure p_w and of the temperature, T:

$$\rho_w = \rho_{w,0}\left(1 + \frac{p_w - p_{w,0}}{\chi_w} - \alpha_w(T - T_0)\right) \tag{2.72}$$

where $\rho_{w,0}$ is the liquid water density at the reference water pressure, $p_{w,0}$, T_0 is the initial temperature, χ_w is the liquid water isotropic bulk modulus and α_w is the volumetric thermal expansion coefficient of water.

2.5.2.3   Gas density variation

The gas phase is considered as an ideal mixture of ideal gases, in this work dry air and water vapor. It comes :

$$p_g = p_a + p_v \tag{2.73}$$

23

The density of the gas phase is obtained using Dalton's law :

$$\rho_g = \rho_a + \rho_v \tag{2.74}$$

where ρ_a and ρ_v are respectively the densities of dry air and water vapor.

$$\rho_a = \frac{M_a}{RT} p_a \tag{2.75}$$

$$\rho_v = \frac{M_v}{RT} p_v \tag{2.76}$$

where R is the universal gas constant, T is the absolute temperature in Kelvin, and M_a and M_v are respectively the molecular mass of dry air and water.

2.5.3 Heat diffusion

To be able to simulate the temperature evolution within the medium, we use the classic governing energy balance equation defined previously in the derived balance equation (Eq. 2.47). The enthalpy of the system is expressed as the sum of each constituent enthalpy (Collin (2003)):

$$S_T = (nS_{r,w}\rho_w c_{p,w}(T - T_0) + n(1 - S_{r,w})\rho_a c_{p,a}(T - T_0) \tag{2.77}$$
$$+ n(1 - S_{r,w})\rho_v c_{p,v}(T - T_0) + (1 - n)\rho_s c_{p,s}(T - T_0)) \tag{2.78}$$

in which, $c_{p,w}$, $c_{p,a}$, $c_{p,s}$ and $c_{p,v}$ are respectively the water, the air, the solid and the vapor specific heats, ρ_w, ρ_a, ρ_s and ρ_v are respectively the water, the air, the solid and the vapor densities.

The heat flux consists of a conduction term proportional to the thermal conductivity of the porous medium and a convective term related to the heat transported by fluid flows. Since an updated Lagrangian referential basis is used, the convection of the solid phase is automatically taken into account :

$$V_{T,i} = -\Gamma \frac{\partial T}{\partial x_i} + c_{p,w}\rho_w q_{l,i}(T - T_0) + c_{p,a}(\rho_a q_{g,i} + i_{da,i})(T - T_0) \tag{2.79}$$
$$+ c_{p,v}(\rho_v q_{g,i} + i_{v,i})(T - T_0) \tag{2.80}$$

where Γ is the porous medium thermal conductivity, T_0 is the initial temperature and T is the temperature. The thermal conductivity can be described in a few different ways. It can be based on a simple arithmetic average :

$$\Gamma = (1 - n)\Gamma_s + nS_{r,w}\Gamma_l + n(1 - S_{r,w})\Gamma_g \tag{2.81}$$

This formulation represents parallel conductivity between the different phases. The conductivity has also been shown (Gens and Olivella (2001)) to be accurately described by a geometric average of the conductivity of the different phases :

$$\Gamma = \Gamma_s^{(1-n)} + \Gamma_l^{nS_{r,w}} + \Gamma_g^{n(1-S_{r,w})} \tag{2.82}$$

This is a serial conductivity approach. In those approaches, the conductivity depends on the volume fraction of the phases. Semi-empirical formulations have also been expressed, such as :

$$\Gamma = aS_{r,w} + b \tag{2.83}$$

where a and b are model parameters. In this case, the conductivity is only function of the water saturation degree.

The energy required for the evaporation depends on the quantity of water switching phases which can be obtained when looking at the vapor balanced equation (cf. Eq. 2.43):

$$\dot{E}^{w-v}_{H_2O} = \frac{\partial}{\partial t}\left(m_g^w\right) + \frac{\partial}{\partial x_i}(f_{g,i}^w) \tag{2.84}$$

So the terms linked to the evaporation of water in Eq. 2.47 are expressed as:

$$\frac{\partial}{\partial t}\left(m_g^w\right)L = \frac{\partial}{\partial t}(n(1 - S_{r,w})\rho_v)L \tag{2.85}$$

$$\frac{\partial}{\partial x_i}(f_{g,i}^w)L = \frac{\partial}{\partial x_i}(\rho_v q_{g,i} + i_{v,i})L \tag{2.86}$$

2.5.4 Mechanical model

The momentum balance equation 5.3 introduces the total stress tensor but the mechanical behavior of a porous media is not controlled only by the total stress but also by the pore fluid pressures. Alternative stress definitions are thus necessary to describe that behavior. For unsaturated porous media, two main approaches exist : the extended effective stress approach or the independent variables approach.
No mechanical constitutive law is presented in this section. The mechanical law will be presented in chapter 5 and chapter 7 describing the simulation of the drying behavior of each of the studied materials.

2.5.4.1 Effective stress approach

Terzaghi introduced the notion of effective stress in 1936 (Terzaghi (1936)) to describe the behavior of saturated porous media. This was based on observations that the change in bulk volume was only influenced by the difference between confining and pore pressures. The effective stress is thus the stress effectively acting between solid grains. Terzaghi suggested the following formulation :

$$\sigma'_{ij} = \sigma_{ij} - p_w\delta_{ij} \tag{2.87}$$

where δ_{ij} is the Kronecker symbol defined as :

$$\delta_{ij} = \begin{cases} 1, & \text{if } i = j \\ 0, & \text{if } i \neq j \end{cases} \tag{2.88}$$

For unsaturated porous media, Terzaghi's formulation is extended to include the effect of both fluids. The most famous formulation is the one suggested by Bishop (Bishop (1959)):

$$\sigma'_{ij} = \sigma_{ij} - p_g \delta_{ij} + \chi(p_g - p_w)\delta_{ij} \tag{2.89}$$

where χ is a material parameter called Bishop's parameter which depends on the saturation degree. It varies from 0 for a dry medium to 1 for a saturated one (and the formulation is thus equivalent to Terzaghi's formulation). Following experimental studies on unsaturated soils, number of authors have also been able to link Bishop's parameter to various factors such as soil type, microstructure and followed stress paths (Bishop and Blight (1963); Jennings and Burland (1962)). Nontheless, the most common formulation has been suggested by Schrefler (1984) and considers χ equal to $S_{r,w}$ and even though it is a simplification, this formulation will be used in the rest of this work.

When working with constitutive models for unsaturated parous media, the main advantage of the effective stress approach is that the models previously developed for saturated media are easily extended to the unsaturated domain. In addition, there is a continuous and smooth transition from saturated to unsaturated states. However, the determination of the different model parameters from laboratory tests is often complex. In addition, the effective stress approach is incapable of reproducing the collapse phenomenon upon wetting paths under high stress levels. Indeed, upon hydration, the fluid pressure increases, producing a decrease in the effective stress and the sample swells whereas compaction is experimentally observed. This problem is solved by introducing suction as a variable and defining a Loading-Collapse curve (Jommi and di Prisco (1994).

2.5.4.2 Independent variables approach

According to Fredlund and Rahardjo (1993), the number of independent variables is directly linked to the number of phases. For a saturated porous material, only one variable is required: the effective stress. For partially saturated soils, Bishop and Blight (1963), Fredlund and Morgenstern (1978) and Alonso et al. (1990), among others, showed that two independent variables enable to overcome the limitations of the single effective stress. In particular, Fredlund and Morgenstern (1978) demonstrated that any pair of $\sigma_{ij} = \sigma_{tot,ij} - p_g \delta_{ij}$ (the net stress tensor), $\sigma'_{ij} = \sigma_{tot,ij} - p_w \delta_{ij}$ (the effective stress tensor) and suction $s = p_g - p_w$ could be used to describe the behavior of unsaturated soils. In most cases, the net stress and suction are selected to work in the unsaturated domain. The choice of this couple of variables is justified by the fact that the variables are directly accessible during experimental tests. Once that the material is saturated, the effective stress is often used instead of the net stress. The main drawbacks of the independent variables approach are that the extension of constitutive models for saturated materials is not straightforward and that there might not be any continuity in the transition between saturated and unsaturated states.

The first and most famous complete constitutive model for unsaturated soils is the Barcelona Basic Model (BBM) developed by Alonso et al. (1990). The model uses suction and net stress as independent variables. An important contribution of the BBM is the definition of the Loading-Collapse (LC) curve. This yield surface represents the evolution of the preconsolidation pressure with suction, and allows to reproduce the collapse phenomenon upon wetting under high stress level.

2.5.4.3 Solid grain density variation

In the case of an anisothermal problem, the solid grains density ρ_s is a function of temperature T :

$$\rho_s = \rho_{s,0}\left(1 - \alpha_s(T - T_0)\right) \tag{2.90}$$

where $\rho_{s,0}$ is the solid grain density at the reference temperature, T_0, and α_s is the thermal expansion coefficient of the solid grains.

2.5.4.4 Thermal expansion of the solid skeleton

When the temperature increases, all the constituents of a porous medium dilate according to their volumetric thermal expansion coefficient (cf. sections 2.5.2.2 and 2.5.4.3). Following their work on ceramics, Kingery (1976) proposed a formulation to determine the global linear expansion coefficient of a composite material :

$$\alpha = \frac{\sum_i \alpha_i \eta_i K_i / \rho}{\sum_i \eta_i K_i / \rho} \tag{2.91}$$

where η_i is the volume fraction of the phase, K_i is the bulk modulus of the phase and ρ is the bulk density of the mixture. The bulk modulus of the phase intervenes because each particle's expansion is restrained by the surrounding particles. Hence, the most rigid particles expand more easily than compressible particles. Gas does not affect the macroscopic thermal expansion of the medium because of its very high compressibility. In the rest of this work, the expansion coefficient is a constant.

2.6 Equilibrium restrictions

Equilibrium restrictions are required to link the different phases of each species and are obtained by assuming thermodynamic equilibrium between the different phases of the species.

2.6.1 Kelvin's Law

In this work, we assume that water vapor is always in thermodynamic equilibrium with liquid water. Kelvin's law expresses the pressure of water vapor, p_v, as a function of the suction, s :

$$p_v = p_v^0 e^{\left(\frac{-sM_w}{RT\rho_w}\right)} \tag{2.92}$$

where p_v^0 is the saturated pressure of water vapor. For a given temperature, the saturated pressure of water vapor is a constant (Garrels and Christ (1965); Ewen and Thomas (1989)). M_w is the molar mass of water, R is the universal gas constant and T is the temperature.

2.6.2 Henry's law

Henry's law expresses the equilibrium between dissolved air in the liquid phase and dry air in the gas phase. Under constant temperature, the molar fraction of dissolved air, x_l^a, is proportional to the air's partial pressure :

$$p_a = K_l^a x_l^a \tag{2.93}$$

where K_l^a is a constant. It can also be written in terms of densities and gives :

$$\rho_{da} = H_a \rho_a \tag{2.94}$$

where H_a is Henry's coefficient. Its value depends on temperature, pressure and gas type.

2.7 Thermo-hydro-mechanical couplings

In this section, all the couplings encountered in the framework presented in this chapter are emphasized. A summary is displayed at Fig.2.12:
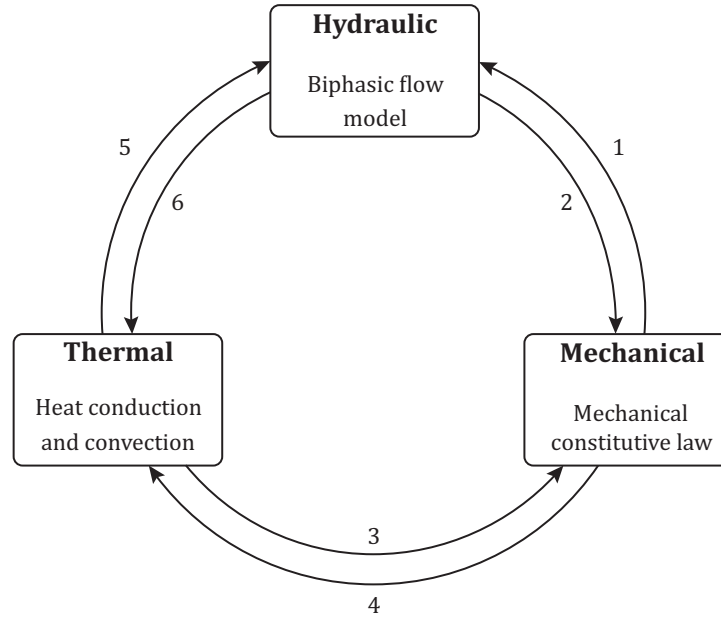

Figure 2.12: Summary of all the coupling encountered in the thermo-hydro-mechanical framework

As can be seen there are six different couplings :

- **1 M-H** Changes in porosity affect the fluids' storage capacity and the permeability of the porous medium. Since the changes in porosity are linked to a change in volume through equation 2.42 they are directly linked to the mechanical constitutive law chosen. In the case of drying and more specifically of desiccation cracking, the fractures created constitute preferential flow paths with increased permeability.

- **2 M-H** Variation of the pore pressure and suction directly affect the mechanical state of the porous medium through the use of Bishop's effective stress formulation (or in the case of independent variables the use of a couple of stresses - net stress and suction) for unsaturated porous media (cf. Eq. 2.89). There is also a lesser effect manifested in a change of apparent density of the mixture with a change in saturation degree.

- **3 T-M** When the temperature increases the solid skelleton as well as the solid grains will dilate with respect to Eq. 2.90.

- **4 M-T** This coupling is very similar to **1 - H-M**. Changes in porosity affect the heat storage capacity of the medium as well and the thermal conductivity (cf. Eq. 2.82).

- **5 T-H** Temperature affects the properties of the fluids. Particularly, the viscosity and density of the fluids are directly related to a change in temperature through Eq. 2.72, Eq. 2.75 and Eq. 2.76.

- **5 - H-T** The heat convection through the fluid phases is an obvious hydro-thermal coupling because the quantity of heat transferred depends on the fluid flows as seen in Eq. 2.80.

2.8   Conclusion

This chapter focuses on the conceptual modeling of the thermo-hydro-mechanical processes at the macroscopic scale. Its objective is to introduce the existing framework used to represent the **T-H-M** behavior of drying materials and it does not aim at presenting any new contributions. The approach adopted in this work consists in representing the studied materials as unsaturated porous media composed of solid, liquid and gas phases, which are assumed to be in thermodynamic equilibrium.
The governing balance equations are expressed in the usual differential local form. They are developed in updated Lagrangian configuration which is typical of large deformation problems. The compositional approach is used to express them for each species rather than for each phase. The balance of momentum is expressed for the entire mixture.
Constitutive relations are defined to link the governing equations to the variables of the problem. A water retention model, a multiphasic flow model, a heat diffusion law are detailed. No mechanical constitutive law is presented in this section. The mechanical laws will be presented in the chapters describing the simulations of each of the studied material's drying behavior. However, the link between pore fluid pressure and mechanical behavior is addressed and the notion of effective stress is introduced and explained.

This thesis is about the drying, shrinkage and desiccation cracking of porous media. Hence, the theory of porous medium was obviously a required stepping stone before going any further. Now that the first milestone is cleared, the next step towards the end goal of this work is to talk about drying. The next chapter focuses on the establishment of all the notions and models specific to the drying process.

Chapter 3

Drying and shrinkage processes

Contents

3.1 Introduction

From the beginning, man has been conducting drying experiments, willingly or not. From the very first clay bowl to the modern lyophilization, drying has played an important role in our daily life. A good understanding of the mechanisms at play has proved crucial to the improvement of many industrial processes. Indeed, drying is an essential operation in chemical and pharmaceutical industries as well as for conservation in the food industry or in manufacturing processes involving granules or powders. It is also essential to the civil engineer because drying and its most direct consequence, shrinkage, can have catastrophic consequences on the stability of infrastructures.

In this thesis, the influence of drying on the shrinkage and cracking of porous materials is studied. In the previous chapter, the notion of porous medium and the different concepts associated

with it were introduced. Following the same pattern of starting by laying down a comprehensive knowledge base to introduce the concepts required to understand the physic at play, this chapter starts by defining a series of notions specific to drying experiments. Then an overview of the different means of drying is presented. In this work, convective drying with a wind tunnel like technique is used. Since this work is based on a convective drying method, a detailed analysis of the drying kinetics that can be obtained with such a method is presented. A short review of the history of convective drying is also produced followed by a detailed presentation of the *boundary layer model*. It is added to the set of governing equations presented in chapter 2 to take into account the porous medium - atmosphere interactions. Finally the shrinkage phenomenon is explained.

3.2 Definition

In Chapter 2, all the concepts required to understand the behavior of porous media were introduced and the different phenomena and their interactions were explained. But drying is an engineering field at the junction between soil (porous medium) and chemical engineering and as such possesses its own vocabulary that needs to be defined.

Drying and shrinkage Drying refers to the mass transfer process consisting of the removal of a solvent from a solid by evaporation and the elimination of the gas phase formed (Leonard (2002)). In most cases, the solvent is water. Desiccation can be considered as a synonym to drying. However, it should be noted that in most scientific fields, the word has been used in a less restrictive sense, with the idea that drying was coupled with changes affecting the solid (shrinkage for example). More specifically, in the field of soil mechanics, desiccation commonly refers to the loss of water by evaporation linked either to a preconsolidation or an air invasion mechanism (Terzaghi (1936)). Throughout this work, the word "drying" will refer to "moisture removal initiated by evaporation" and when changes of bulk volume will be considered, the term "drying shrinkage" or "shrinkage" will be adopted.

Relative humidity Most drying processes involve the use of humid air at a controlled temperature and relative humidity. This leads to the necessity of defining the concept of *relative humidity*, RH. The relative humidity is the ratio of the partial pressure of water vapor, p_v, to the equilibrium vapor pressure of water, p_v^0, at a given temperature:

$$RH = \frac{p_v}{p_v^0} \tag{3.1}$$

Relative humidity depends on the temperature and pressure of the system. It requires less water vapor to attain high relative humidity at low temperatures, for example.

Dry bulb temperature The dry-bulb temperature, T_{db}, is the temperature read on a thermometer exposed to air but shielded from radiation and moisture. It is commonly called the "ambient air temperature". It is the true thermodynamic temperature since it is directly proportional to the kinetic energy of the air molecules. The temperature is usually measured in degrees Celsius $[°C]$ but the SI unit is the Kelvin $[K]$.

Wet bulb temperature   The wet-bulb temperature, T_{wb}, is the temperature a volume of air would have if it was adiabatically brought to saturation by evaporation of water. This means that all the latent heat required for the evaporation is supplied by the volume of air leading to a decrease in temperature while the vapor pressure increases due to evaporation (cf. Fig. 3.1).
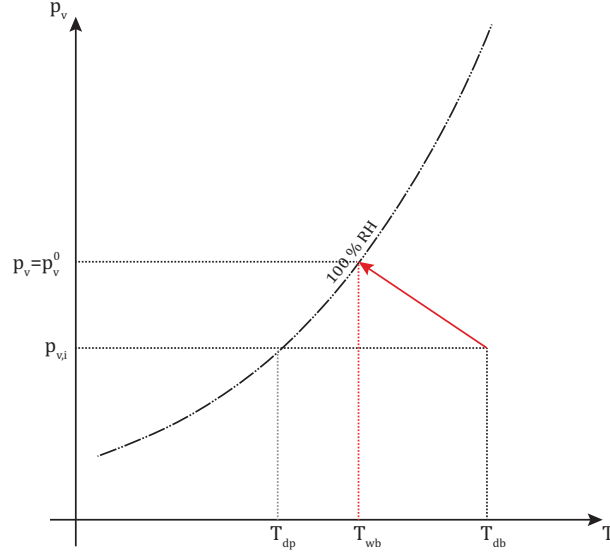

Figure 3.1: Wet bulb temperature

It is thus the lowest temperature that can be reached under ambient conditions by the evaporation cooling only. Wet-bulb temperature is determined by air temperature and the amount of moisture in it. It can be measured by using a thermometer with the bulb wrapped in wet muslin (Dunlop (2008)). At 100% relative humidity, the wet-bulb temperature equals the ambient air temperature. The wet bulb temperature can be determined using the following iterative formulation (Gerard (2011)):

$$T_{wb} = \frac{1810.8\left(p_v^0\left(T_{wb}\right) - p_v\right) - T_{db}\left(p_{atm} - p_v^0\left(T_{wb}\right)\right)}{2p_v^0\left(T_{wb}\right) - p_v - p_{atm}} \tag{3.2}$$

where p_{atm} is the standard atmospheric pressure defined as $101300\,[Pa]$.

Dew point temperature   The Dew Point, T_{dp}, is the temperature where water vapor starts to condense out of the air (the temperature at which air becomes completely saturated). Above this temperature the moisture stays in the air. A higher relative humidity means that the dew point is closer to the ambient air temperature.

3.3   Different types of drying processes

In the introduction 1, we showed that drying is used in a vast variety of engineering fields. Depending on the material, the end result desired, the means available or the scale of the process, different forms of drying processes can be employed. In the following section, a summary of a number of drying methods applied to the field of soil engineering is presented. Other methods

such as freeze drying and radiation drying are very briefly brought up since they are mostly applied to the fields of food-drying and pharmaceutical industry and are not relevant to the materials studied in this thesis.

Most drying techniques in the field of soil mechanics revolve around a simple principle : the imposition of a controlled temperature and relative humidity at the boundary of the porous medium being dried. This boundary condition leads to a change in capillary pressure inside the medium and thus to a change in saturation or water content. Many experimental set-ups have been developed over the years to apply that principle. In particular, the suction control methods and convective drying methods will be detailed in this work.

3.3.1 Suction control methods

Three main techniques have been developed to control suction within a porous medium sample.

Vapor control technique   This technique consists in imposing a constant relative humidity to a sample through the use of saline solutions. The sample is placed in an hermetically closed chamber containing the saline solution as depicted in Fig. 3.2. The nature and the concentration of the saline solution will dictate the relative humidity inside the chamber (Delage et al. (1998)). Water transfer happens in vapor phase and the total suction is therefore controlled. This technique can impose a total suction of up to several hundreds of MPa. The water transfers are recorded using a high accuracy scale to measure the mass variation of the sample. The relative humidity inside the chamber is also influenced by the temperature. This is why it is important to place the chamber in a room with a constant and controlled temperature. The temperature and relative humidity inside the chamber are nonetheless controlled to check the validity of the experiment. The main drawback of the method is the very long time needed for the sample to reach the desired total suction. It is a method commonly applied to soil samples to study the influence of suction on the material properties. (see for examples Oteo-Mazo et al. (1995) ; Alonso and Oldecop (2003))
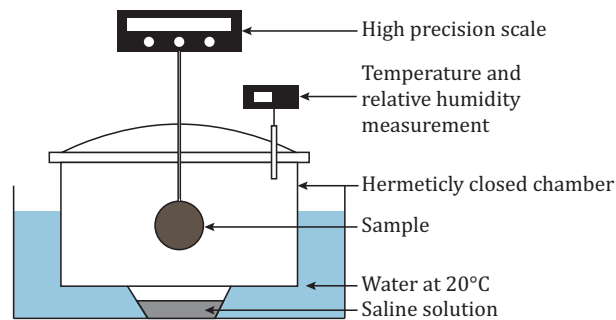

Figure 3.2: Suction control using saline solutions

3.3.1.1 Axis translation (Hilf (1956))

The principle of the axis translation technique is based on the definition of the matric suction $s = p_g - p_w$, where p_g and p_w are respectively the air and water pore pressures. The method

involves the translation of the reference pore gas pressure p_g through an artificial increase of the air pressure inside the sample. The water pressure p_w within the sample is controlled, so that a matric suction is imposed to the sample. In order to maintain this suction, a high air-entry value ceramic disc is used at the interface between the unsaturated sample and the water in the measuring system (cf. Fig. 3.3). The air-entry value of the ceramic disc limits the application of the axis translation technique to suctions up to $1.5 MPa$.
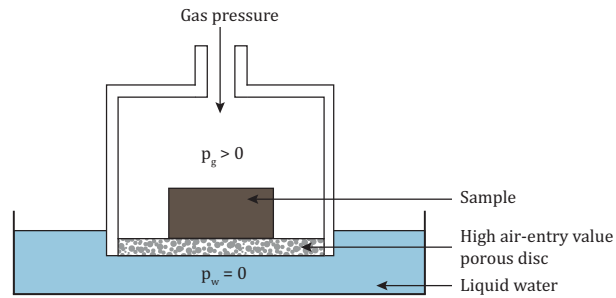

Figure 3.3: Principle of the axis translation method (Richards (1941))

3.3.1.2 Osmotic method (Cui and Delage (1996))

The osmotic technique is based on the principle of osmosis. It consists in placing in contact, through a semi-permeable membrane, a soil specimen and an aqueous solution of large sized polyethylene glycol (PEG) molecules (cf. Fig. 3.4). Since PEG molecules cannot cross the membrane, a difference of chemical concentration, hence osmotic suction, is maintained between the sample and the PEG solution. In order to balance the water potentials, water transfer occurs between the soil and the PEG solution until reaching a given matric suction. Depending on the PEG concentration, suctions ranging between 0.1 and 10 MPa may be imposed.
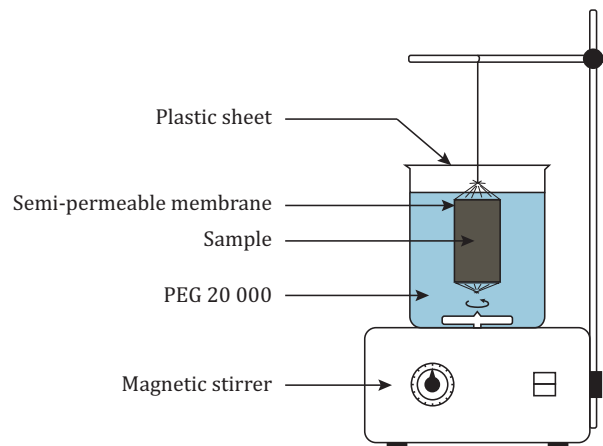

Figure 3.4: Principle of the osmotic method (modified after Delage et al. (2001))

3.3.2 Evaporation

3.3.2.1 Free water evaporation

The principle of this test is very simple : a stainless steel recipient is filled with water and left in the *in situ* field. The water level in the recipient is measured at regular intervals which makes it possible, knowing the dimensions of the recipient, to calculate the mass variation and thus the evaporation flux. This is an *in situ* method and it thus presents the advantage of measuring the mass transfer in the exact field conditions. It is also very easy to use. Its main drawbacks are that those conditions (i.e. air temperature, air flow velocity, relative humidity) are not controlled and are subject to important and frequent variations which makes model calibration based on this method tedious and difficult. It is, also, only able to measure the potential evaporation rate (i.e. the water flux from a free surface of water under given atmospheric conditions (Wilson et al. (1994)). It thus completely neglects the variation in evaporation flux due to the development of capillary effects in a porous medium.

3.3.2.2 Lysimeter or *in situ* evaporation

A lysimeter is a measuring device which can be used to measure the evaporation. By recording the amount of precipitation that an area receives and the amount lost through the soil, the amount of water lost by evaporation can be calculated (Liu et al. (2002)). A sketch of the setup can be seen in Fig. 3.5. A large tank is filled with soil within which *in situ* conditions are reproduced as accurately as possible. Under the tank is a measurement unit that records the mass variation of the soil within the tank. If the system is well designed, installed and maintained it is the most accurate evaporation measurement system (Johnson et al. (2005)).
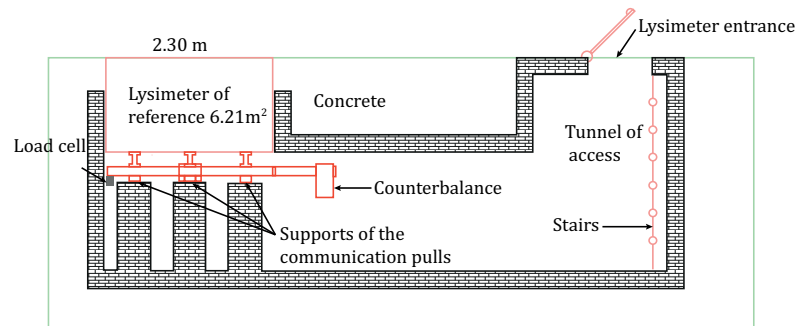

Figure 3.5: Exemple of a lysimeter (LOP (2006))

3.3.2.3 Soil column

A cylindrical container (most commonly made of stainless steel or plastic) is filled with a granular material (most commonly soil) (see Fig 3.6). The material is installed in the container under controlled conditions (i.e. density and water content) with the goal of reproducing as closely as possible *in situ* conditions. The mass variation is recorded through a scale located under the column. Sensors can also be installed at different heights throughout the column to measure local parameters such as suction and temperature (Wilson et al. (1997)). The influence of the groundwater table level on the drying kinetics can also be studied with this experiment (Hernández-López et al. (2014)).
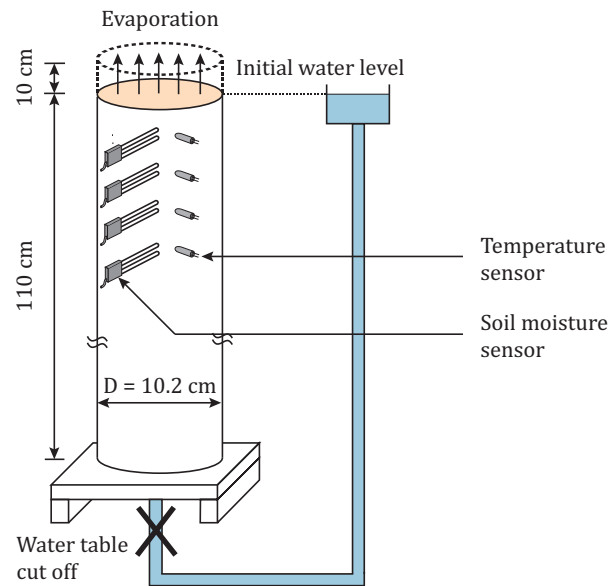
Figure 3.6: Evaporation in a soil column set up (after Smits et al. (2011))

3.3.3 Convective drying methods

Convective drying refers to methods in which a warm humid air flow is used to transfer the energy needed for the water to evaporate and the subsequent transport of the water vapor out of the medium. Different apparatus can be used to impose the air flow and measure the subsequent water transfers. The most common ones are presented hereafter.

3.3.3.1 Environmental chamber

This setup includes an environmental chamber (for example a transparent acrylic tank). The chamber is filled with a compacted soil (to a chosen density). Some more sophisticated designs also include an air supply and an air collection unit to control the air flow properties. If the influence of the water table is of concern, a water supply unit can also be installed. Such an evolved design has been used by Song et al. (2013) and can be seen in Fig. 3.7. Upon initiation of the drying test, the wind supply unit blows an air stream with a controlled air-flow rate, temperature, and relative humidity to the chamber. The air collection unit records the temperature and relative humidity of the moist air passing through the chamber. The water supply unit can control the water table level. The difference between the relative humidity of the injected and collected air flows gives us the moisture balance and thus the water mass evaporated from the granular material. Different sensors can be placed inside the granular material to record the local evolution of the temperature or the water content during the experiment. Note that depending on the design, this experiment is an evaporation or a convective drying setup.

3.3.3.2 Wind Tunnel

This system consists is an artificial tunnel in which a humid air flow is imposed. The sample is placed on a tray inside the tunnel (cf. Fig 3.8). The relative humidity, temperature and
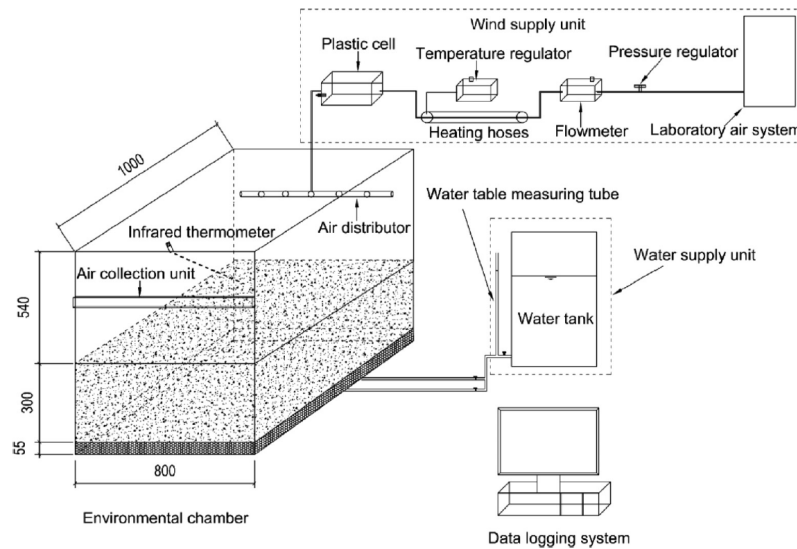
Figure 3.7: Experimental setup of the environmental chamber used by Song et al. (2013)

velocity of the air flow are controlled. During the experiment, the sample is weighed at regular intervals to determine the drying kinetics. This is the drying method chosen to perform the drying experiments conducted in the framework of this thesis. This method has been chosen because the samples used are of small dimensions and do not require the use of heavier setups like soil columns or environmental chambers. In the following chapter and until the end of this thesis the term "*convective drying*" will refer to a wind tunnel like technique.
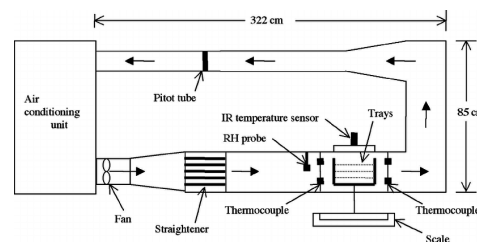
Figure 3.8: Scheme of a convective dryer of wind tunnel type

3.3.4 Other drying methods

3.3.4.1 Freeze drying (Nireesha et al. (2013))

Freeze-drying - technically known as lyophilization, or cryodesiccation - is a dehydration process typically used to preserve a perishable material or make the material more convenient for transport. Freeze-drying works by freezing the material and then reducing the surrounding pressure to allow the frozen water in the material to sublime directly from the solid phase to the gas phase.

3.3.4.2 Radiation drying

Radiant heat is transmitted by electromagnetic waves rather than by contact between two surfaces. Heat from a radiant heater will pass through air (or water) and heat the sample directly. The solid will then deliver that heat to the water by conduction (assuming that the solid's conduction is high enough). The heat delivered to the water will facilitate its evaporation while more heat is added to overcome evaporative cooling (Ekechukwu and Norton (1999)). A low flow of dry air over the surface being dried will accelerate evaporation. Radiation drying can be used to dry a sample through a transparent material.

3.4 Drying Kinetics (in the case of convective drying)

Classical experimental convective drying devices allow for the measurement of the mass during the experiment. The drying kinetics can be expressed based on those weight measurements (Figure 3.9(a)).

Those measurements can be used to produce the two other curves that can be used to analyse the drying kinetics : drying rate vs. time (it is actually a flux since it is per surface area) (Fig. 3.9(b)) and drying rate vs. water content (Fig. 3.9(c)), called Krischer's curve (Kemp et al. (2001)). Krischer's curve is used because it gives a clearer picture of the drying kinetics of materials (Léonard et al. (2002); Kowalski (2012)). Krischer's curve is studied in parallel with the changes in temperature (Figure 3.9(d)) at the surface of the sample. The behavior observed in the case where the drying air temperature is significantly higher than the sample's initial temperature (Gerard et al. (2010)) is visible in Figure 3.9(d). This was also measured experimentally by Musielak and Jacek (2007).

If the material is un-deformable then the drying rate is directly obtained through derivation of the mass loss with time. Otherwise, the variation of the external drying surface is needed as visible in Eq. 3.3:

$$q = \frac{\delta m}{\delta t} \frac{1}{S(w)} \tag{3.3}$$

where m is the medium mass, t is the time, S is the external drying surface and w is the gravimetric water content.

Based on those curves, three periods can be observed (Idso et al. (1974)):

- I : Preheating Period

- II : Constant Rate Period (CRP)

- III : Falling Rate Period (FRP)

3.4.0.1 Preheating period

The first phase is very short and corresponds to an increase in drying rate. The temperature at the surface of the sample increases from its initial value to the temperature of the wet bulb (Gerard et al. (2010)).
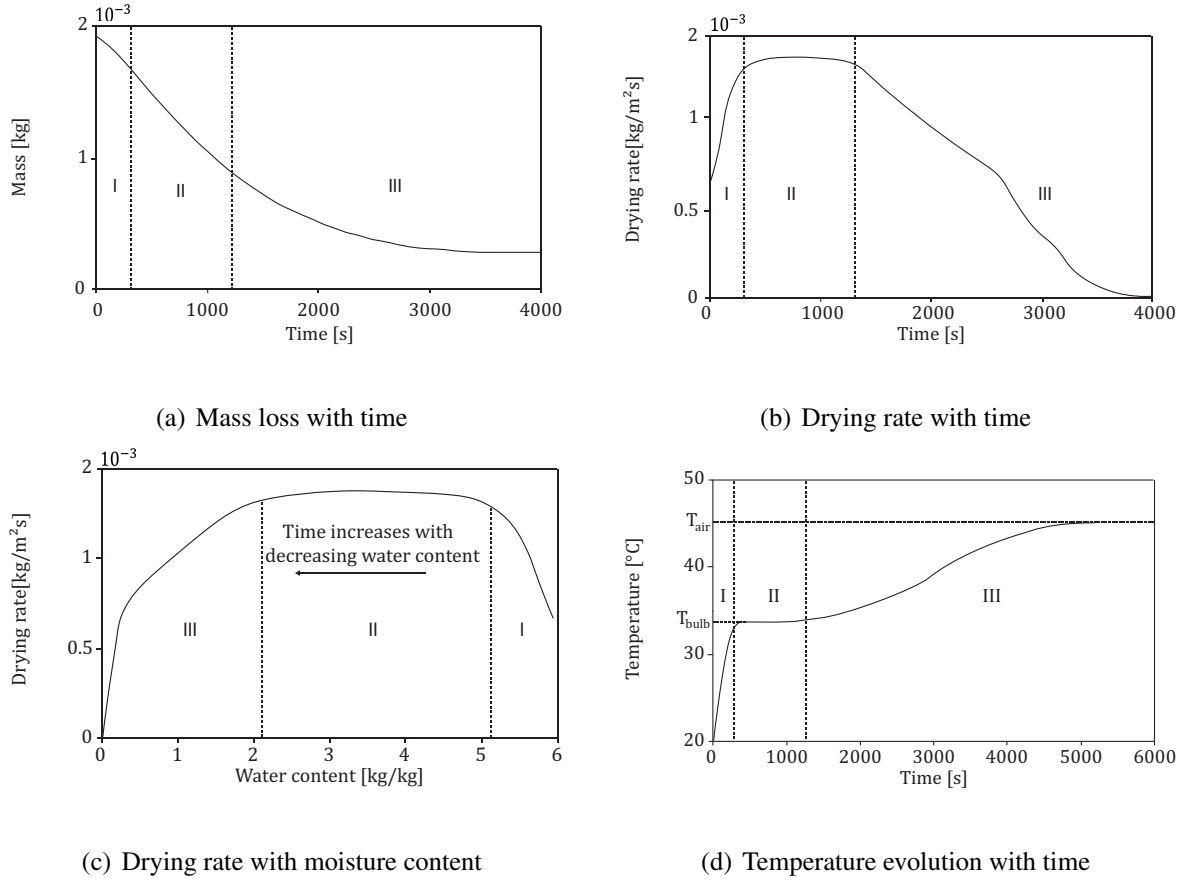
(a) Mass loss with time

(b) Drying rate with time

(c) Drying rate with moisture content

(d) Temperature evolution with time

Figure 3.9: Drying kinetics

3.4.0.2 Constant Rate Period (CRP)

Experimentally, the Constant rate period is observable at the begining of the drying experiment. The drying rate reaches a plateau even though the saturation of the medium decreases. The heat from the drying air is completely used for the evaporation of the liquid water at the surface of the sample and the temperature therefore remains constant and equal to the temperature of the wet bulb. The evaporation occurs in a saturated boundary layer. During this phase, the internal water transfers, namely liquid water advection and liquid water and vapor diffusion, are intense enough for the drying process to be limited by the capacity of the drying air to evaporate the water at the drying surface. The drying process is thus mostly influenced by external conditions, i.e. the drying temperature and the air velocity (Nadeau and Puiggali (1995); Geankoplis (1993)). This period will last until the sample saturation decreases enough and internal transfers start to influence the drying rate.

3.4.0.3 Parameters influencing the CRP

The drying rate during the CRP is assumed to be almost only dependent on the external conditions but previous works have shown (Shaw 1987) that the drying rate for a porous medium is higher than the one observed for a free water surface under the same drying conditions. Shaw's experiments showed that the drying rate from a cell filled with glass beads and water was higher

40

than the one recorded from the same cell but only filled with water. This is suggested to be due to the circulation of water along the punctual contacts between particles, which maintains a continuous water flux to the surface whereas in the case of the free water surface, water transfers are limited to vapor diffusion through air. Tournier (2006) confirmed that theory with experiments conducted on free water surfaces and soil samples. Tournier (2006)'s experiments also exhibited that the drying rates differ from a material to another. Gerard (2011) arrived to the same conclusion when he found different water transfer coefficients for different soils (silt and clay).

To explain that difference from one porous material to another, the effective drying surface has been suggested to be the deciding parameter. The effective drying surface is the surface of water in contact with the atmosphere. Tournier (2006) proved, using optical rugosimetry, that the effective drying surface of a rock (or soil) is bigger than the macroscopic section of the sample (and thus bigger than the equivalent free water surface) because of capillary and adsorption effects. The effective drying surface is dependent on pore size and distribution and saturation degree.

3.4.0.4 Falling Rate Period (FRP)

As the saturation of the medium decreases, the water's relative permeability also decreases and the internal transfers start limiting the drying process. This is followed by a decreasing drying rate until the medium reaches the equilibrium water content corresponding to the drying conditions (this equilibrium water content is only dependent on the temperature and the relative humidity of the drying air). The FRP is also characterized by an increase in the dried body temperature from the wet bulb temperature to the drying air temperature since there is, now, an excess in heat supply.

3.4.1 Transition between the CRP and the FRP

Until recently only two approaches were traditionally considered to explain the decrease in drying rate : the "receding front model" and the "wetted surface model". But recently more and more works describe the concept of "Hydraulic connection layer".

3.4.1.1 The receding front model

In this model, the transition from the CRP to the FRP happens when all the free water at the surface of the sample has been removed. This corresponds to the first decrease in drying rate as visible on Fig. 3.10. This moment is defined by a critical water content, w_{crit}. After this point, the drying front that was at the surface progresses through the medium and the internal resistances to water and heat transfers will control the drying rate. When all the free water has been removed, a second decrease in drying rate occurs as shown on Fig. 3.10 because of the strong bonds anchoring the bound water to the solid skeleton.

3.4.1.2 The wetted surface model

The decrease in drying rate is linked to the presence of dry zones at the surface of the sample. If the drying rate is compared to the portion of the surface that is wet, it is constant. This decrease lasts until the drying surface is completely dry (Keey (1979) ; Nadeau and Puiggali (1995)).
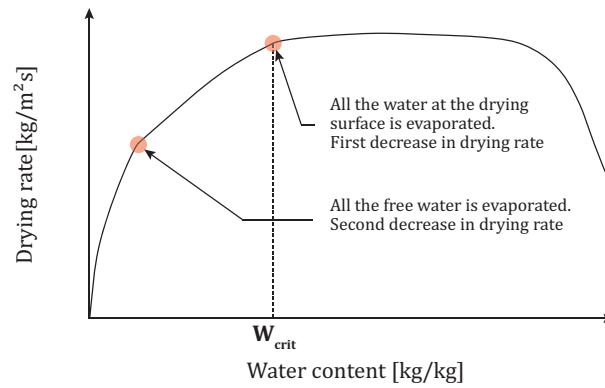
Figure 3.10: First and second decrease in drying rate on Krischer's curve as seen in the receding front model

The drying rate further decreases (change of slope of the drying during the FRP) due to the diffusion of water inside the medium.

Remarks There are a few critics that can be raised concerning those two models :

- Neither can explain how the water transfers continuously supply the drying surface during the CRP and why this transfer is lost during the CRP.

- Also, the work of Van Brakel (1980) on the convective drying of glass beads shows that there is an important decrease of the drying surface saturation during the CRP which is in direct opposition with the "wetted surface model".

- Another problem that is recurrent to both models is that none of them take into account any form of scale factor. A bigger sample should have a different critical water content, w_{crit}, than a smaller sample. Otherwise this would suppose that the desaturation of the sample is homogeneous and that there is no water content gradient between the core and the surface of the sample which is not the case for low permeability materials even on small samples.

- Finally the drying process is a complex combination of many simultaneous transfer processes (advection, diffusion, etc.) and none of these theories can explain why some materials do not exhibit any CRP.

3.4.1.3 Hydraulically connected transition zone ("film region")

Recent works are pushing forward the idea that the transition from the CRP to the FRP is due to an interruption of the liquid water transfer to the drying surface of the material or the vanishing of capillary driving forces. One of the first scientists to emit this theory is Shaw (1987) whose work proves the importance of water upward fluxes along the grains to explain the drying rate of glass beads during the CRP. This theory has been refined with the years (see the work of Laurindo and Prat (1998) on 2D geometries for instance) and the postulate

is now that those water fluxes are due to micro-capillarity effects. An hydraulic connection between the drying front and the evaporation surface is maintained through a network of water filled pores (spanning liquid cluster (Yiotis et al. (2003))). Yiotis et al. (2006) have shown numerically that a constant drying rate is maintained while liquid connections between the evaporating surface and the drying front are maintained and that flow rates are sufficient to supply the evaporation rate at the surface (see Fig. 3.11).
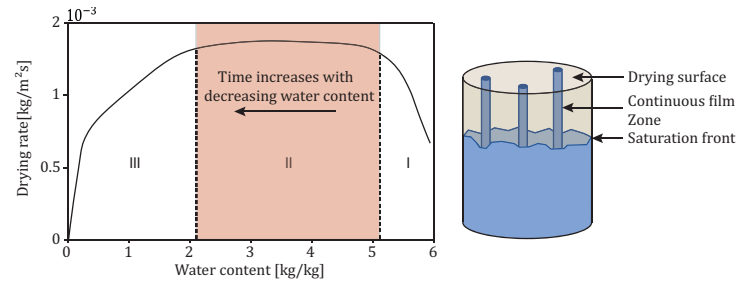

Figure 3.11: Continuous film zone during the CRP

Thus, the length of the CRP is directly controlled by the size of those spanning liquid clusters and thus on the water retention properties of the porous medium. As soon as the hydraulic connection is lost between the surface and the drying front, the drying rate quickly decreases (Fig 3.12).
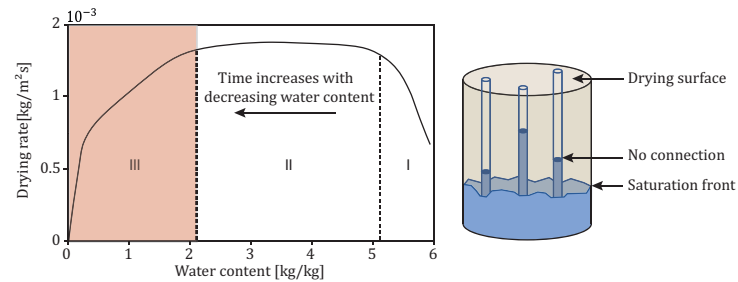

Figure 3.12: Loss of the hydraulic connection during the FRP

The drying front is at the interface between completely liquid-filled pores and partially filled pores. The drying front width is the distance between the minimum and maximum positions of the interface (the drying front). It was shown to depend on both the mean pore size and width of the pore size distribution (Yortsos et al. (1997)).

The hydraulic connections layer, or "film region" as it is called by Yiotis et al. (2006) is the maximum distance that water reaching the surface can come from. In other words, as soon as the drying front depth exceeds this length, liquid connections between the surface and the drying front stop and evaporation proceeds via vapor transports at a reduced drying rate. Active "films" are comprised of liquid-filled crevices, pendular water at grain contacts and surface roughness, and are much thicker than films adsorbed by solid surface forces. Yiotis et al. (2003) denoted the water retained in crevices as "thick films" and the adsorbed water as "thin films." Tuller and Or (2001) used the terms "corner flow" and "film flow" to quantify the viscous resistances associated with these two liquid configurations in partially saturated media. Yiotis

et al. (2005) have shown that the flow along liquid films to the surface enhances the drying rate compared to drying based only on vapor diffusion through the pore spaces.

The length of the hydraulic connection layer depends on capillary driving forces generated by the difference between capillary pressure in large pores at the drying front and capillary pressure in small pores near the drying surface (Scherer (1990)). This capillary pressure gradient is opposed by gravitational forces and viscous dissipation.

To illustrate this principle, let us consider a system composed of a pair of hydraulically connected capillaries of radius r_1 and r_2 respectively with $r_1 < r_2$ (see Fig. 3.13).
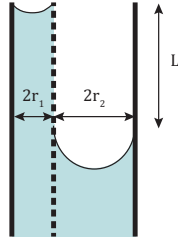

Figure 3.13: System composed of two capillaries of radius r_1 and r_2

These capillaries are initially filled with water. As the evaporation progresses, capillary menisci form at the top of the capillaries which leads to a change of capillary pressure, p_c, of :

$$p_{c,1} = \frac{2\sigma}{r_1} cos\theta \tag{3.4}$$

$$p_{c,2} = \frac{2\sigma}{r_2} cos\theta \tag{3.5}$$

where θ is the contact angle between the water and the capillary tube and σ is the surface tension (see section 2.5.1.1). The largest capillary pressure attainable in the larger capillary of radius r_2 is given for a contact angle $\theta = 0$ obtained when the meniscus' curvature is maximal (and the pore fluid is water). It is given by :

$$p_{c,2} = \frac{2\sigma}{r_2} \tag{3.6}$$

Subsequent evaporation will not change the curvature of the meniscus in the larger capillary. Thus, a capillary pressure difference forms between the small and the large capillary :

$$\Delta p_c = 2\sigma \left(\frac{cos\theta}{r_1} - \frac{1}{r_2} \right) \tag{3.7}$$

This creates a water flow from the large capillary to the small one. It can also be expressed in terms of hydraulic head as :

$$\Delta h_{cap} = \frac{2\sigma}{\rho_w g} \left(\frac{cos\theta}{r_1} - \frac{1}{r_2} \right) \tag{3.8}$$

where ρ_w is the water density. As evaporation keeps on, the meniscus in the larger capillary keeps on receding leading to a change of curvature of the meniscus in the smaller capillary and so until it reaches its maximum curvature. The maximum capillary driving force for two capillaries is thus given by :

$$\Delta h_{cap} = \frac{2\sigma}{\rho_w g} \left(\frac{1}{r_1} - \frac{1}{r_2} \right) \tag{3.9}$$

After this moment, the capillary driving force cannot exceed the resisting efforts and the meniscus in the smaller capillary also starts to recede stopping the hydraulic connection between the saturation front and the evaporation surface. If we consider that the only opposing force is gravity then we have :

$$\Delta h_{cap} = \Delta h_{grav} = L \tag{3.10}$$

where L is the distance between the menisci in the large and in the small capillaries.

Viscous dissipation The liquid flow towards the evaporation surface in the small capillary involves viscous dissipation. This pressure drop is proportional to the velocity of the flow in the capillary. If the capillaries are submitted to a drying rate e_0 $[m/s]$ (positive for inflow) supplied by a water flow q $[m/s]$ through the small capillary of radius r_1 then :

$$- e_0 A = q\pi r_1^2 \longleftrightarrow e_0 \left(\pi r_1^2 + \pi r_2^2 \right) = q\pi r_1^2 \tag{3.11}$$

$$q = -e_0 \left(1 + \frac{r_2^2}{r_1^2} \right) \tag{3.12}$$

The liquid flow can be expressed by the Hagen-Poiseuille equation in a cylinder :

$$q = -\frac{r_1^2 \Delta p}{8\mu_w L} \tag{3.13}$$

where μ_w is the water dynamic viscosity, Δp is the pressure drop along the capillary (with $\Delta p < 0$ in the flow direction). It can also be written in terms of hydraulic head :

$$q = -\frac{\rho_w g r_1^2 \Delta h_{visc}}{8\mu_w L} \tag{3.14}$$

By combining Eq. 3.13 and Eq. 3.14, it comes :

$$\Delta h_{visc} = \frac{8\mu_w L e_0 (r_1^2 + r_2^2)}{\rho_w g r_1^4} \tag{3.15}$$

If we now combine gravitational and viscous effects, we get :

$$\Delta h_{cap} = \Delta h_{grav} + \Delta h_{visc} \tag{3.16}$$

$$\frac{2\sigma}{\rho_w g} \left(\frac{1}{r_1} - \frac{1}{r_2} \right) = L + \frac{8\mu_w L e_0 (r_1^2 + r_2^2)}{\rho_w g r_1^4} \qquad \longleftrightarrow \qquad L = \frac{\frac{2\sigma}{\rho_w g} \left(\frac{1}{r_1} - \frac{1}{r_2} \right)}{\frac{8\mu_w e_0 (r_1^2 + r_2^2)}{\rho_w g r_1^4} + 1} \tag{3.17}$$

Eq. 3.17 gives the length of the hydraulic connection layer for two capillaries. Lehmann et al. (2008) applied this approach to a porous medium with a given pore size distribution (represented by its water retention curve) and his formulation is related here.

To estimate the capillary pressure required to drain the largest and smallest pores in the range corresponding to the thick film region (connection layer), Lehmann et al. (2008) suggest using the slope of the tangent to the water retention curve at the inflection point to express the capillary hydraulic head. In the case of the water retention curve given by van Genuchten's formulation, it comes :

$$\Delta h_{cap} = \frac{\alpha_{vG}}{(n_{vG} - 1)\rho_w g} \left(\frac{(2n_{vG} - 1)}{n_{vG}} \right)^{(\frac{(2n_{vG}-1)}{n_{vG}})} \left(\frac{(n_{vG} - 1)}{n_{vG}} \right)^{(\frac{(1-n_{vG})}{n_{vG}})} \quad (3.18)$$

where α_{vG} and n_{vG} are van Genuchten's model parameters.
Viscous head loss is given by Eq. 3.15 in which the term $\frac{r_1^4}{r_1^2 + r_2^2}$ corresponds to the unsaturated water permeability of the system composed of the two capillaries. If we now transpose that to the case of a porous medium whose unsaturated macroscopic water permeability for a Darcy flow is given by $k_{rel,w}(S_{r,w})k_{sat}$ then Eq. 3.15 can be rewritten as :

$$\Delta h_{visc} = \frac{L_{crit}e_0\mu_w}{k_{rel,w}(S_{r,w})k_{sat}\rho_w g} \quad (3.19)$$

where, L_{crit}, is the length of the hydraulic connection layer. It is assumed that the water content decreases linearly from the drying front to the drying surface and the mean permeability between those two points is used to determine viscous resistance (Lehmann et al. (2008)). The gravitational head loss is directly linked to the length of the connection layer and is expressed :

$$\Delta h_{grav} = L_{crit} \quad (3.20)$$

Now, substituting Eq. 3.18, Eq. 3.19 and Eq. 3.20 in Eq. 3.16, it gives :

$$L_{crit} = \frac{\Delta h_{cap}}{1 + \frac{e_0\mu_w}{k_{rel,w}(S_{r,w})k_{sat}\rho_w g}} \quad (3.21)$$

If the sample size is higher than the connection layer length obtained for a saturated state ($k_{rel,w}(S_{r,w}) = 1$) then as soon as the porous medium starts to desaturate, the hydraulic connection will be lost and such samples will exhibit almost no CRP.

3.5 History of convective drying models

The first engineering analysis of the drying process of solids is attributed to Lewis (1921) who suggested that the drying process was driven by two phenomena : the diffusion of the moisture from the interior of the solid to its surface and the evaporation of the fluid at the surface. Sherwood (1929) followed the idea that drying was mainly driven by diffusion and introduced a model based on a diffusion equation of the form :

$$\frac{\partial C}{\partial t} = D\frac{\partial^2 C}{\partial x^2} \quad (3.22)$$

where C is the moisture content and D is a parameter called the diffusion coefficient which is determined experimentally. This formulation meant that the only mechanism governing the mass transfer was a moisture content gradient. Sherwood also discussed the possibility that diffusion and convection of vapor in the gas phase as well as heat transfer might be associated with drying. Still, none of these phenomena were considered to play an important role and the predominant process was considered to be diffusion. The formulation of Sherwood was extensively applied and modifications were made to adapt it to different geometries (see Newman (1931) for example). Gilliland and Sherwood (1933) used this formulation to estimate the duration of the constant rate period and it seemed that a complete understanding of the drying process was reached using diffusion mechanisms only.

At the time, soil scientists and ceramists were explaining the movement of moisture in porous medium as the result of capillary effects (see section 2.5.1.1) (Gardner and Widtsoe (1920) ; Richards (1931)). These studies demonstrated that the capillary effects could not be neglected when considering liquid motion in unsaturated porous medium. Following these results, Comings and Sherwood (1934) conducted a series of drying experiments on clay and concluded that capillarity was indeed an important phenomenon in moisture movement during a drying experiment. Based on those conclusions, Ceaglske and Hougen (1937) emitted the following postulate : "*The drying rate of a granular substance is determined not by diffusion but by capillary action*". They founded that assessment on their ability to predict the saturation distribution in sand samples. To link the capillary effects to the water content they used the extensive work of Haines (Haines (1927) ; Haines (1930)). Hougen et al. (1940) compared the solutions obtained using a diffusion only model with the ones obtained using a capillary effect based model and experimental data obtained through drying tests on a set of different materials (clay, sand, paper, etc.). The results visible in Fig. 3.5 clearly show that the theoretical curves obtained using the capillary model produce better results.

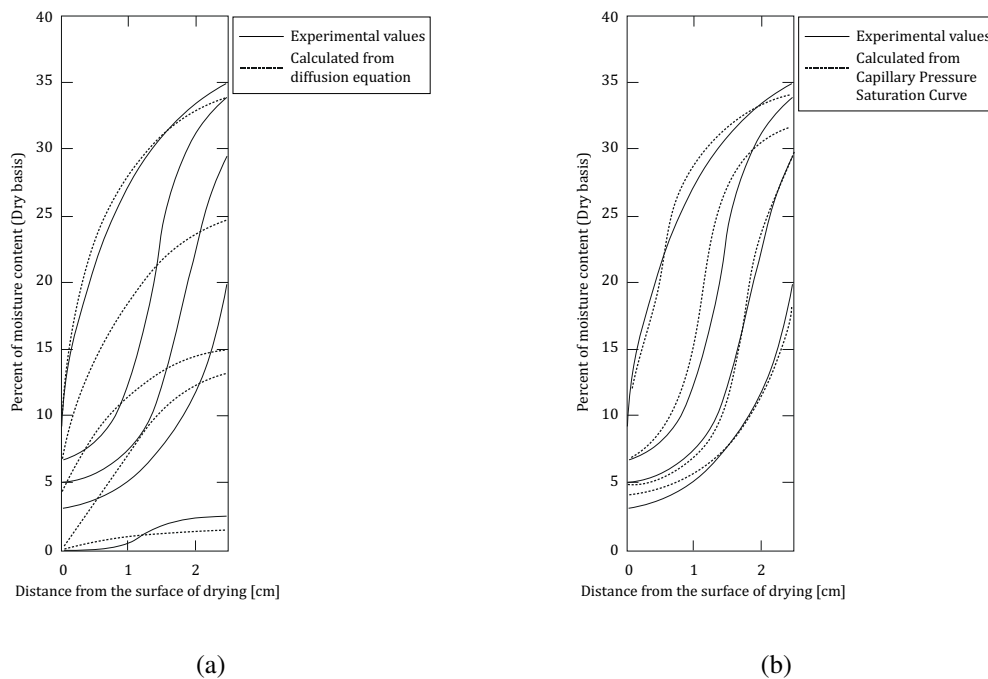(a)   (b)

Figure 3.14: Moisture distribution during the drying of sand calculated with (a) the diffusion theory and (b) the capillary theory (Hougen et al. (1940))

At the same time, Krischer (Krischer (1938); Krischer (1940)) published a series of papers in which he reevaluated the importance of the heat transfer on the overall drying process. Because of the work of Ceaglske and Hougen (1937), the diffusion theory was being heavily criticized despite clear evidence that it could model accurately the later stages of drying. As it is now clear, this is due to the fact that in the pendular state (see section 2.5.1.2) the capillary effects are greatly reduced and convection and diffusion of vapor are the dominant mechanisms. To rehabilitate the diffusion theory, it was then suggested (van Arsdel (1947)) to use a variable diffusivity coefficient depending on the water content. The diffusion formulation became :

$$\frac{\partial C}{\partial t} = \frac{\partial}{\partial x}\left(D\frac{\partial C}{\partial x}\right)$$

(3.23)

Formulations of this type are still being used today (Pel et al. (1996) ; McDonald et al. (1996)). Good results can be obtained but require the diffusivity coefficient to be a complex empirical function of the water content which is not supported by any physical evidence.

Philip and De Vries (1957) were the first ones to distinguish and *associate* capillary effects and vapor transport. Refining this approach, Whitaker (1977) suggested a multi-transfer and multi-physics model by adding to the diffusion theory the continuum physics governing equations for liquid transfers, gas transfers and energy. This formulation is one of the most commonly used today to model the drying process.

3.6 Boundary layer model

The models presented in the historical summary in the previous section considered that everything (i.e. water transfers in the porous medium and at the surface of the porous medium) could be represented using a simple diffusion like equation or a capillary pressure mechanism. Whitaker (1977) was the first one to differentiate the water transfer inside and outside the porous medium. The model used throughout this work to simulate the heat and mass transfers between a porous medium and the atmosphere is the *boundary layer model*. In the spirit of the work of Whitaker (1977), this model adds a pair of diffusion like equations - to take into account the mass and heat transfer at the surface of the sample - to the set of classical governing equations of continuum mechanics presented in the previous chapter (see section 2.4). In this section, the *boundary layer model* is detailed.

This model is based on the assumption of the existence of a boundary layer all around the sample where the mass and heat transfers are assumed to take place (Kowalski (2012)).

3.6.0.1 Mass transfer

The water content at the drying surface of the sample is supposed to be in equilibrium with the partial pressure of water vapor. The water flow, $\bar{q}$, from the materials to the surroundings is thus proportional to the difference between the vapor density of the drying air, $\rho_{v,air}$ $[kg/m^3]$, and the vapor density at the surface of the sample, $\rho_{v,surf}$ $[kg/m^3]$, (Gerard et al. (2008); Léonard et al. (2005a)). It is a diffusion like mass transfer and the "diffusion coefficient" is a mass transfer coefficient, α, characterizing the surface's transfer properties. The water flow is expressed as:

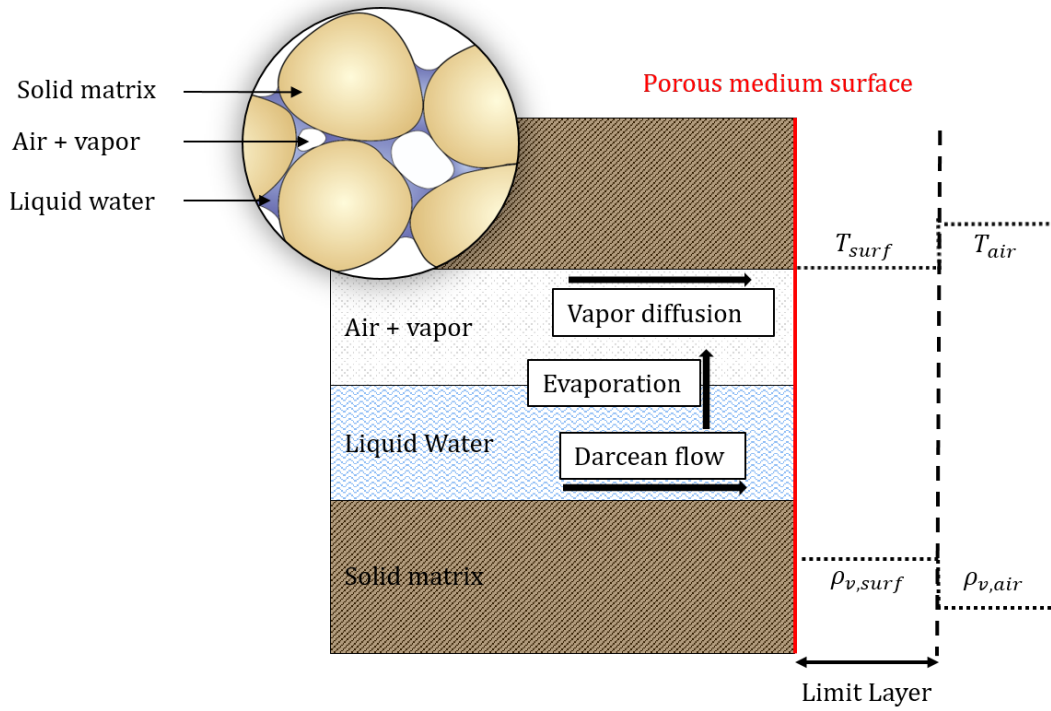$$q = \alpha(\rho_{v,surf} - \rho_{v,air})$$

(3.24)

Figure 3.15: Boundary layer model

3.6.0.2 Heat transfer

The heat flux, $\bar{f}$, from the boundary to the drying air is expressed as:

$$f = Lq - \beta(T_{air} - T_{surf}) \tag{3.25}$$

where T_{air} is the temperature of the drying air, T_{surf} is the temperature at the surface of the sample, β $[W/m^2/K]$ is a heat transfer coefficient and L is the water evaporation latent heat (2500 kJ/kg). $L\bar{q}$ is thus the heat used to evaporate the water at the surface and the term $\beta(T_{air} - T_{surf})$ is the heat transferred to the system by convection.

3.6.0.3 Transfer coefficient

Based on the drying kinetics, it is possible to determine the transfer coefficients (Eq. 3.24 and Eq. 3.25). The value of the drying rate during the CRP is directly linked to the capacity of the drying air to evaporate the water at the surface of the porous medium, and is therefore linked to the value of the mass transfer coefficient. Only the value of the drying rate during the CRP, q_{CRP} is required to determine the transfer coefficient. Indeed, the vapor density of the drying air, $\rho_{v,air}$, is known since its temperature and relative humidity are controlled (and can be easily measured with a classical thermometer for temperature and with an hygrometer for relative humidity). The vapor density at the surface, $\rho_{v,surf}$, corresponds to the equilibrium vapor density. Indeed, during the CRP, the surface of the sample is considered saturated and the temperature corresponds to the wet bulb temperature (which can be analytically determined). No temperature measurements at the surface of the sample are thus required.

$$\alpha = \frac{q_{CRP}}{\rho_{v,surf} - \rho_{v,air}} \tag{3.26}$$

All the heat is used to evaporate the water at the surface of the sample and the heat flux to the sample can thus be considered null during the CRP. It leads to :

$$\beta = \frac{L \, q_{CRP}}{T_{air} - T_{wb}} \tag{3.27}$$

3.7 Shrinkage

Until now, the drying phenomenon has been described with a complete disregard for the mechanical aspect of the problem and only the mass and heat transfers have been described. However, during a drying experiment, a deformable porous medium shrinks. As defined in section 3.2, shrinkage is the change of bulk volume that occurs following a change in moisture content. At a given time, the shrinkage is given by the ratio of the bulk volume at that time and the initial bulk volume.

Several mechanisms can be the cause of shrinkage : chemical reactions, osmotic forces, van der Waals forces and capillary forces. Capillarity has been described in section 2.5.1.1. The other mechanisms are briefly described in the following paragraphs.

- **Chemical reactions** This form of shrinkage describes the decrease in volume following a chemical reaction. For example, the absolute volume of cement plus water decreases during the hydration reaction (Tazawa et al. (1995)).

- **Osmotic forces** This shrinkage occurs at low water content in polar materials (such as clayey materials)(Fang and Chaney (1997)). The bound water(i.e. adsorbed, chemically bound, etc.) forms a diffuse layer with a concentration in cations increasing the closer the water is from the surface of the particles due to an electrical field caused by negative charges at the surface of the clay particles (Verwey et al. (1948)). The electrical field also acts as a semi-permeable membrane preventing the migration of the cations. This configuration creates an osmotic pressure in the diffuse layer proportional to the difference between water potential inside the diffuse layer and water potential of the bulk of water in the capillary further from the grains' surface. This osmotic pressure can be the cause of shrinkage but is only really a relevant mechanism for interparticle distances greater than 50 Angstrom and low salt content (Hueckel (1992)).

- **van der Waals forces** van der Waals forces are intermolecular forces working for very small intermolecular distances ($< 0.6 \, [nm]$). They result from a transient shift in electron density. They have four major contributions :

  - A repulsive component resulting from the Pauli exclusion principle
  - Dipole-Dipole attractive or repulsive electrostatic interaction
  - Induction interaction due to the capacity of a molecule to become polar when placed in the electrical field created by another polar molecule.
  - Dispersion interaction which is an attractive interaction that affects any pair of molecules (even non-polar) due to quantum fluctuation of electron position.

In the case of drying, the loss of moisture content is going to create capillary forces of a far greater order than osmotic or Van der Waals forces. Hence, the predominant mechanisms is a decrease in water pressure (or an increase of suction) at the level of the capillary menisci due to the evaporation of water. Shrinkage is thus a consequence of an effective stress increase (Coussy (2004)). The order of magnitude of shrinkage is dependent on the porous medium's liquid retention properties and solid matrix compressibility.

Shrinkage is said to be ideal as long as the volume loss to shrinkage is directly proportional to the volume of water lost through evaporation (an example can be seen in Fig. 3.16). The ideal shrinkage thus occurs at constant saturation since the pores remain filled with water.
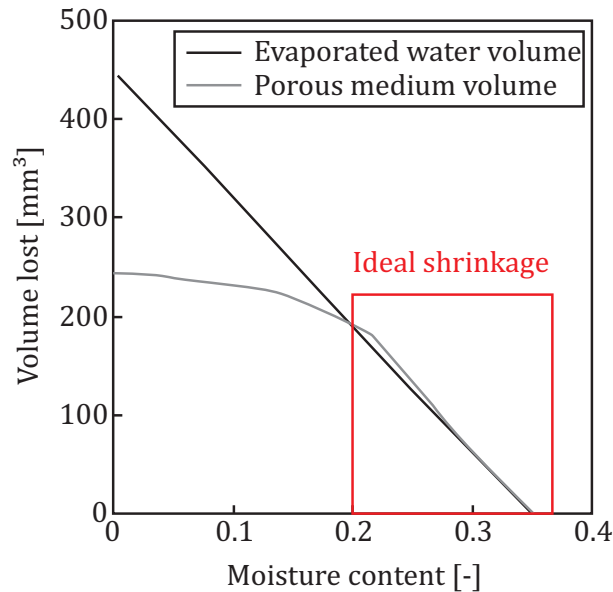

Figure 3.16: Ideal shrinkage (from Prime et al. (2015))

3.7.1 Tensile stress generation

It was just explained that shrinkage is due to an increase of effective stress. This increase in effective stress leads to a decrease in bulk volume and void ratio. The order of magnitude of that volume change is obviously dependent on the material's stiffness. If the shrinkage is free then the volume decreases until equilibrium without any tensile stress generation. On the other hand, if the shrinkage is prevented by any form of constraint then it leads to tensile stress and potentially to "*desiccation cracking*". The shrinkage can be prevented by several mechanisms :

- It can be due to the presence of a boundary condition. For example, if the sample being dried is held from both extremities, its shrinkage will be limited leading to tensile stress generation (Hueckel (1992)).

- It can be due to self equilibrating stresses (Colina and Roux (2000)). If a strong water pressure gradient develops during drying, a strong suction gradient develops as well leading to differential shrinkage. If the different "zones" of the material were free to deform

independently then no tensile stresses would be generated. However, the material is a continuum and even though it is deformable, it possesses a certain stiffness. To maintain material continuity, self equilibrating stresses appear as exhibited in Fig.3.17 :

- It can be due to material texture and/or structure leading to a specific shrinkage pattern restraining it in certain directions (Scherer (1997).

3.8   Conclusion

This chapter introduced all the notions required to understand and analyze the results of a drying experiment. It started by defining a few terms specific to the field of drying and then a short review of the most common drying techniques used in the field of soil engineering was presented. Particularly, suction control methods, free evaporation and convective drying methods were presented. In this work, the drying experiments conducted were done using a convective drying (wind tunnel like) method. The drying kinetics were analyzed as a means to understand the different processes going on during a convective drying experiment. Three phases can be distinguished : the pre-heating period, the constant rate period (CRP) and the falling rate period (FRP). The CRP and FRP are detailed and their transition described with a few different approaches. The prevalent one, at this moment, is the "*hydraulic connection layer*" which is thoroughly explained. Then, a short review of the history of convective drying models is produced. The *boundary layer model*, the model chosen to describe the interactions between the porous medium and the atmosphere is presented. It is added to the set of governing equations presented in chapter 2 to take into account the porous medium - atmosphere interactions. Finally the shrinkage phenomenon is explained and the origin of the tensile stresses leading to desiccation cracking is briefly introduced.

The porous medium and the drying process have both been presented and assimilated. We are now able to analyze drying experiments and have the mathematical background to model it. But since numerical simulations will be involved to simulate the drying process, one last step must be cleared before proceeding to the experiments and their simulations. To be able to numerically solve the system of equations introduced this far, a set of initial and boundary conditions will be necessary as well as spatio-temporal discretization. This is done using the Finite Element Method (F.E.M.). The next chapter will briefly present those conditions as well as the formulation of the elements used to conduct the simulations.
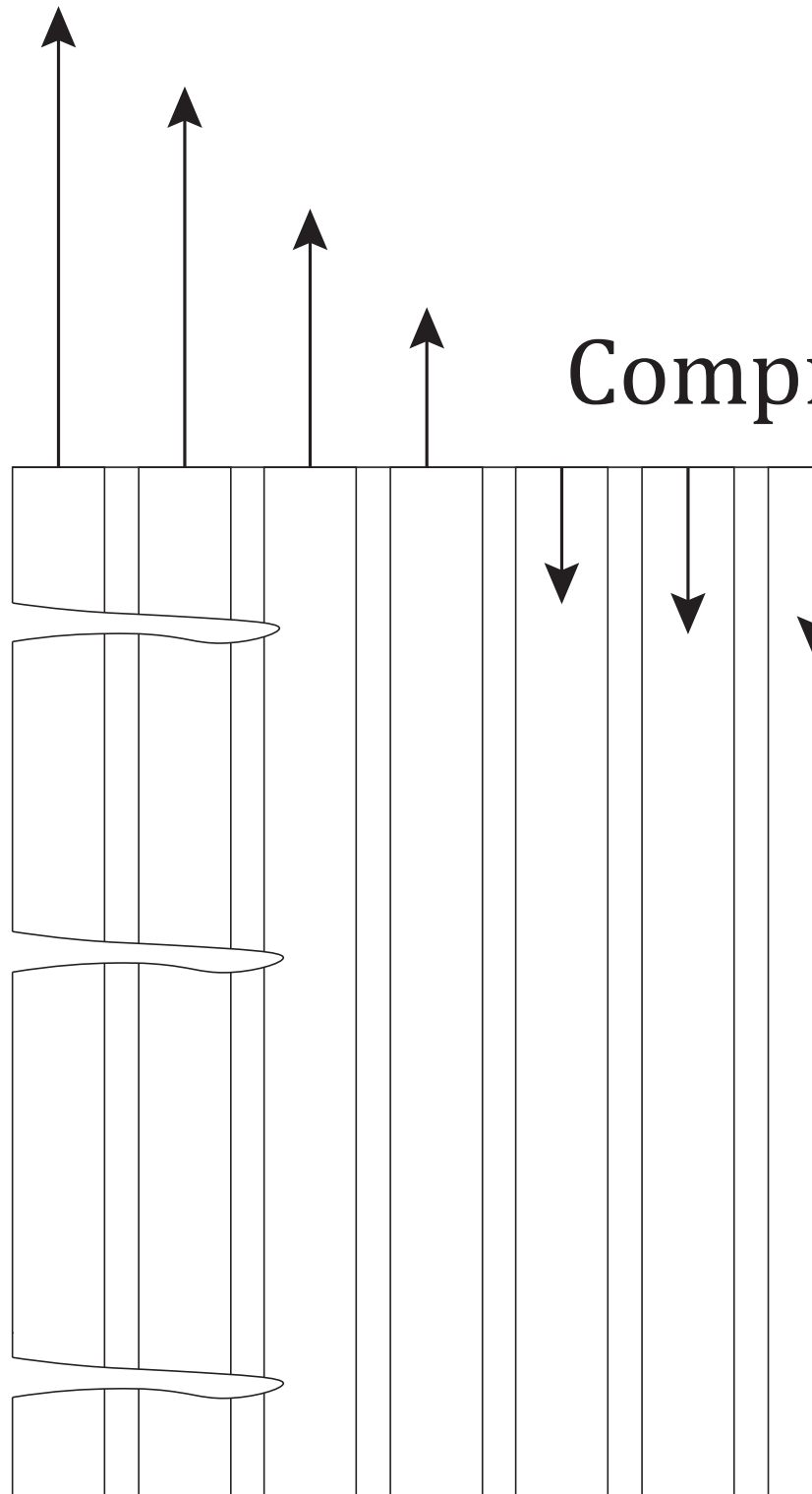
Tensile stresses

Comp

Figure 3.17: Self equilibrating stresses

Chapter 4

Finite element formulation

Contents

4.1   Introduction

The thermo-hydro-mechanical model introduced in the two previous chapters is governed by a system of balance equations in differential form expressing the local equilibrium at the level of an arbitrary control volume. However, to be able to solve the problem, initial and boundary conditions are required. The particular case of the boundary layer model is also discussed. To address large domain boundary-value problems in finite element analysis, the balance equations need to be expressed in weak form. The numerical formulation in finite elements requires the discretization of time and space into finite time steps and finite elements of the continuous body. Finally the system of non-linear equations obtained is solved to give the global solution of the problem.

4.2   Initial and boundary conditions

Initial and boundary conditions are necessary for model closure (Lewis and Schrefler (1987)). Initial conditions describe the displacement, water pressure, gas pressure and temperature fields

at the beginning of the simulation.

$$\Delta x_i = \Delta x_{i,0} \qquad\qquad p_g = p_{g,0} \qquad\qquad (4.1)$$

$$p_w = p_{w,0} \qquad\qquad T = T_0 \qquad\qquad (4.2)$$

Boundary conditions express the equilibrium at the external surface of the system. They can be of two types :

- **Dirichelet boundary conditions** They impose displacements, fluid pressures or temperature at the boundary of the system :

$$\Delta x_i = \Delta \hat{x}_i \quad on\ \delta\Gamma_{\Delta x_i} \qquad\qquad p_g = \hat{p}_g \quad on\ \delta\Gamma_g \qquad (4.3)$$

$$p_w = \hat{p}_w \quad on\ \delta\Gamma_w \qquad\qquad T = \hat{T} \quad on\ \delta\Gamma_T \qquad (4.4)$$

- **Neumann boundary conditions** They impose forces, fluid or heat fluxes. For the displacement field, the external traction force per unit area on a part of the external surface reads (cf. Eq.2.25) :

$$T_i - n_j \sigma_{ij} = 0 \qquad\qquad (4.5)$$

where n_i is the normal vector to the boundary, T_i is the imposed traction vector and σ_{ij} is the Cauchy total stress tensor. For fluids, the boundary condition is :

$$q^w + n_i f_i^w = 0 \quad on\ \delta\Gamma_{q^w} \qquad\qquad (4.6)$$

$$q^a + n_i f_i^a = 0 \quad on\ \delta\Gamma_{q^a} \qquad\qquad (4.7)$$

where q^w and q^a are the water and air fluxes imposed at the external surface (positive for inflow). f_i^w and f_i^a are the inside total fluxes for water and gas respectively and are defined as :

$$f_i^w = f_{l,i}^w + f_{g,i}^w \qquad\qquad (4.8)$$

$$f_i^g = f_{l,i}^g + f_{g,i}^g \qquad\qquad (4.9)$$

where $f_{l,i}^w$, $f_{g,i}^w$, $f_{l,i}^g$, $f_{g,i}^g$ are the mass fluxes for the water and gas species in both liquid and gas phases defined from Eq.2.57 to Eq. 2.60. For temperature, it writes :

$$q^T + V_{T,i} n_i = 0 \quad on\ \delta\Gamma_{q^T} \qquad\qquad (4.10)$$

where q^T is the heat flux imposed at the external surface and $V_{T,i}$ is the internal heat flux defined in Eq.2.80.

4.2.1 Boundary layer model and finite element method

The boundary layer model introduced in section 3.6 is actually nothing more than a special kind of boundary condition. It implies that the imposed water flux, q^w, and heat flux, q^T, in Eq. 4.6 and Eq. 4.10 are not constant. They depend on the configuration and thus on the time through Eq. 3.24 and Eq. 3.25. To take that into account a 1D boundary condition element has been developed by Gerard (2011). It is a 4 node element as visible in Fig. 4.1.

The first three nodes (N1, N2, N3) are located at the boundary of the sample and are shared with the 2D coupled element (MWAT2D). They are used to discretize the water and gas pressure fields as well as the temperature field at the boundary. The fourth node, $N4$, is used to impose the atmospheric conditions (relative humidity and temperature). The mass and heat fluxes between N4 and the other nodes are controlled by Eq. 3.24 and Eq. 3.25 of the boundary layer model.
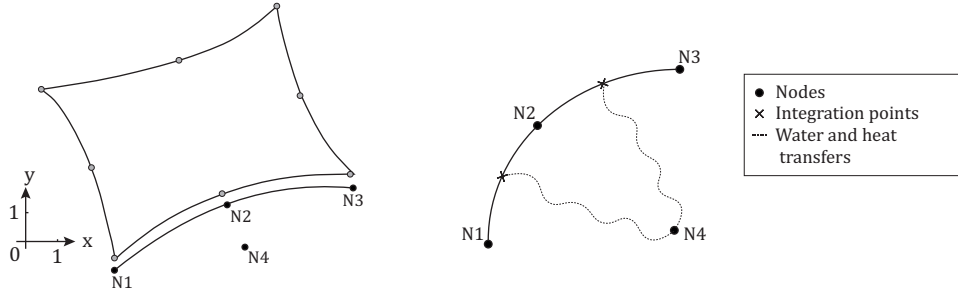
Figure 4.1: (left) 1D boundary element with 2D coupled elements (right) 1D boundary element description (Gerard (2011))

4.3 Weak form of the balance equations

The balance equations are local equations and to be able to solve the problem over large domains, weak forms of the equations are required.

The weak form of the balance of momentum is obtained using the principle of virtual work. It states that for a kinematically admissible (i.e. which respects the solid continuity and boundary conditions) virtual velocity field, ν_i^*, the equilibrium is verified if the internal virtual power, W_I^* is equal to the external one, W_E^*.

$$W_I^* = \int_V \sigma_{ij} \dot{\varepsilon}_{ij}^* \, \mathrm{d}V \tag{4.11}$$

$$W_E^* = \int_V \rho g_i \nu_i^* \, \mathrm{d}V + \int_A t_i \nu_i^* \, \mathrm{d}A \tag{4.12}$$

$$\tag{4.13}$$

If you inject Eq. 2.27 and Eq. 5.3 in the expression of the external virtual power you get :

$$W_E^* = \int_V -\frac{\partial \sigma_{ij}}{\partial x_j} \nu_i^* \, \mathrm{d}V + \int_A n_j \sigma_{ij} \nu_i^* \, \mathrm{d}A \tag{4.14}$$

Using Gauss' theorem, we can change the integral over the boundary to an integral over a volume. It comes :

$$W_E^* = \int_V -\frac{\partial \sigma_{ij}}{\partial x_j} \nu_i^* \, \mathrm{d}V + \int_V \frac{\partial \sigma_{ij} \nu_i^*}{\partial x_j} \, \mathrm{d}V \tag{4.15}$$

which reduces to :

$$W_E^* = \int_V \sigma_{ij} \frac{\partial \nu_i^*}{\partial x_j} \, \mathrm{d}V \tag{4.16}$$

Accounting for the symmetry of the stress tensor, $\sigma_{ij} = \sigma_{ji}$, and the definition of the Cauchy strain, $\varepsilon_i j$, (cf. Eq. 2.12) equation 4.16 writes :

$$W_E^* = \int_V \sigma_{ij} \frac{1}{2} \left(\frac{\partial \nu_j^*}{\partial x_i} + \frac{\partial \nu_i^*}{\partial x_j} \right) \, \mathrm{d}V \tag{4.17}$$

$$= \int_V \sigma_{ij} \dot{\varepsilon}_{ij}^* \, \mathrm{d}V = W_I^* \tag{4.18}$$

By analogy with the mechanical problem, the fluids or energy mass balance equations may also be written using the principle of virtual work. For a virtual water pressure field, p_w^*, it writes :

$$W_E^* = \int_V Q_w p_w^* \, \mathrm{d}V + \int_A q^w p_w^* \, \mathrm{d}A \qquad = \int_V \frac{\partial m^w}{\partial t} p_w^* - f_i^w \frac{\partial p_w^*}{\partial x_i} \, \mathrm{d}V \qquad (4.19)$$

$$= W_I^* \qquad (4.20)$$

For a virtual gas pressure field, p_g^*, it writes :

$$W_E^* = \int_V Q_a p_g^* \, \mathrm{d}V + \int_A q^a p_g^* \, \mathrm{d}A \qquad (4.21)$$

$$= \int_V \frac{\partial m^a}{\partial t} p_g^* - f_i^g \frac{\partial p_g^*}{\partial x_i} \, \mathrm{d}V = W_I^* \qquad (4.22)$$

$$(4.23)$$

where Q_w and Q_a are the source/sink terms of water and air respectively. m^w and m^a are the total mass of water and air respectively and are given by :

$$m^w = m_l^w + m_g^w \qquad (4.24)$$

$$m^a = m_l^a + m_g^a \qquad (4.25)$$

where m_l^w, m_g^w, m_l^a, m_g^a are the mass of liquid water, of water vapor, of dissolved air and of dry air respectively. They are given by :

$$m_l^w = n S_{r,w} \rho_w \qquad (4.26)$$

$$m_g^w = n(1 - S_{r,w}) \rho_v \qquad (4.27)$$

$$m_l^a = n S_{r,w} \rho_{da} \qquad (4.28)$$

$$m_g^a = n(1 - S_{r,w}) \rho_a \qquad (4.29)$$

$$(4.30)$$

And finally, for a virtual temperature field, T^*, the principle writes :

$$W_E^* = \int_V Q_T T^* \, \mathrm{d}V + \int_A q^T T^* \, \mathrm{d}A \qquad (4.31)$$

$$= \int_V \frac{\partial S_T}{\partial t} T^* - V_{T,i} \frac{\partial T^*}{\partial x_i} + \frac{\partial E_{H_2O}^{w-v}}{\partial t} L T^* \, \mathrm{d}V = W_I^* \qquad (4.32)$$

where S_t is the enthalpy of the system, $V_{T,i}$ is the heat flux, $E_{H_2O}^{w-v}$ is the energy required for the change of phase from liquid water to vapor and Q_T is the heat source/sink term.

4.4 Discretization

4.4.1 Time discratization

The balance equations should be verified at any time t. However, to be able to numerically solve the boundary problem, the continuous time has to be descritized into finite time steps,

Δt. The problem can then be solve for any time $t = \sum_{i=1}^{k} \Delta t_i \forall k \in \mathbb{N}$. A fully implicit finite difference scheme is used to express the time derivative of the displacement, water pressure, gas pressure and temperature fields :

$$\Delta \dot{X}_i^{t+\Delta t} = \frac{\Delta X_i^{t+\Delta t} - \Delta X_i^t}{\Delta t} \qquad \dot{p}_w^{t+\Delta t} = \frac{p_w^{t+\Delta t} - p_w^t}{\Delta t} \qquad (4.33)$$

$$\dot{p}_g^{t+\Delta t} = \frac{p_g^{t+\Delta t} - p_g^t}{\Delta t} \qquad \dot{T}^{t+\Delta t} = \frac{T^{t+\Delta t} - T^t}{\Delta t} \qquad (4.34)$$

4.4.2 Spatial discretization

The finite element method is based on the spatial discretization of each body into finite elements. A coupled finite element is used, the finite element MWAT 2D, to model solid bodies (Collin et al. (2002b)). It is an isoparameteric element with eight nodes and four integration points as shown in Fig. 4.2. Each node has five degrees of freedom ; the spatial coordinates, water pressure, gas pressure and temperature.
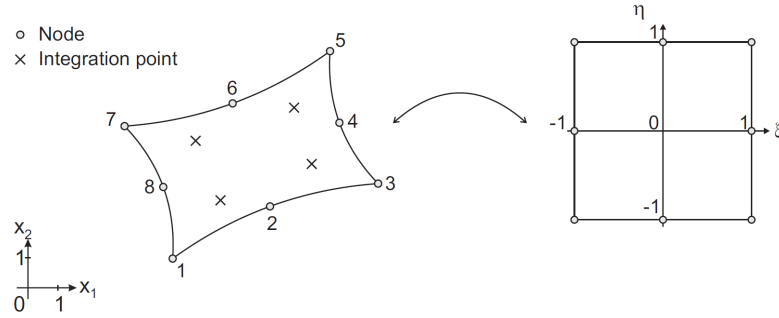

Figure 4.2: Two-dimensional finite element MWAT 2D with eight nodes and four integration points (left) and its corresponding parent element (right) (based on Dieudonné (2016))

The Jacobian of the matrix J_{ij} of the transformation from the global coordinates (x_1, x_2) to the local coordinates (ξ, η) is defined by :

$$J_{ij} = \begin{pmatrix} \frac{\partial x_1}{\partial \xi} & \frac{\partial x_1}{\partial \eta} \\ \frac{\partial x_2}{\partial \xi} & \frac{\partial x_2}{\partial \eta} \end{pmatrix} \qquad (4.35)$$

Nodal unknowns, $u_l^{(k)}$ are interpolated over the element using quadratic shape functions $N^{(k)}(\xi, \eta)$ (Zienkiewicz and Taylor (2000)):

$$u_l^e(\xi, \eta) = \sum_{k=1}^{8} N^{(k)}(\xi, \eta) u_l^{(k)} \qquad (4.36)$$

where k is the number of nodes and l the degrees of freedom associated to that node. We can express the mechanical part of the virtual internal power of a single element, V_e, using Eq. 4.11 :

$$W_I^* = \int_{V_e} \sigma_{ij} \frac{\partial \nu_i^{*\,(k)}}{\partial x_j} \, \mathrm{d}V_e \tag{4.37}$$

$$= \sum_{k=1}^{8} \int_{V_e} \sigma_{ij} \frac{\partial N^{(k)}}{\partial x_j} \, \mathrm{d}V_e \nu_i^{*\,(k)} \tag{4.38}$$

$$= \sum_{k=1}^{8} \left[F_{I,i_k}^{V_e} \right]^T \nu_i^{*\,(k)} \tag{4.39}$$

The integration of $F_{I,i}^{V_e\,(k)}$ over the deformed element is carried out numerically using a Gauss integration scheme :

$$\int_{V_e} \sigma_{ij} \frac{\partial N^{(k)}}{\partial x_j} \, \mathrm{d}V_e = \sum_{IP} \left[\sigma_{ij} \frac{\partial N^{(k)}}{\partial x_j} \right]_{IP} det(J_{ij}) W_G \tag{4.40}$$

where IP is the number of integration points and W_G is the Gauss weight corresponding to the integration point IP. The same method can be applied to integrate the hydraulic and thermal nodal forces using the corresponding weak forms of the balance equations. The forces can then be gathered in the same vector $F_{I,i}^{V_e\,(k)}$ which is the vector of internal energetically equivalent nodal forces associated to node k of the element V_e.

A continuous body is discretized into n finite elements of individual volume, V_e, and the total volume is given by :

$$V = \bigcup_{e=1}^{n} V_e \tag{4.41}$$

The global vector of the nodal forces thus reads :

$$F_{I,i}^{(k)} = \bigcup_{e=1}^{n} F_{I,i}^{V_e\,(k)} \tag{4.42}$$

4.5   Global solution of the problem

Equilibrium is reached when the energetically equivalent internal nodal forces, $F^{(k)}{}_{I,i}$, are equal to the external ones, $F^{(k)}{}_{E,i}$. However, due to the evolution of the loads, these nodal forces are most probably not at equilibrium at the beginning of any given time step. A measurement of this imbalance is given by the out of balance nodal forces :

$$F^{(k)}{}_{OB,i} = F^{(k)}{}_{E,i} - F^{(k)}{}_{I,i} \tag{4.43}$$

If, $F^{(k)}{}_{OB,i}$ is different from zero, the generalized degrees of freedom must be corrected to verify the equilibrium. To that end, the system of non-linear equations (because of the couplings and the complex constitutive models),composed of the weak forms of the balance equations (cf. Eq. 4.18 to Eq. 4.32) is linearized and numerically solved using a Newton-Raphson scheme.

A criterion has to be defined to determine if the equilibrium is reached or not because out of balance forces will probably not be exactly null. If we expand the out of balance forces using a first order Taylor series, it comes :

$$F_{OB,i}^{t+\Delta t\ (k)} \approx F_{OB,i}^{t\ (k)} + \frac{\partial F_{OB,i_k}^t}{\partial u_m^{(n)}} \Delta u_m^{(n)} \tag{4.44}$$

where the derivative term is the variation of the nodal out of balance force, F_{OB,i_k}^t relative to the degree of freedom i at node k, due to a variation, u_{m_n}, of the degree of freedom m at node n. The generalized degrees of freedom are corrected at each iteration by :

$$\Delta u_m^{(n)} = - \left[\frac{\partial F_{OB,i}^{t\ (k)}}{\partial u_m^{(n)}}\right]^{-1} F_{OB,i}^{t\ (k)} = - \left[K_{lm}^{t\ (k)(n)}\right]^{-1} F_{OB,i}^{t\ (k)} \tag{4.45}$$

where $K_{lm}^{t\ (k)(n)}$ is the stiffness matrix at time t. A fully coupled procedure is adopted where the entire stiffness matrix is computed at each iteration of the Newton-Raphson procedure.

4.6 Conclusion

This chapter is the final step to be cleared before numerical simulations of drying experiments can be performed. In this chapter, the general formulation of 2D coupled finite elements is presented. In particular, the initial and boundary conditions required to solve the problem are introduced as well as their modification to account for the boundary layer model. The governing balance equations introduced in chapter 2 are expressed in weak form to be able to solve the problem over a large domain since the equations in differential form express a local equilibrium. The continuous time and space are discretized to be able to numerically solve the system of equations. Finally, said system of non-linear equation is solved and the global solution of the problem has been presented.

Since this last step has now been cleared, the next chapter will be dedicated to the drying experiment conducted as well as the application of the framework we have introduced so far to analyze the experimental results and to try to numerically reproduce them.

Chapter 5

Boom Clay

Contents

5.1 Introduction

All the notions required to study the drying process have finally been introduced. In the general introduction (cf. chapter 1), drying is defined as a process encountered in a huge variety of engineering fields. For the civil engineer, one of the main reason to study the drying process is its influence on earthen man-made structures. Such a problem has been thoroughly studied at the University of Liège : *the deep geological storage of nuclear wastes* (Dizier (2011); Gerard (2011); Pardoen (2015); Salehnia (2015); Dieudonné (2016)). During the operation of the deep geological storage tunnels, the host rock is exposed to temperature and relative humidity changes leading to desiccation. This desiccation induces shrinkage and can lead to cracking. Given the importance of sealing these wastes away from the biosphere, a good understanding of the drying behavior of the host rock is an important challenge. In Belgium, Boom clay is considered as a potential host rock and is thus thoroughly studied. This chapter is focused on the experimental and numerical study of Boom Clay. First, the scope of this part of the thesis, the deep geological storage of nuclear wastes, will be addressed in depth. Then, the studied material, Boom Clay, will be introduced and its properties will be presented. The experimental campaign conducted will be detailed and its results will be discussed. Finally, the framework introduced in the previous chapters will be used to numerically simulate the observed experiments.

5.2 Deep geological storage

Nuclear power plants produce energy efficiently but also generate long-lived highly radioactive waste. The later is hazardous to both environment and human health, and needs to be isolated from the biosphere until the radioactivity has sufficiently decayed. For that reason, it is subject to very restrictive regulations by national agencies. In Belgium, isolation procedures are based on a waste classification established by ONDRAF (Organisme National des Déchets Radioactifs et des matières Fissiles enrichies) in collaboration with the European Commission. The wastes classification is based on waste activity and half life (Belgium Profile (2013)) :

- **Class A** Wastes in class A are defined by small amounts of mostly short-lived radioactivity. They are generated by the medical industry, the military industry, nuclear energy production (filter, etc.). They are suitable for shallow land burial and weak shielding and will only need to be isolated for 300 years.

- **Class B** Wastes in class B are defined by low to intermediate level of activity and are intermediate between class A and class C. Their half life is too long to be in class A but they are not producing enough heat to be in class C. They are by-product of nuclear combustible treatment. Their isolation procedure is identical to class C.

- **Class C** Class C wastes are high activity long lived wastes that generate a lot of heat ($> 20 \ [W.m^{-3}]$). They are fission products and elements generated in the reactor core. They account for over 95 percent of the total radioactivity produced in the process of nuclear electricity generation. They need to be cooled before long term storage.

The long term management of class B and class C wastes is internationally studied and the most promising solution seems to be deep geological storage (NEA (2008)). This concept,

detailed in the following section, aims at sealing the wastes away for a period long enough for the activity of the first radionucleide to reach the biosphere to be at or under the natural radioactivity level. This method is considered by many countries and a number of them have built underground research facilities (see Fig. 5.1) in selected host rock formations to study the feasibility of the method.
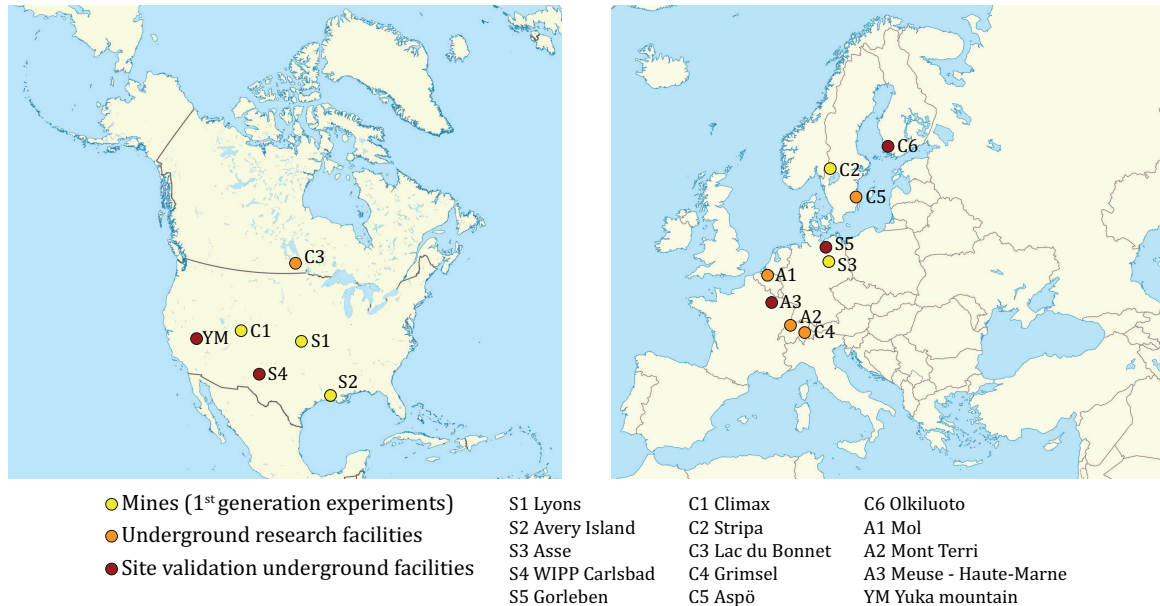

● Mines (1st generation experiments)	S1 Lyons	C1 Climax	C6 Olkiluoto
● Underground research facilities	S2 Avery Island	C2 Stripa	A1 Mol
● Site validation underground facilities	S3 Asse	C3 Lac du Bonnet	A2 Mont Terri
	S4 WIPP Carlsbad	C4 Grimsel	A3 Meuse - Haute-Marne
	S5 Gorleben	C5 Aspö	YM Yuka mountain

Figure 5.1: Underground facilities locations in the World (based on Lebon (2009))

In Belgium, the research facility has been build in Mol near Antwerp (site A1 on Fig.5.1) because of the presence of a rock formation called Boom Clay, which presents characteristics making it a good candidate for deep geological storage. The laboratory is located at a depth of around 230 m (See the left part of Fig. 5.2) and its current layout is visible in Fig. 5.2 on the right.
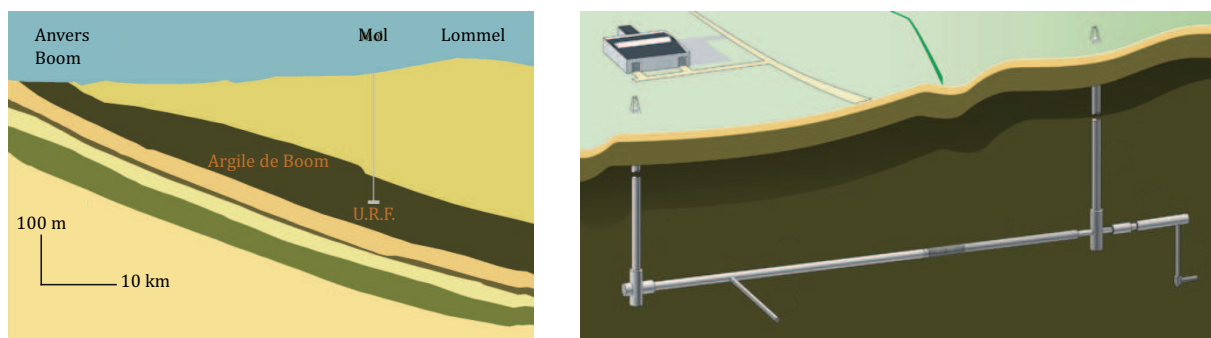
Figure 5.2: Location (left) and schematic layout (right) of the underground research facility in Mol (Bernier et al. (2007))

Wastes isolation is guaranteed by the combination of natural and engineered barriers, referred to as the multi-barriers principle. The natural barrier is the geological layer, preferably with

a very low permeability IEAA (2003). In Belgium, the principle for the engineered barrier is visible on Fig. 5.3. The wastes are placed in super-containers formed of different layers that all have a specific role with the goal of decreasing the *risk* of biosphere contamination. The different layers are :

- The canister: a cylindrical carbon steel envelope containing the waste;

- The overpack: a thin carbon steel layer preventing the migration of radionuclides during the thermal phase (from a few hundred years to several thousand depending on the type of waste). It also has to prevent any contact between water and the canister;

- The buffer: a cement based material used to create a favorable geochemical environment protecting the overpack from corrosion. It also provides a good enough short term protection from the radionucleides to allow for the super container manipulation by an operator (Van Humbeeck et al. (2008)).
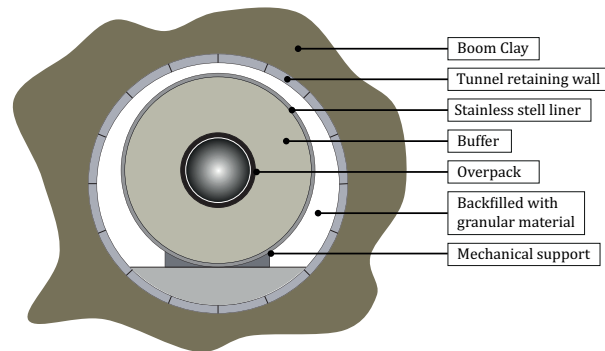
Figure 5.3: Multi-barriers principle Craeye et al. (2009)

Following the Belgian prescriptions, the containers will be placed within tunnels over 200 m deep. These tunnels will be 1 km long and have a 1.5 m radius (Dizier (2011)). As soon as a 30 m section of the tunnel is filled by super-containers, it will be backfilled with a granular material (such as a mix of sand and bentonite) to prevent collapse of the gallery, provide a good enough geochemical environment to prevent corrosion of the containers, and a thermal conductivity that allows enough heat dissipation.

The geological barrier is the last of the multi-barrier principle. Its study is thus of the utmost importance to be sure that it can withstand the thermo-hydro-mechanical loading induced by the nuclear waste storage.

The excavation of the galleries generates stress modifications and eventually fractures in the surrounding medium. The cracks concentrate near the tunnel wall and lead to the creation of an Excavation Damaged Zone (EDZ) (Tsang et al. (2005)). In this zone, important modifications of the hydro-mechanical properties can be observed such as important hydraulic permeability increase (Bossart et al. (2002)). This increase may prevent the geological barrier from playing its containment role because of preferential flow paths for the migration of radionucleides towards the biosphere. The fracturing induced by the excavation is well documented and hydro-mechanical modeling have been performed to reproduce that cracking (see for example Pardoen (2015)).

During the operation phase, the ventilation needed is inducing a variation of the air temperature and relative humidity in the tunnel. The impact of these changes on the host rock is limited by the existing retaining wall but they may still affect the material behavior by draining its water and causing desaturation which may lead to cracking. The damaged zone may thus be influenced by air-host rock interactions due to the ventilation of the tunnel.

Finally, wastes super-containers are placed in their cells which are then backfilled and sealed with swelling clay (Bentonite) and concrete (Dieudonné (2016)). At this phase, the dominant mechanisms is hydraulic resaturation with water flows directed towards the damaged zone which will progressively resaturate. Later, the heat generation which is characteristic of high-level wastes will engender thermal effects, and gas migration will also appear (François (2008); Gerard (2011)).

5.3 Boom Clay

Boom clay is a rock formation located beneath the Mol-Dessel nuclear zone (north-east of Belgium)(Mertens et al. (2004); Bouazza et al. (1996)) and its geographic distribution is visible in Fig. 5.4. Its properties make it one of the formations potentially suitable for deep geological nuclear waste disposal ONDRAF/NIRAS (2001), as explained in section 5.2.
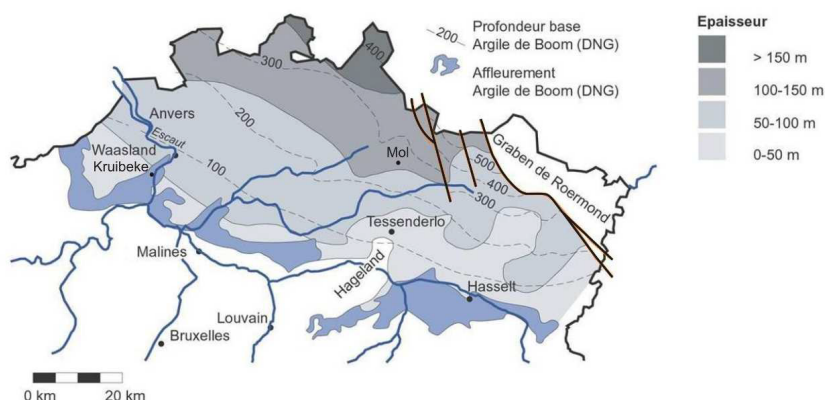

Figure 5.4: Boom Clay location (ONDRAF/NIRAS (2001))

On a geological timescale, this formation belongs to the Rupelian age in the Tertiary Period, which lasted from 36 to 30 million years ago. Its thickness is variable from less than 10 m near the surface at well over 100 m in the deepest parts. In the Mol area, at the laboratory site, the Boom Clay layer is at a depth of about 190 m at its top and has a thickness of about 100 m. In that area, the Boom formation exhibits a slight dipping of 1 to 2 % towards the north - north-east direction along which it thickens (Bernier et al. (2007)).

This formation is constituted of an alternation of silty clay layer and more clayey layer. This alternation gives way to color variation in the grey color range. Some layers containing more carbon and other containing higher organic matter content are also present. The former is noticeable by a pale grey while the later is blackish. This alternation has a periodicity of around 0.5 m as shown on Fig. 5.5.

Figure 5.5: Rumst clay pit view with alternating layers (Wouters and Vandenberghe (1994))

In term of mineralogical composition, Boom clay is made of illite, kaolinite, interbedded illite-smectite, quartz and organic matter in proportions given (variable depending on the authors) by Table 5.1.

Mineral composition in %	Al-Mukhtar et al. (1996)	Wouters and Vandenberghe (1994)	Decleer et al. (1983)	Horseman et al. (1987)
Quartz	$20 - 25$	20	$23.8 - 58.3$	30
Interbedded Illite-Smectite	33	$40 - 50$		
Illite	16	$25 - 35$	$3 - 23$	19
Smectite			$19 - 42$	22
Kaolinite	13	$15 - 25$	$1 - 9$	29
Feldspath	$8 - 10$	$5 - 10$	$9.7 - 17.5$	
Chlorite		$5 - 10$		
Pyrite	$4 - 5$	$1 - 5$	$0.7 - 2.5$	
Carbonate	traces	$1 - 5$	$0.0 - 4.3$	
Organic matter		$1 - 5$		

Table 5.1: Literature review of mineralogical composition of Boom Clay (after Dizier (2011))

Detailed information about the composition and history of Boom clay can be found in Wemaere et al. (2008).

5.3.1 Boom Clay geotechnical properties

Boom clay is characterized by important porosity and water content. Many of its properties are favorable to the choice of this formation as an host rock for radioactive waste storage (Li (2008); Barnichon and Volckaert (2003)) :

- Boom clay has very low water permeability ;

68

- Good radionucleides retention capacity ;

- Good stability for millions of years ;

- Self sealing properties.

A summary of its main geotechnical properties can be found in Table 5.2.

Table 5.2: Literature review of Boom Clay geotechnical properties (after François (2008))

Parameter	Units	Bernier et al. (2007)	Bastiaens et al. (2006)	Mertens et al. (2004)	Belanteur et al. (1997)	Dehandschutter et al. (2005)	Delage et al. (2000)	Gens et al. (2007)	Laloui (1993)	Baldi et al. (1991, 1987)	SCK-CEN (1997)
Bulk density (saturated)	$[g/cm^3]$			1.9-2.1							1.9-2.1
Dry density	$[g/cm^3]$					1.9		1.61-1.78		1.9	
Porosity	$[\%]$	39	39	36-40		35	40	>30		37.5	33-40
Solid density	$[g/cm^3]$				2.67						
Natural water content	$[\%]$		30-40	19-24		25-30	24-30	>9.5			22-27
Natural degree of saturation	$[\%]$										95-100
Liquid limit	$[\%]$				59-76	70				66.6	70-83
Plastic limit	$[\%]$				22-26	25					25-28
Unconfined compression strength	$[MPa]$	2	2	2.2-2.8				2			
Young's modulus	$[MPa]$	300	200-400	200-400				200-400	330		
Poisson ratio	$[-]$	0.125	0.4-0.45	0.4		0.4			0.134		
Internal friction angle	$[°]$	18		11		18			19.5		
Cohesion	$[MPa]$	0.3	0.5-1	0.396							0.6-1.2
Dilatancy angle	$[°]$	0-10							23		
Horizontal water permeability	$10^{-19}[m^2]$	2-4	1			1	2.5-3.5	2-5			4
Vertical water permeability	$10^{-19}[m^2]$	2-4	1			1	2.5-3.5	2-5			2
Specific heat	$[J/K/kg]$										1400
Thermal conductivity	$[W/K/m]$										1.69
Solid thermal dilatation coefficient	$[K^{-1}]$								$1.3 \cdot 10^{-5}$	10^{-5}	

70

As can be seen, Boom Clay has been the subject of numerous experimental studies in the past 30 years. They were mainly aimed at characterizing the geological and geotechnical properties to better understand its thermo-hydro-mechanical behavior. Based on the results obtained by those studies, Boom clay is considered as a plastic, moderately over-consolidated clay with higher than average clayey material mechanical strength (Horseman et al. (1987)). Wemaere et al. (2008), Aertsens et al. (2004) and Blümling et al. (2007) have shown that it presents a strong anisotropy induced by the clay structure (horizontal bedding with alternating clay and silt layers).

5.3.2 *In situ* conditions

At the level of the underground research laboratory, the Boom Clay layer is almost horizontal with water bearing sand layer located above or below it. It is thus assumed to be saturated and the *in situ* stresses are (Chen et al. (2011)) :

- Total stress : $\sigma_v = 4.5 \, [MPa]$

- Water pore pressure : $p_w = 2.25 \, [MPa]$

- Effective stress : $\sigma'_v = 2.25 \, [MPa]$

Boom Clay also presents an *in situ* stresses anisotropy with earth pressure coefficient at rest ranging from 0.85 to 1 (Chen et al. (2011)) but the exact value of the K_0 coefficient is still an open question (Li et al. (2010)).

5.4 Experimental campaign

Convective drying tests were performed on Boom clay samples (Prime et al. (2015)). In this section, the experimental campaign conducted is detailed from the sample preparation to data acquisition. The goal of the experimental campaign was to get a better understanding of the mass and heat transfer mechanisms in porous media and more specifically in Boom clay. Different samples size were tested to determine if there was a scale effect or not.

5.4.1 Sample preparation

Cylindrical samples around 35 mm in diameter and in height were water-drilled (cf. Fig. 5.6 on the right) from the cores (Fig. 5.6 on the left) received from the Mol laboratory. The drilling was made parallel to the bedding direction to allow for a faster saturation process. Smaller samples were taken from the cores to determine the water retention curve.

These were placed in a triaxial cell to saturate them under *in situ* conditions. The following steps were taken:

- Stabilization phase under 100 kPa confinement;

- Isotropic confinement increased to 2.5 MPa (close to *in situ* value) under drained conditions;
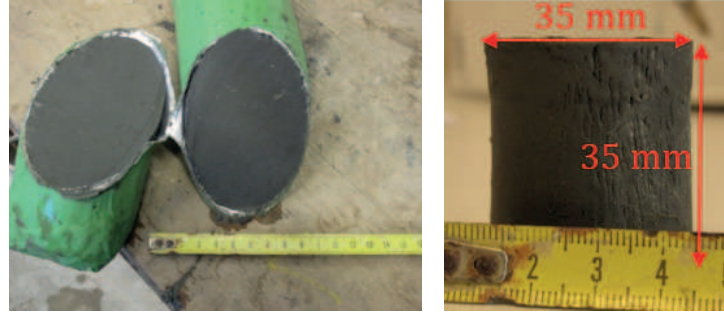
Figure 5.6: Samples preparation : Initial core from the Mol laboratory (left) and samples extracted from it on (right)

- Saturation phase: Synthetic Boom Clay Water whose composition is similar to the *in situ* interstitial water is injected. The injected pressure is fixed at 0.2 MPa and the confinement is increased to 2.7 MPa so that the effective confinement pressure remains constant and the porous structure is not affected by the injection phase;

Figure 5.7: Sample saturation using triaxial press

The next step is to control the saturation level of the samples using Skempton coefficient measurement. The principle is quite simple: the drainage is closed, a confinement pressure increment is applied, Δp, and the interstitial pressure variation, Δu, is measured, then the confinement pressure is brought back to its initial pressure and the drainage condition is restored. The closer the Skempton coefficient, $\frac{\Delta u}{\Delta p}$, is to 1 the more the sample is saturated. Indeed, if a load is applied on a sample saturated and with drainage prevented, considering the almost incompressible nature of the soil grains and water, there cannot be any deformation and the load is completely transferred to the interstitial water. The samples studied presented very high saturation level with Skempton coefficient going from 0.83 to 1 but it took around two months to saturate them.

Since saturation is a time consuming process, it was necessary to optimize the use of the saturated samples to perform a sufficient number of drying tests to insure the results would be reliable. The saturated samples were divided into smaller cylinders 5, 10 and 15 mm high. Those smaller cylinders were then cut in four quarters from which a 15 mm diameter cylinder is extracted. So from a single saturated sample, twelve smaller cylindrical samples are

obtained. This can be seen in Fig. 5.8. Finally, the samples were weighed and dipped in two paraffin baths: a warm bath to ensure good adherence between paraffin and sample, and a colder one to obtain a thick enough layer for efficient sealing (Fig. 5.8 on the right). The finished products were stored into a desiccator saturated with water. The entire process was done as quickly as possible to minimize drying prior to the experiments.

Figure 5.8: Division of the saturated samples (left) to obtain the samples to dry (right)

5.4.2 Drying tests

Twelve samples were dried using a micro-convective dryer designed in the Laboratory of Chemical Engineering of the University of Liège Leonard (2002) and visible in Fig. 5.9 (a)). The dryer is suited for drying light samples using a convective air flow with controlled temperature and velocity. The samples are named using the following method : sample height in millimeters followed by the sample number (e.g. 5-1 for the first 5 mm high sample).

(a)   (b)
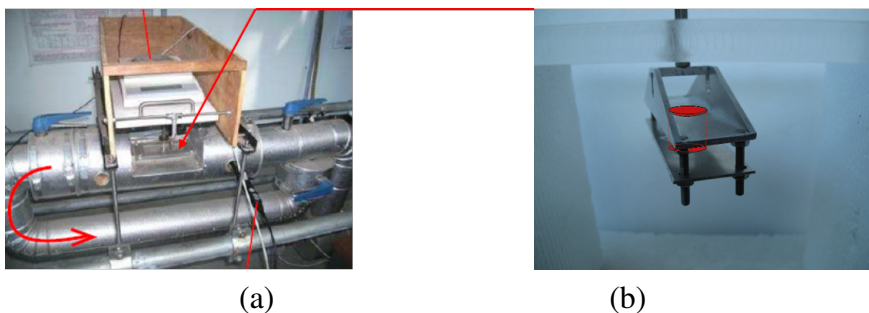
Figure 5.9: Convective dryer and sample holder

The paraffin on the top surface of the samples is removed to constrain the drying to only one side. This choice was made for two reasons : first, in the nuclear wastes storage tunnels, the host rock is only dried from one side, the one exposed and second to limit the problem to a mainly one directional one. They are then placed vertically in an homemade holder in the drier (Fig. 5.9 (b)), and subjected to a convective air flow of 0.8 m/s at $25°C$, and with a relative humidity of around 3.5%. The conditions were chosen to insure that the sample being dried would crack during the experiment. The air flow was kept as parallel as possible to the drying surface to reproduce as closely as possible *in situ* conditions (i.e. drying from only one side with tangent air flow to the surface of the tunnel wall).

5.4.3 Data acquisitions

The sample holder is attached to a scale, allowing to weigh the sample every 30 seconds during the test.

Furthermore, X-ray microtomography was used to scan the samples beforehand and then every hour for four hours (until the mass variation became negligible), and once more at the end of the drying test. For the tomographic acquisitions the samples had to be removed from the dryer, they were sealed immediately after the removal and during the scan, before returning in the drier. The weighings showed no more than 2 mg variation (0.1 % of the total mass) which is assumed to be linked to the scale precision and the potential evaporation during the scan, and can therefore be neglected.

Acquisitions were made on a Skyscan 1172 from Bruker microCT, at a pixel size of 31.86 or 34.63 μm. The X-ray source was set at 100 kV and a 0.5 mm Aluminium filter was used to harden the beam and limit these artefacts in the reconstructions. For each scan 256 projections were taken, limiting the scanning duration to 6 minutes so as to minimize the impact of the drying interruption. Reconstruction was performed using Bruker's NRecon software, making use of their ring artifact correction, set at a strength of 5.

5.5 Analysis of the tomographic reconstructions

Prime presented the results of the convective drying campaign in Prime et al. (2015) but further image processing has since been performed, extracting more accurate measurements. Fig. 5.10 shows vertical cross-sections in the tomographic reconstructions of one of the samples, at the saturated state and after 72h of drying. The clay seems relatively homogeneous except for a few small wiry pyrite inclusions that appear as dark discs on the cross-sections, as can be seen in Fig. 5.10(a). Cracks begin to appear fairly rapidly during the drying process, and are clearly visible in Fig. 5.10(b).

(a) Saturated (b) Dry
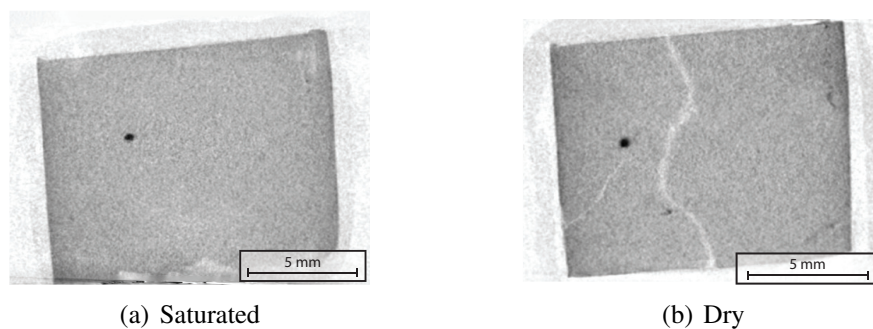
Figure 5.10: Vertical cross-sections in sample 10-1, at roughly the same location, before and after complete drying

To find the cross-sectional area of the samples, we must distinguish between the pixels of the sample, representing the clay and other solid phases, as well as the cracks, and pixels outside the sample. This separation is performed in two parts: the first segments the solid from the void phase, and the second uses this result to find the outer edge of the sample.

Because of the noise level and the beam hardening artifacts still present (manifested by an artificially darker outer layer), a simple thresholding could not properly distinguish pixels rep-

resenting the clay from the others. To perform this segmentation, a watershed transformation was performed on the inverse of the image gradient, using as markers for the two regions to separate (clay and air) a low and high threshold of the reconstruction. It is implemented as morphological region-growing algorithm as described in Vincent and Soille (1991). The gradient was computed with a Sobel mask, and the Euclidean norm was used.

Since the same parameters were used to scan and reconstruct all images, the low and high thresholds remain constant throughout. These were empirically chosen at 29 and 97. In the image histograms, the minimum between the two peaks, representing the air and the sample respectively, is always around 50. The two thresholds should be far enough from this value to counteract the noise and other image artifacts, but still in a reasonable range as not to unnecessarily increase the computation time.

The histogram for the image shown in Fig. 5.10(b) is presented in Fig. 5.11(a), with the blue and red zones representing the greylevel regions that define the pixels of the two markers mentioned previously. The result of this algorithm is shown as the red and blue colors of the horizontal cross-section in Fig. 5.11(b). For the sake of relativity, the reconstruction was overlayed on the coloring.

Fig. 5.11(b) shows that some of the pixels in the cracks have been marked as clay, but this does not affect the subsequent determination of the outer interface of the samples.

| (a) Histogram | (b) Segmentation |
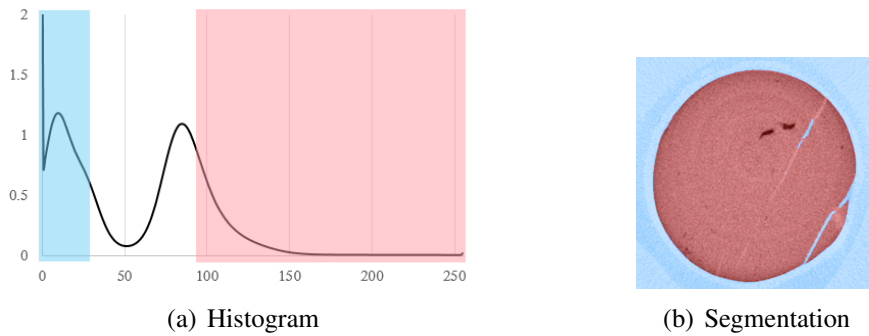
Figure 5.11: Typical histogram of the reconstructions, with the greyscale regions that define the two markers in the watershed segmentation, and a cross-section of the result, in color and overlayed with the original image.

To extract the sample outer boundary, a simple method combining connected component analysis, distance transforms, and thresholding, was used, and is summarised in Fig. 5.12. In this procedure, the first extraction of the largest connected component removes any solid particles outside the sample. After thresholding the first distance transform, the largest connected component is again extracted because some open regions inside the sample surface, might not have been *erased* by the previous thresholding. The two thresholding procedures must use the same value, and in this case was empirically set at 10, which is sufficient to obtain the desired result. The drying rate, a measure of interest in our study, is inversely proportional to the evaporation surface. A good approximating lower bound of this surface can be defined, from the result of the previous procedure, as a horizontal cross-section right below the surface, as shown in Fig. 5.13.

The shrinkage during the drying is taken into account in the mechanical part of the proposed model. We observe that the shrinkage is relative to the bedding plane orientation, i.e. is orthotropic. The samples were prepared in such a way to have these bedding planes in a vertical
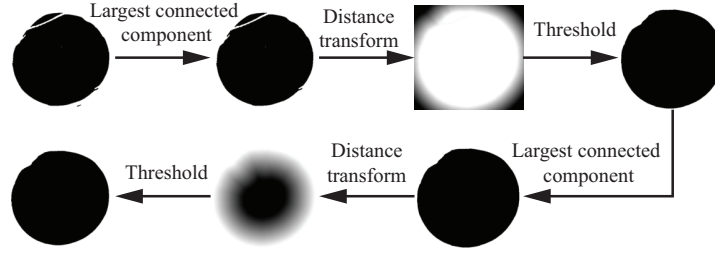
Figure 5.12: Diagram showing the sequence of operations to obtain the outer interface of the samples. To illustrate each step, a horizontal cross-section of intermediate results are shown for sample 10-1.
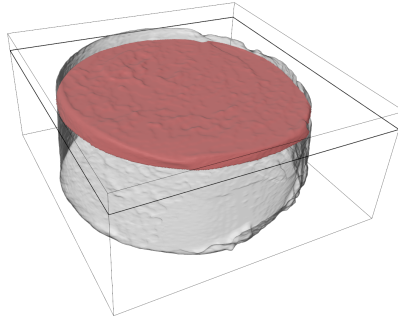

Figure 5.13: Illustration of the determination of the evaporation surface on sample 5-2 before drying. The transparent grey surface shows the outer interface of the sample, the red cross-section indicating the surface used to approximate the evaporation surface. The thick black frame indicating the height at which the cross-section was taken.

position. Therefore the two shrinkage measures needed, parallel and normal to the bedding plane, can be determined by measuring the evolution of the radius of the cylindrical sample in two perpendicular directions.

Contrary to the measure of cross-sectional surface area, radius measurement is much more sensitive to small variations in sample geometry, therefore special care was taken to define where the radius is measured and over what area to average the measure, in order to smooth out local variations.

The methodology is based on previous works focused on 3D registration (Plougonven and Bernard (2006)). To define a radius in a cylindrical sample, a approximating cylinder must first be determined. The method examines the interface pixels on each cross-section and finds the smallest enclosing circle Elzinga and Hearn (1972). From the set of circle centers, an iterative linear regression (with the least squares approach) is performed. The iterative portion is intended to remove the few outliers mostly found at the top and bottom of the sample. If we note the set of circle centers C, a subset $C' \subset C$, and the resulting line from a linear regression L, then the method can be summarized by these four steps:

1. Set $C' = C$

2. Perform a linear regression on C' to find L

3. Set $c_0 = \max_{x \in C} d(x, L)$ and $c_1 = \max_{x \in C'} d(x, L)$

76

4. If $d(c_1, L) > kd(c_0, L)$, then remove c_1 from C' and return to step 2

where $d(x, L)$ is the Euclidean distance between the point x and line L, and k is a user-defined parameter that affects the amount of points rejected in the regression. We have found that a value of 0.1 produced acceptable results, and removed on average around 7% of the centers. Fig. 5.14 shows the result on sample 5-1.
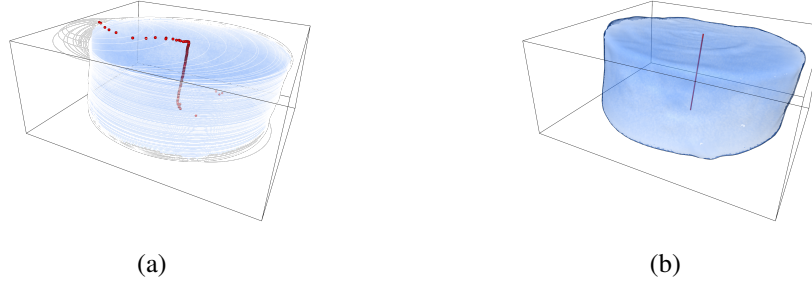

(a)   (b)

Figure 5.14: Determination of the cylinder axis on sample 5-1. (a) shows the set of circles along with their centers in red. Because of the asperities in the sample the top and bottom points should not be used in the linear regression. (b) shows the resulting axis, overlayed with the sample outer interface in transparent.

The circle radii are not relevant here, as we only need the cylinder axis, which we define as the result of this linear regression. It is used to transform the coordinate system on the sample interface points from Cartesian to cylindrical, i.e. in the form (h, r, α), where h is the height along the axis (the origin is chosen arbitrarily), r is the distance from the axis, and α is the angle around it. As a convention, we chose an angle of 0 to be parallel to the bedding plane. The plane direction was set by manual observation of the images, locating the crack directions. As no cracks appear in the saturated samples, we used other features visible in the tomographic reconstructions, such as the pyrite inclusions, and related those to the cracks in the images after drying.

The set of interface points in cylindrical coordinates is then decomposed into 2 subsets based on height and angle. We chose to study the interface points in the middle vertical portion of the sample as they would be less influenced by edge effect, i.e. with a height in the range of $h = \pm 50$ pixels around the median (almost no variation can be observed in function of the height range (study from 10 -50 pixels). For the measurements in the two perpendicular directions, we chose angular wedge of $45°$ around $0°$ and $180°$ for the parallel measurements, and $90°$ and $270°$ for the perpendicular one. These two subsets contain on average 15000 points, which gives a good representativity. Finally, in each subset the average radius is determined, and if we call r_0 and r_∞ this average radius at the saturated stage and at the dry stage respectively, then the shrinkage will equal $1 - \frac{r_\infty}{r_0}$.

5.6 Experimental results

Prime presented the results of the convective drying campaign in Prime et al. (2015) but based on the same data acquisition the image processing has changed as described in 5.5 and was improved upon with help from the department of Chemical Engineering from the University of
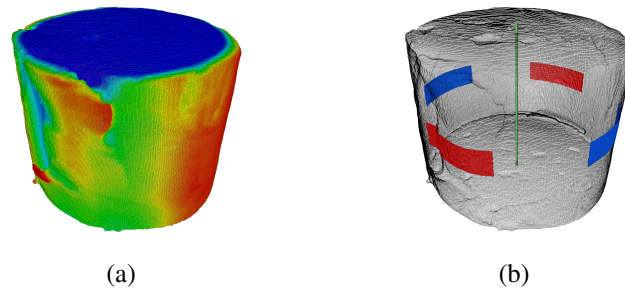
Figure 5.15: Illustration of the radius measurements on sample 10-1. (a) shows the interface points colored by radius, the colormap, from blue to red, is centered around the average radius. (b) shows the two subsets, colored in red and blue, used for the determination of the perpendicular and parallel radii.

Liège. The goal was to have a more consistent approach to obtain more accurate surface results. The main challenges to overcome were to precisely take into account the axial shrinkage and the initial out-of-plumb (or straightness default).

From the constant weighing of the samples during the drying process, drying kinetics can be determined. The shrinkage profile is obtained using the surface area measurement based on the cross-sections of the reconstructions.

5.6.1 Drying kinetics

Mass as a function of drying time is plotted in Fig. 5.16, Fig. 5.17 and Fig. 5.18 for the 5, 10 and 15 mm samples respectively. Based on those results, we can conclude that most the the drying takes place during the first 2 or 3 hours of the test irrespective of the sample size. However, the taller the sample, the longer it takes for it to reach the "dry" state. For example, 5 mm samples take around 20 hours to reach it (see Fig. 5.16) whereas the 15 mm sample reached it after around 60 hours of drying (see Fig. 5.18). It would thus seem that the drying rate of all the samples must be close since a sample 3 times taller takes around 3 times longer to dry.
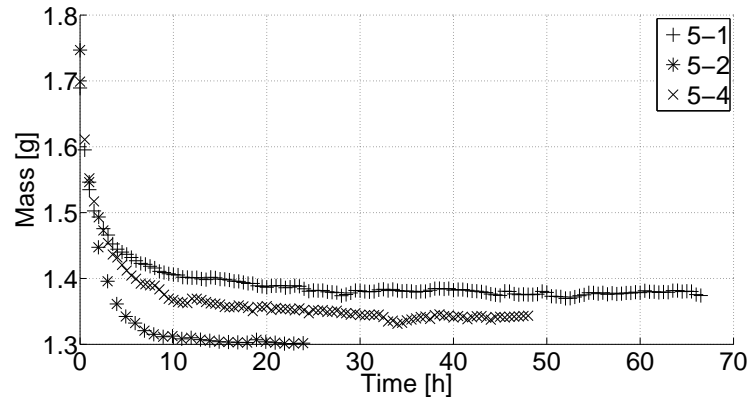
Figure 5.16: Observed mass loss for all the 5 mm samples
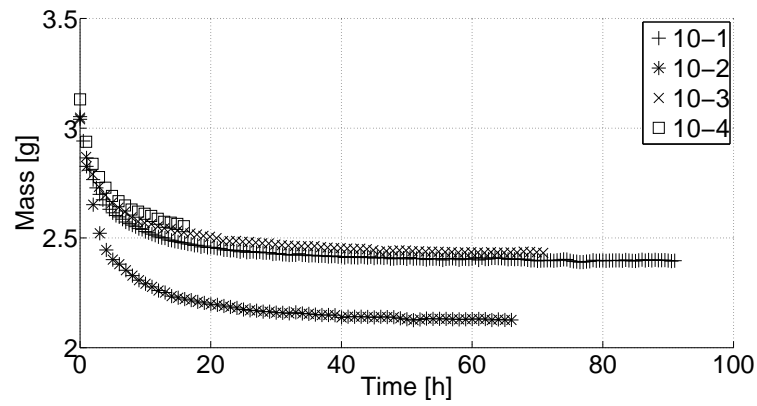
Figure 5.17: Observed mass loss for all the 10 mm samples
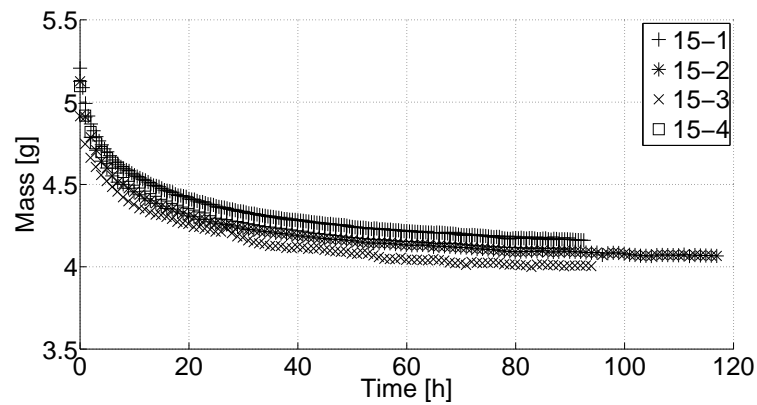
Figure 5.18: Observed mass loss for all the 15 mm samples

The drying rate can be calculated based on the mass loss and the evaporation surface:

$$q = -\frac{1}{S}\frac{dm}{dt} \qquad (5.1)$$

where m and S are respectively the measured mass and drying surface of the sample (in this specific case, the top surface). Since clay undergoes shrinkage during drying, this phenomenon has to be taken into account to calculate the drying rate. This changes was evaluated using the measures of cross-sectional area from the tomographic reconstructions (see Fig. 5.13).

The drying rate presents heavy fluctuations when the raw data from the weight measurements are used due to the small time steps between two weighings, during which mass may not vary enough. Consequently, the curves have been smoothed with a Lanczos filter (cf. Fig. 5.19) (Lanczos (1988)).
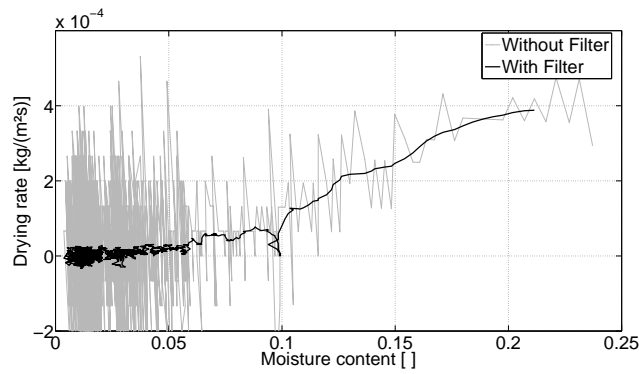
Figure 5.19: Krischer curve with and without Lanczos filter

Using these smoothed data, the drying rate can then be plotted as a function of time (see Fig. 5.20 to 5.22) or as a function of the water content (Krischer curve)(see Fig. 5.23 to 5.25). The first observation is that the water content on Fig. 5.23 to 5.25 is continuous, confirming our assumption that the evaporation of water during the scanning could be neglected.
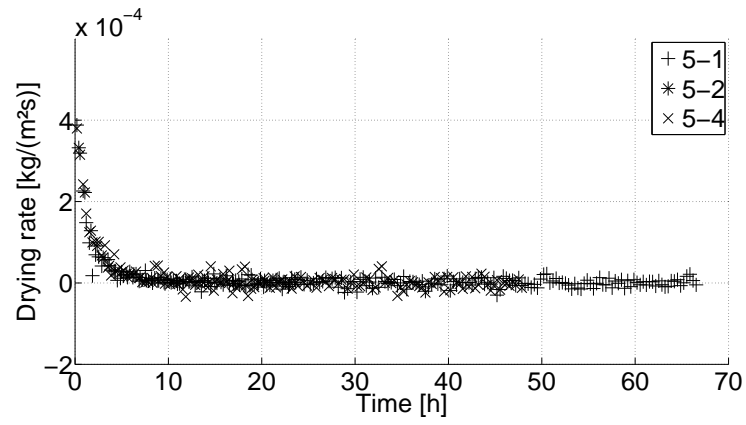
Figure 5.20: Observed drying rate for all the 5mm samples
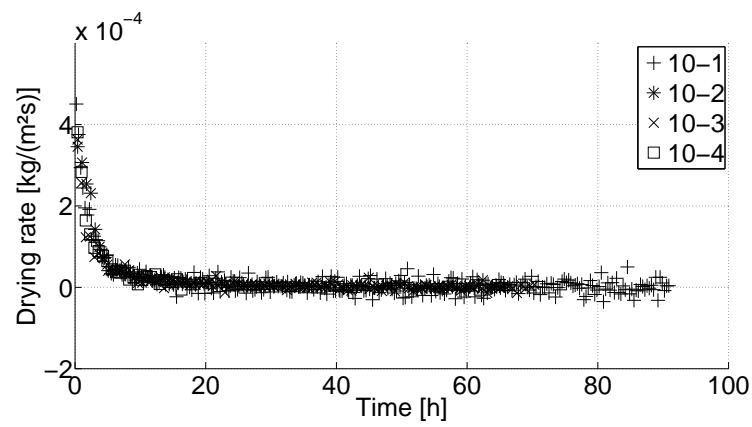
Figure 5.21: Observed drying rate for all the 10mm samples
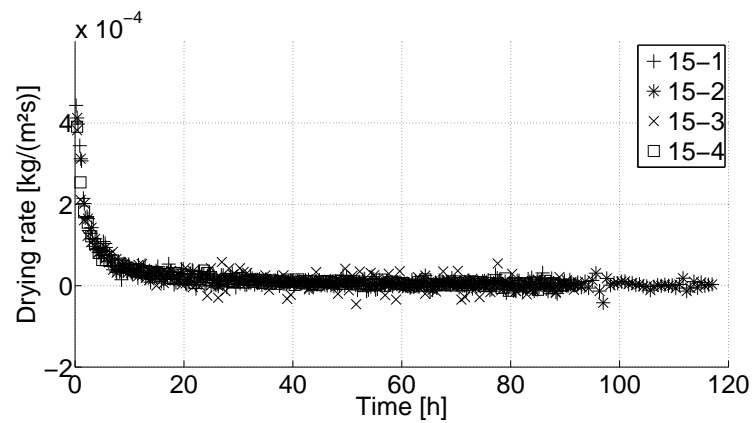
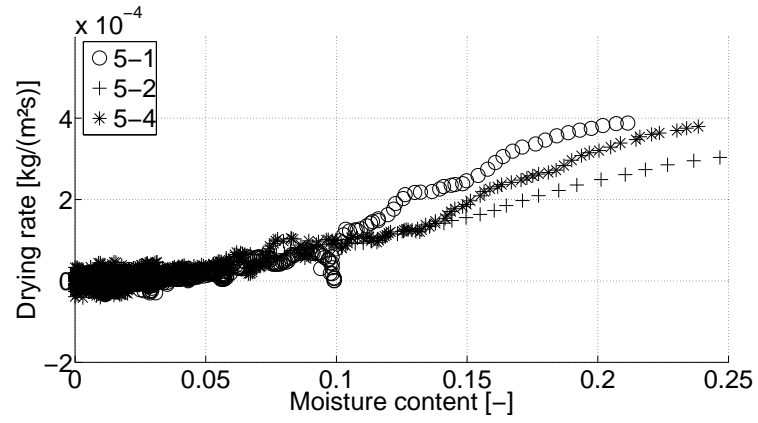Figure 5.22: Observed drying rate for all the 15mm samples

81

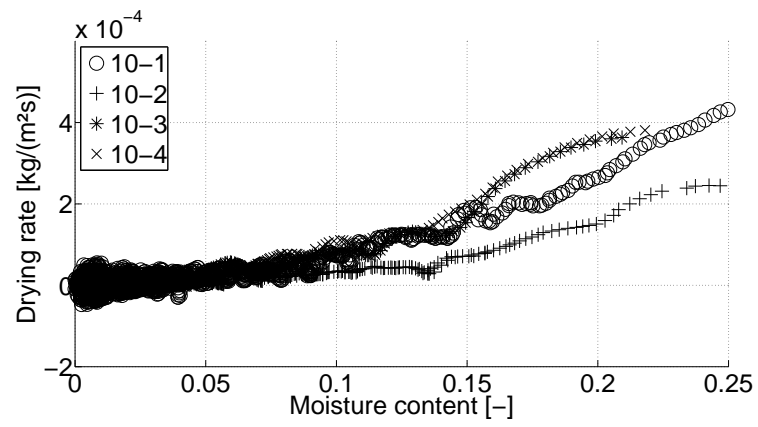Figure 5.23: Observed Krischer curve for all the 5mm samples

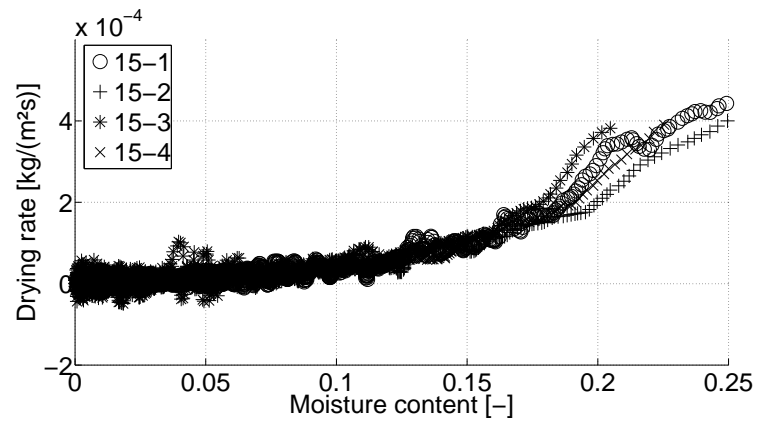Figure 5.24: Observed Krischer curve for all the 10mm samples

Figure 5.25: Observed Krischer curve for all the 15mm samples

82

Contrary to the theoretical curve, little to no CRP are observable on the experimental results. This can be explained using Lehmann's theory (Lehmann et al. (2008)) already presented in chapter 3. His studies aimed at characterizing an hydraulic connection layer between the evaporation surface and the drying front. This connection layer has been shown to be necessary to observe a constant drying rate Yiotis et al. (2003). In the case of Boom clay :

$$L_{crit} = \frac{\Delta h_{cap}}{1 + \frac{\frac{q_{max}}{\rho_w} \mu_w}{k_{rel,w}(S_{r,w})k_{sat}\rho_w g}} \tag{5.2}$$

Based on our experimental results ($q_{max} = 3,8.10^{-4}$ $[kg/m^2/s]$) and our material properties ($k_{sat} = 6.10^{-19}$ $[m^2]$), the value of the critical length is $L_{crit} = 4.91$ mm. That length is smaller than any of our sample height and thus none of the curves present a clear CRP. Some sample may exhibit short CRP like behavior because the value of the hydraulic connection layer calculated is based on strong hypothesis (such as linear water pressure field distribution from the surface to the drying front or the chosen range of pore pressure considered to calculate the capillary head). This means that the length determined is more an indicative order of magnitude than a precise assessment. Our samples are of the same order of magnitude as the hydraulic connection length and some very short CRP is thus possible. Note that no significant difference can be seen between the different sample sizes. To prove this point, all the Krischer's curves have been grouped on a single figure (see Fig. 5.26).
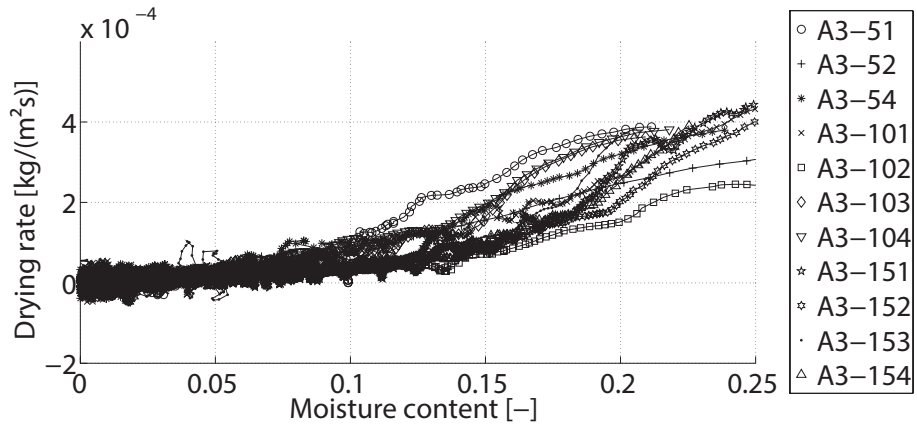

Figure 5.26: Observed Krischer curve for all the sample tested grouped on one figure

Since no noticeable scale effect can be exhibited, further results will be presented for the first series (i.e. the 5 mm tall samples) only.
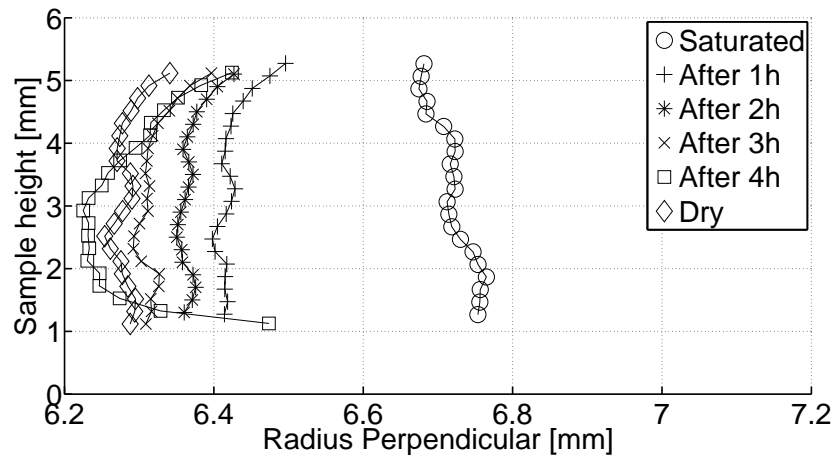
5.6.2 Shrinkage

Using the micro-tomographic scans, it is possible to follow the evolution of the cross sections of the sample along its height or to follow the evolution of a chosen cross section (Fig. 5.28). From that evolution, and knowing the bedding direction, the evolution of the radii parallel and perpendicular to the bedding plane can be determined (Fig. 5.27(a) and Fig. 5.27(b)). On both Fig. 5.28 and Fig. 5.27, it can be observed that most of the shrinkage takes place at the very beginning of the drying (around 2/3 of the final strain has developed after 1 hour). Fig. 5.27 also shows that the shrinkage quickly becomes uniform on the sample height. An other

83

information that can be taken from both figures is that the results after 4h are incoherent for sample 5-1. It is especially showing on Fig. 5.27 where the radius increases. This is due to problems with the reconstruction of the tomographic scans.
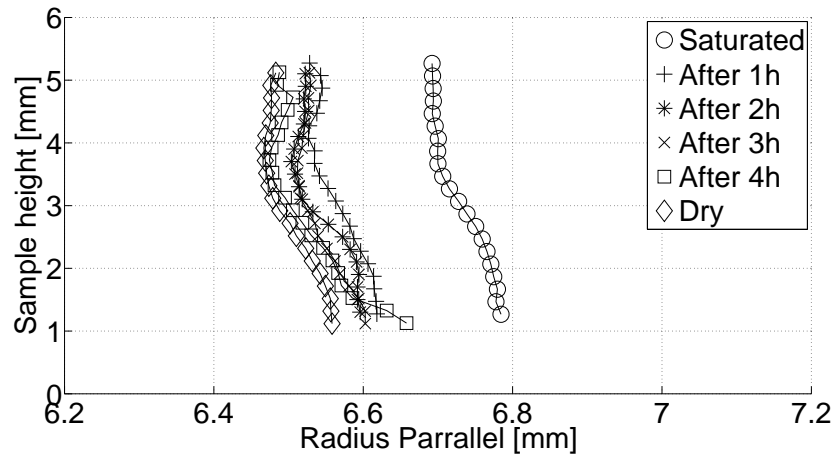
(a) Evolution of the radius parallel to the bedding plane with time

(b) Evolution of the radius perpendicular to the bedding plane with time

Figure 5.27: Evolution of the radii for sample 5-1

To prove that the shrinkage of all the samples is, just as the drying kinetics, very similar for all the samples, the final shrinkage in the three principal directions for all the samples tested is presented in Fig.5.29.

5.7 Numerical modeling

In this section, the thermo-hydro-mechanical model described in chapter 2 is used to reproduce the drying behavior of the Boom Clay samples tested during the experimental campaign (cf. section 5.4). A summary of the governing equations of the aforementioned model is given below. The mechanical framework used to simulate Boom clay behavior is also detailed.

As shown in section 5.6, variability between samples is low and their behavior is very similar because the hydraulic connection layer is shorter than the height of any of the samples
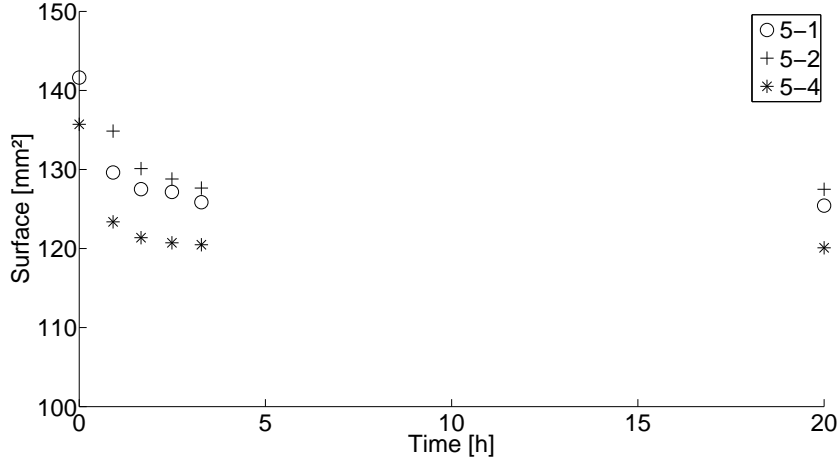
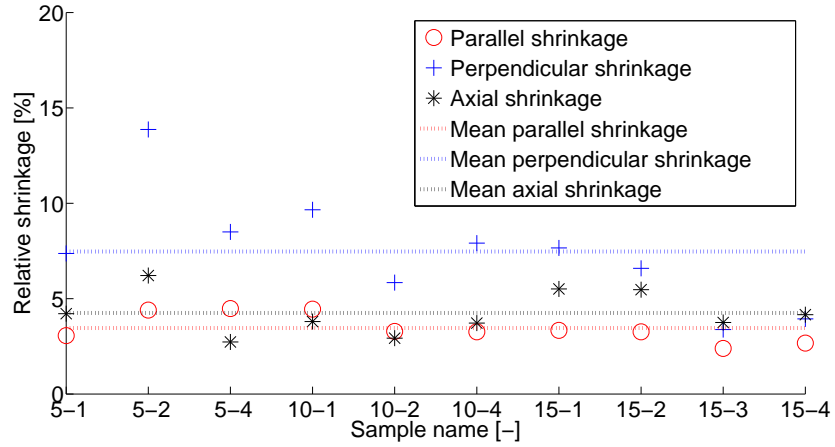Figure 5.28: Evolution of the surface of a chosen cross section (top of the sample)

Figure 5.29: Final shrinkage for all the sample tested

experimentally tested. Therefore using only one sample to perform the model validation is acceptable. Sample 5-1 was arbitrarily chosen. The study was conducted using the finite element code LAGAMINE developped at the University of Liège (Collin et al. (2002b)).

5.7.1 Governing equations

In this section, a summary of the equations used to solve the boundary value problem is presented to remind the reader of the system of equations solved using the finite element method.

Momentum balance

$$\frac{\partial \sigma_{ij}}{\partial x_j} + \rho g_i = 0 \tag{5.3}$$

where g_i is the gravitational acceleration vector and ρ is the density of the mixture :

$$\rho = \rho_s(1-n) + \rho_l S_{r,l} n + \rho_g(1 - S_{r,l})n \tag{5.4}$$

where ρ_l, ρ_g are respectively the densities of the liquid and gas phases.

Water transfers The water transfers are governed by Richard's equation:

$$\underbrace{\frac{\partial(\rho_w n S_{r,w})}{\partial t} + \frac{\partial}{\partial x_i}(\rho_w q_{l,i})}_{\text{Liquid water}} + \underbrace{\frac{\partial(\rho_v n S_{r,g})}{\partial t} + \frac{\partial}{\partial x_i}(\rho_v q_{g,i} + i_{v,i})}_{\text{Water vapor}} = Q_w \qquad (5.5)$$

where ρ_w and ρ_v are the liquid water and the vapor densities, n is the porosity, $S_{r,w}$ and $S_{r,g}$ are the water and gas saturation degrees in volume, t is the time, Q_w is the injected flux. $q_{l,i}$, $q_{g,i}$ are the advective fluxes of the liquid and of the gas phases with respect to the solid phase and $i_{v,i}$ is the non-advective fluxes (diffusion) of water vapor. The detailed formulation of these terms can be found in chapter 2. It is also important to note that Boom clay being an anisotropic material we are using an intrinsic permeability tensor of the form :

$$\underline{\underline{k}}_{sat} = \begin{pmatrix} k_{sat,/\!/} & 0 & 0 \\ 0 & k_{sat,\perp} & 0 \\ 0 & 0 & k_{sat,/\!/} \end{pmatrix} \qquad (5.6)$$

where $k_{sat,/\!/}$ and $k_{sat,\perp}$ are the intrinsic permeabilities parallel and perpendicular to the stratification, respectively.

Gas transfer In this work, the pressure field is assumed to be homogeneous on the whole geometry and constant with time. Hence, the gas mass balance equation is not a part of our system of equations and is thus not solved.

Heat transfer The energy balance equation is :

$$\dot{S}_T + \frac{\partial V_{T,i}}{\partial x_i} + \dot{E}_{H_2O}^{w-v}.L - Q_T = 0 \qquad (5.7)$$

where S_T is the enthalpy of the system, V_T is the heat flux, Q_T is the heat production term and L is the water evaporation latent heat.

5.7.2 Mechanical model

The governing equation of the different mechanisms have been recalled in the previous section. Since no mechanical law was presented in chapter 2, the mechanical part of the model is going to be more thoroughly addressed in this section. Bishop's effective stress (cf. section 2.5.4.1) has been chosen to describe the stress-strain relation because it directly incorporates the effect of the suction. Classically, a couple of stresses (net stress and suction Gens and Alonso (1992) is used to reproduce plastic collapse during wetting path but for drying path, the effective stress allows to reproduce the observed behavior. As a reminder, Bishop's effective stress writes :

$$\sigma'_{ij} = \sigma_{ij} - p_g \delta_{ij} + S_{r,w}(p_g - p_w)\delta_{ij} \qquad (5.8)$$

where σ'_{ij} is the effective stress tensor, σ_{ij} is the total stress tensor, $S_{r,w}$ is the water saturation and δ_{ij} is Kronecker's tensor. p_g and p_w denote respectively gas and water pressure $[Pa]$.

Linear elasticity theory A linear elastic relationship can be written to link the elastic strain rate, $\dot{\epsilon}_{ij}^e$, to the effective stress tensor. That relation is Hooke's law :

$$\dot{\epsilon}_{ij}^e = D_{ijkl}^e \dot{\sigma}_{kl}' \tag{5.9}$$

$$\dot{\sigma}_{ij}' = C_{ijkl}^e \dot{\epsilon}_{kl}^e \tag{5.10}$$

where C_{ijkl}^e is Hooke elastic constitutive tangent tensor that must be symmetric because of thermodynamic requirement (Greenhill (1893)) and D_{ijkl}^e is the elastic compliance tensor corresponding to the inverse of the Hooke elastic tensor. For an isotropic material, the compliance tensor is defined by two parameters, ν and E or K and G, and is given by :

$$D_{ijkl}^e = \begin{bmatrix} \frac{1}{E} & -\frac{\nu}{E} & -\frac{\nu}{E} & 0 & 0 & 0 \\ -\frac{\nu}{E} & \frac{1}{E} & -\frac{\nu}{E} & 0 & 0 & 0 \\ -\frac{\nu}{E} & -\frac{\nu}{E} & \frac{1}{E} & 0 & 0 & 0 \\ 0 & 0 & 0 & \frac{1+\nu}{E} & 0 & 0 \\ 0 & 0 & 0 & 0 & \frac{1+\nu}{E} & 0 \\ 0 & 0 & 0 & 0 & 0 & \frac{1+\nu}{E} \end{bmatrix} \tag{5.11}$$

where E is the isotropic Young's modulus and ν is Poisson's ratio. The shear modulus, G, and the bulk modulus, K, are respectively given by :

$$G = \frac{E}{2(1+\nu)} \qquad\qquad K = \frac{E}{3(1-2\nu)} \tag{5.12}$$

Anisotropy As presented in section 5.3, Boom clay is characterized by a strong anisotropy of the mechanical properties between the direction parallel and perpendicular to the bedding planes (a ratio of around 2 between the elastic modulus in the direction parallel and perpendicular (Dizier (2011))). Our drying experiments clay also exhibited that anisotropy (cf. shrinkage results in section 5.6). Its mechanical behavior is thus modeled using an orthotropic model (Chen et al. (2011)). In the case of an orthotropic material, the elastic compliance tensor, D_{ijkl}^e, is given by :

$$D_{ijkl}^e = \begin{bmatrix} \frac{1}{E_{/\!/}} & -\frac{\nu_{\perp,/\!/}}{E_\perp} & -\frac{\nu_{z,/\!/}}{E_z} & 0 & 0 & 0 \\ -\frac{\nu_{/\!/,\perp}}{E_{/\!/}} & \frac{1}{E_\perp} & -\frac{\nu_{z,\perp}}{E_z} & 0 & 0 & 0 \\ -\frac{\nu_{/\!/,z}}{E_{/\!/}} & -\frac{\nu_{\perp,z}}{E_\perp} & \frac{1}{E_z} & 0 & 0 & 0 \\ 0 & 0 & 0 & \frac{1}{2G_{/\!/,\perp}} & 0 & 0 \\ 0 & 0 & 0 & 0 & \frac{1}{2G_{/\!/,z}} & 0 \\ 0 & 0 & 0 & 0 & 0 & \frac{1}{2G_{\perp,z}} \end{bmatrix} \tag{5.13}$$

The symmetry of the stiffness matrix imposes that:

$$\frac{\nu_{\perp,/\!/}}{E_\perp} = \frac{\nu_{/\!/,\perp}}{E_{/\!/}}, \frac{\nu_{z,/\!/}}{E_z} = \frac{\nu_{/\!/,z}}{E_{/\!/}}, \frac{\nu_{\perp,z}}{E_\perp} = \frac{\nu_{z,\perp}}{E_z} \tag{5.14}$$

The symbol, $/\!/$, refers to the radial direction parallel to the bedding plane while $\perp$ refers to the radial direction perpendicular to the bedding plane and z to the axial direction of the cylinder. The axial direction is also parallel to the bedding plane but due to the slightly different values of the shrinkage found on the experimental results (cf. Fig. 5.49), a different elastic modulus is used. Hence, one uses an orthotropic model and not a transverse isotropic one.

Plasticity   Most of the time in the literature, Boom clay has been modeled using a CamClay model (Hueckel et al. (1988), Laloui et al. (2002)). However, during a drying experiment, loading and boundary conditions (free shrinkage) lead to an almost isotropic stress path with stresses staying below the preconsolidation pressure, p_0 ($p_0 = 6[MPa]$ (Coll (2005))). For these reasons, we decided to restrict the mechanical modeling to an elastic orthotropic model and to not include a yield criterion to simulate the drying experiments of Boom clay.

Cracking   It has to be noted that while cracking is experimentally observed, no tensile strength criterion is included because Boom Clay presents very clear bedding planes which were experimentally proved to be the cause of cracks initiation. It would thus be better suited to use initial defaults at the level of the bedding planes and work in a crack propagation framework based on required energy or crack toughness. Another possible method would be to calibrate a cohesive interface mechanism (Cerfontaine et al. (2015)).

5.7.3   Mesh, initial and boundary conditions

Here, the mesh used to reproduce the sample studied (i.e. sample number 5-1) is presented as well as all the initial and boundary conditions.

Mesh   Because of Boom clay orthotropy, it is not possible to represent the cylindrical sample using a 2D axisymmetric mesh. A 3D mesh is thus required and since the sample is bi-symmetric, only a quarter of the geometry is represented. Since most of the fluxes are vertical (i.e. z direction) as few elements as possible are used in the horizontal plane (i.e. x-y plane). To study the dependency of the results on mesh density, simulations have been performed with 10, 30 and 50 vertical layers (cf. Fig. 5.30). The simulations are purely hydraulic.
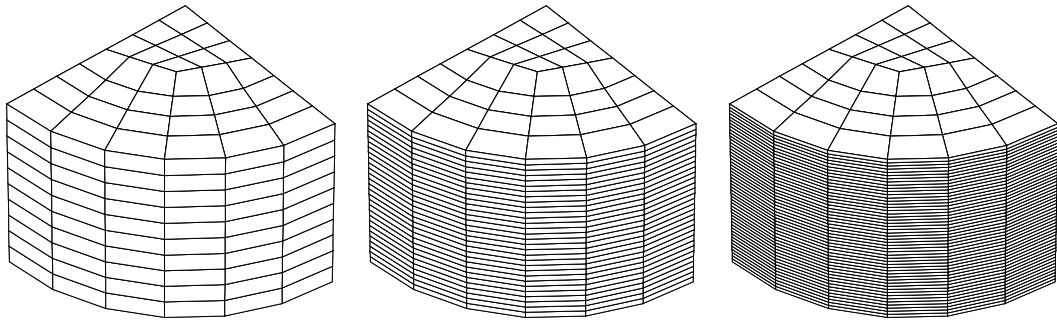

Figure 5.30: Different meshes considered for the sensitivity study on mesh density : 10 (left), 30 (middle) and 50 (right) vertical layers

As can be seen in Fig. 5.31, displaying the Krischer curves for the different meshes, the 10 layer mesh is slightly less accurate. Since no significant difference can be seen between the 30 and 50 layers simulations, 30 vertical layer will be used further on. Also we decided to use a mesh denser near the drying surface because this is where the water pressure gradient is the most important (see Fig. 5.32). The final mesh is visible in Fig. 5.33.
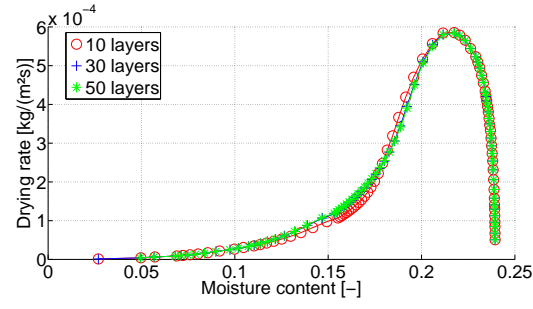
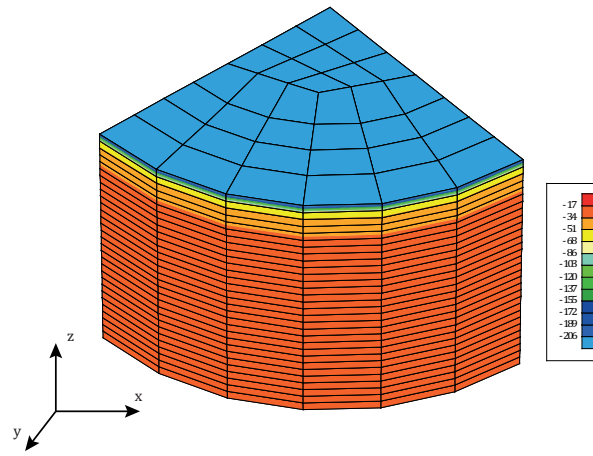Figure 5.31: Krischer curves for the different meshes tested

Figure 5.32: Water pressure distribution ([MPa]) on the 30 vertical layers mesh
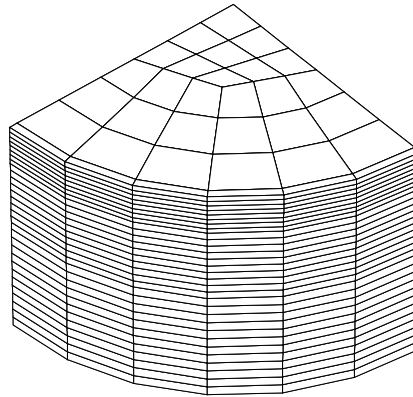

Figure 5.33: Final mesh

Boundary conditions   The vertical displacements at the bottom of the sample are prevented. The atmospheric pressure is also applied at all the external boundaries. The boundary layer boundary conditions is implemented through a water pressure and a temperature at the envi-

ronmental node (cf. section 4.2.1). The temperature imposed corresponds to the temperature of the drying air (i.e. 25 °C) and the water pressure is calculated based on the temperature and relative humidity using Kelvin's Law :

$$p_c = p_g - p_w = -\frac{\rho_w RT}{M} ln(RH) \tag{5.15}$$

where ρ_w is the water density, R is the gas constant, M is the water molar mass and T and RH are the temperature and relative humidity of the drying air.

Initial conditions The sample is initially at rest ($\sigma' = 0\ [MPa]$), saturated and at room temperature :

Degree of Freedom	Values	Units
$p_{w,ini}$	100	[kPa]
$p_{g,ini}$	100	[kPa]
T_{ini}	17	[° C]

Table 5.3: Initial conditions

5.7.4 Numerical results

In this section, the results obtained for the different simulations performed on Boom clay are presented. In order to highlight the influence of each mechanism, simulations are performed with increasing coupling and complexity from a simple pure hydraulic model to a thermo-hydro-mechanical model.

5.7.4.1 Hydraulic simulation

The objective of the following numerical simulation is, in a first approach, to analyse if a simple hydraulic model allows to reproduce the drying kinetics observed experimentally in Boom clay. The hydraulic parameters used are presented in Table 5.4 as well as the van Genuchten formulation for saturation degree and relative permeability. As a reminder, the van Genuchten formulation writes :

$$S_{r,w} = S_{res} + (S_{sat} - S_{res})(1 + (\frac{s}{\alpha_{vG}})^{n_{vG}})^{-m_{vG}} \tag{5.16}$$

$$k_{rel,w} = \sqrt{S_{r,w}}(1 - (1 - S_{r,w}^{\frac{1}{m_{vG}}})^{m_{vG}})^2 \tag{5.17}$$

where n_{vG}, m_{vG} are model parameters. α_{vG} is a parameter related to the air entry pressure, S_{res} is the water residual saturation, S_{sat} is the water maximal saturation and s is the suction. In this case, if the relative water permeability, $k_{rel,w}$ becomes lower than the minimum acceptable relative permeability, $k_{r,min}$, then $k_{rel,w} = k_{r,min}$. This parameter is necessary to avoid permeability too low leading to very weak water flows and to numerical convergence problems. The values of the water permeability are not directly extracted from Table 5.2 which presented a literature review of Boom clay properties but are in accordance with the range suggested. The

Parameters	Values	Units
Hydraulic parameters		
$k_{sat,/\!/}$	6.10^{-19}	$[m^2]$
$k_{sat,\perp}$	3.10^{-19}	$[m^2]$
n	0.39	$[-]$
τ	0.1	$[-]$
van Genuchten parameters		
α_{vG}	12.5	$[MPa]$
n_{vG}	1.7	$[-]$
S_{sat}	1	$[-]$
S_{res}	0.01	$[-]$
$k_{r,min}$	10^{-7}	[-]

Table 5.4: Hydraulic model parameters
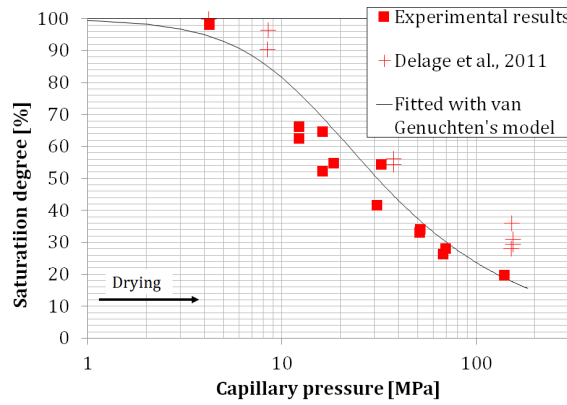
Figure 5.34: Experimental data and van Genuchten model fitting

parameters of the van Genuchten model are based on fitting of the model to our experimental data as visible on Fig 5.34.

The mass and heat transfer coefficients, α and β, are calculated using the following expressions :

$$q = \alpha(\rho_{v,surf} - \rho_{v,air}) \tag{5.18}$$

$$f = Lq - \beta(T_{air} - T_{surf}) \tag{5.19}$$

where q is the drying rate during the CRP, $\rho_{v,air}$ is vapor density of the drying air, $\rho_{v,surf}$ is the vapor density at the surface of the sample, T_{air} is the temperature of the drying air, T_{surf} is the temperature at the surface of the sample and L is the water evaporation latent heat (2500 kJ/kg). Since we know, from the experiments, the drying rate during the CRP and that all the other parameters are known since we impose the boundary conditions, α and β can be determined. The following values are obtained for the sample considered (Table 8.9)

Using these parameters and the presented hydraulic model, the following results are obtained (see Fig. 5.35).

The first observation that can be made based on Fig. 5.35 is that the drying kinetics do not correspond to the experimental results. Is it because of the parameters chosen or because of

Parameters	Values	Units
α	0.048	$[m/s]$
β	53	$[W/m^2/K]$

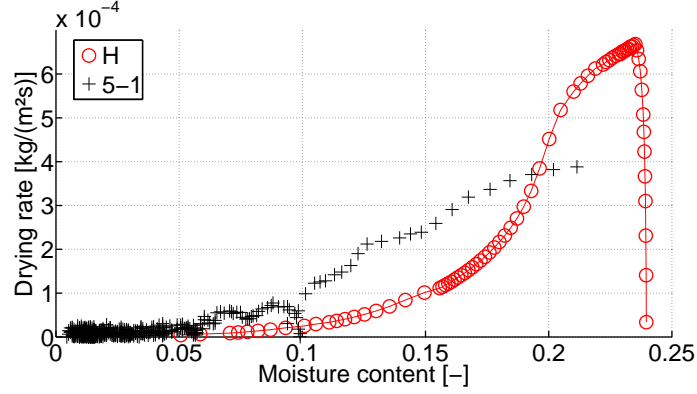Table 5.5: Transfer coefficient for the considered sample

Figure 5.35: Comparison of experimental and numerical Krisher's curve for sample 5-1 using a hydraulic model only

the physics involved (i.e. do we make too big of an assumption by neglecting the thermal and mechanical aspects of the problem)? To answer that question, we need to add more coupling and see if they improve the overall concordance.

As can be seen in Table 5.4, one of the parameters defined is the minimal value of the relative permeability, $k_{r,min}$. As it was just explained, this parameter is used to avoid convergence problems but if the value chosen is too important, it will lead to artificially important water flows and thus to higher drying rate during the CRP. To choose an appropriate value of $k_{r,min}$, a sensitivity study was conducted which results can be seen in Fig. 5.36.
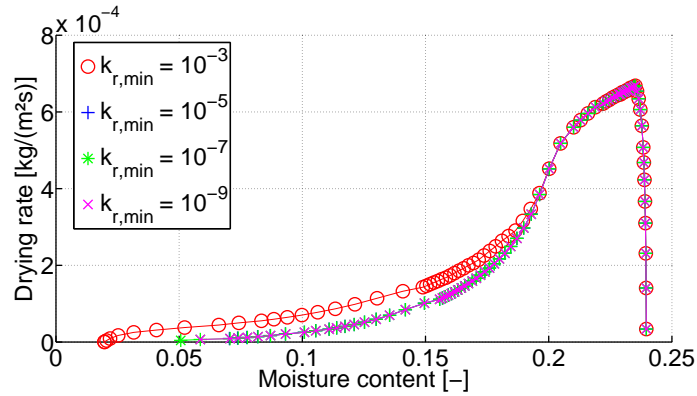

Figure 5.36: Krischer curves for the different minimal relative permeability considered

The drying rate for $k_{r,min} = 10^{-3}$ is "forced" to remain higher than it should by a permeability artificially too important. The three other curves are perfectly superimposed. To be sure that the value chosen will not pose any problem but will allow for good enough numerical convergence, a value of $k_{r,min} = 10^{-7}$ was chosen.

5.7.4.2 Hydro-mechanical simulation

The objective of this simulation is to determine whether adding the mechanical aspect of the problem improves the fitting of the drying kinetics. The mechanical law used is a linear orthotropic elastic one (presented in section 5.7.2) and the parameters are given in Table 5.6.

References	Parameters	Values	Units
	$E_{/\!/}$	350	$[MPa]$
	$E_\perp$	175	$[MPa]$
Dizier (2011)	E_z	300	$[MPa]$
	$\nu_{/\!/,\perp}$	0.125	$[-]$
	$\nu_{/\!/,z}$	0.0625	$[-]$
	$\nu_{\perp,z}$	0.0625	$[-]$
	$G_{\perp,/\!/}$	140	$[MPa]$
	$G_{\perp,z}$	140	$[MPa]$

Table 5.6: Linear elasticity mechanical law parameters

A ratio $\frac{E_{/\!/}}{E_\perp} = 2$ is used which is consistant with studies on the transverse anisotropy of over-consolidated clay (Garnier (1973); Gatmiri (1989)) and this range of value was already used for Boom clay in the work of Dizier (2011). The value used for E_z is different even though it is also in a direction parallel to the bedding plane because the observed axial shrinkage is higher then the shrinkage parallel to the bedding plane (see Fig. 5.29).
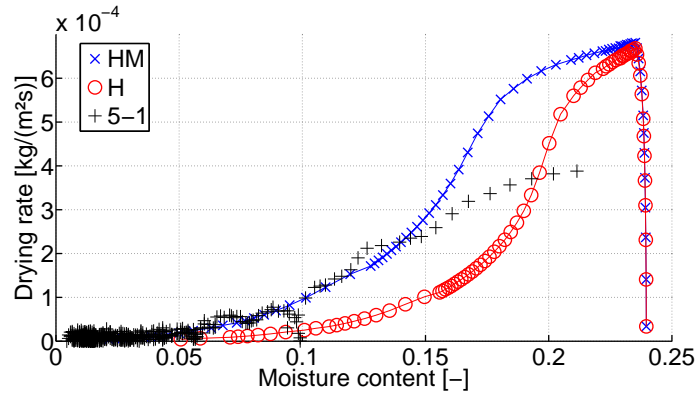The following results are obtained (cf. Fig. 5.37)

Figure 5.37: Comparison of experimental and numerical Krisher's curve for sample 5-1 using a hydro-mechanical model

It can be observed that the drying rate is already closer to the experimental data even though the results is not satisfying yet. Indeed, by neglecting the mechanical aspect of the problem, we do not consider the influence of shrinkage in the drying surface. From Eq. 5.1, it can be deduced that when the drying surface decreases due to shrinkage - ceteris paribus - the drying rate increases. In this case, this leads to a drying rate decreasing more slowly which is closer to the experimental behavior. The initial drying rate is still too important though. The results in terms of shrinkage are also presented since the mechanical aspect is included. The results

93

are presented as the variation of a chosen cross section (1 mm under the drying surface). It can be seen (Fig. 5.38) that the numerical simulation leads to a final surface much smaller than the experimental one and thus the samples shrinks too much. Also, the numerical shrinkage rate
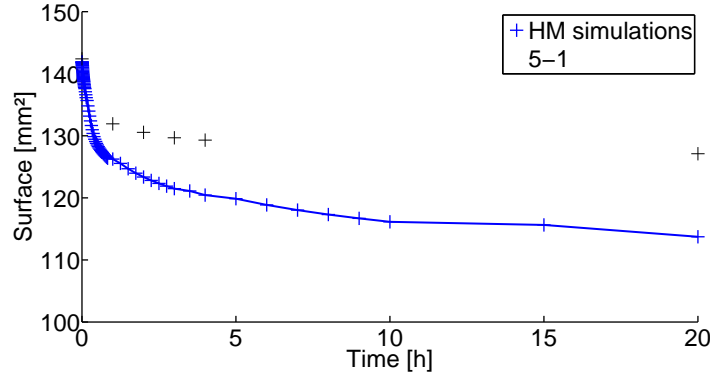

Figure 5.38: Comparison of experimental and numerical surface with time for sample 5-1 using a hydro-mechanical model

does not decrease enough with time. The numerical results are obtained with a constant elastic modulus and leads to too much shrinkage. This indicates that there is a change in material behavior during drying that is not only controlled by the drying rate (i.e. the material stiffens while drying explaining a more important decrease in shrinkage rate compared to our numerical simulation with a constant elastic modulus).

5.7.4.3 Thermo-hydro-mechanical simulation

The previous simulation improved the concordance but the results are not satisfying yet. To emphasize the influence of the thermal part of the problem, a thermo-hydro-mechanical simulation is performed. The parameters of the thermal law are given in Table 5.7 :
The drying kinetics is now much closer to the experiments (see Fig. 5.39). Since our drying experiments are conducted at low temperature (25 °C) one could have thought that temperature would play a minor role in the problem. However, the fact that the temperature is fixed artificially imposes a higher drying rate during the CRP because of equation 3.25. Indeed, the term $T_{surf} - T_{air}$ is a constant and f is null. Since the temperature at the surface is not decreasing toward the wet bulb temperature, it means that it allows for more heat to be used for the evaporation of water, leading to higher drying rate. As clearly shown on Fig. 5.40, the thermal aspect of the problem has very little effect on the shrinkage. This is logical since the temperature gradient is low, leading to low thermal expansion. We can now conclude that adding the mechanical and thermal aspect of the problem allowed us to reproduce the drying kinetics of Boom clay but something is still missing in the model to be able to accurately reproduce the shrinkage.

5.7.4.4 Non-linear elasticity

The shrinkage numerically obtained is far too important. The most direct way to solve this problem is to increase the elastic moduli of the material. To achieve the correct final shrinkage as can be seen in Fig. 5.41, $E_{\parallel,ref} = 700[MPa]$ and $E_{\perp,ref}350[MPa]$ are required.

References	Parameters	Values	Units
	ρ_w	1000	$[kg/m^3]$
	$c_{p,w}$	4185	$[J/kg/K]$
	Γ_w	0.6	$[W/m/K]$
	α_w	7.10^{-6}	$[1/K]$
	ρ_a	1.2	$[kg/m^3]$
	$c_{p,a}$	1004	$[J/kg/K]$
	Γ_a	0.025	$[W/m/K]$
	ρ_v	0.59	$[kg/m^3]$
	$c_{p,v}$	1864	$[J/kg/K]$
	Γ_v	0.02	$[W/m/K]$
Bernier et al. (2007)	ρ_s	2670	$[kg/m^3]$
Wouters and Vandenberghe (1994)	$c_{p,s}$	1400	$[J/kg/K]$
SCK-CEN (1997)	Γ_s	1.69	$[W/m/K]$
SCK-CEN (1997)	α_s	10^{-5}	$[1/K]$

Table 5.7: Thermal model parameters
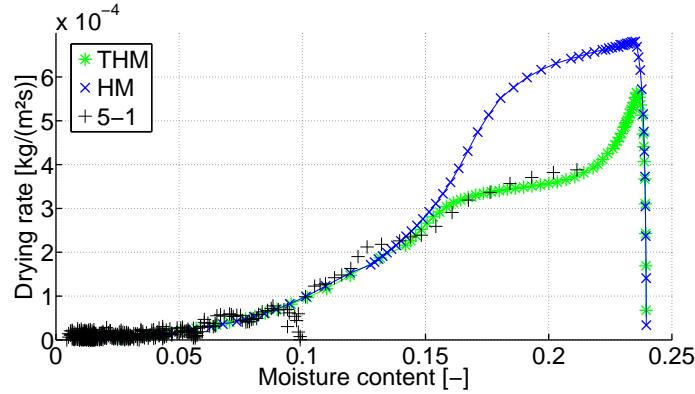
Figure 5.39: Comparison of experimental and numerical Krisher's curve for sample 5-1 using a thermo-hydro-mechanical model

It can be observed that even though the final surface is very close to the experimental data, intermediate values are not correct and the shrinkage rate is thus too slow (i.e. at the beginning of the drying experiment, the surface decreases faster experimentally than numerically). This means that the initial moduli are too important. Nonetheless, lower elastic moduli do not reproduced the final surface properly and lead to too much shrinkage. This comforts the earlier analysis that Boom clay stiffens during drying leading to an increase in elastic moduli. To take this feature into account, a non linear elasticity law is used.We suggest to use a non linear elasticity law with a dependence of Young's modulus on the stress state (based on the formulation of Modaressi and Laloui (1997)) :

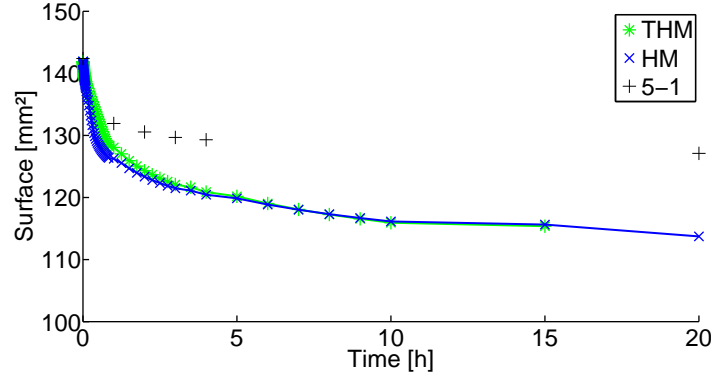$$E_i = E_{0,i} + E_{ref,i}(\frac{p'}{p_{ref}})^b \tag{5.20}$$

Figure 5.40: Comparison of experimental and numerical surface with time for sample 5-1 using a thermo-hydro-mechanical model
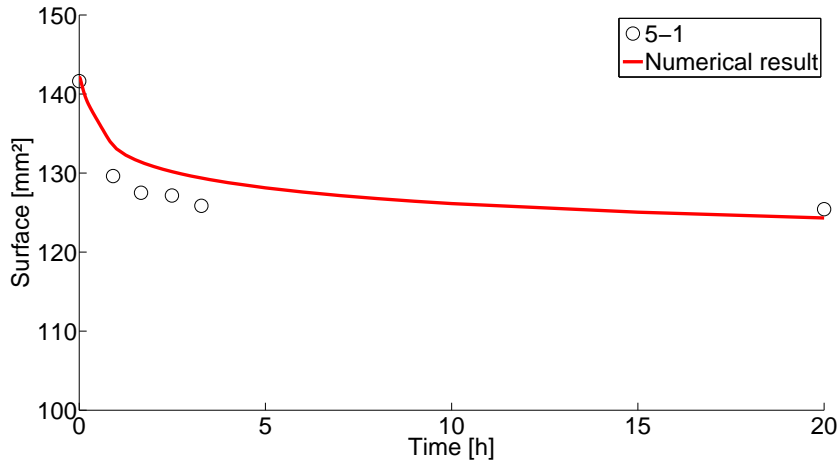

Figure 5.41: Comparison of the numerical and experimental shrinkage for elastic moduli of $E_{/\!/} = 700[MPa]$ and $E_{\perp}350[MPa]$

where E_{ref} is the Young modulus at the reference mean effective stress, p_{ref}, and b is a model parameter. $E_{0,i}$ is used to avoid null Young's modulus when the effective stress state vanishes. The dependence on the stress state means, through the use of Bishop's effective stress, that the moduli are dependent on the suction thus on the water content. The parameters of the non linear elasticity law are given in Table 5.8

Parameters	Values	Units
$E_{/\!/,ref}$	350	$[MPa]$
$E_{\perp,ref}$	175	$[MPa]$
$E_{z,ref}$	300	$[MPa]$
$E_{0,i}$	$\frac{E_{i,ref}}{5}$	$[MPa]$
b	0.8	$[-]$

Table 5.8: Non Linear elasticity mechanical law parameters

96

The parameters of this non linear law are based on retrofitting but are found to be in good accordance with the work of François (2008) using a similar non-linear elastic law on Boom clay.

Adding this element to the previously used model, we perform a final simulation which is used to obtain as close a fit as possible to all the experimental data available. In the final validation simulation, the imposition of the boundary condition has been progressively applied over 1000 seconds to account for the time needed for the air in the boundary layer around the top of the sample to reach the desired drying temperature and relative humidity. This has been done by imposing a linear variation of the temperature and water pressure at the environmental node of the boundary element (see section **??**) from the ambient to the drying conditions.

Drying kinetics Fig. 5.42, Fig. 5.43, and Fig. 5.44, which present mass loss, drying rate, and Krisher's curve, all show a good fit with the experimental results, confirming the ability of the suggested model to represent the drying behavior of this unsaturated porous material.
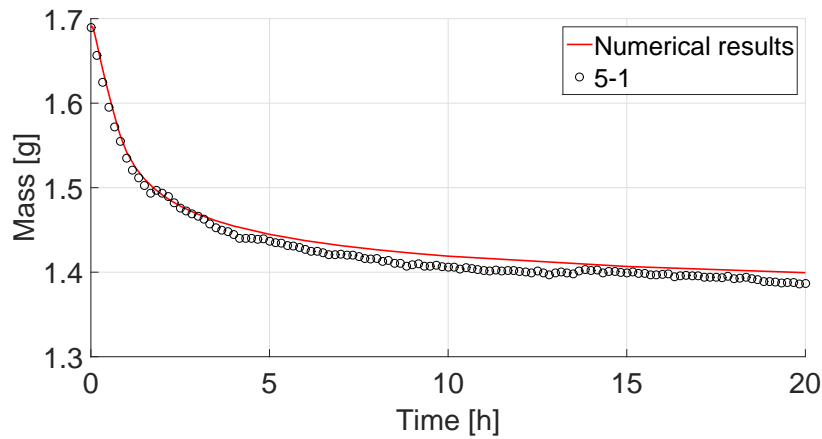
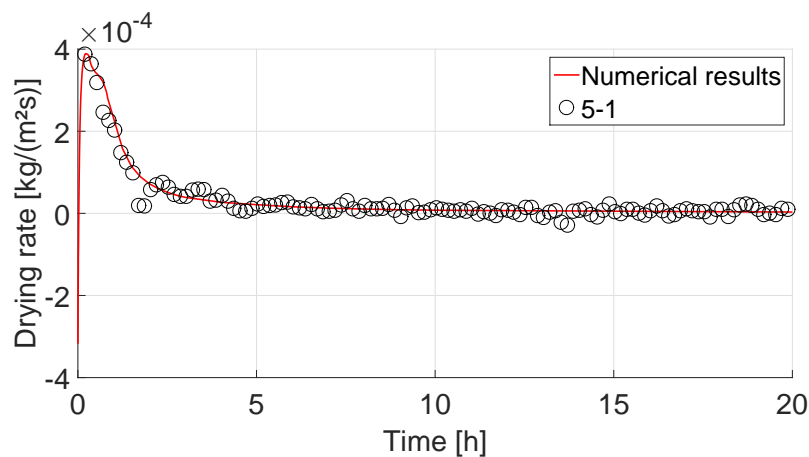Figure 5.42: Comparison of experimental and numerical mass loss for sample 5-1

Figure 5.43: Comparison of experimental and numerical drying rate evolution with time for sample 5-1
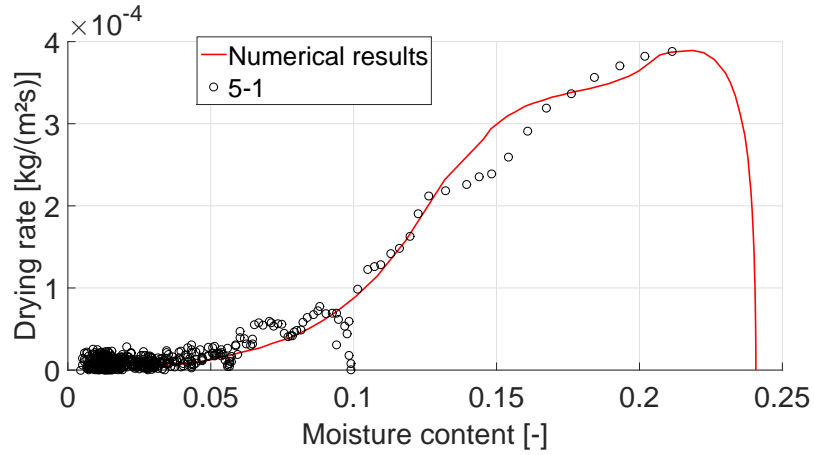
97

Figure 5.44: Comparison of experimental and numerical Krisher's curve for sample 5-1

We can see that staggering the imposition of the boundary condition suppresses the initial "peak" that was visible in Fig.5.39 leading to a very close fit of the experimental results.

Temperature Since the temperature of the sample was not recorded during the drying test, validation of the numerical results is not possible. They are however presented in Fig. 5.45. The temperature decreases from its initial value of $17°C$ (temperature of the room) to a minimum around $8°C$. This is logical since the drying air temperature $(25°C)$ is not very high and therefore cannot provide sufficient heat to enable the evaporation on its own. Heat from the porous medium is used and the temperature of the sample decreases until it reaches the temperature of the wet bulb. No constant temperature period is observed since we have no CRP. As already explained, the temperature remains at a constant value equal to the wet bulb temperature if and only if there is a CRP. When the drying rate decreases, the evaporation process is less intense and the heat supply is more than the quantity needed for the evaporation, so the temperature of the sample increases until it reaches the temperature of the drying air.
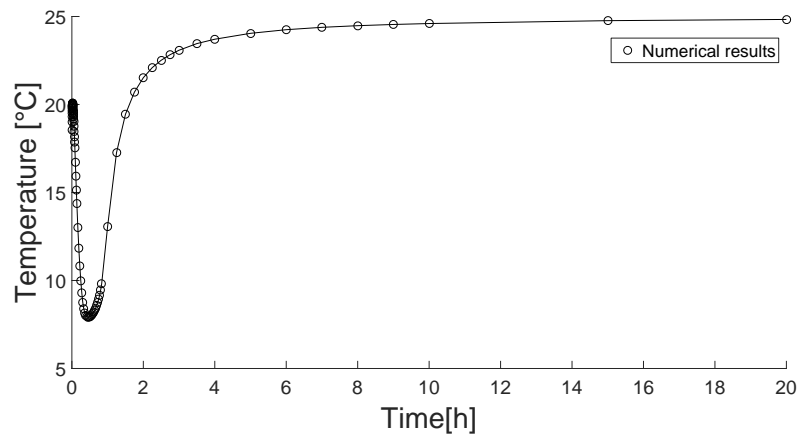

Figure 5.45: Numerical variation of the temperature with time at the drying surface

Shrinkage Fig. 5.46 shows the variation of a chosen cross section (1mm under the drying surface) of the sample with time. Non linear elasticity allows to reproduce the material stiffening and lead to a good fit of the experimental results. Fig. 5.47 shows the evolution of the
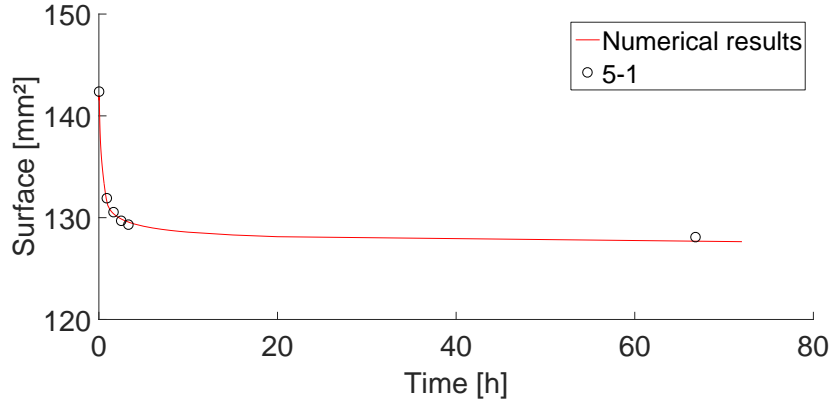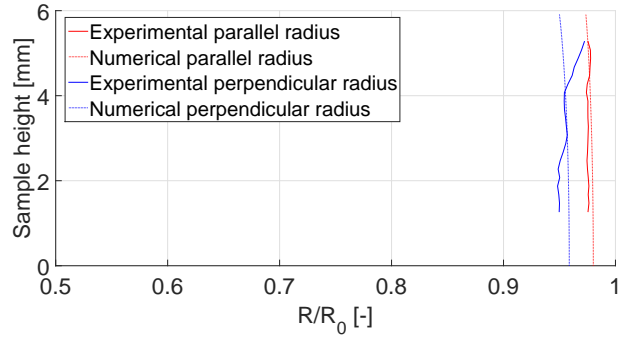

Figure 5.46: Comparison of experimental and numerical surface with time

radii parallel and perpendicular to the bedding plane at different time steps. The results are expressed as a ratio of the original radius to avoid surface effects linked to the original shape of the sample (cf. Fig. 5.27 in section 5.6). As can be seen the fit is also good with errors never exceeding 2%. The differences that can be seen around the top and the bottom of the sample are caused by the non parallelism of the external surfaces but also by damages done to the samples while preparing them. This means that the extremities of the sample are very uneven and measurements inconsistent. Volume is not as accurately estimated because of the accumulated error on the different sections along the sample height. Nonetheless, the numerical results are still close to the experimental value with errors inferior to 2% as visible on Fig. 5.48. Fig. 5.49 shows the final shrinkage in all the principal directions, averaged over the tested samples. We note that the simulated shrinkage is very close to the experiments, in all directions. This was made possible using an orthotropic mechanical law.

5.8 Sensitivity study

A few parameters have already been studied such as the minimal value of the relative permeability or the mesh density. For the former, no value was available in the literature and for the latter it is a modeling choice. To choose their value carefully and with hindsight, sensitivity studies were conducted. But there are other parameters which values are well documented that have a great influence on the numerical behavior. To get a better understanding of their influence, sensitivity studies have been performed on those parameters also. First, the influence of water permeability is analyzed to show when internal transfers govern or not the drying process. Then, the influence of water retention and water permeability curves is investigated. Finally, the influence of Young's modulus is studied.
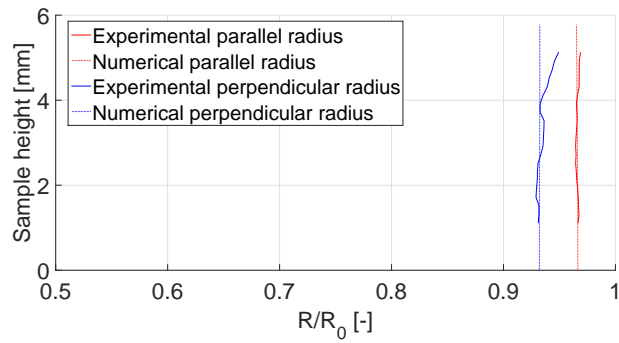
(a) After 1h of drying
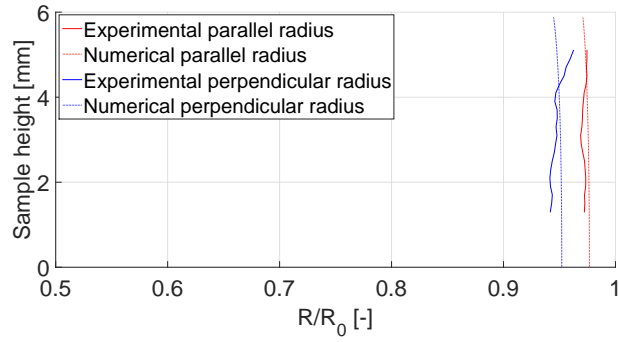
(b) After 2h of drying
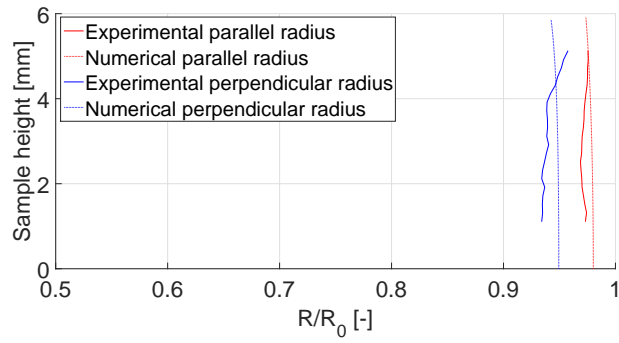
(c) After 3h of drying

(d) Dried samples

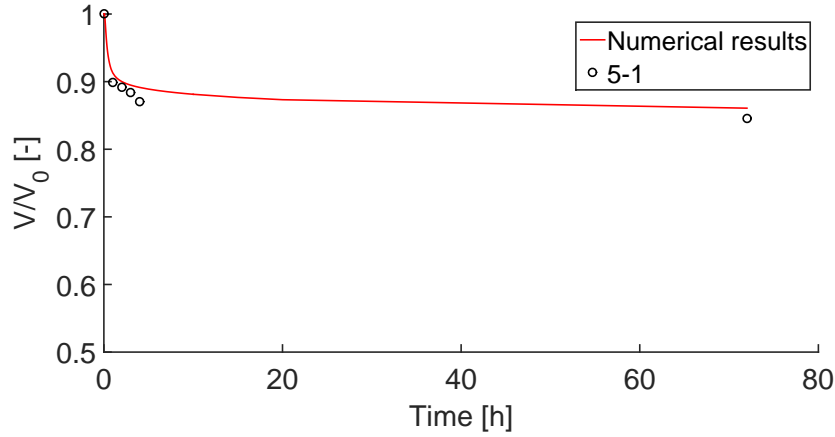Figure 5.47: Evolution of the radii for sample 5-1 at different times

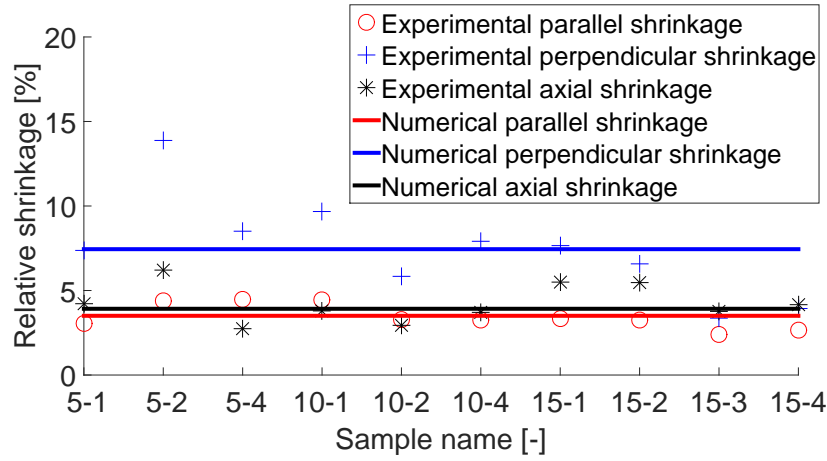Figure 5.48: Comparison of experimental and numerical volume evolution with time

Figure 5.49: Comparison between numerical and experimental shrinkage values for all the samples tested

5.8.1 Permeability

The permeability of the porous medium is a key parameter controlling the drying kinetics. Indeed, if the permeability is important enough, the water will easily reach the surface and the drying rate will be governed by the capacity of the drying air to evaporate the water at the surface of the porous medium. On the contrary, if the permeability is very low, the drying rate will quickly drop after the evaporation of the water at or very near the surface because of the time the rest of the water will need to reach that evaporating surface. Using the notion of connection layer Lehmann et al. (2008) introduced in section 5.6, several values of permeability are chosen to perform this sensitivity study. Knowing the maximum drying rate and the capillary hydraulic head in equation 3.21, it is possible to determine the water permeability of the medium to get a chosen connection layer length. We decided to use critical lengths equal to 10000 times, 10 times, 1 time and 1 tenth of the sample length. It gives respectively intrinsic permeability of $8.10^{-15} \ [m^2]$, $8.10^{-18} \ [m^2]$, $8.10^{-19} \ [m^2]$ and $8.10^{-20} \ [m^2]$.

Fig. 5.50 shows the different drying rates obtained with the different intrinsic permeability chosen. For $k_{sat,/\!/} = 8.10^{-15} \ [m^2]$, a long CRP is observable which is linked to the fact that the
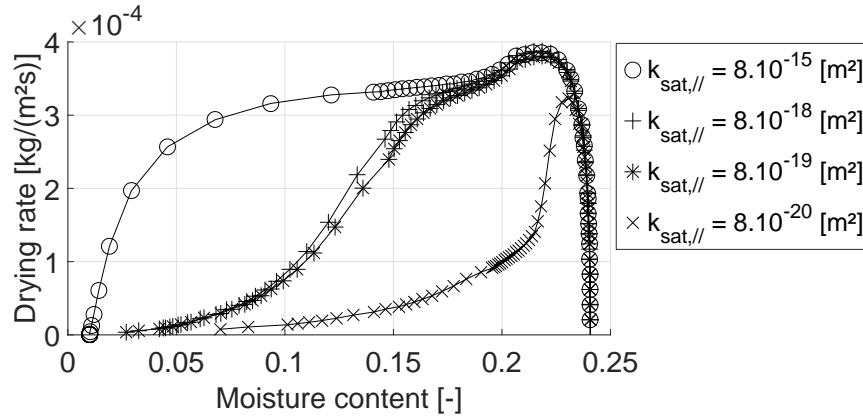
Figure 5.50: Sensitivity to the water permeability of the porous medium

permeability has to decrease a lot before the critical length becomes smaller than the sample size and the CRP ends since the critical length is much higher than the sample length. For the $k_{sat,/\!/} = 8.10^{-18} [m^2]$ curve or $k_{sat,/\!/} = 8.10^{-19} [m^2]$, the CRP is limited as explained in section 5.6. Finally, the $k_{sat,/\!/} = 8.10^{-20} [m^2]$ curve presents no CRP at all since the critical length is initially smaller than the sample size and no CRP is thus possible. That kind of behavior can be observed experimentally with material presenting very different permeabilities as seen in Fig. 5.51.
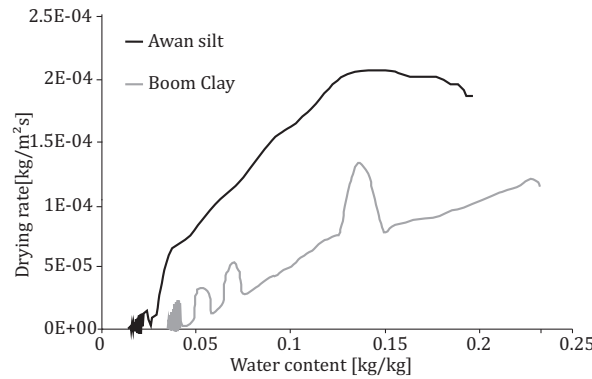

Figure 5.51: Experimental drying rate for silty material and for clayey material Gerard (2011)

The following simulations are based on an intrinsic permeability of $k_{sat,/\!/} = 8.10^{-15} [m^2]$. This value was chosen since it allows for a well defined CRP which is useful to more clearly exhibit the effects of other parameters.

5.8.2 Retention curve

Fig. 5.52(a) shows the drying kinetics for different water retention curves. They differ by the value of the α_{vG} parameter in van Genuchten's formulation (Eq.8.4), which is directly correlated to the air entry pressure. When α_{vG} is high, the porous medium remains saturated for higher suction values. The drying rate is therefore lower since very little water is allowed to leave the medium before the suction reaches high values. Then the drying rate decreases

slowly due to the quantity of water still to be evaporated and the permeability still being quite high. On the other hand, when α_{vG} is low, the water inside the porous medium becomes quickly available leading to a higher drying rate but steeper decrease due to the low quantity of water left.
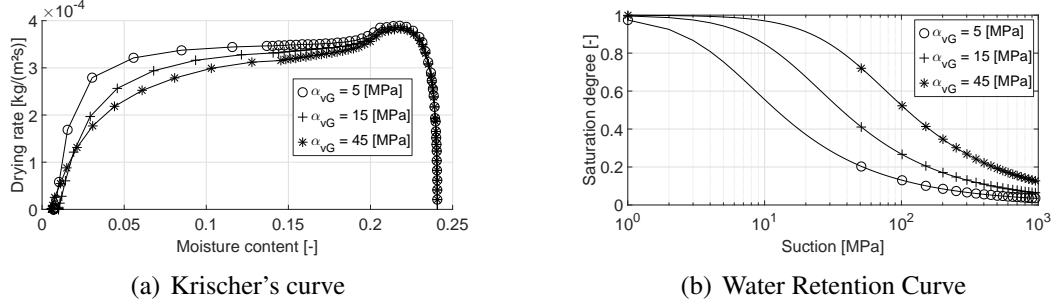

(a) Krischer's curve

(b) Water Retention Curve

Figure 5.52: Sensitivity to the water retention curve chosen

5.8.3 Young's modulus

Young's modulus mostly affects the shrinkage of the drying surface. The lower the modulus, the more shrinkage there is and thus the smaller the drying surface. This leads to a higher drying rate (Fig. 5.53) since the surface term is smaller in Eq. 5.1. The second effect of a low modulus is that the deformation of the porous medium follows exactly the mass loss so that the sample remains saturated for much higher suction values. This leads to higher relative permeability and thus higher drying rates.
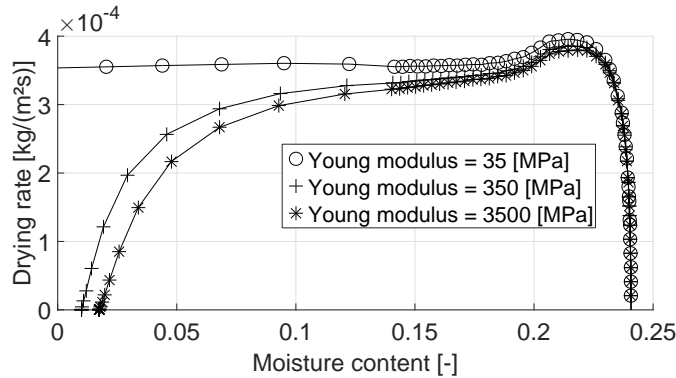
Figure 5.53: Sensitivity to the Young modulus

5.9 Influence of desiccation cracking on the drying kinetics

The strongest hypothesis made throughout our work on Boom clay is that we can study the drying behavior irrespective of the cracking that occurs during a drying experiment. This hypothesis is obviously a bit too strong since cracking will create preferential flow path and must thus have an effect on the drying kinetics. Implementing a cracking mechanism is one of the

main goal of this work but quantifying the influence of cracks formation on the permeability is not an easy task. It depends on crack opening, roughness, etc.

Here, we have performed a few "worst case scenario" simulations by considering fully opened cracks (i.e. crack starting at the top of the sample and reaching the bottom) from the onset of the drying experiments. During our experimental campaign the maximum percentage of any section to be cracked was 4% as can be seen in Fig.5.54.

We also noticed that, of the 12 samples tested, 7 of them only presents one open (sometimes partially) crack, 2 of them had 2 opened cracks and 2 had 3 opened cracks. Some examples are provided at Fig. 5.54.
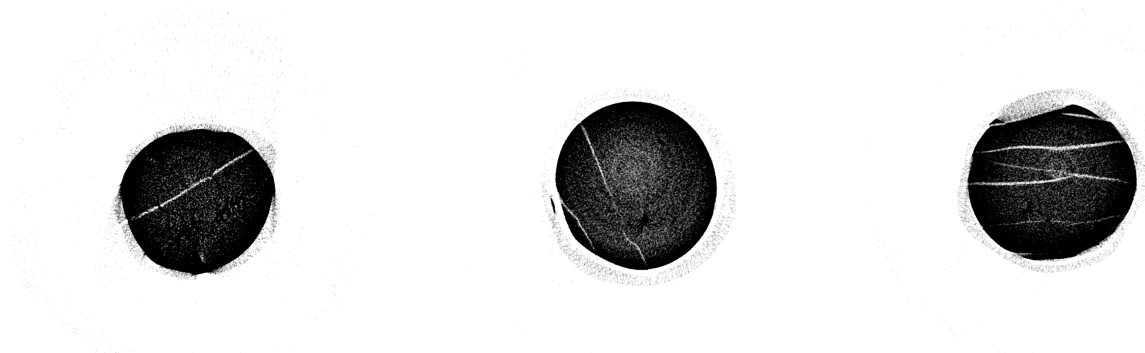

Figure 5.54: Examples of samples with 1 (left), 2 (middle) and 3 (right) cracks

Based on those experimental data we decided to work with two different mesh : one with a single crack (see Fig. 5.55 on the left) and a second one with 3 cracks (Fig. 5.55 on the right).
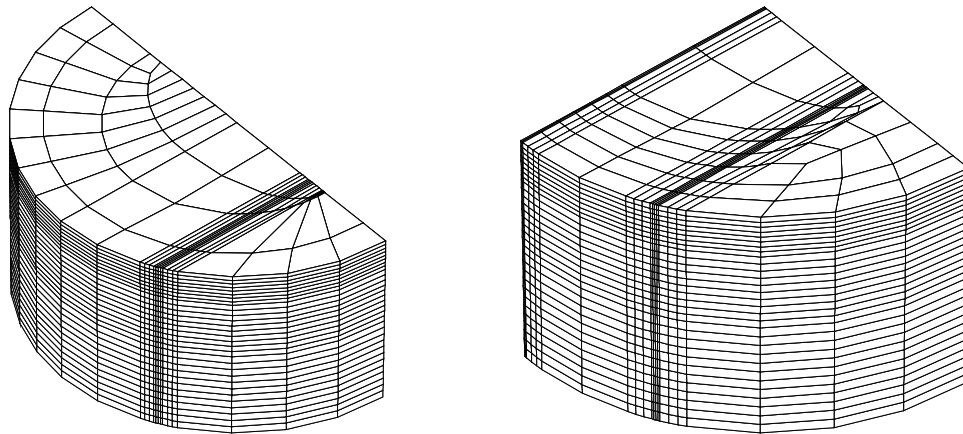
Figure 5.55: Meshes with 1 crack (left) and with 3 cracks (right)

The total surface of the cracks is equivalent to 4% of the total surface. The cracked zone is considered to have a permeability three order of magnitude higher than the undisturbed material which is again a worst case scenario hypothesis. Indeed, cracked zones in clayey material usually see an increase of permeability of one or two order of magnitude maximum (). By making all these negative assumptions, we are making sure that if little to no difference can be observed then cracks influence can reliably be neglected when studying the drying kinetics of

Boom clay. The Krischer curves obtained for these simulations are compared with a our final simulation with no cracks (cf. Fig. 5.56).
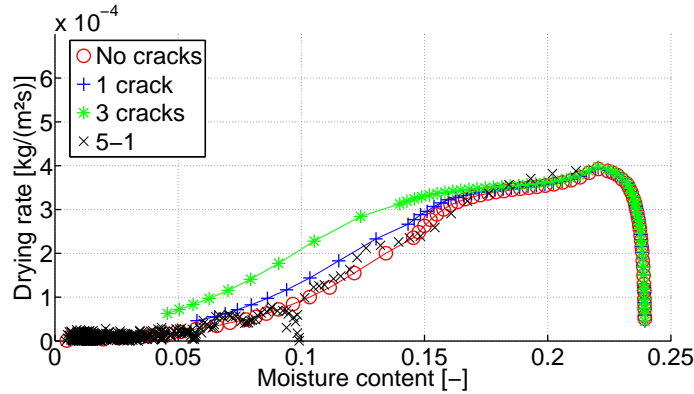

Figure 5.56: Influence of the pre-opened cracks on the drying rate of Boom clay samples

The simulation with a single crack presents very little difference to the reference simulation. This is due to the permeability perpendicular to the bedding (and thus cracks) plane : it takes so much time for the water to reach that preferential permeability zone that the dominant water transfer in most of the sample remains vertical water flows. In the case of 3 cracks, a bigger difference exists. The reason is the same as the one stated before: by considering 3 cracks, we have reduced the distance that water has to travel to reach the preferential flow path, increasing their effect on the overall behavior. Nonetheless, the difference is not very significant despite very strong hypothesis. This leads us to be quite confident in the validity of our first hypothesis : neglecting the effect of cracking of the drying kinetics is acceptable for the study of Boom clay.

5.10 Conclusion

All the notions required to study and try to numerically reproduce the drying behavior of materials have been presented in previous chapters. This chapter starts by introducing the material studied and the reason its drying behavior is of interest. In particular, the nuclear waste disposal problem is addressed. In this framework, Boom clay is studied as a potential host material. Its geological properties as well as its mineralogical composition are briefly introduced. A literature review of Boom clay geotechnical properties is also presented. Then, the experimental campaign carried to study the mass and heat transfer mechanisms during the convective drying of Boom clay is presented with emphasis on the data acquisition and post-treatment. Twelve samples were tested with different sample heights being considered to investigate scale effect. The experimental results are presented in terms of drying kinetics as well as in terms of shrinkage. It was concluded that no significant scale effect could be observed in the range of sample height tested. The experimental campaign also provided an important amount of exploitable data for numerical validation. Coincidentally, the goal of this section is to be able to numerically reproduce the observed behavior. To do so, a numerical model is used. It has been detailed in chapter 2 but a summary of the governing equations - adapted to this context - is presented as well as the mechanical law used to account for the stress-strain relationship. The mesh, initial and boundary conditions of the problems are also detailed. Using the aforementioned

material, simulation are performed with increasing degree of complexity until the experimental behavior is accurately reproduced. Each addition to the model complexity has brought significant change in behavior emphasizing the importance of taking into account all the coupling to properly simulate the drying behavior of Boom clay. Then a sensitivity study to a few "key" parameters in conducted to better understand their influence on the whole process. Finally, the influence of cracking - a process neglected in our study of the drying kinetics of Boom clay - is studied to determine if the initial hypothesis is acceptable. Following this sensitivity analysis, we are comfortable in saying that the influence of cracking can be neglected when considering the drying behavior of Boom clay under the specified drying conditions.

All the chapters up until lead to the simulations performed in this chapter. Those simulation proved the ability of the exposed model to accurately simulate the drying behavior of a porous material. Now, that this milestone has been cleared the next objective is to be able to predict desiccation crack genesis. To do so, the first step is to understand the mechanisms at play behind desiccation cracking. The next chapter will be devoted to a literature review of the desiccation cracking phenomenon with an emphasis on the state of the art in terms of modeling.

Chapter 6

Desiccation cracking

Contents

6.1 Introduction

Desiccation cracking is a consequence of tensile failure but it occurs at an apparent absence of external tensile forces (Hueckel et al. (2014)). The tensile stresses are the consequence of internal kinematic incompatibilities or boundary conditions preventing free shrinkage. The former creates self- equilibrating tensile stresses and the latter generates tensile reaction forces at the level of the boundary condition. These stresses may concentrate in the vicinity of a pre-existing flaw (most commonly a micro-crack but a study by Hueckel et al. (2014) suggests that an air entry "finger" could also be a starting point for crack propagation). In the previous

chapters, the drying phenomenon and its most direct mechanical consequence - shrinkage - were thoroughly studied but the desiccation cracking that may result from said shrinkage has been neglected up until now. The end goal of this work is to be able to numerically predict cracking onset, therefore a good understanding of the cracking mechanism is required. This chapter starts with the definition of a crack as well as the distinction of the different opening modes. Then, mode I crack - the mechanism involved in desiccation cracking (Péron (2008)) - is detailed from a microscopic and macroscopic point of view. The notion of material tensile strength is introduced and the different experimental methods available to determine it are presented. Finally, a review of the desiccation cracking criteria found in the literature concludes this chapter.

6.2 Definition

A fracture is the separation of a material into two or more parts under the action of stresses. From a macroscopic continuum mechanics point of view, it is a discontinuity characterized by two faces and a front (cf Fig. 6.1).
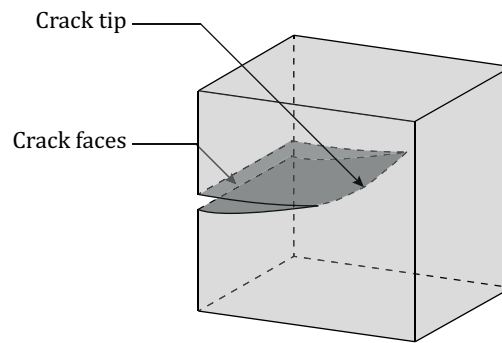

Figure 6.1: Cracked body (after Gross and Seelig (2017))

It most often appears due to displacement discontinuity within the solid. The reasons for these discontinuities are varied but most often depend on microscopic properties of the material. Concerning the formation of a crack, there exist three types of opening modes which are shown in Fig. 6.2. Mode I denotes a symmetric crack opening with respect to the x-z plane. Mode II is characterized by an antisymmetric separation of the crack surfaces due to relative displacements in the x direction (normal to the crack front). Finally, mode III describes a separation due to relative displacements in the z direction (tangential to the crack front (Gross and Seelig (2017))).

6.3 Mode I cracking

Experimental evidence (Konrad and Ayad (1997); Péron (2008); Morris et al. (1992)) clearly shows that desiccation cracking mainly occurs in mode I (i.e. opening mode). This means that cracking is the result of soil tensile strength mobilization. In the following section, we look into the mode I opening mechanism from a microscopic and then macroscopic point of view.
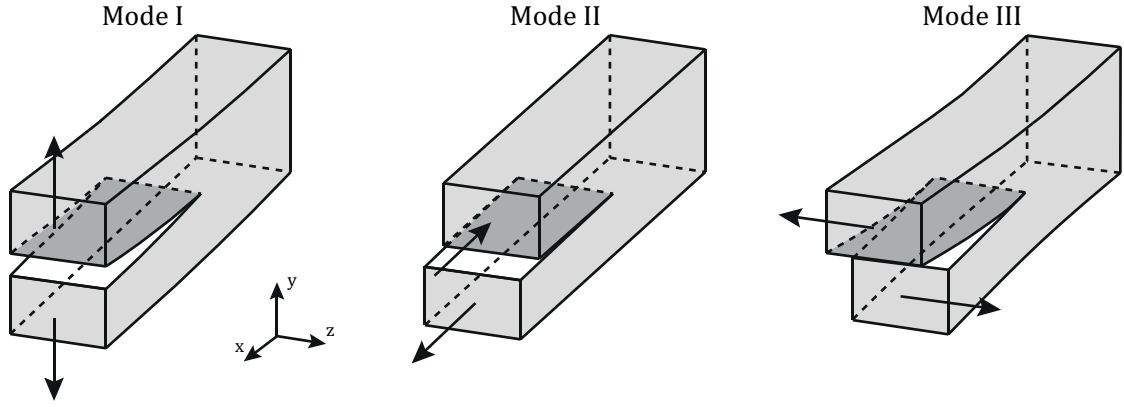
Figure 6.2: Crack opening modes (after Gross and Seelig (2017))

6.3.1 Microscopic aspects

At the microscopic level, a fracture is the consequence of the breakage of the bonds between components (atom, molecules, etc.). The bonding force between two components can be derived from an interaction potential, ϕ. A typical expression for this potential (for atoms) is the Lennard-Jones potential (Jones (1924a) Jones (1924b)):

$$\phi = -\frac{A}{r^6} + \frac{B}{r^{12}}$$ (6.1)

where the first term accounts for the attractive van der Waals forces and the second term for the short range repulsive forces. The bounding force is thus obtained as :

$$F = -\frac{\partial \phi}{\partial r} = -\frac{A}{r^7} + \frac{B}{r^{13}}$$ (6.2)

but it can be generalized for other particles as (cf. Fig. **??** on the left) :

$$F = -\frac{A}{r^m} + \frac{B}{r^n}$$ (6.3)

where A, B, m($<$n) and n are constants which depend on the type of bonds. Based on this formulation, let us try to determine the expression of the theoretical tensile strength of a material. To do that, we consider the simplified case of the separation, in tensile regime, of two atom lattice planes in a crystalline structure. For the separation stress, σ, we assume a dependence on the separation displacement, x, similar to the bonding force (cf. Fig. 6.3 in the middle). The expression of the separation stress can be approached by :

$$\sigma = \sigma_c sin(\pi \frac{x}{a})$$ (6.4)

where σ_c is the theoritical tensile strength of the material. For a small displacement from the equilibrium position, d_0, this expression can be linearized :

$$\sigma \approx \sigma_c \pi \frac{x}{a}$$ (6.5)

And if the material is considered as linear elastic, the separation stress can be written using Hooke's law :

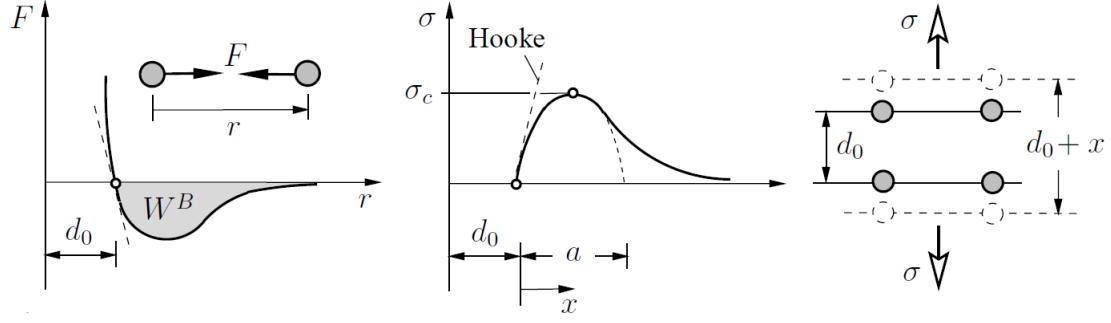$$\sigma = E\varepsilon = E\frac{(d_0 + x) - d_0}{d_0} = E\frac{x}{d_0}$$ (6.6)

Figure 6.3: Theoritical strength (after Gross and Seelig (2017))

Equaling Eq. 6.5 and Eq. 6.6 yields :

$$\sigma_c = \frac{Ea}{\pi d_0} \tag{6.7}$$

Assuming that the bond between particles is completely broken for a distance $a = d_0$, then :

$$\sigma_c = \frac{E}{\pi} \tag{6.8}$$

And this is the expression of theoretical strength of the material.

As a consequence of separation, changes occur in the immediate neighborhood of the newly created surface. If this dissipative process is neglected and the material is, from the macroscopic point of view, considered as a continuum, the work of bonding forces is transferred into surface energy of the body (i.e., the energy stored at the body's surface). We can now determine that surface energy, γ^0. Since two new surfaces are created during separation we have :

$$2\gamma^0 = \int_0^\infty \sigma \, \mathrm{d}x \approx \int_0^a \sigma_c sin(\frac{\pi x}{a}) \, \mathrm{d}x = \sigma_c \frac{2a}{\pi} \tag{6.9}$$

Inserting Eq. 6.8 in Eq. 6.9 it comes :

$$\gamma^0 = \frac{Ea}{\pi^2} = \frac{Ed_0}{\pi^2} \tag{6.10}$$

The real value of the theoretical strength of a material would however be significantly lower than the value calculated using Eq. 6.8 because of microstructural properties such as inhomegeneities or defects (Gross and Seelig (2017)). In amorph material such inhomegeneities can come from grains orientation leading to anisotropic behavior or grain density leading to non-homogeneous strength. Defects are most usually foreign particles (inclusion with very different properties) or microvoids.

6.3.2 Macroscopic aspects

At the macroscopic level, mode I failure requires the definition of a tensile strength criterion. **?** noticed that polished surfaces and materials with smaller sized cracks have enhanced strength against rupture as opposed to materials with scratched surfaces and larger sized cracks. These

observations were not satisfactorily explained by the existing hypotheses of rupture in materials. **?** thus introduced his alternate criterion, which is solely based on energy minimization :

"*According to the well-known "theorem of minimum energy," the equilibrium state of an elastic body, deformed by specified surface forces, is such that the potential energy of the whole system is a minimum. The new criterion of rupture is obtained by adding to this theorem the statement that the equilibrium position, if equilibrium is possible, must be one in which rupture of the solid has occurred, if the system can pass from the unbroken to the broken condition by a process involving a continuous decrease in potential energy.*"

Thus, Griffith's criterion is nothing but a necessary, thermodynamic criterion. In other words, if the elastic energy due to the presence of a crack can be relieved by opening the crack up, the system will do so — provided the cost paid to open it up (in terms of the creation of newer surfaces, cf. γ^0 in section 6.3.1) is more than compensated by the elastic energy gain.

Later Griffith (1924) considered the numerous pre-existing micro-cracks in the materials and suggested that the reason these small cracks lowered the overall strength of a material was because when a load is applied, these cracks induce stress concentrations. His failure criterion provides a fundamental starting point for any fracture problem. The criterion takes into account the potential flaws of a given volume of material and these flaws are considered to be randomly distributed inside the given volume. When the sample is loaded, these flaws lead to stress concentration near the flaws extremities. According to the orientation of these flaws and the type of loading, failure can occur by the propagation of a crack starting from one of these flaws when the concentration of stress reaches a critical value in the considered zone. Using linear elasticity, it is possible to analytically determine the stress field around a cavity of a given shape. Griffith (1924) considered a two dimensional case and studied the variation of the tangential stress component in the surface of a flat elliptical cavity with a semi major axis ι, submitted to a two-dimensional loading (total stresses σ_1 and σ_3) at infinity. He assumed that this sharp elliptical cavity represented a pre-existing microcrack. Griffith determined the orientation of the stresses (σ_1, σ_3) that maximizes the tangential stress component in the surface of the cavity and the possible values of these maxima, denoted $\sigma_{t,max}$. The calculation led to the definition of two cases.

First case

$$\sigma_1 + 3\sigma_3 \leq 0 \tag{6.11}$$

where σ_3 is negative (tension) and normal to the plane of the flaw. The greatest tensile stress at the flaw surface, $\sigma_{t,max}$, occurs at the micro-cracks tip, and has the following value:

$$\sigma_{t,max} = -\frac{2\sigma_3}{\varepsilon_0} \tag{6.12}$$

where ε_0 is given by :

$$\varepsilon_0 = cosh^{-1}\left(\frac{\iota}{\omega}\right) \tag{6.13}$$

where ι is the semi major axis and ω is the linear eccentricity of the flat elliptical cavity. The critical flaw is perpendicular to the direction of the maximal tensile stress applied to the sample σ_3. According to Griffith, the ratio of σ_3 to $\sigma_{t,max}$ is thus independent of the material elastic

constant (Inglis 1913, Griffith 1924). Finally, the macroscopic failure criterion is given by the simple relationship :

$$\sigma_3 = -\sigma_t \qquad\qquad\qquad \sigma_1 \leq -3\sigma_3 \qquad\qquad (6.14)$$

where σ_t is defined as the macroscopic tensile strength. This is the first segment of the Griffith criterion in Fig. 6.4.
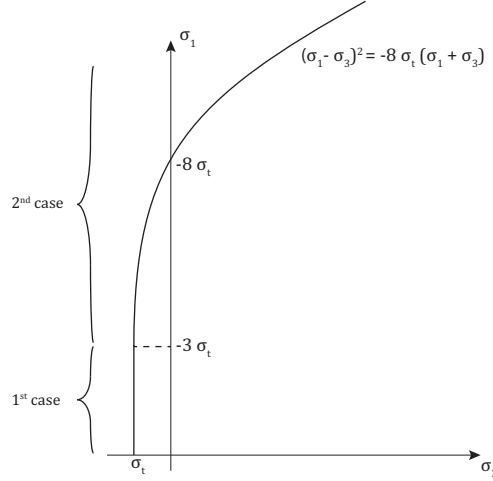

Figure 6.4: Griffith criterion

Second case

$$\sigma_1 + 3\sigma_3 > 0 \qquad\qquad (6.15)$$

Griffith showed that the maximum tensile stress at the surface of the cavity is then given for a flaw that is inclined relative to the direction of the principal stress. This lead to the following expression of the criterion :

$$(\sigma_1 - \sigma_3)^2 = -8\sigma_t(\sigma_1 + \sigma_3) \qquad\qquad (6.16)$$

The criterion then has a parabolic shape in the principal stress plane (cf. Fig. 6.4). This last part of the criterion is not suitable for soils. In such a stress state, failure in soils occurs through shearing and another criterion is required (for example Mohr-Coulomb or Drucker Prager).

6.4   Tensile Strength measurements

In the previous section, we introduced the notion of tensile strength, σ_t, that is used to define tensile failure criterion. The different methods available to experimentally measure that strength are presented hereafter.

6.4.1 Indirect tension test

Contrary to more homogeneous and coherent materials, rocks and soils are difficult to test in tension. Indeed, it is very complicated to perform uniaxial tension test because of the inherent problem of holding a non cemented material or, in the case of rocks, because of the difficulty of shaping the sample in a "bone" shape like would usually be done to avoid boundary conditions effect on the test results. To circumvent those problems, indirect tension test were developed. The principle behind indirect tension tests consists in applying a compressive stress or bending moment to a sample with a chosen geometry to induce tensile stresses leading to mode I failure in a predetermined plane. The indirect methods all suffer from a major shortcoming which is that they are relying on the hypothesis that the material follows a linear elastic behavior. Without this hypothesis, it is not possible to determine the stress field in the sample and thus to determine the tensile strength of the material.

6.4.1.1 Brazilian test

The so called Brazilian test was developed in 1943 by the Brazilian engineer Fernando Carneiro for concrete tensile strength measurements. The principle of the test is to place a cylindrical specimen horizontally between two plates so that the load is applied directly along the vertical diameter of the sample (cf. Fig. 6.5). As the plates used to apply the load are very rigid, the load can be considered to be applied punctually. The load is continuously increased at a
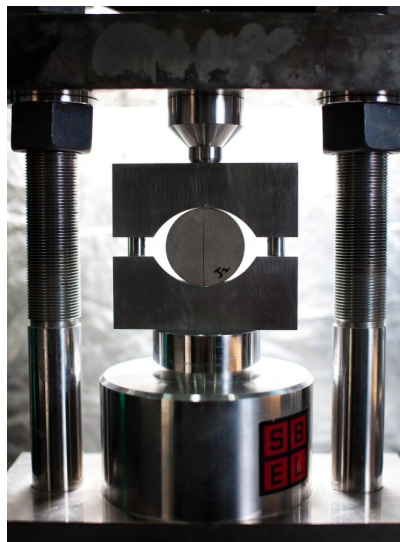
Figure 6.5: Brazilian test apparatus (Deichmann Rock Mechanics Laboratory)

constant rate until failure. Note that it can also be controlled in displacement rather than load. Due to its simplicity and efficiency, it is one of the most common laboratory tests to measure tensile strength. An analytical solution of the stress field in the sample can be found in Jaeger et al. (2009). The stresses along the vertical axis (y axis in Fig. 6.6) are given by :
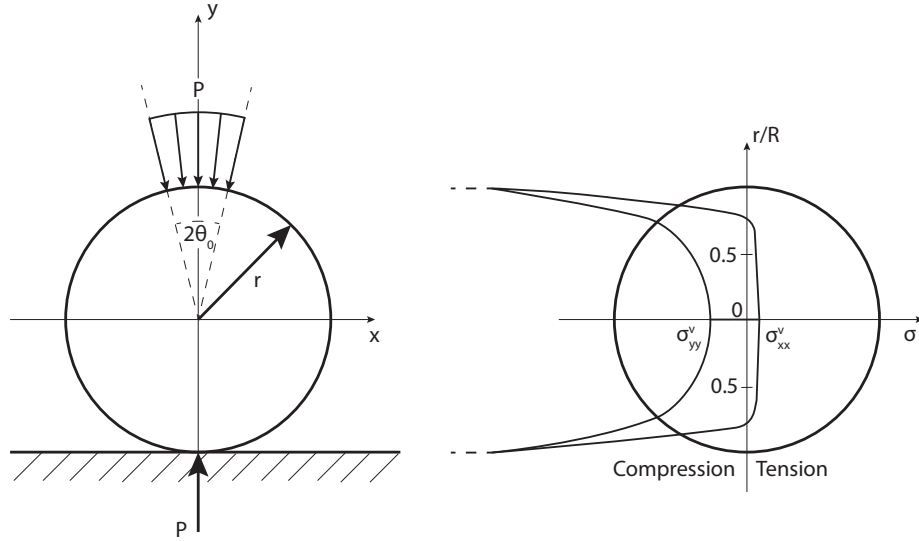
Figure 6.6: Cylinder compressed between two parallel planes by a load P (after Jaeger et al. (2009)) and typical stress distribution along the vertical axis

$$\sigma_{xx}^v = \frac{-2p}{\pi L}\left[\frac{\left(1-\left(\frac{r}{R}\right)^2\right)\sin 2\theta_0}{1-2\left(\frac{r}{R}\right)^2\cos 2\theta_0+\left(\frac{r}{R}\right)^4} - arctan\left(\frac{\left(1+\left(\frac{r}{R}\right)^2\right)}{\left(1-\left(\frac{r}{R}\right)^2\right)}\right)\right] \tag{6.17}$$

$$\sigma_{yy}^v = \frac{-2p}{\pi L}\left[\frac{\left(1-\left(\frac{r}{R}\right)^2\right)\sin 2\theta_0}{1-2\left(\frac{r}{R}\right)^2\cos 2\theta_0+\left(\frac{r}{R}\right)^4} + arctan\left(\frac{\left(1+\left(\frac{r}{R}\right)^2\right)}{\left(1-\left(\frac{r}{R}\right)^2\right)}\right)\right] \tag{6.18}$$

And the stresses along the horizontal axis, perpendicular to the load, are given by :

$$\sigma_{xx}^h = \frac{-2p}{\pi L}\left[\frac{\left(1-\left(\frac{r}{R}\right)^2\right)\sin 2\theta_0}{1+2\left(\frac{r}{R}\right)^2\cos 2\theta_0+\left(\frac{r}{R}\right)^4} - arctan\left(\frac{\left(1-\left(\frac{r}{R}\right)^2\right)}{\left(1+\left(\frac{r}{R}\right)^2\right)}\right)\right] \tag{6.19}$$

$$\sigma_{yy}^h = \frac{-2p}{\pi L}\left[\frac{\left(1-\left(\frac{r}{R}\right)^2\right)\sin 2\theta_0}{1+2\left(\frac{r}{R}\right)^2\cos 2\theta_0+\left(\frac{r}{R}\right)^4} + arctan\left(\frac{\left(1+\left(\frac{r}{R}\right)^2\right)}{\left(1-\left(\frac{r}{R}\right)^2\right)}\right)\right] \tag{6.20}$$

where r is the distance from the center, R is the radius of the cylinder and p is the radial stress applied at the surface of the cylinder over a portion comprised between $\pm\theta_0$ (cf. Fig. 6.6). L is the length of the cylindrical sample. If we consider the stress to be applied punctually (θ_0 is small) then the Eq. 6.17 to Eq. 6.20 can be simplified to (Jaeger et al. (2009)) :

$$\sigma_{xx}^v = \frac{-P}{\pi RL} \qquad\qquad \sigma_{yy}^v = \frac{P(3+(\frac{r}{R})^2)}{\pi RL(1-(\frac{r}{R})^2)} \tag{6.21}$$

$$\sigma_{xx}^h = \frac{-P}{\pi R}\frac{P(1-(\frac{r}{R})^2)}{\pi RL(1+(\frac{r}{R})^2)} \qquad\qquad \sigma_{yy}^h = \frac{P(3-2(\frac{r}{R})^2)}{\pi RL(1+(\frac{r}{R})^2)} \tag{6.22}$$

These stresses are principal stresses because of the sample symmetry. As the cylinder is in a state of plane stress , the third principal stress, σ_{zz}^v, is equal to zero. The largest and smallest
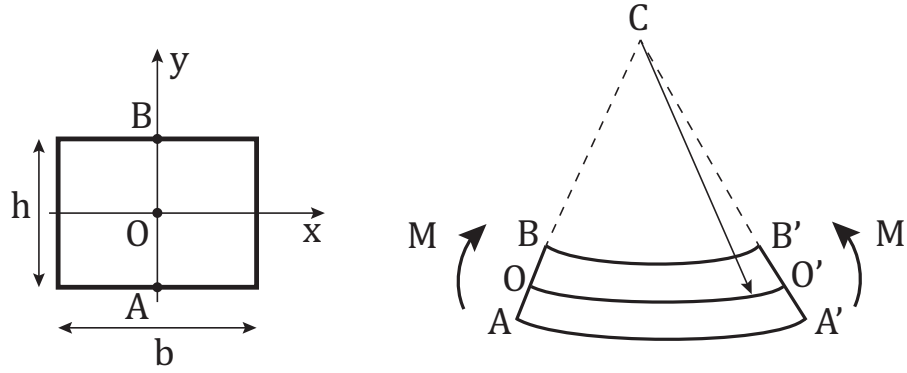
114

Figure 6.7: Bending of a prismatic beam : cross section (left) and deformed configuration (right) (after Jaeger et al. (2009))

principal stresses are found along the vertical axis (σ_{xx}^v and σ_{yy}^v). The minimum principal stress, σ_{xx}^v, is uniform and in tension along the axis. At the center of the cylinder ($r = 0$), it comes :

$$\sigma_{xx}^v = \frac{-P}{\pi RL} \qquad\qquad \sigma_{yy}^v = \frac{3P}{\pi RL} \qquad\qquad (6.23)$$

And the stress state at the center of the cylinder thus respects :

$$\sigma_{yy}^v + 3\sigma_{xx}^v = 0 \qquad\qquad (6.24)$$

which is directly on the tensile part of Griffith's criterion. This means that when a sample is compressed in a Brazilian test, failure occurs in mode I in or close to the loaded diametrical plane and starting at the center of the sample. Failure happens for a certain value of the applied load, P resulting in the tensile stress, $\sigma_{xx}^y = \frac{-P}{\pi RL}$. The tensile strength of the material is thus determined to be :

$$\sigma_t = \frac{P}{\pi RL} \qquad\qquad (6.25)$$

The main problem of this test (in supplement to the problems recurrent to all indirect tension tests) is that it creates a strongly non homogeneous stress field with stresses tending toward infinity near the application points of the external forces (cf. Fig. 6.6 on the right).

6.4.1.2   Bending tests

Bending tests are used to measure Young modulus and tensile strength (Coviello et al. (2005)). Bending produces regions of tensile stresses (near the bottom side of the sample) and compressive stresses (near the upper side). Let us consider an idealized configuration to see how we can use such a testing method to determine the tensile strength of materials. Consider a rectangular beam of width, b, height, h, and length L (cf Fig. 6.7) which is submitted to a bending moment M about the x axis. According to the Euler-Bernoulli theory, each planar section in a x-y plane remains plane after deformation. This forces lines which were straight to form curves. The neutral axis of the beam ($y = 0$) does not change length so that $|OO'| = L$ and the curvature

radius of the beam is thus given by $R = L/\theta$. The upper fiber, $y < 0$, is now in compression because the deformed length $|BB'|$ is now equal to $(R - h/2)\theta$ which leads to :

$$\varepsilon_{zz} = \frac{(R - h/2)\theta - L}{L} = \frac{(R - h/2)\theta - R\theta}{R\theta} = \frac{-h}{2R} \tag{6.26}$$

which is in compression. The lower fiber, on the other hand, is in tension with strain equal to :

$$\varepsilon_{zz} = \frac{h}{2R} \tag{6.27}$$

For a given height in the cross section, the strain is actually :

$$\varepsilon_{zz} = \frac{y}{R} \tag{6.28}$$

and thus the longitudinal stress is given by :

$$\sigma_{zz} = \frac{yE}{R} \tag{6.29}$$

The bending moment can be calculated as :

$$M = \int_{-h/2}^{h/2} \int_{-b/2}^{b/2} \sigma_{zz} y \, dx \, dy = \frac{bh^3 E}{12R} = \frac{EI}{R} \tag{6.30}$$

where, I, is the moment of inertia of the section. This is a well known mechanics result. From it, it is possible to determine the elastic modulus of the material. Indeed, the bending moment applied is known and the curvature of the deformed beam can be measured. The maximum tensile stress possible on the lower fiber is given by :

$$\sigma_{zz} = \frac{hE}{2R} = \frac{Mh}{2I} \tag{6.31}$$

And knowing the applied bending moment when tensile failure occurs is thus sufficient to determine the tensile strength. This demonstration was done on a simplified case where the applied bending moment is constant along the z axis which is difficult to reproduce in laboratory tests. In practice, the following bending tests are commonly performed.

The three points bending   A prismatic beam is place on two parallel supporting pins and is loaded through a third pin placed at the center of the opposite side (cf Fig. 6.8). The load is progressively increased until failure. In this configuration, the moment along the z axis is not constant and is given by :

$$M = \frac{F}{4}(l - z) \quad \forall z \in [0; L/2] \tag{6.32}$$

and the maximum tensile stress occurs at midpoint where the bending moment, M, is maximum (cf. Fig. 6.9) and is given by :

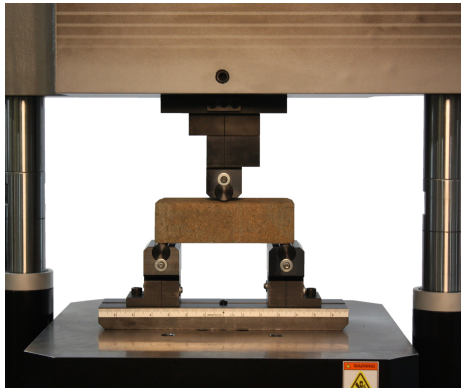$$\sigma_{zz} = \frac{M_{max}h}{2I} = \frac{FLh}{8I} \tag{6.33}$$

116

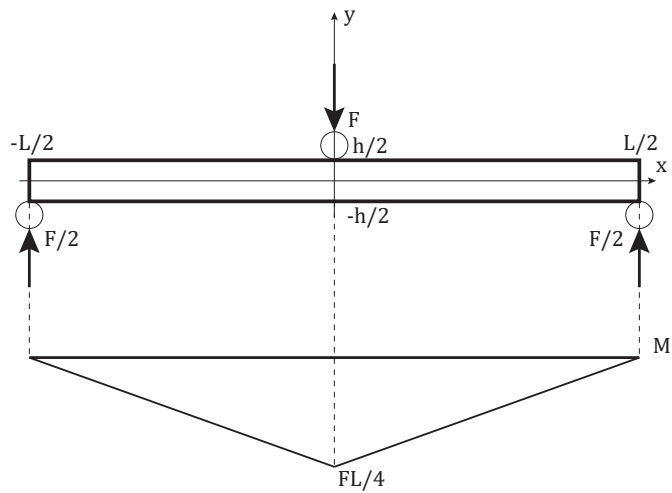Figure 6.8: Three points bending apparatus (tests catalog (????))

Figure 6.9: Three points loading and corresponding bending moment
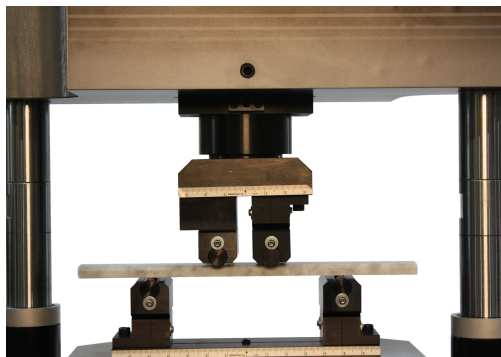

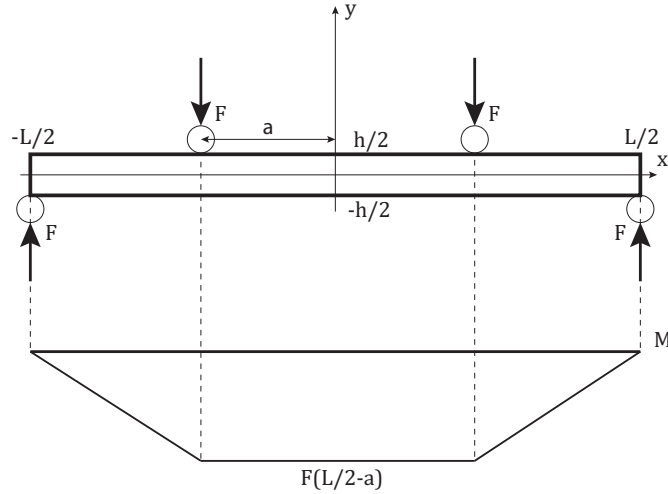Figure 6.10: Four points bending apparatus (tests catalog (????))

Figure 6.11: Four points loading and corresponding bending moment

Four points bending   The configuration is very similar to the three points bending test except that the load is applied by two pins rather than one (cf. Fig. 6.10).   This method was developed to counter the main flaw of the three points bending which is that the maximum bending moment appears beneath the point of application of the load which is probably not exactly the case experimentally.   In the case of the four points bending test, the whole area in between the two loading pins is at a constant (and maximum) bending moment (cf. Fig. 6.11). In this configuration, the bending moment is given by :

$$M = F(L/2 - a) \quad \forall z \in [0, a] \tag{6.34}$$

$$M = F(L/2 - z) \quad \forall z \in [a, L/2] \tag{6.35}$$

with similar expressions for $z < 0$. The maximum tensile stress is :

$$\sigma_{zz} = \frac{M_{max}h}{2I} = \frac{F(L/2 - a)h}{2I} \tag{6.36}$$

6.4.1.3   Hollow cylinder method

This method, much less common than the previous ones, has been developed by Al-Hussaini (1981) to measure soils tensile strength. The specimen is compacted into a hollow cylinder mold. The sample produced (cf. Fig. 6.12) is then placed into two annular platens with drainage ports (to be able to saturate the sample and alternatively to monitor pore pressure changes) and covered from the inside and outside by two thin rubber membranes. It is then placed within a pressure chamber (cf. Fig6.13). LVDT are placed on both inner and outer sides of the sample to measure the radial deformations. Compressed air is used to provide a confining pressure inside the chamber.
Next, the "ram" (cf. Fig. 6.13) is used to increase the air pressure in the inner volume of the hollow cylinder until failure. Failure occurs suddenly and along the vertical axis (parallel to the sample axis). In this test, orthoradial tensile stresses are calculated based on thick walled tube formulae. The average value of the tensile stress at failure is assumed to be the tensile
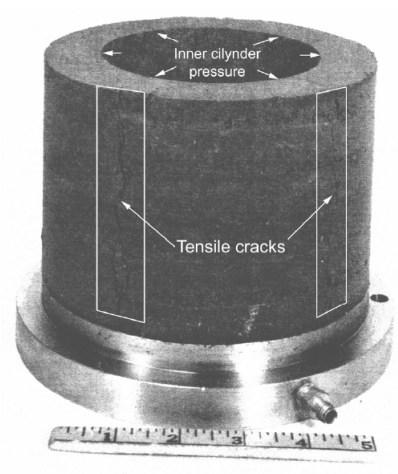
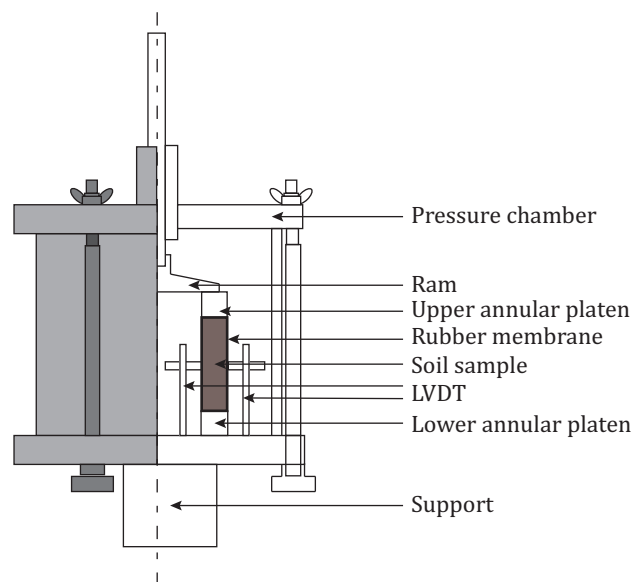Figure 6.12: Hollow cylinder soil sample (Al-Hussaini (1981))

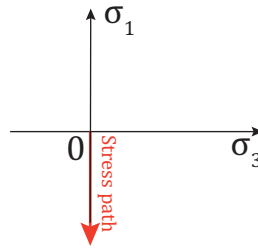Figure 6.13: Hollow cylinder test apparatus scheme

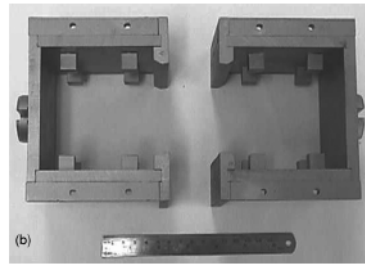Figure 6.14: Stress path followed during a uniaxial tension test

Figure 6.15: Direct tension retaining mold (Nahlawi et al. (2004))

strength of the sample even though the stress is not uniform in thick walled tubes. Another feature of this test is that it allows to determine the elastic modulus using outer and inner radii deformations measured by the LVDT. As for all indirect method, this one suffers from the hypothesis of linear elastic behavior of the material to determine the tensile strength.

6.4.2 Direct tension test

Direct tension tests involve a sample being hold at one extremity and being pulled at the other. This leads to an homogeneous tensile stress field throughout the sample and to a theoretically known stress path visible in Fig. 6.14. For soils, tests can be performed either with a specifically designed mold holding the soil (cf. Fig. 6.15) or by directly binding the sample to the tension apparatus (cf. Fig. 6.16).

The first method is the most common and many examples can be found in the literature (Mikulitsch and Gudehus (1995); Nahlawi et al. (2004)). The main problem of this method is that the apparatus design most often involves some sort of grip to hold the soil in the mold. These grips induce shear stresses at the interface soil-mold and that means that the part where the crack is assumed to appear has to be free of any grip. Moreover, the tensile stress in the sample is most probably different from the one imposed at the level of the mold because of poor boundary condition control. Hence, the fact that this is not a very accurate method.

In the second method, a binder is required to make sure that the sample sticks to the tension apparatus. It can be an epoxy resin (Farrell et al. (1967)) or any other strong adhesive. The main problem with this test is its complexity. The literature contains many examples where the soil did not bind correctly to the apparatus preventing the test (Nahlawi et al. (2004); Tang and
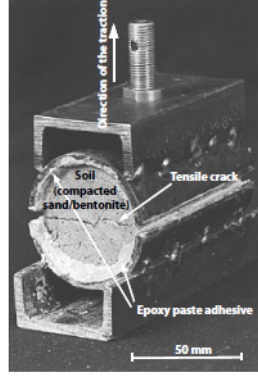
Figure 6.16: View of failed sample stuck to the mould after the direct tension test (Tang and Graham (2000))

Graham (2000)). It is also possible to experience imperfect binding. The binding is sufficient for the sample to stick to the apparatus and the test can be performed but it is not strong enough to insure good control over the boundary conditions (as is the case with the first method). Moreover, even if the test is performed perfectly, the binding process can significantly disturb the sample tested.

6.4.3 Other methods

6.4.3.1 Triaxial traction method

An original method to generate a generalized tensile stress state without a retaining system is described by Bishop et al. (1969). This method uses a sample with a reduced center section placed in a triaxial cell as visible in Fig. 6.17.
After consolidation, the axial stress is decreased while maintaining confining pressure constant. In this configuration and because of the sample reduced section, tensile stresses develop in the center section of the sample. The vertical effective stress in section E (cf. Fig. 6.17) is given by:

$$\sigma_y'^E = \sigma_{cell} - \frac{T_E}{A_E} - p_w \tag{6.37}$$

where A_E is the sample top section, T_E, is the tension applied to decrease the axial stress, $\sigma_y'^E$ which is initially equal to the confinement pressure, σ_{cell} and p_w is the pore water pressure. The vertical effective stress $\sigma_y'^C$ at the centre section C (cf. Fig. 6.17) is:

$$\sigma_y'^C = \sigma_{cell} - \frac{T_E}{A_C} - p_w \tag{6.38}$$

As T_E is increased, $\sigma_y'^E$ and $\sigma_y'^C$ decrease. Because the cross section in C is smaller than in E, the vertical stress decreases faster in section C and reaches tensile value before $\sigma_y'^E$ drops to zero. When $\sigma_y'^E$ is effectively zero, the end cap will detach from the sample. The limiting value of T_E, given by the condition $\sigma_y'^E = 0$ allows us to determine the value of the smallest possible tensile stress in section C and thus the tensile strength of the material.

$$\sigma_y'^{C,min} = -(\sigma_{cell} - p_w)(\frac{A_E}{A_C} - 1) \tag{6.39}$$
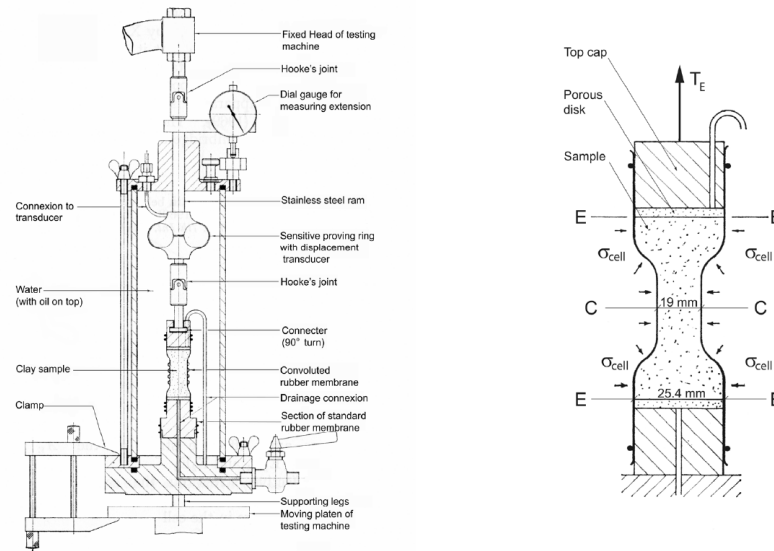
Figure 6.17: Triaxial traction method apparatus : On the left, the Triaxial cell with reduced centre section sample for traction tests and on the right the sample itselft (after Bishop et al. (1969))
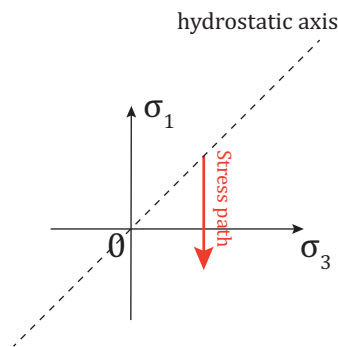
Figure 6.18: Stress path followed during a triaxial traction test

The stress path followed can be seen in Fig. 6.18. The strength of this method is that it allows to follow similar path to direct tension tests (i.e. decrease in minor effective stress at constant major effective stress) while solving the inherent problems of clamping or binding the sample to the experimental apparatus. Peron during his PhD thesis (Péron (2008)) performed tests adapting this method to include suction control.

6.4.3.2 Triaxial deconsolidation method

This original method has been developed by Péron (2008) to determine the tensile stress of Bioley silt using a conventional triaxial apparatus. The goal is to follow a decreasing mean effective stress path at various deviatoric stress values. Those deviatoric stresses are obtained by increasing or decreasing the axial stress while keeping the confinement pressure constant. The stress path is achieved either by increasing pore water pressure or by decreasing confining pressure until failure. The stress path followed are parallel to the hydrostatic axis (cf. Fig. 6.19) and each one (corresponding to a chosen starting deviatoric stress) gives a different point

of the tensile strength criterion. The triaxial apparatus was chosen because it allows to control (or measure) the values of stresses, strains and pore pressures (or suction) during the test.

Figure 6.19: Stress paths followed during a triaxial deconsolidation test (after Péron (2008))

6.5 Review of constitutive models for desiccation cracking

In this section, a review of existing constitutive models that attempted to describe desiccation cracking behavior of porous multiphasic material is presented (the cited models were developed for the study of soils but can be extended to other porous material).
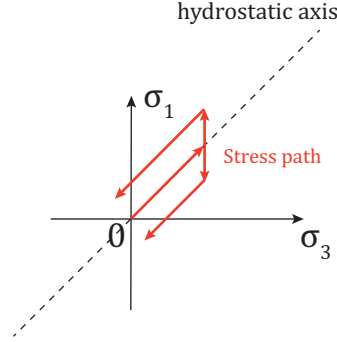
6.5.1 State surface concept

Morris et al. (1992) developed several one dimensional solutions for the depth of cracking in soil column dried from its top surface. One of them is based on the state surface concept for unsaturated soil behavior (Fredlund and Rahardjo (1993)). This concept has already been described in chapter 2 but is recalled here. According to Fredlund and Rahardjo (1993), the number of independent variables is directly linked to the number of phases and so for a partially saturated porous medium two are required. In particular, Fredlund and Morgenstern (1978) demonstrated that any pair of $\sigma_{ij} = \sigma_{tot,ij} - p_g \delta_{ij}$ (the net stress tensor), $\sigma'_{ij} = \sigma_{tot,ij} - p_w \delta_{ij}$ (the effective stress tensor) and suction $s = p_g - p_w$ could be used to describe the behavior of unsaturated soils. Morris et al. (1992) choose to use the net stress-suction couple of variables to express the constitutive relations of their model. The model itself is linear elastic and applied to unsaturated soils.

Morris et al. (1992) directly uses the following linear relationship (only principal components are given):

$$\begin{Bmatrix} \varepsilon_x \\ \varepsilon_y \\ \varepsilon_z \end{Bmatrix} = \begin{bmatrix} \frac{1}{E} & -\frac{\nu}{E} & -\frac{\nu}{E} \\ -\frac{\nu}{E} & \frac{1}{E} & -\frac{\nu}{E} \\ -\frac{\nu}{E} & -\frac{\nu}{E} & \frac{1}{E} \end{bmatrix} \begin{Bmatrix} \sigma_x - p_a \\ \sigma_y - p_a \\ \sigma_z - p_a \end{Bmatrix} + \begin{bmatrix} \frac{1}{H_s} & 0 & 0 \\ 0 & \frac{1}{H_s} & 0 \\ 0 & 0 & \frac{1}{H_s} \end{bmatrix} \begin{Bmatrix} p_a - p_w \\ p_a - p_w \\ p_a - p_w \end{Bmatrix} \quad (6.40)$$

where x is the horizontal direction perpendicular to the cracking plane, y is the horizontal direction parallel to the cracking plane, z is the vertical direction. ν is Poisson's coefficient. H_s is a modulus of elasticity for the solid skeleton with respect to a change in suction. The elastic

parameter E is with respect to a change in net stress. H_s does not depend on net stress and E and ν do not depend on suction. The constitutive relationships graphically define a state surface, for instance, in the space of volumetric strains, net stress and suction. Stress state must lie on this surface and can move on it along any monotonic path. Actually, different state surfaces must be defined for unloading and loading conditions (Fredlund and Rahardjo 1993).

Morris et al. (1992) try to determine the depth of cracking in the case of the soil column. In this configuration and assuming isotropic elasticity is applicable, the problem is forced to be one dimensionnal ($\sigma_x = \sigma_y \neq \sigma_z$ and $\varepsilon_x = \varepsilon_y = 0$). Morris et al. (1992) thus deduce from Eq. 6.40 that:

$$\varepsilon_x = 0 = \frac{\sigma_x - p_a}{E} - \frac{\nu}{E}(\sigma_y + \sigma_z - 2p_a) + \frac{p_a - p_w}{H_s} \tag{6.41}$$

and thus

$$(\sigma_x - p_a) = \frac{\nu}{(1-\nu)}(\sigma_z - p_a) - \frac{E}{H_s(1-\nu)}(p_a - p_w) \tag{6.42}$$

Considering that the material will crack when the horizontal net stress exceeds the tensile strength of the material ($\sigma_x - p_a = \sigma_t$) it is possible to determine the depth of cracking by making a few more assumptions. The atmospheric pressure, p_a is taken at zero which means that $\sigma_z - p_a = \gamma z$ and the suction is assumed to be constant at value ($p_a - p_w = S_0$). Then the depth of cracking is given by

$$\sigma_t = -\frac{\nu}{(1-\nu)}\gamma z_c + \frac{E}{H_s(1-\nu)}S_0 \tag{6.43}$$

$$z_c = -\frac{(1-\nu)}{\nu}\sigma_t + \frac{E}{H_s}\frac{1}{\nu}S_0 \tag{6.44}$$

Morris et al. (1992) further assumed that the degree of saturation near the tip of a propagation crack remains high which led them to the conclusion that the soil would behave similarly whether it is subjected to an externally applied net stress change or to an internal change of suction. This hypothesis allowed them to derive the ratio $\frac{E}{H_s}$ from the expression of the volumetric strains :

$$\varepsilon_v = \frac{1}{E}(\sigma_z - p_a) - \frac{\nu}{E}(2\sigma_x - 2p_a) \tag{6.45}$$

Inserting Eq. 6.42 into Eq. 6.45, it comes :

$$\varepsilon_v = \frac{1 - \nu - 2\nu^2}{E(1-\nu)}(\sigma_z - p_a) + \frac{(1+\nu)}{H_s(1-\nu)}(p_a - p_w) \tag{6.46}$$

The $\frac{E}{H_s}$ ratio is thus equal to $(1 - 2\nu)$ and the final expression of crack depth is :

$$z_c = \frac{(1-\nu)}{\nu}\sigma_t + \frac{(1-2\nu)}{\nu}S_0 \tag{6.47}$$

6.5.2 Failure envelope

A second solution for the depth of cracking suggested by Morris et al. (1992) is based on a failure envelope. This failure criterion is visible in Fig. 6.20 in a mean net stress ($p - p_a$), deviatoric stress $q$plane. The figure on the right show the evolution of the envelope with suction.
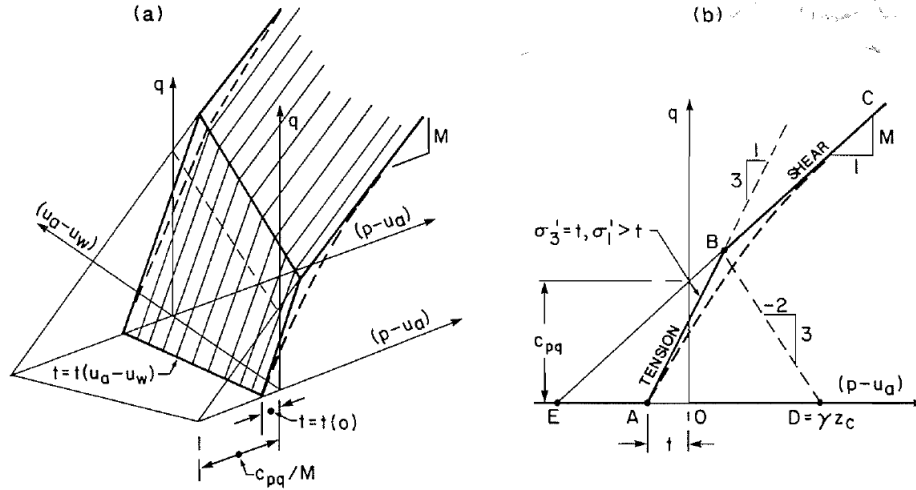
Figure 6.20: Schematic view of failure envelope in tension and the effect of suctiont (left) (after Morris et al. (1992))

The net vertical stress is constant and equal to the weight of the soil column. This defines in the $(p - p_a; q)$ plane a linear stress path with constant slope -3/2. Cracking is likely to occur only when the tensile strength envelope is met ($\sigma_3 - p_a = -\sigma_t$). Otherwise, the material will fail in shear, when the vertical stress becomes sufficiently large to inhibit failure in tension. Therefore, the value of the soil column weight determines the intercept of the stress path with the failure criterion, and thus the mode of failure (tension or shear).

6.5.2.1 Tensile failure criterion

Both analyses suggest a criterion for cracking initiation based on a modification of the Mohr-Coulomb criterion when tensile range is met. Such modification introduces a tension cut-off to lower the tensile strength given by the Mohr-Coulomb theory. In addition it is assumed that the soil experiences tensile strength and apparent cohesion increases, related to the increase of suction :

$$c_{app} = c' + s \, tan\phi_b \tag{6.48}$$

with c' being the effective cohesion and ϕ_b describing how the strength increases with suction. Let ϕ now be the friction angle. With the suggestion of the authors to lower the maximum value of the tensile strength, the strength criterion σ_t becomes:

$$\sigma_t = \alpha_t(c' + s \, tan\phi_b)cotan\phi' \tag{6.49}$$

where α_t is a coefficient, based on experimental evidence from prior studies. In addition to α_t, one has to know the value of the parameter ϕ_b (controlling the evolution of tensile strength with suction). Comparisons of predicted and observed crack depths in Australian coal mine tailings deposits suggest both approaches of Morris et al. (1992) provide solutions for the depth of cracks that are of the correct order of magnitude. Yet a more extended validation, in particular addressing prediction of the cracking initiation, is not available.

125

6.5.3 Model of Peron

Peron in his PhD thesis (Péron (2008)) suggested a framework to model desiccation cracking quite similar, in principle to the work of Morris et al. (1992). He integrated said criterion in the ACMEG environment (François and Laloui (2008)). The ACMEG model is an elasto-plastic model making use of Bishop's effective stress (cf. chapter 2). It includes two mechanisms :

- An isotropic yield mechanism, f_{iso} written :

$$f_{iso} \equiv p' - p'_c r_{iso} = 0 \qquad (6.50)$$

  where p'_c is the preconsolidation pressure, r_{iso} is the degree of mobilization of the isotropic mechanism, which makes possible a progressive mobilization of the isotropic yield limit before the state of stress reaches it. It has been introduced to avoid the sudden change in strain rate occurring when preconsolidation pressure is reached (Hujeux 1979).

- A deviatoric yield mechanism, f_{dev} of the Cam-clay type :

$$f_{dev} \equiv q - Mp'(1 - b \, log(\frac{p'}{p'_{CR}}))r_{dev} = 0 \qquad (6.51)$$

  where M is the slope of the critical state line, b is a material parameter, p_{CR} is the critical pressure (the intercept of f_{dev} with the M line) and r_{dev} is the degree of mobilization of the deviatoric mechanism and has the same goal as r_{iso}.

6.5.3.1 Tensile failure criterion

The criterion suggested by Peron is a macroscopic Griffith like criterion. It assumes the existence of a tension cut-off and therefore failure occurs as soon as the minor principal effective stress becomes lower than the uniaxial tensile strength of the material (expressed in terms of Bishop's generalized effective stress) :

$$f_{cut} \equiv \sigma'_3 = -\sigma'_t \qquad (6.52)$$

This is a variation, expressed in terms of effective stress, of the work Morris et al. (1992). The fact that the criterion is expressed in effective stress means that when suction increases, σ'_t lies in the negative range (which means that $-\sigma'_t$ is in compression). However the total stress is, of course, in tension. When the criterion is met, the sample has cracked and no plastic strains are computed.

Based on the experiment he conducted and the data available in the literature, Peron concluded that the tensile strength of a material evolved with suction. All the results compiled (Péron (2008)) pointed to an increase of the tensile strength with suction. His analysis of the data lead Peron to suggest the following formulation to take into account the effect of suction on tensile strength :

$$\sigma'_t = \sigma'^{sat}_t + k_2\left[1 - exp\left(-\frac{k_1 s}{k_2}\right)\right] \qquad (6.53)$$

where σ'^{sat}_t is the tensile strength at the saturated state (s = 0), namely the saturated tensile strength, k_1 and k_2 are material parameters accounting for the increase in tensile strength as suction increases. k_2 has the dimension of a stress, and k_1 has no dimension (cf. Fig. 6.22)
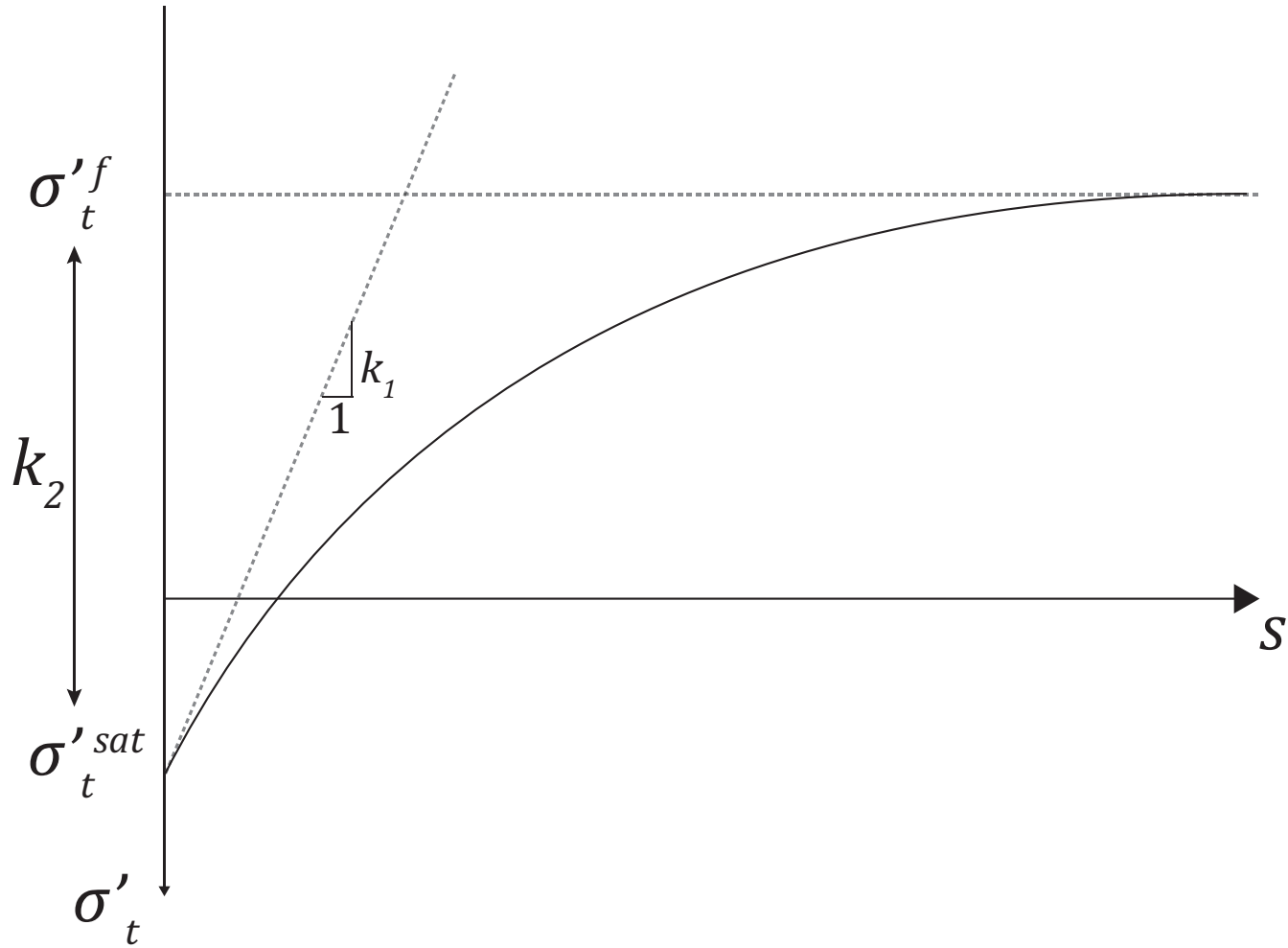
Figure 6.21: Evolution of the tensile strength with suction (after Péron (2008))

The tensile failure criterion is independent from the deviatoric and isotropic mechanisms. Therefore the tensile failure criterion does not depend on hardening variables of deviatoric and isotropic mechanisms. The non-dependence of tensile failure criterion on preconsolidation pressure implies that such failure mechanism is indeed independent from deviatoric and isotropic mechanisms. The tensile failure criterion is a "Griffith-like" criterion leading to a brittle failure mechanism controlled at the microscopic level by the size of internal defects, and also liquid tension surface, or solid skeleton surface energy. The deviatoric and isotropic mechanisms are respectively a frictional and a compressive plastic mechanism controlled mainly by friction angle and plastic compressibility. It is actually possible that the mechanisms are related due to the complexity of the microscopic features (grain surface properties, solid skeleton arrangement, liquid / solid skeleton interactions, etc.). Peron also assumed that the tensile failure mechanism is activated for any stress value that would reach the corresponding criterion. This may be not the case in the region close to the interception of the two mechanisms. The tensile failure criterion, combined with the deviatoric and isotropic mechansim can be seen in Fig. 6.22 in a normalized biaxial plane :
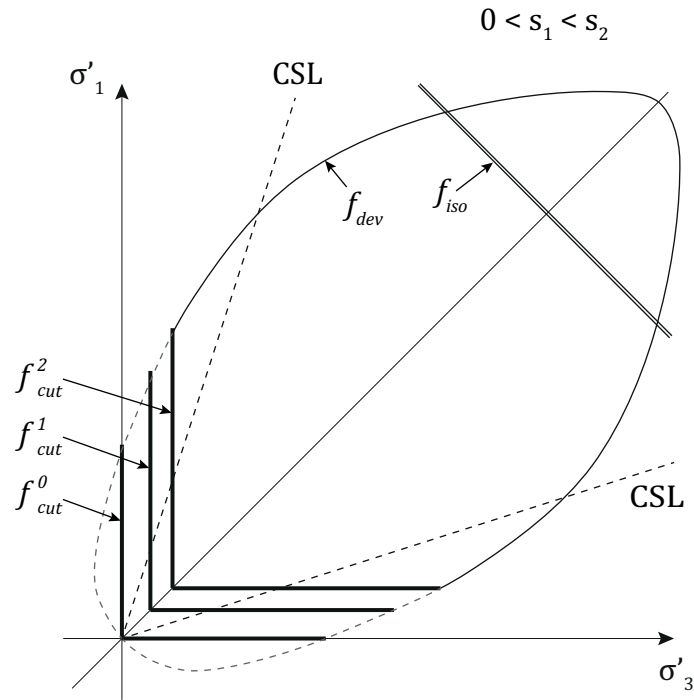
127

Figure 6.22: Form of the tensile criterion in the biaxial plane (after Péron (2008))

6.5.4 Effective stress approach

The theoretical model of Abu-Hejleh (1993) and Abu-Hejleh and Znidarcic (1995) was developed to study the desiccation of soft waste disposal sites and the studied material was kaolinite. They studied homogeneous soil column (same situation as Morris et al. (1992)) and their model includes four phases :

- one dimensional consolidation ;

- one dimensional shrinkage ;

- propagation of a vertical crack with tensile stress relief ;

- three dimensional shrinkage.

,
Only the one dimensional problem until crack initiation is considered hereafter. The theory of Abu-Hejleh (1993) is based on the assumption that the soil remains saturated until the void ratio reaches limit void ratio (end of perfect shrinkage). The effective stress is thus directly equal to the total stress minus the water pressure and the air pressure is never considered.
The theoretical stress path followed during drying is shown in Fig. 6.23. Total and effective stress path are presented in the mean stress($p = \frac{\sigma_1 + \sigma_2 + \sigma_3}{3}$) - deviatoric stress($q = \sigma_3 - \sigma_1$) plane. The initial pore pressure (caused by the overburden pressure) is the distance between total stress state W and effective stress state O, here set at zero for the sake of simplicity.
The model starts with a consolidation phase followed by desiccation and as to consolidation and desiccation progress, pore water pressure decreases. Following Morris et al. (1992), the

Figure 6.23: Effective and total stress paths during desiccation proposed by Abu-Hejleh (1993), Konrad and Ayad (1997) and Avila (2004). (after Péron (2008))

total stress path is assumed to develop with a -3/2 slope in the net stress plane. Prior to cracking, the lateral strain remains nul (soil column with prevented lateral displacement) and the effective stress path during consolidation and desiccation occurs under K_0 conditions (K0 is the coefficient of lateral earth pressure at rest).

Along total stress path WK and effective stress path OK (Fig. 6.23), pore water pressure remains positive and the paths describe the consolidation process. Along subsequent paths (KB and KM), pore water is increasingly negative and the paths describes desiccation. Therefore, the point K represent the state where the pore water pressure is nul and is thus the transition between the first and the second phase of Abu-Hejleh model. Cracking criterion is formulated in total stresses. Cracking initiates once the developed lateral total stress, σ_h , reaches the tensile strength, σ_t, that is:

$$\sigma_h = -\sigma_t \tag{6.54}$$

This situation is denoted by points M and B along total and effective stress paths, respectively, in Fig. 6.23. The expression of tensile strength σ_t (total stress) is related to void ratio e by the following relationship:

$$\sigma_t = -Y_1 10^{\frac{Y_2-e}{Y_3}} \tag{6.55}$$

where Y_1, Y_2 and Y_3 are soil parameters to be determined experimentally by drying a bar-

shaped sample clamped at its two extremities, and measuring void ratio at crack initiation. A constitutive relationship is proposed to model void ratio, e, evolution under one-dimensional consolidation and desiccation:

$$e = X_1(\sigma'_v + X_2)^{X_3} \tag{6.56}$$

where σ'_v is the effective vertical stress, and X_1, X_2 and X_3 are soil parameters, which differ for consolidation and desiccation, respectively. A similar expression is proposed to model the evolution of permeability with respect to void ratio.

Using Eq.6.55 and Eq. 6.56, the definition of effective stress and the relationship between lateral and vertical effective stresses (K_0 conditions), a "cracking function" is derived. This function relates the cracking void ratio to the vertical total stress, and allows for determination of the profile of cracking void ratio along the depth in the soil column. With the known distribution of void ratios along the same soil column, one can define the crack depth. The "cracking function," together with the constitutive relationship (Eq. 6.56), and the additional assumption of constant K0) are included in a simplified hydro-mechanical formulation solved using a finite element scheme. No direct validation of the model is proposed, partly due to the lack of data on tensile strength and cracking (Péron (2008)).

6.5.4.1 Tensile failure criterion

Avila (2004) makes an attempt to justify the model of Abu-Hejleh (1993) by adding a tensile failure criterion expressed in terms of effective stress. The criterion is actually an apparent failure line, which collects the effective stress values obtained at the time of failure during uniaxial traction tests, at various suctions. A possible shape of the criterion proposed by Avila (2004) is also been represented in Fig. 6.23. An observation can be made regarding the work of Avila (2004). The slope of the tensile criterion is lower than the extension slope. This would mean that the criterion is reached for effective stress lower than that predicted by classical Mohr-Coulomb theory.

6.5.5 Elastic fracture mechanics

Linear Elastic Fracture Mechanics (LEFM) is a commonly used method to assess the damage tolerant design of materials in many fields of engineering e.g. aerospace, nuclear, shipping industries etc. The fundamental principles of LEFM are briefly summarized and an application of the method to the study of desiccation cracking is presented.

LEFM is based on a series of assumptions (Stirling (2014)):

- A crack has been initiated and has begun to propagate. In the context of materials testing, this may be a flaw on the microscopic scale;

- The material is isotropic;

- The material is linear elastic;

- The plastic zone in the vicinity of the crack tip is small compared to the local geometry;

- Any given point of analysis is near the crack tip ($< 10\%$ of the crack length).

For mode I opening, consider the stress field geometry presented in Fig. 6.24 where stresses are given by Eq. 6.57 to Eq. 6.60.
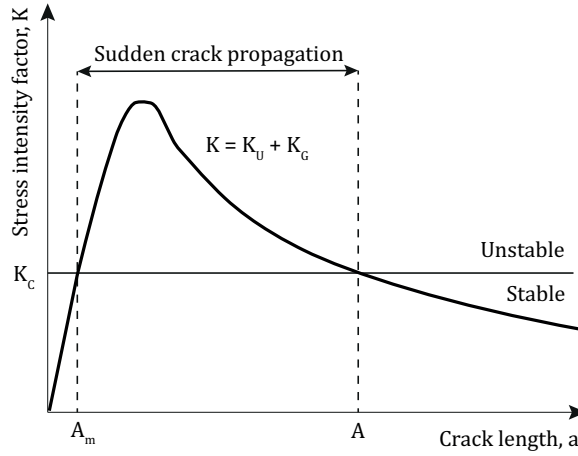

Figure 6.24: Stress intensity factor and crack propagation according to LEFM (after Konrad and Ayad 1997)

$$\sigma_y = \frac{K}{\sqrt{2\pi r}} cos\frac{\theta}{2}\left(1 + sin\frac{\theta}{2}sin3\frac{\theta}{2}\right) \tag{6.57}$$

$$\sigma_x = \frac{K}{\sqrt{2\pi r}} cos\frac{\theta}{2}\left(1 - sin\frac{\theta}{2}sin3\frac{\theta}{2}\right) \tag{6.58}$$

$$\tau_{xy} = \frac{K}{\sqrt{2\pi r}} cos\frac{\theta}{2}sin\frac{\theta}{2}cos3\frac{\theta}{2} \tag{6.59}$$

$$\sigma_z = \tau_{xz} = \tau_{yz} = 0 \quad (for\ plane\ stress) \tag{6.60}$$

where r and θ form the polar coordinate system used to define the position of the studied point relative to the crack tip. The stresses are dependent on K, the stress intensity factor. The stress intensity factor is a theoretical construct and a fundamental parameter in LEFM. It depends on the loading mode, crack shape and material geometry and analytical formulation of the stress intensity factor are available for common configuration in books such as Tada et al. (2000) and Rooke and Cartwright (1976)). A crack will grow when the stress at the crack tip exceeds a critical value. Since the stress intensity factor determines the amplitude of the crack tip stress for a given geometry and loading, unstable crack propagation may be considered to occur when $K \geq K_c$ where K_c denotes the fracture toughness. The stress intensity factor may be calculated; however, the fracture toughness is determined experimentally. Fracture toughness is dependent on the material, temperature, strain rate, environment and material thickness. In plane strain conditions, fracture toughness is considered to be an intrinsic material property (independent of thickness). Several experimental methods to determine the fracture toughness of geomaterials exist including ISRM (1988). Fig. 6.24 shows that as r tends towards zero, the elastic stress in the y-direction tends towards infinity. This is not possible and in reality a plastic zone will form ahead of the crack tip. No modification to the elastic solution is required if the plastic zone radius is small relative to the local geometry.

131

Application of LEFM to desiccation cracking   The principles of LEFM have historically been applied to the study of cracking depth and spacing. Hereafter is presented an application of LEFM to desiccation cracking.

The framework proposed by Konrad and Ayad (1997) is composed of three parts (Stirling (2014)):

- A one-dimensional mass transport model to determine an effective stress profile that satisfies the crack initiation criterion;

- LEFM to determine ultimate crack depth under the previously calculated stress field;

- A finite element model to determine average crack spacing from stress relief following crack propagation.

The suction profile is determined on the basis of a given rate of water removal using the differential equation for water flow in transient conditions. With respect to the constitutive aspects, the Konrad and Ayad (1997) model essentially includes those of the Abu-Hejleh (1993) model. The formulation of Abu-Hejleh is used to determine a critical suction, s_{cr}. The value of the critical suction is derived from the tensile strength and the effective stress path and corresponds to the distance MB on Fig. 6.23. That critical suction defines the moment when cracking occurs. The cracking criterion is only formulated in terms of critical suction without any determination of the deformational state (no explicit constitutive relationship is proposed, contrary to Abu-Hejleh 1993). It is also assumed that tensile strength is a constant soil parameter. At the moment of cracking, the suction is equal to its critical value, s_{cr}. Assuming the cracking criterion is fulfilled, it yields:

$$-\sigma_t = \sigma_3 = \sigma_3' - s_{cr} = K_0\sigma_1' - s_{cr} = K_0(\sigma_1 + s_{cr}) - s_{cr} \tag{6.61}$$

It is then considered that on soil top surface, total major (vertical) stress is zero, and K_0 is approximated by Jacky's formula, which induces:

$$s_{cr} = \frac{\sigma_t}{sin\phi'} \tag{6.62}$$

where ϕ' is the soil friction angle.

LEFM is then used to determine the depth of crack propagation. The stress intensity factor is calculated based on the stress state at the moment suction equal critical suction.

6.6   Conclusion

This chapter was devoted to desiccation cracking and starts with the introduction of the notion of crack as well as the different crack opening mode. Mode I is then more thoroughly studied because experimental data showed that desiccation cracking is mainly a mode I mechanism. This introduced the notion of material tensile strength. A selection of existing apparatuses and test procedures devoted to tensile strength measurement is reviewed. In particular direct and indirect tension test are presented and their strength and weakness are discussed. An analysis of both methods showed that direct tension tests are preferable to indirect ones because of the strong heterogeneous stress field created during indirect tension tests. However, the main

concerns of most direct tests involve connecting the specimen to the traction system, controlling the exact stress field, and drainage conditions. A few, less common, original methods to measure the tension strength of soil while circumventing the problem inherent to direct and indirect tension test methods are also presented. Finally, a review of the models found in the literature to predict desiccation cracking initiation and crack depth is presented. Most of them don't account simultaneously for drying constitutive behavior and the tensile failure criterion. The most consistent model found is the one formulated by Péron (2008) which is now going to be integrated into the the inhouse built FEM code LAGAMINE. Its implementation and its validation on simple boundary value problems will be the subject of the next chapter.

Chapter 7

Tensile strength constitutive law implementation

Contents

7.1 Introduction

In the previous chapter, a review of the different approaches proposed in the litterature to predict desiccation cracking was presented. Though the methods were different, the tensile failure criterion itself remained mostly unchanged. It is a Griffith like tension cut-off (Griffith (1924)). In this chapter, the implementation into Liège's in house built finite element code - LAGAMINE - of a similar tensile failure criterion is presented. The chapter starts with a presentation of the mechanical framework. Specifically, the two failure mechanisms are detailed : a cohesive

frictional failure mechanism and the chosen tensile failure mechanism. A discussion about the hypothesis and shortcomings of the tensile failure criterion is also included. Then, the implementation of the model into the finite element code is presented. It is followed by some validation of the model at the material point.

Choice of a general framework   The process of desiccation cracking essentially results from a strain compensation mechanism. This means that, due to suction increase, shrinkage strains tend to be generated, which are hindered by a constraining mechanism (resulting from displacement or traction boundary conditions). Such process requires a hydromechanical formulation of the problem. Furthermore, it was shown that temperature also plays a dominant role in the drying behavior of porous materials. The Thermo-Hydro-Mechanical general framework has already been presented in chapter 5. Only the mechanical part is significantly improved upon and as such only the mechanical constitutive model is detailed in the following section. But before expressing the constitutive equations and describing their implementation into a finite element code, it is useful to look at the requirements that the mechanical framework has to fulfill.

The strains due to drying are the consequence of a change in water content therefore, the use of suction as a variable of the problem is required. A drying material gains rigidity during drying (marked by a clear decrease in shrinkage rate not only explained by the decreasing saturation term in Bishop's effective stress). Non linear elasticity is thus also a requirement. A material undergoing desiccation cracking is obviously submitted to irreversible strains and the framework has to be elasto-plastic. As previously stated, desiccation cracking is a mode I failure and the mechanical framework must include a tensile failure criterion. To be consistent with the use of effective stress to model the stress path, said criterion should also be expressed in effective stress. Finally, experimental evidences (Péron (2008)) show that the tensile strength of materials depends on suction and the model must include that feature.

Now that all the requirements have been set, our suggestion of a mechanical constitutive model that features all of the these requirements is presented.

7.2   Mechanical constitutive model

As was the case in chapter 5, for the modeling of Boom clay drying behavior, Bishop's effective stress has been chosen to describe the stress-strain relation because it directly incorporates the effect of a change in suction:

$$\sigma'_{ij} = \sigma_{ij} - p_g \delta_{ij} + S_{r,w}(p_g - p_w)\delta_{ij} \tag{7.1}$$

where σ'_{ij} is the effective stress tensor, σ_{ij} is the total stress tensor, $S_{r,w}$ is the water saturation and δ_{ij} is Kronecker's tensor. p_g and p_w denote respectively gas and water pressure $[Pa]$.

7.2.1   Elasto-plastic framework

As explained in the introduction of this chapter, an elasto-plastic framework is required. Elasto-plasticity is based on the decomposition of the total strain increment, $d\varepsilon_{ij}$ into a reversible elastic strain increment, $d\varepsilon^e_{ij}$, and an irreversible plastic strain increment, $d\varepsilon^p_{ij}$:

$$d\varepsilon_{ij} = d\varepsilon_{ij}^e + d\varepsilon_{ij}^p \tag{7.2}$$

The plastic strain is said to be irreversible because it can not be recovered even if the applied stress is removed.

7.2.1.1 Elastic strain

Hooke's law describes the relationship between the elastic strain rate, $\dot{\varepsilon}_{ij}^e$ and the effective stress tensor :

$$\dot{\sigma}'_{ij} = C_{ijkl}^e \dot{\varepsilon}_{kl}^e \tag{7.3}$$

where C_{ijkl}^e is Hooke's elastic constitutive tangent tensor. Its formulation for isotropic and orthotropic materials has already been presented in chapter 5. A material subjected to a decrease in water content tends to stiffen and thus the non linear elasticity introduced in chapter 5 is used in this framework. The formulation used is Modaressi and Laloui (1997):

$$E_i = E_{0,i} + E_{ref,i}\left(\frac{p'}{p_{ref}}\right)^b \tag{7.4}$$

where E_{ref} is the Young modulus at the reference mean effective stress, p_{ref}. b is a model parameter and $E_{0,i}$ is used to avoid null Young's modulus when the effective stress state vanishes.

7.2.1.2 Plastic strain

Most soil mechanics elasto-plastic constitutive frameworks are based on the concept of yield criterion. A yield criterion is a condition that defines the limit of the elastic domain and the beginning of plastic strain. In our case, the yield criteria are defined in terms of effective stress, σ'_{ij}, and depend on a vector of internal plastic variables, κ_m, and on suction, s:

$$f(\sigma'_{ij}, \kappa_m, s) \le 0 \tag{7.5}$$

When the stress path reaches the yield limit, $f(\sigma'_{ij}, \kappa_m, s) = 0$, only three configurations are possible (Prager (1949)) (cf. Fig.7.1) :

- Unloading : $df < 0$;

- Neutral loading : $df = 0$;

- Loading : $df > 0$;

In the latter case, the zone outside the yield surface cannot, by definition, be reached. Hence, the yield function, f, must adapt (this process is called hardening/softening) to make sure that the yield criterion is always satisfied. This requirement is the consistency condition. The yield function needs to satisfy the consistency condition:

$$df \equiv \frac{\partial f}{\partial \sigma'_{ij}} d\sigma'_{ij} + \frac{\partial f}{\partial \kappa_m} d\kappa_m + \frac{\partial f}{\partial s} ds = 0 \tag{7.6}$$

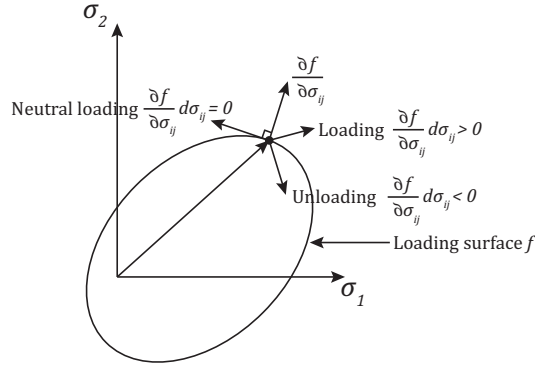In this work, we consider that hardening is only due to plastic strains.

Figure 7.1: Different loading configurations

7.2.2 Yield surfaces

The tensile stress range allowed by the cohesive-frictional failure model is dependent on the cohesion and friction angle of the material. It has been proven (Risnes et al. (1999)) to lead to an overestimation of the material tensile strength. To deal with that issue, the mechanical framework suggested is composed of two different mechanisms : a cohesive frictional failure mechanism and a tensile failure mechanism (see Fig. 7.2). The total plastic strain increment is
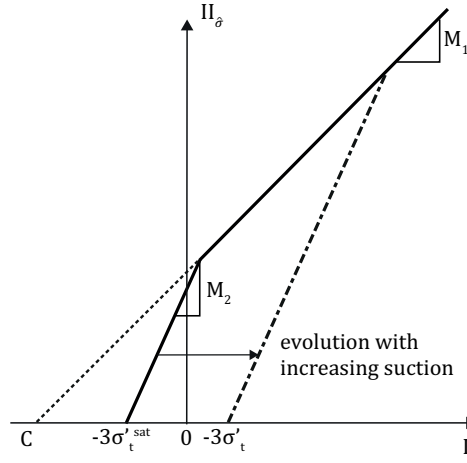

Figure 7.2: Yield surfaces in the stress invariant plane

thus the sum of two plastic strain increments induced by two independent mechanisms:

$$d\varepsilon_{ij}^{p} = d\varepsilon_{ij}^{p\,1} + d\varepsilon_{ij}^{p\,2} \tag{7.7}$$

7.2.2.1 Cohesive frictional failure mechanism

Shear failure is most often represented using a cohesive frictional failure criterion. The most famous of which is without a doubt the Mohr-Coulomb criterion. The Mohr-Coulomb criterion is expressed, in the principal stress plane, by :

$$f^1 \equiv \sigma'_1 - \sigma'_3 + (\sigma'_1 + \sigma'_3)sin\phi + 2c\,cos\phi = 0 \tag{7.8}$$

138

where c is the cohesion and ϕ is the friction angle. The criterion corresponds to a hexagonal-based pyramid as depicted in Fig. 7.3 on the right. The form of the criterion in the deviatoric plane is also visible on Fig. 7.3 on the left. The criterion is expressed in principal stresses but
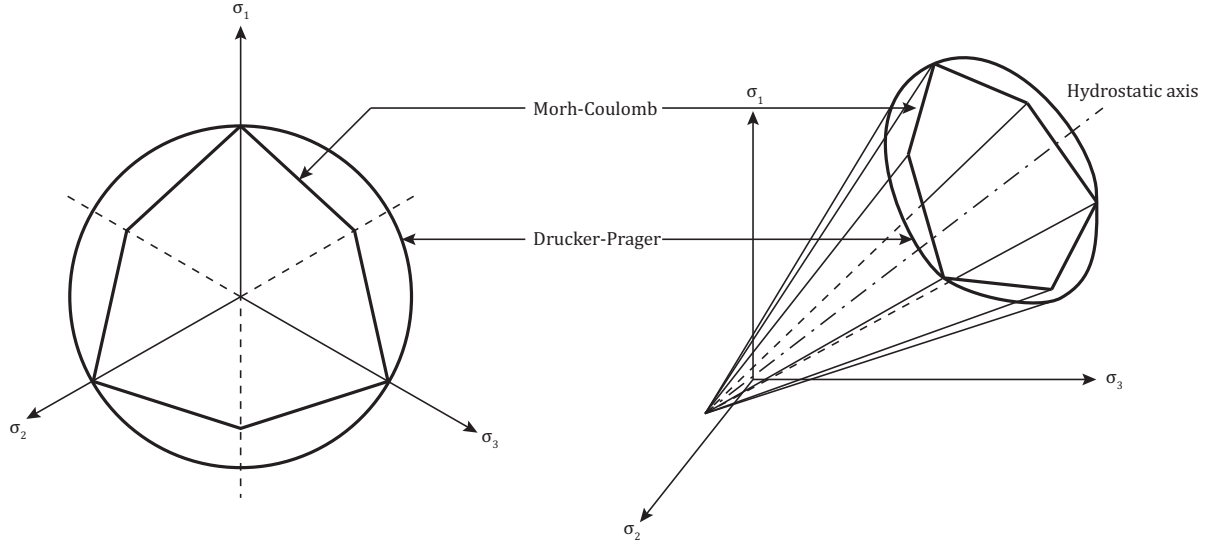

Figure 7.3: Mohr-Coulomb and Drucker Prager criteria in the deviatoric plane

most constitutive laws in LAGAMINE are expressed in terms of stress invariants.

Stress invariants I_σ, $II_{\hat{\sigma}}$, $III_{\hat{\sigma}}$ and β represent respectively the first invariant of the stress tensor, the second invariant of the deviatoric stress tensor, the third invariant of the deviatoric stress tensor and the Lode angle defined by :

$$I_\sigma = \sigma'_{ii} \tag{7.9}$$

$$II_{\hat{\sigma}} = \sqrt{\frac{1}{2}\hat{\sigma}'_{ij}\hat{\sigma}'_{ij}} \tag{7.10}$$

where

$$\hat{\sigma}'_{ij} = \sigma'_{ij} - \frac{I_\sigma}{3}\delta_{ij} \tag{7.11}$$

$$III_{\hat{\sigma}} = \frac{1}{3}\hat{\sigma}'_{ij}\hat{\sigma}'_{jk}\hat{\sigma}'_{kl} \tag{7.12}$$

$$\beta = -\frac{1}{3}arcsin\left(\frac{3\sqrt{3}}{2}\frac{III_{\hat{\sigma}}}{II_{\hat{\sigma}}^3}\right) \tag{7.13}$$

It is possible to express the principal stresses as a combination of the stress invariants (cf. full development in Appendix A) :

$$\begin{pmatrix} \sigma'_1 \\ \sigma'_2 \\ \sigma'_3 \end{pmatrix} = \begin{pmatrix} \frac{I_\sigma}{3} \\ \frac{I_\sigma}{3} \\ \frac{I_\sigma}{3} \end{pmatrix} + \frac{2II_{\hat{\sigma}}}{\sqrt{3}}\begin{pmatrix} cos\theta \\ cos\left(\theta - \frac{2\pi}{3}\right) \\ cos\left(\theta + \frac{2\pi}{3}\right) \end{pmatrix} \tag{7.14}$$

Using Eq. 7.14, it is possible to express the yield criterion in terms of stress invariants. The full development is also available in Appendix A. The criterion then becomes :

$$f^1 \equiv II_{\hat{\sigma}} - M_{MC}(I_\sigma + C) = 0 \qquad (7.15)$$

where $M_{MC} = \frac{sin\phi}{3cos\beta - \sqrt{3}sin\beta sin\phi}$ is the slope of the criterion and $C = \frac{3c}{\tan\phi}$ is its intersection with the horizontal axis and both are dependent on the cohesion, c, and the frictional angle, ϕ. This model is not convenient to implement into a classical plasticity framework because the gradient is undefined on the corners of the hexagon. To overcome this difficulty, an alternative yield function has been suggested by Drucker and Prager (1952) using a linear relationship between the first invariant of the stress tensor and the second invariant of the deviatoric stress tensor. In the case where the compression cone is chosen, the Drucker-Prager yield surface is the circumscribed circle to the Mohr-Coulomb yield surface in the deviatoric plane (see Fig. 7.3 on the left) and it is given by :

$$f^1 \equiv II_{\hat{\sigma}} - M_1(I_\sigma + C) = 0 \qquad (7.16)$$

where $M_1 = \frac{2sin\phi}{\sqrt{3}(3 - sin\phi)}$. This is a particular case of the Mohr-Coulomb criterion where the Lode angle is equal to $\frac{\pi}{6}$. The form of the Drucker-Prager criterion is visible in Fig. 7.3 on the right.

Flow rule For the cohesive failure mechanism, a non associated flow rule is used :

$$g^1 \equiv II_{\hat{\sigma}} - \frac{2\sin\psi}{\sqrt{3}(3 - \sin\psi)}(I_\sigma + \frac{3c}{\tan\phi}) = 0 \qquad (7.17)$$

where ψ is the dilatancy angle. For associated plasticity, the dilatancy angle just has to be equal to the friction angle of the material.

Hardening rule The hardening rule intends to adapt the yield surface so that the consistency condition is always verified. As already mentioned, we consider that hardening is only due to plastic strains. For the cohesive frictional failure mechanisms, there are only two independent hardening variables : the cohesion, c, and the friction angle ϕ. An hyperbolic relationship is used to link the internal plastic variables to the deviatoric plastic strain, ε_d^p :

$$\phi = \phi_0 + \frac{(\phi_f - \phi_0)\varepsilon_d^p}{B_\phi + \varepsilon_d^p} \qquad (7.18)$$

$$c = c_0 + \frac{(c_f - c_0)\varepsilon_d^p}{B_c + \varepsilon_d^p} \qquad (7.19)$$

where ϕ_0 and c_0 are respectively the initial values of the friction angle and of the cohesion and ϕ_f and c_f are the final values. The coefficient B_ϕ and B_c correspond to the deviatoric plastic strain at half the variation between the initial and final values of the friction angle and the cohesion respectively. The deviatoric plastic strain, ε_d^p is given by :

$$\varepsilon_d^p = \int_0^t \dot{\varepsilon}_d^p dt \qquad (7.20)$$

where $\dot{\varepsilon}_d^p$ is given by :

$$\dot{\varepsilon}_d^p = \sqrt{\frac{2}{3}\dot{\hat{\varepsilon}}_{ij}^p \dot{\hat{\varepsilon}}_{ij}^p} \qquad (7.21)$$

7.2.2.2 Tensile failure criterion

As already mentioned in the introduction of this chapter, we propose to adopt a macroscopic Griffith like criterion for tensile failure. It assumes the existence of a tension cut-off. Similar hypothesis are common in tensile failure modeling. The failure occurs when the minor principal effective stress reaches the effective tensile strength of the material. This is the cut off criterion as it is introduced in the work of Morris et al. (1992) but expressed in effective stress. Its form in the deviatoric plane is visible in Fig. 7.4 on the left and in three dimensions on the right. As can be seen, it corresponds to three defined surfaces :

$$f^2 \equiv \sigma_3' = -\sigma_t' \tag{7.22}$$

$$f^3 \equiv \sigma_2' = -\sigma_t' \tag{7.23}$$

$$f^4 \equiv \sigma_1' = -\sigma_t' \tag{7.24}$$

where σ_t' is the uniaxial tensile strength of the material (defined as a positive quantity).
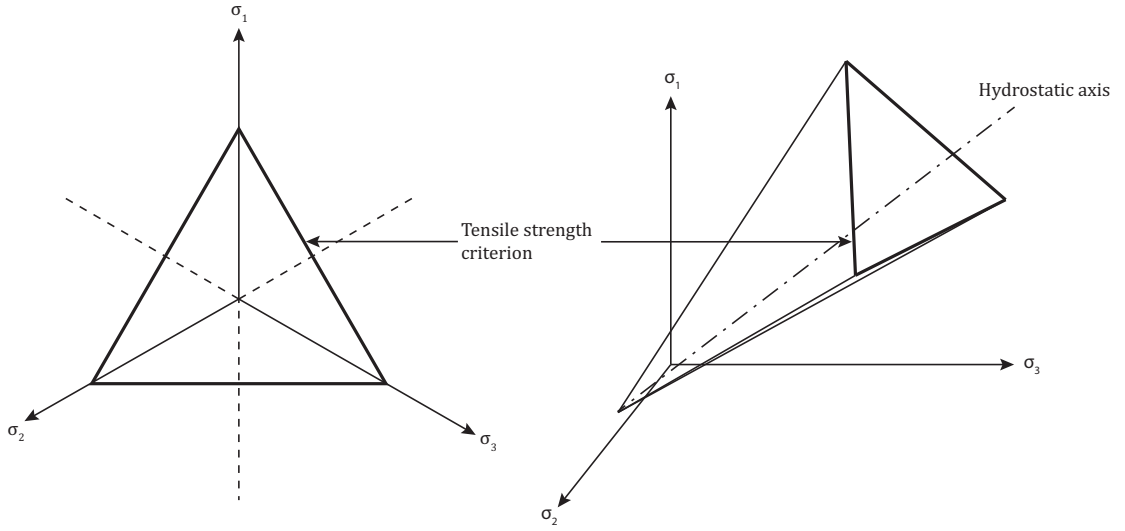

Figure 7.4: Tensile failure criterion in the deviatoric plane

Again, the criteria are expressed in principal stresses and using Eq. 7.14 they can be expressed in terms of stress invariants. The full development is available in Appendix A. The tensile criterion can thus be written as :

$$f^2 \equiv II_{\hat{\sigma}} + \frac{1}{-3cos\beta - \sqrt{3}sin\beta}(I_\sigma + 3\sigma_t) = 0 \tag{7.25}$$

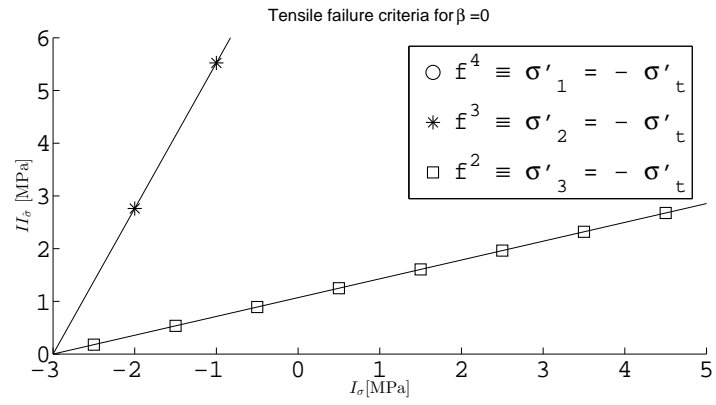$$f^3 \equiv II_{\hat{\sigma}} + \frac{1}{2\sqrt{3}sin\beta}(I_\sigma + 3\sigma_t) = 0 \tag{7.26}$$

$$f^4 \equiv II_{\hat{\sigma}} + \frac{1}{3cos\beta - \sqrt{3}sin\beta}(I_\sigma + 3\sigma_t) = 0 \tag{7.27}$$
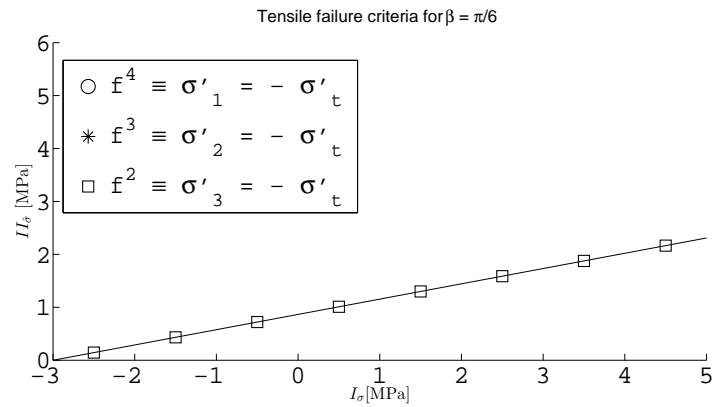
We draw those surfaces for three values of Lode's angle in the stress invariant plane (see Fig. 7.5). In Fig. 7.5, it clearly appears that the first surface met by any stress path is f^2. This is actually logical by definition of the principal stresses : f^4 cannot be activated except for
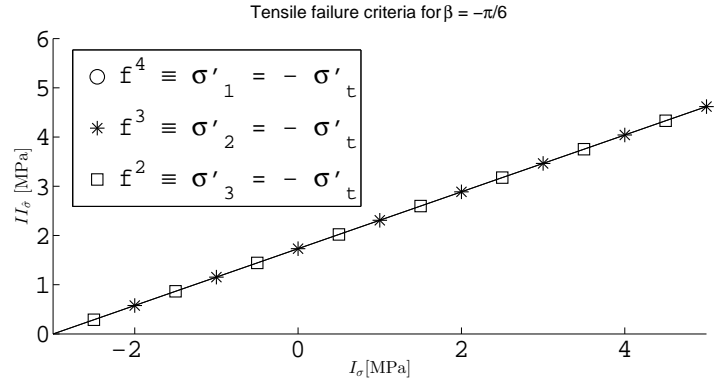
Figure 7.5: The three tension cut offs in the stress invariants plane

the particular case where $\sigma_1' = \sigma_2' = \sigma_3' = -\sigma_t'$ corresponding to the apex of the pyramid. Similarly, the surface f^3 can only be activated when it is superimposed on f^2, or in other terms when $\sigma_2' = \sigma_3' = -\sigma_t'$. f^2 is thus the only relevant surface and f^3 and f^4 will therefore not be considered further on.

In the previous chapter (Chapter 7 - Section 6.5), the formulation suggested by Péron (2008) was presented. His formulation is based on experimental results obtained from tensile strength measurement tests he performed or found in the literature. The main feature of this formulation is that the effective tensile strength, σ_t' of the material is a function of suction, s (cf. Fig. 7.6) :

$$\sigma_t' = \sigma_t'^{sat} - k_2 \left[1 - exp\left(-\frac{k_1 s}{k_{2,0}}\right)\right] \tag{7.28}$$

where $\sigma_t'^{sat}$ is the effective tensile strength at the saturated state (s = 0), k_1 and k_2 are material parameters accounting for the increase in tensile strength as suction increases. k_2 has the dimension of a stress, and k_1 has no dimension. k_2 is actually the variation of tensile strength from the saturated, $\sigma_t'^{sat}$, to the dried state, $\sigma_t'^f$:

$$k_2 = \sigma_t'^{sat} - \sigma_t'^f \tag{7.29}$$

This model means that the *effective* tensile strength may lie in the negative range due to the contribution of the suction. This allows for the activation of the tensile strength criterion at high suction levels.

Flow rule The formulation of the tensile strength criterion in terms of stress invariant is very much akin to the formulation of a Mohr-Coulomb criterion ($\equiv II_{\hat\sigma} - \frac{sin\phi}{3cos\beta - \sqrt{3}sin\beta sin\phi}(I_\sigma + \frac{3c}{tg\phi}) = 0$) in which the slope would correspond to a 90° friction angle. A non associated flow rule is attached to the f^2 surface based on the similitude between the tensile criterion and the Mohr-Coulomb criterion, a similar flow rule is suggested:

$$g^2 \equiv II_{\hat\sigma} - \frac{sin\psi_2}{3cos\beta - \sqrt{3}sin\beta sin\psi_2}(I_\sigma + 3\sigma_t') = 0 \tag{7.30}$$

$$\tag{7.31}$$

where ψ_2 is the dilatancy angle.

Hardening rule For the tensile failure criterion, the two hardening variables are the saturated uniaxial tensile strength, $\sigma_t'^{sat}$ and the variation of effective tensile strength, k_2. k_2 needs to be an hardening variable because the increase in tensile strength due to decreasing water content should also be degradable in case of material damage. On Fig. 7.7, we consider $\sigma_t'^{dry}$ to be the dried value of the effective tensile stress of a material whose saturated effective tensile stress is nul ($\sigma_t'^{sat} = 0$). The increase of the material strength is related to the suction term in Bishop's effective stress formulation (i.e. $\sigma_t'^{dry,} = S_{r,w} s$). We can see that without k_2 as an hardening/softening variable, the maximum degradation of the tensile strength would not correspond to a nul tensile strength in the damaged material.

A hyperbolic relationship is once again used to link the internal plastic variables to the volumetric plastic strain, ε_v^p :

$$\sigma_t'^{sat} = \sigma_{t,0}'^{sat} + \frac{(\sigma_{t,f}'^{sat} - \sigma_{t,0}'^{sat})\varepsilon_v^p}{B_{\sigma_t} + \varepsilon_v^p} \tag{7.32}$$
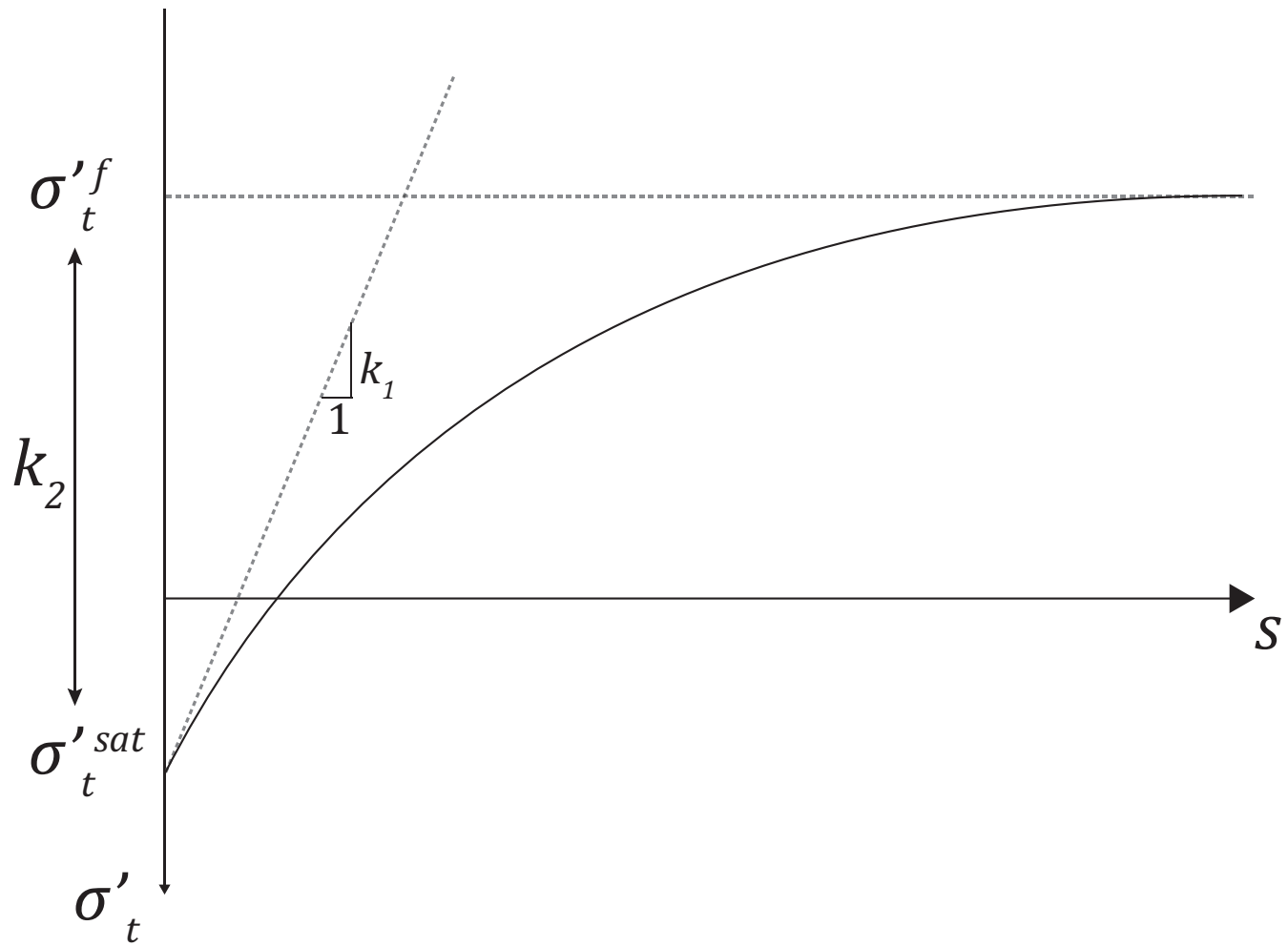
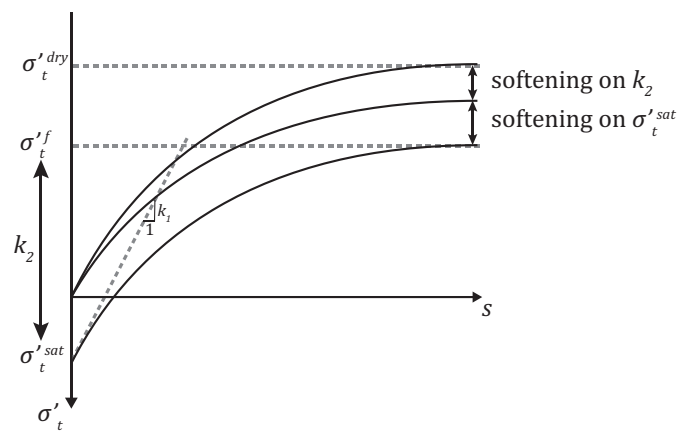Figure 7.6: Formulation suggestion by Péron (2008)

Figure 7.7: Softening with Perron's formulation

where $\sigma_{t,0}^{\prime sat}$ and $\sigma_{t,f}^{\prime sat}$ are respectively the initial and final values of the saturated uniaxial tensile strength.

$$k_2 = k_{2,0} + \frac{(k_{2,f} - k_{2,0})\varepsilon_v^p}{B_{\sigma_t} + \varepsilon_v^p} \tag{7.33}$$

where $k_{2,0}$ and $k_{2,f}$ are respectively the initial and final values of final increment of effective tensile strength. The coefficient B_{σ_t} corresponds to the volumetric plastic strain at half the variation between the initial and final values of the internal plastic variables and is thus regulating the softening rate. The same coefficient was used for both parameters because there is no reason to assume that the variation of the two parameters would happen at different rates. The volumetric plastic strain, ε_v^p is given by :

$$\varepsilon_v^p = \varepsilon_1^p + \varepsilon_2^p + \varepsilon_3^p \tag{7.34}$$

7.2.3 Apex of the tensile yield surface

The tensile failure criterion is a triangular pyramid (cf. Fig. 7.4) with its apex located at the value $I_\sigma = 3\sigma_t'$. This point is a singularity in the yield surface because its derivatives don't exist at that point. Since tensile experiments may lead to this extreme tensile stress state, it is important to find a method to handle that singularity. The method suggested here is to truncate the pyramid at a position defined as :

$$I_\sigma = 3(\sigma_t' - TRUNC) \tag{7.35}$$

where $TRUNC$ is arbitrarily fixed at :

$$TRUNC = \frac{\sigma_{t,0}^{\prime sat} * 10^{-4}}{\frac{3}{-3cos\beta - \sqrt{3}sin\beta}} \tag{7.36}$$

which is chosen as small as possible to limit the underevaluation of the material's tensile strength. That truncation leads to a new associated yield surface, f_5 defined as :

$$f_5 \equiv I_{\sigma_t} + 3(\sigma_t' - TRUNC) = 0 \tag{7.37}$$

Any trial state that would verify this surface would be mapped back onto the truncated yield surface.

7.3 Implementation in LAGAMINE

The formulated law is written in the form of an incremental relationship:

$$\tilde{\sigma}_{ij} = f(\dot{\varepsilon}_{ij}, \sigma_{ij}', s, \kappa_m) \tag{7.38}$$

where $\tilde{\sigma}_{ij}$ is Jaumann's stress rate, σ_{ij}' is the effectif stress state, s is the suction and κ_m is a vector of internal plastic variables.
The finite element formulation requires the stress state at the end of the time step and not the stress rate. The integration thus needs to be done over each time step. Given a known strain increment over the time step, the integration routine computes the constitutive equations to
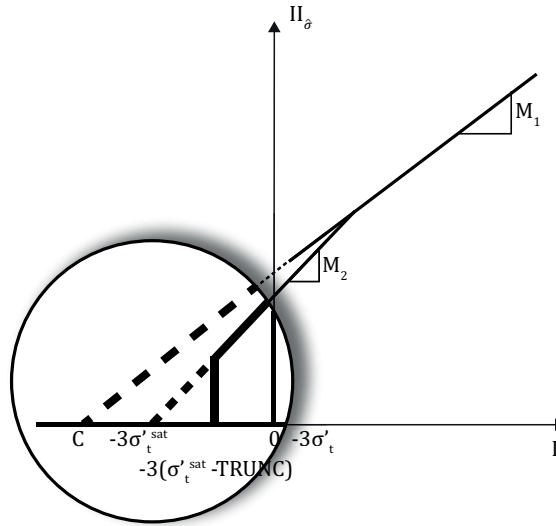
Figure 7.8: Truncation of the tensile yield surface

update the stress state. Different integration schemes for unsaturated soils have been suggested through the years (Collin et al. (2002a) Sheng et al. (2003)). A return mapping algorithm (Simo and Taylor (1985)) is used as the integration algorithm. First, the material response is assumed to be purely elastic and a trial stress (elastic predictor) is computed. The yield criteria are evaluated at this step. Three configurations are possible as shown in Fig. 7.9.
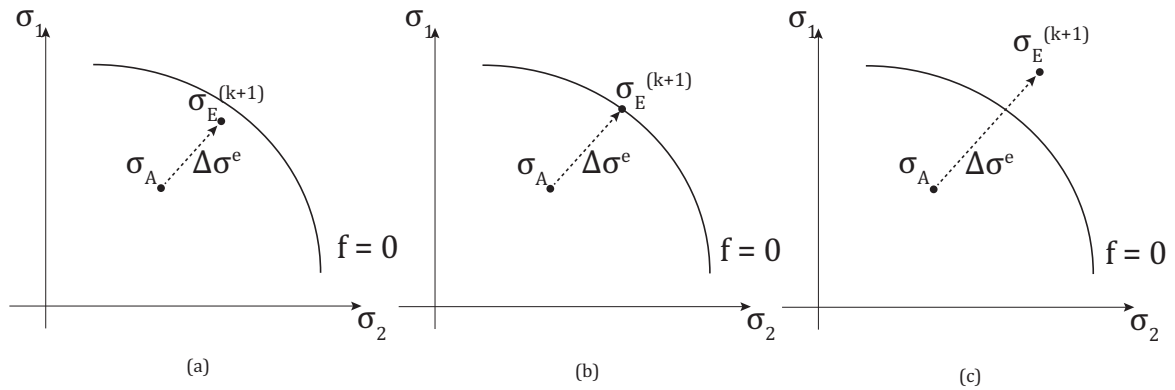

Figure 7.9: Evaluation of the yield criterion at stress state σ_E

If the stress state respects the yield criterion ($f(\sigma_E'^{(k+1)}) \leq 0$ corresponding to configuration (a) and (b) on Fig. 7.9), then the material response is indeed elastic and the final stress state is equal to the trial stress. If one or more yield criteria are violated then a plastic corrector is computed to return the stress state onto the yield surface and fulfill the consistency conditions. To restore the consistency of the mechanical state, a cutting plane algorithm is used (Ortiz and Simo (1986)). It is an explicit scheme where at every iteration, updated stresses are computed by projecting the previous iteration stress onto a plane defined by a linearized yield criterion, f, around the current value of the stress. This plane becomes tangent to the yield surface and plastic consistency is restored at the end of the law integration (Simo and Taylor (1985)).

146

7.3.1 Elastic predictor

Starting from the stress state, σ_A, at the beginning of the time step, the stress increment, $\Delta\sigma^e$, is computed based on a purely elastic response of the material :

$$\Delta\sigma_{ij}^{\prime e\ (k+1)} = C_{ijkl}^e(\sigma_{E,ij}^{\prime(k)})\Delta\varepsilon_{kl} \tag{7.39}$$

where C_{ijkl}^e is the elastic stiffness matrix and σ_E is the new stress state computed. As presented, non linear elasticity is a feature of this mechanical framework and thus the elastic stiffness matrix depends on the stress state. The stress state at the beginning of the time step is used to calculate the updated Young modulus to limit the non linearity in the elastic domain :

$$\sigma_{E,ij}^{\prime(k+1)} = \sigma_{A,ij}^{\prime} + \Delta\sigma_{ij}^{\prime e\ (k+1)} \tag{7.40}$$

where k is the iteration number.

7.3.2 Plastic corrector

When the trial stress violates one or more yield criteria, plastic strains are computed. A plastic potential function (cf. Eq. 7.17 and Eq. 7.30) defines their direction :

$$n_i = \frac{\partial g}{\partial\sigma_{ij}^{\prime}} \tag{7.41}$$

and the consistency equation (cf. Eq. 7.47) enables to determine their amplitude :

$$\Delta\varepsilon_{ij}^p = \Delta\lambda^p \frac{\partial g}{\partial\sigma_{ij}^{\prime}} \tag{7.42}$$

The mechanical framework used is composed of three yield criteria : a cohesive frictional failure mechanism, a tensile failure mechanism and the truncation of the tensile failure criterion at the apex. The integration algorithm has to be able to handle the activation of either criterion or of both at the same time.

Note that the different derivatives involved in the following equations can be found in Appendix B.

7.3.2.1 Activation of a single criterion

Let us consider that one yield surface f is activated. The updated stress state σ_B is determined iteratively by the application of Euler forward steps :

$$\sigma_{B,ij}^{\prime(k+1)} = \sigma_{B,ij}^{\prime(k)} + \Delta\sigma_{ij}^{\prime p\ (k+1)} \tag{7.43}$$

where $\Delta\sigma_{ij}^{\prime p\ (k+1)}$ is the plastic stress increment. The trial state is used as a starting point for the iterative process. The plastic strain increment is given by :

$$\Delta\sigma_{ij}^{\prime p\ (k+1)} = -C_{ijkl}^e(\sigma_{B,ij}^{\prime(k)})\Delta\varepsilon_{kl}^{p\ (k+1)} \tag{7.44}$$

where $\Delta\varepsilon_{kl}^{p\,(k+1)}$ is the plastic strain increment at iteration $(k+1)$ and is given by :

$$\Delta\varepsilon_{kl}^{p\,(k+1)} = \Delta\lambda^p \frac{\partial g}{\partial\sigma_{E,ij}^{'(k+1)}} \tag{7.45}$$

where $\Delta\lambda^p$ is the plastic multiplier and g is the flow rule associated to the yield surface f. At every iteration, the yield criterion is linearized around the current value of the trial stress and plastic state variables to compute the plastic multiplier increment. A first order Taylor series expansion is used to linearize the yield criterion. Note that the yield criterion is considered to only depend on the stress state and the plastic variables. This is different from the expression presented before (Eq. 7.5) because during the iterative process the suction does not change.

$$f_B^{(k+1)} = f(\sigma_{E,ij}^{'(k+1)} + \Delta\sigma_{ij}^{'p\,(k+1)}, \kappa_{E,m}^{(k+1)} + \Delta\kappa_m^{(k+1)}) \tag{7.46}$$

$$= f(\sigma_{E,ij}^{'(k+1)}, \kappa_{E,m}^{(k+1)}) + \frac{\partial f}{\partial\sigma_{E,ij}^{'(k+1)}} \Delta\sigma_{ij}^{'p\,(k+1)} + \frac{\partial f}{\partial\kappa_{E,m}^{(k+1)}} \Delta\kappa_m^{(k+1)} = 0 \tag{7.47}$$

Cohesive frictional failure mechanism activated   This is a deviatoric mechanism and its hardening rule depends on von Mises equivalent strain, ε_d^p. It is thus necessary to particularize a bit :

$$\Delta\varepsilon_d^{p\,(k+1)} = \Delta\lambda^{p\,1} val^1 \tag{7.48}$$

where val^1 is the relation between the plastic multiplier and the von Mises equivalent strain rate :

$$val^1 = \sqrt{\frac{2}{3}\left(\frac{\partial g^1}{\partial\sigma_{ij}'}\frac{\partial g^1}{\partial\sigma_{ji}'} - \frac{1}{3}\frac{\partial g^1}{\partial\sigma_{kk}'}\frac{\partial g^1}{\partial\sigma_{ll}'}\right)} \tag{7.49}$$

Also, $\Delta\kappa_m^{(k+1)}$ in Eq. 7.47 can be expressed as :

$$\Delta\kappa_m^{1\,(k+1)} = \frac{d\kappa_m^1}{d\varepsilon_{ij}^{p\,(k+1)}} \Delta\varepsilon_{ij}^{p\,(k+1)} = \Delta\lambda^p \frac{d\kappa_m^1}{d\varepsilon_d^{p\,(k+1)}} val^1 \tag{7.50}$$

By enforcing the consistency equation, $f_B^{1\,(k+1)} = 0$, it comes :

$$\Delta\lambda^{p\,1} = \frac{f(\sigma_{E,ij}^{'(k+1)}, \kappa_{E,m}^{1\,(k+1)})}{\frac{\partial f^1}{\partial\sigma_{E,ij}^{'(k+1)}} C_{ijkl}^e \frac{\partial g^1}{\partial\sigma_{E,ij}^{'(k+1)}} - \frac{\partial f^1}{\partial\kappa_{E,m}^{1\,(k+1)}} \frac{d\kappa_m^1}{d\varepsilon_d^{p\,(k+1)}} val^1} \tag{7.51}$$

and thus the stress state can be updated using Eq. 7.43

Tensile criterion activated   This mechanism depends on the volumic plastic strain and thus :

$$\Delta\varepsilon_v^{p\,(k+1)} = \Delta\lambda^p \frac{\partial g^2}{\partial\sigma_{E,ii}^{'(k+1)}} \tag{7.52}$$

And $\Delta\kappa_m^{(k+1)}$ in Eq. 7.47 can be expressed as :

$$\Delta\kappa_m^{2\,(k+1)} = \frac{d\kappa_m^2}{d\varepsilon_{ij}^{p\,(k+1)}} \Delta\varepsilon_{ij}^{p\,(k+1)} = \Delta\lambda^p \frac{d\kappa_m^2}{d\varepsilon_v^{p\,(k+1)}} \frac{\partial g^2}{\partial\sigma_{E,ii}^{'(k+1)}} \tag{7.53}$$

and again by enforcing the consistency equation, $f_B^{2\,(k+1)} = 0$, it comes :

$$\Delta\lambda^{p\,2} = \frac{f(\sigma_{E,ij}^{'(k+1)}, \kappa_{E,m}^{2\,(k+1)})}{\dfrac{\partial f^2}{\partial\sigma_{E,ij}^{'(k+1)}}C_{ijkl}^e \dfrac{\partial g^2}{\partial\sigma_{E,ij}^{'(k+1)}} - \dfrac{\partial f^2}{\partial\kappa_{E,m}^{2\,(k+1)}}\dfrac{d\kappa_m^2}{d\varepsilon_v^{p\,(k+1)}}\dfrac{\partial g^2}{\partial\sigma_{E,ii}^{'(k+1)}}} \tag{7.54}$$

and thus the stress state can be updated using Eq. 7.43.

7.3.2.2 Activation of two mechanisms

There is one case where two mechanisms can be activated at the same time : the Drucker-Prager criterion is activated at the same time as the tensile criterion. In the case where both failure mechanisms are activated at the same time, then the consistency equations have to be verified for both surfaces. One of the hypothesis of our model is that the two mechanisms are independent and the plastic deformation is thus :

$$\varepsilon_{ij}^p = \varepsilon_{ij}^{p\,1} + \varepsilon_{ij}^{p\,2} \tag{7.55}$$

The plastic variables of each yield surface are not influenced by the plastic strain caused by the other mechanism. Since both mechanisms are independent, the total plastic strain increment is the sum of the increments brought by each mechanism :

$$\Delta\varepsilon^p = \Delta\varepsilon^{p\,1} + \Delta\varepsilon^{p\,2} \tag{7.56}$$

$$= \Delta\lambda^{p\,1}\frac{\partial g^1}{\partial\sigma_{E,ij}^{'(k+1)}} + \Delta\lambda^{p\,2}\frac{\partial g^2}{\partial\sigma_{E,ij}^{'(k+1)}} \tag{7.57}$$

If we still consider that the yield surfaces only depend on the stress state and the plastic variables, a first order taylor series expansion for the two surfaces gives :

$$f^{1\,(k+1)} = f^1(\sigma_{E,ij}^{'(k+1)} + \Delta\sigma_{ij}^{'p\,(k+1)}, \kappa_{E,m}^{1\,(k+1)} + \Delta\kappa_m^{1\,(k+1)})$$
$$= f^1(\sigma_{E,ij}^{'(k+1)}, \kappa_{E,m}^{1\,(k+1)}) + \frac{\partial f^1}{\partial\sigma_{E,ij}^{'(k+1)}}\Delta\sigma_{ij}^{'p\,(k+1)} + \frac{\partial f^1}{\partial\kappa_{E,m}^{1\,(k+1)}}\Delta\kappa_m^{1\,(k+1)} \tag{7.58}$$

$$f^{2\,(k+1)} = f^2(\sigma_{E,ij}^{'(k+1)} + \Delta\sigma_{ij}^{'p\,(k+1)}, \kappa_{E,m}^{2\,(k+1)} + \Delta\kappa_m^{2\,(k+1)})$$
$$= f^2(\sigma_{E,ij}^{'(k+1)}, \kappa_{E,m}^{2\,(k+1)}) + \frac{\partial f^2}{\partial\sigma_{E,ij}^{'(k+1)}}\Delta\sigma_{ij}^{'p\,(k+1)} + \frac{\partial f^2}{\partial\kappa_{E,m}^{2\,(k+1)}}\Delta\kappa_m^{2\,(k+1)} \tag{7.59}$$

Given Eq. 7.44, Eq. 7.53 and Eq. 7.50 and by forcing the consistency conditions, it comes :

$$f^1 - \frac{\partial f^1}{\partial\sigma_{E,ij}^{'(k+1)}}C_{ijkl}^e\left(\Delta\lambda^{p\,1}\frac{\partial g^1}{\partial\sigma_{E,ij}^{'(k+1)}} + \Delta\lambda^{p\,2}\frac{\partial g^2}{\partial\sigma_{E,ij}^{'(k+1)}}\right)$$
$$+ \frac{\partial f^1}{\partial\kappa_{E,m}^{(1\,k+1)}}\frac{d\kappa_m^1}{d\varepsilon_d^{p\,1\,(k+1)}}\Delta\lambda^{p\,1}val^1 = 0 \tag{7.60}$$

$$f^2 - \frac{\partial f^2}{\partial\sigma_{E,ij}^{'(k+1)}}C_{ijkl}^e\left(\Delta\lambda^{p\,1}\frac{\partial g^1}{\partial\sigma_{E,ij}^{'(k+1)}} + \Delta\lambda^{p\,2}\frac{\partial g^2}{\partial\sigma_{E,ij}^{'(k+1)}}\right)$$
$$+ \frac{\partial f^2}{\partial\kappa_{E,m}^{2\,(k+1)}}\frac{d\kappa_m^2}{d\varepsilon_v^{p\,2\,(k+1)}}\Delta\lambda^{p\,2}\frac{\partial g^2}{\partial\sigma_{E,ii}^{'(k+1)}} = 0 \tag{7.61}$$

By solving this system of equations, the values of the plastic multipliers can be obtained :

$$\Delta\lambda^{p\,1} = \frac{f^1 - \Delta\lambda^{p\,2}\dfrac{\partial f^1}{\partial\sigma'^{(k+1)}_{E,ij}}C^e_{ijkl}\dfrac{\partial g^2}{\partial\sigma'^{(k+1)}_{E,ij}}}{\dfrac{\partial f^1}{\partial\sigma'^{(k+1)}_{E,ij}}C^e_{ijkl}\dfrac{\partial g^1}{\partial\sigma'^{(k+1)}_{E,ij}} - \dfrac{\partial f^1}{\partial\kappa^{1\,(k+1)}_{E,m}}\dfrac{d\kappa^1_i}{d\varepsilon^{p\,1\,(k+1)}_d}val^1} \tag{7.62}$$

$$\Delta\lambda^{p\,2} = \frac{f^2 - f^1\dfrac{\dfrac{\partial f^2}{\partial\sigma'^{(k+1)}_{E,ij}}C^e_{ijkl}\dfrac{\partial g^1}{\partial\sigma'^{(k+1)}_{E,ij}}}{\dfrac{\partial f^1}{\partial\sigma'^{(k+1)}_{E,ij}}C^e_{ijkl}\dfrac{\partial g^1}{\partial\sigma'^{(k+1)}_{E,ij}} - \dfrac{\partial f^1}{\partial\kappa^{1\,(k+1)}_{E,m}}\dfrac{d\kappa^1_m}{d\varepsilon^{p\,1\,(k+1)}_d}val^1}}{\dfrac{\partial f^2}{\partial\sigma'^{(k+1)}_{E,ij}}C^e_{ijkl}\dfrac{\partial g^2}{\partial\sigma'^{(k+1)}_{E,ij}} - \dfrac{\partial f^2}{\partial\kappa^{2\,(k+1)}_{E,m}}\dfrac{d\kappa^2}{d\varepsilon^{p\,2\,(k+1)}_v}\dfrac{\partial g^2}{\partial\sigma'^{(k+1)}_{E,ii}}}$$
$$+ \frac{\dfrac{\partial f^1}{\partial\sigma'^{(k+1)}_{E,ij}}C^e_{ijkl}\dfrac{\partial g^2}{\partial\sigma'^{(k+1)}_{E,ij}}\dfrac{\partial f^2}{\partial\sigma'^{(k+1)}_{E,ij}}C^e_{ijkl}\dfrac{\partial g^1}{\partial\sigma'^{(k+1)}_{E,ij}}}{\dfrac{\partial f^1}{\partial\sigma'^{(k+1)}_{E,ij}}C^e_{ijkl}\dfrac{\partial g^1}{\partial\sigma'^{(k+1)}_{E,ij}} - \dfrac{\partial f^1}{\partial\kappa^{1\,(k+1)}_{E,m}}\dfrac{d\kappa^1_m}{d\varepsilon^{p\,1\,(k+1)}_d}val^1} \tag{7.63}$$

These expressions are, however, only true if both multipliers are positive. Otherwise, if one of the values is negative, the corresponding mechanism should not be activated and the calculus must be redone with only the other surface active.

Activation of the tensile criterion at the apex   The truncation yield surface introduced to solve the apex problem is considered to be a part of the tensile strength criterion and as such the two mechanisms are not independent since they both depend on the volumetric plastic strain and they share the same plastic variables :

$$\Delta\kappa^{(k+1)}_m = \frac{d\kappa_m}{d\varepsilon^{p\,(k+1)}_v}\Delta\varepsilon^{p\,(k+1)}_v \tag{7.64}$$

$$= \frac{d\kappa_m}{d\varepsilon^{p\,(k+1)}_v}(\Delta\varepsilon^{p\,2}_v + \Delta\varepsilon^{p\,5}_v) \tag{7.65}$$

$$= \frac{d\kappa_m}{d\varepsilon^{p\,(k+1)}_v}(\Delta\lambda^{p\,2}\frac{\partial g^2}{\partial\sigma'^{(k+1)}_{E,ii}} + \Delta\lambda^{p\,5}\frac{\partial g^5}{\partial\sigma'^{(k+1)}_{E,ii}}) \tag{7.66}$$

Similarly to the previous section, a first order Taylor series expansion for the two surfaces is used to linearize the expressions :

$$f^{2\,(k+1)} = f^2(\sigma'^{(k+1)}_{E,ij} + \Delta\sigma'^{p\,(k+1)}_{ij}, \kappa^{(k+1)}_{E,m} + \Delta\kappa^{(k+1)}_m)$$
$$= f^2(\sigma'^{(k+1)}_{E,ij}, \kappa^{(k+1)}_{E,m}) + \frac{\partial f^2}{\partial\sigma'^{(k+1)}_{E,ij}}\Delta\sigma'^{p\,(k+1)}_{ij} + \frac{\partial f^2}{\partial\kappa^{(k+1)}_{E,m}}\Delta\kappa^{(k+1)}_m \tag{7.67}$$

$$f^{5\,(k+1)} = f^5(\sigma'^{(k+1)}_{E,ij} + \Delta\sigma'^{p\,(k+1)}_{ij}, \kappa^{(k+1)}_{E,m} + \Delta\kappa^{(k+1)}_m)$$
$$= f^5(\sigma'^{(k+1)}_{E,ij}, \kappa^{(k+1)}_{E,m}) + \frac{\partial f^5}{\partial\sigma'^{(k+1)}_{E,ij}}\Delta\sigma'^{p\,(k+1)}_{ij} + \frac{\partial f^5}{\partial\kappa^{(k+1)}_{E,m}}\Delta\kappa^{(k+1)}_m \tag{7.68}$$

Given Eq. 7.44 and Eq.7.66 and by forcing the consistency conditions, it comes :

$$f^2 - \frac{\partial f^2}{\partial \sigma_{E,ij}'^{(k+1)}} C_{ijkl}^e \left(\Delta\lambda^{p\,2} \frac{\partial g^2}{\partial \sigma_{E,ij}'^{(k+1)}} + \Delta\lambda^{p\,5} \frac{\partial g^5}{\partial \sigma_{E,ij}'^{(k+1)}} \right)$$

$$+ \frac{\partial f^2}{\partial \kappa_{E,m}^{(k+1)}} \frac{d\kappa_m}{d\varepsilon_v^{p\,2\,(k+1)}} \left(\Delta\lambda^{p\,2} \frac{\partial g^2}{\partial \sigma_{E,ii}'^{(k+1)}} + \Delta\lambda^{p\,5} \frac{\partial g^5}{\partial \sigma_{E,ii}'} \right) = 0 \qquad (7.69)$$

$$f^5 - \frac{\partial f^5}{\partial \sigma_{E,ij}'^{(k+1)}} C_{ijkl}^e \left(\Delta\lambda^{p\,2} \frac{\partial g^2}{\partial \sigma_{E,ij}'^{(k+1)}} + \Delta\lambda^{p\,5} \frac{\partial g^5}{\partial \sigma_{E,ij}'^{(k+1)}} \right)$$

$$+ \frac{\partial f^5}{\partial \kappa_{E,m}^{(k+1)}} \frac{d\kappa_m}{d\varepsilon_v^{p\,(k+1)}} \left(\Delta\lambda^{p\,2} \frac{\partial g^2}{\partial \sigma_{E,ii}'^{(k+1)}} + \Delta\lambda^{p\,5} \frac{\partial g^5}{\partial \sigma_{ii}'} \right) = 0 \qquad (7.70)$$

And solving this system of equations gives :

$$\Delta\lambda^{p\,2} = \frac{f^2 - \Delta\lambda^{p\,5} \left(\frac{\partial f^2}{\partial \sigma_{E,ij}'^{(k+1)}} C_{ijkl}^e \frac{\partial g^5}{\partial \sigma_{E,ij}'^{(k+1)}} - \frac{\partial f^2}{\partial \kappa_{E,m}^{(k+1)}} \frac{d\kappa_m}{d\varepsilon_v^{p\,2\,(k+1)}} \frac{\partial g^5}{\partial \sigma_{E,ii}'^{(k+1)}} \right)}{\frac{\partial f^2}{\partial \sigma_{E,ij}'^{(k+1)}} C_{ijkl}^e \frac{\partial g^2}{\partial \sigma_{E,ij}'^{(k+1)}} - \frac{\partial f^2}{\partial \kappa_{E,m}^{(k+1)}} \frac{d\kappa_m}{d\varepsilon_v^{p\,2\,(k+1)}} \frac{\partial g^2}{\partial \sigma_{E,ii}'^{(k+1)}}} \qquad (7.71)$$

$$\Delta\lambda^{p\,5} = \frac{f^5 - f^2 \left(\dfrac{\frac{\partial f^5}{\partial \sigma_{E,ij}'^{(k+1)}} C_{ijkl}^e \frac{\partial g^2}{\partial \sigma_{E,ij}'^{(k+1)}} - \frac{\partial f^5}{\partial \kappa_{E,m}^{(k+1)}} \frac{d\kappa_m}{d\varepsilon_v^{p\,5\,(k+1)}} \frac{\partial g^2}{\partial \sigma_{E,ii}'^{(k+1)}}}{\frac{\partial f^2}{\partial \sigma_{E,ij}'^{(k+1)}} C_{ijkl}^e \frac{\partial g^2}{\partial \sigma_{E,ij}'^{(k+1)}} - \frac{\partial f^2}{\partial \kappa_{E,m}^{(k+1)}} \frac{d\kappa_m}{d\varepsilon_v^{p\,2\,(k+1)}} \frac{\partial g_2}{\partial \sigma_{E,ii}'^{(k+1)}}} \right)}{\frac{\partial f^5}{\partial \sigma_{E,ij}'^{(k+1)}} C_{ijkl}^e \frac{\partial g^5}{\partial \sigma_{E,ij}'^{(k+1)}} - \frac{\partial f^5}{\partial \kappa_{E,m}^{(k+1)}} \frac{d\kappa}{d\varepsilon_v^{p\,5\,(k+1)}} \frac{\partial g^5}{\partial \sigma_{E,ii}'^{(k+1)}}}$$

$$+ \frac{\left(\frac{\partial f^2}{\partial \sigma_{E,ij}'^{(k+1)}} C_{ijkl}^e \frac{\partial g^5}{\partial \sigma_{E,ij}'^{(k+1)}} - \frac{\partial f^2}{\partial \kappa_{E,m}^{(k+1)}} \frac{d\kappa_m}{d\varepsilon_v^{p\,2(k+1)}} \frac{\partial g^5}{\partial \sigma_{E,ii}'^{(k+1)}} \right) \left(\frac{\partial f^5}{\partial \sigma_{E,ij}'^{(k+1)}} C_{ijkl}^e \frac{\partial g^2}{\partial \sigma_{E,ij}'^{(k+1)}} - \frac{\partial f^5}{\partial \kappa_{E,m}^{(k+1)}} \frac{d\kappa_m}{d\varepsilon_v^{p\,5(k+1)}} \frac{\partial g^2}{\partial \sigma_{E,ii}'^{(k+1)}} \right)}{\frac{\partial f^2}{\partial \sigma_{E,ij}'^{(k+1)}} C_{ijkl}^e \frac{\partial g^2}{\partial \sigma_{E,ij}'^{(k+1)}} - \frac{\partial f^2}{\partial \kappa_{E,m}^{(k+1)}} \frac{d\kappa_m}{d\varepsilon_v^{p\,2\,(k+1)}} \frac{\partial g^2}{\partial \sigma_{E,ii}'^{(k+1)}}}$$

$$(7.72)$$

7.3.3 Convergence condition

Convergence is reached when the consistency conditions are verified :

$$f\big(\sigma_B^{(k+1)}, \kappa_B^{(k+1)}\big) \approx 0 \qquad (7.73)$$

The convergence condition is written in terms of the ratio of the stress increment between two iterations k and k+1 :

$$1 - Prec \le max\left| \frac{\sigma_{ij}'^{(k+1)}}{\sigma_{ij}'^{(k)}} \right| \le 1 + Prec \qquad (7.74)$$

A value of $Prec = 10^{-5}$ has been chosen so that the convergence is reached when the relative variation between two iterations is inferior to 0.001%. The force of this type of convergence condition is that it is independent from the problem and the unit system.

7.3.4 Substepping procedure

The cutting plane algorithm is known to be first-order accurate. During large loading steps where yielding occurs, difficulties may appear in returning back to the yield surface. In such situations, a possible strategy is to use smaller time steps in the global resolution algorithm. However, this solution is not reasonable since the most restrictive integration point will control the global problem. An alternative approach consists in subdividing locally the current time step into several sub-steps (which can be different for each integration point). A sub-stepping procedure is used in the integration of the model within LAGAMINE. A time step Δt is divided into $NINTV$ sub-steps δt :

$$\delta t = \frac{\Delta t}{NINTV} \tag{7.75}$$

and strain is supposed to vary linearly over the time step and thus :

$$\delta \varepsilon_{ij} = \frac{\Delta \varepsilon_{ij}}{NINTV} \tag{7.76}$$

The value of $NINTV$ is computed according to the current normal strain rate, $\dot{\varepsilon}_N$:

$$NTINV = min\left(1 + \frac{\dot{\varepsilon}_N \Delta t}{DIV}, 100\right) \tag{7.77}$$

where DIV is a parameter of the law (a value of 5.10^{-4} most usually provides good results). The normal strain rate is given by :

$$\dot{\varepsilon}_N = \sqrt{\dot{\varepsilon}_{ij}\dot{\varepsilon}_{ij}} \tag{7.78}$$

For each integration point, the number of sub-steps is computed according to the strain rate which means the number of sub-steps is higher where the strains are the most important leading to a more accurate integration of the model.

7.4 Validation

In this section, simple simulations are performed to ensure that the implemented tensile criterion behaves correctly. The tests are performed on a cylindrical sample of 1 cm of height and 1 cm of radius represented by a single element. The simulations performed hereafter use the following set of parameters (cf. Tables 7.1 to 7.3).

Degree of Freedom	Values	Units
$p_{w,ini}$	100	[kPa]
$p_{g,ini}$	100	[kPa]
T_{ini}	20	[° C]

Table 7.1: Initial conditions

Parameters	Values	Units
Hydraulic parameters		
k	5.10^{-17}	$[m^2]$
n	0.7576	$[-]$
τ	0.1	$[-]$
van Genuchten parameters		
α_{vG}	8	$[MPa]$
n_{vG}	2.1	$[-]$
S_{sat}	1	$[-]$
S_{res}	0.00	$[-]$
$k_{r,min}$	10^{-7}	$[-]$

Table 7.2: Hydraulic model parameters

Parameters	Values	Units
E	30	$[MPa]$
ν	0.25	$[-]$
G	18.75	$[MPa]$
σ'_t	0.6	$[MPa]$
Ψ_2	10	$[\check{r}]$

Table 7.3: Mechanical law parameters

7.4.1 Plane strain uniaxial traction test

Plane strain uniaxial simulations are performed. The sample is stretched in the vertical (y) direction at a rate of $10^{-8}m/s$ or $10-4\%$ of axial strain per second. The goal of this reference simulation is to ensure that the material reaches the yield surface for the right value of σ_y.
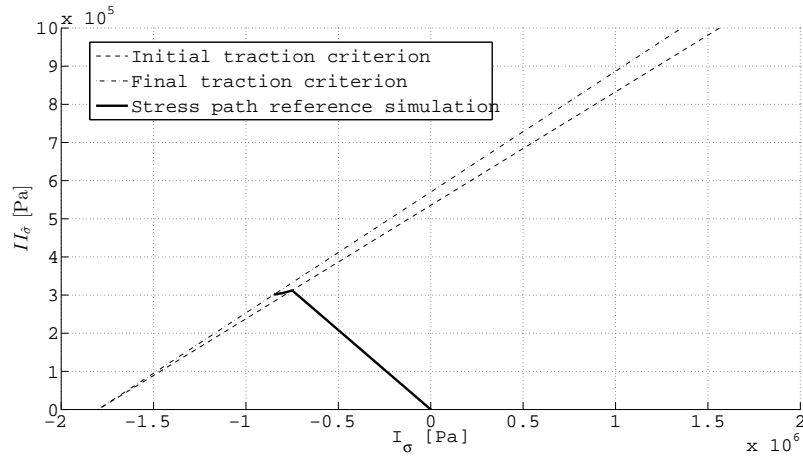

Figure 7.10: Stress path followed during a plane strain uniaxial tension test

Reference simulation Fig. 7.10 shows the stress path followed. The stress path reaches the tensile failure criterion and stays on it as expected. It also shows the evolution of the tensile strength criterion with Lode's angle.
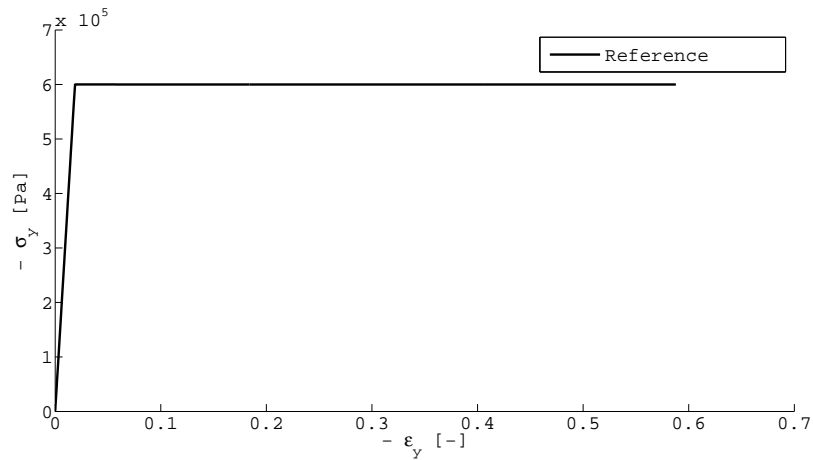

Figure 7.11: Evolution of the vertical stress with the vertical strain

Fig. 7.11 shows the evolution of the vertical stress with the vertical strain. A constant vertical stress is reached and corresponds to the chosen tensile strength. This confirms that a perfectly plastic state is reached as expected.

We also performed simulations with different fixed time steps to check the stability of our law. The simulations were performed with fixed time steps of 1 s ($10^{-4}\%$ of axial strain per step), 10 s ($10^{-3}\%$ of axial strain per step), 100 s (0.01% of axial strain per step), 1000 s (0.1% of axial strain per step). The substepping was, of course, prevented. The results in terms of axial stress, σ_y, for the different time steps were compared to the ones obtained for a time step of 1 second at different chosen total axial strains in the plastic range (1%, 5% and 10% of total axial strain). The following errors are obtained (cf. Table 7.4):

Total axial strain / Strain per time step	1%	5%	10%
$10^{-3}\ \%/s$	0	0	0
$0.01\ \%/s$	0	0	0
$0.1\ \%/s$	0	0	0

Table 7.4: Error related to a change in strain per step for a uniaxial tension test

As can be seen in Table 7.4, there is no dependence of the results on the size of the time step and thus on the "strain step". This is reassuring since these simulations lead to a perfectly plastic state with no possibility to move on the yield criterion which is thus a very stable state and wouldn't justify any variation between simulations.

Undrained The same simulation was performed but this time in undrained conditions. The material was considered to have a dilatancy angle of $10°$ for the tensile criterion. The stress path is visible in Fig. 7.12.
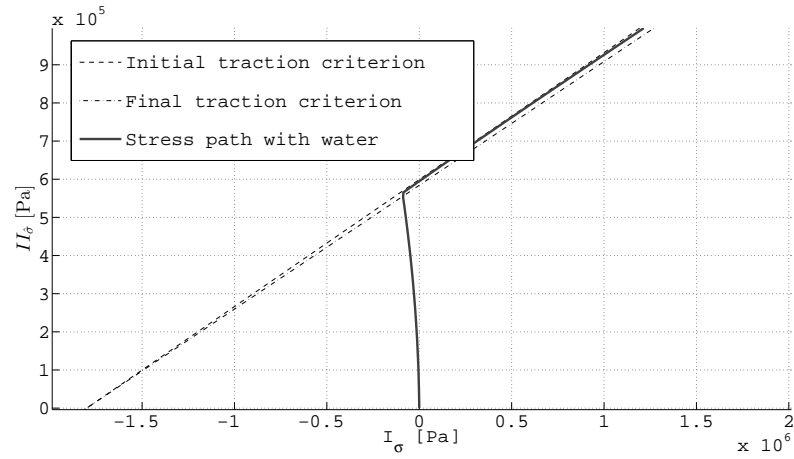
154

Figure 7.12: Stress path followed during a plane strain undrained uniaxial tension test on a dilatant material

The stress path reaches the yield criterion then moves on it with an increasing first invariant because of the dilatancy. Once again the influence of Lode's angle can be seen in the change of slope of the yield criterion. The simulation still leads to a perfectly plastic state as visible on Fig. 7.13. The error was once again calculated using the same method and the following results
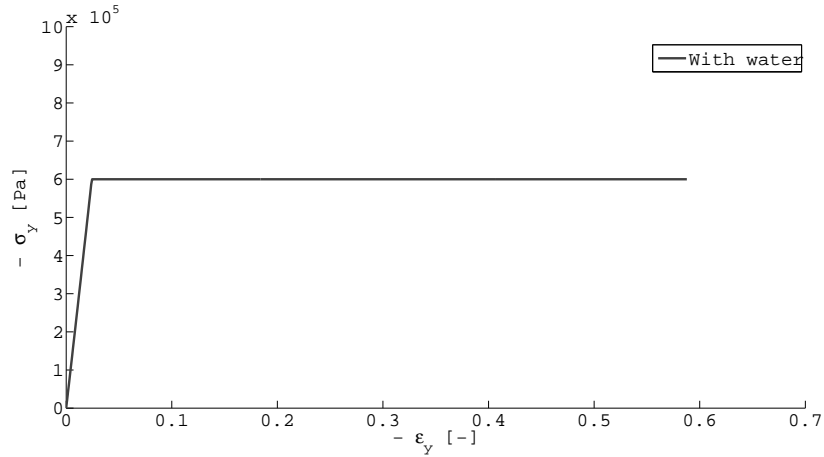

Figure 7.13: Evolution of the vertical stress with the vertical strain

are obtained (cf. Table 7.5) As can be seen in table 7.5, the error stays small overall. Note that the bigger "strain step" simulations are actually more accurate than the smaller ones. As can be seen on Fig. 7.14, the smaller strain step simulations present shear stresses which are, in this case, a sign of a loss of homogeneity on the element. It has been shown by Crochepeyre (1998) that smaller step simulations tend to localize faster than bigger step ones. The calculated error is thus due to that loss of homogeneity. This kind of simulation can also be used to check the capacity of the model to handle the switch from the tensile criterion to the Drucker-Prager. Indeed the dilantacy imposed leads to an increasing first invariant of the stress tensor and the stress state moves on the tensile criterion toward the Drucker-Prager criterion and then switches criterion as shown in Fig. 7.15. In this case, the Drucker Prager criterion parameters were

155

Total axial strain / Strain per time step	1%	5%	10%
$10^{-3}\ \%/s$	$1.936\ 10^{-6}$	$2.422\ 10^{-7}$	$7.264\ 10^{-7}$
$0.01\ \%/s$	$7.141\ 10^{-6}$	$3.918\ 10^{-4}$	$3.634\ 10^{-4}$
$0.1\ \%/s$	$2.093\ 10^{-5}$	$3.830\ 10^{-4}$	$3.585\ 10^{-4}$

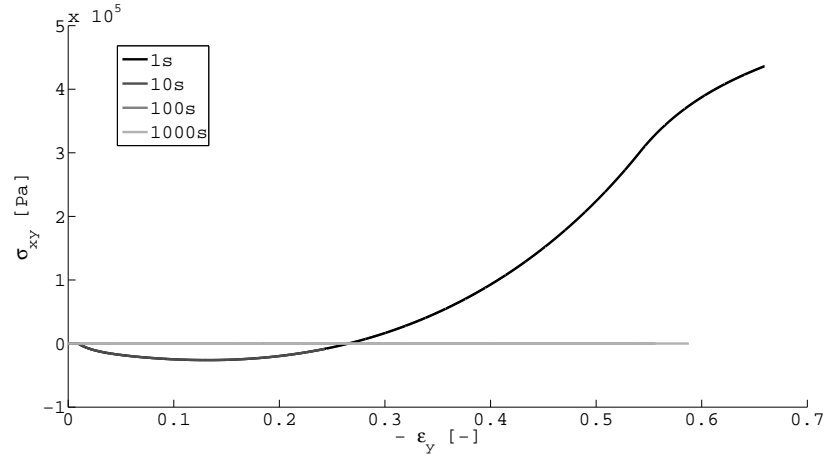Table 7.5: Error related to a change in strain per step for a uniaxial tension test with water

Figure 7.14: Evolution of the shear stress with the axial strain for the different "strain steps"

arbitrarily chosen and are visible in Table 7.6

Undrained with softening The same simulation was once more performed, this time adding softening. The uniaxial tensile strength of the material changes from its initial value to zero with a softening rate of $\beta_{\sigma_t} = 5.10^{-2}$. The stress path is visible in Fig. 7.16.

As can been seen, the yield criterion changes with the variation of the tensile strength and the stress path follows accordingly. Fig. 7.17 shows the evolution of the vertical stress and a clear decrease due to the softening can be clearly observed. The error was once again calculated using the same method and the following results are obtained (cf. Table 7.7). Softening leads to a less stable situation since the stress state keeps on evolving during the simulation. The errors are thus globally more important but the conclusion drawn for the undrained case remains for this simulation as the lower step simulations also exhibit shear stresses (cf. Fig. 7.18) :

Different softening rates have been tested. Eq. 7.32 and Eq. 7.33 govern the hardening rule in which "speed" is controlled by the parameter β_{σ_t}. Value of $\beta_{\sigma_t} = 0.5$, $\beta_{\sigma_t} = 0.05$ and $\beta_{\sigma_t} = 0.005$ have been tested. The evolution of the vertical strength with the vertical strain

Parameters	Values	Units
c	1	$[MPa]$
ϕ	18	$[°]$

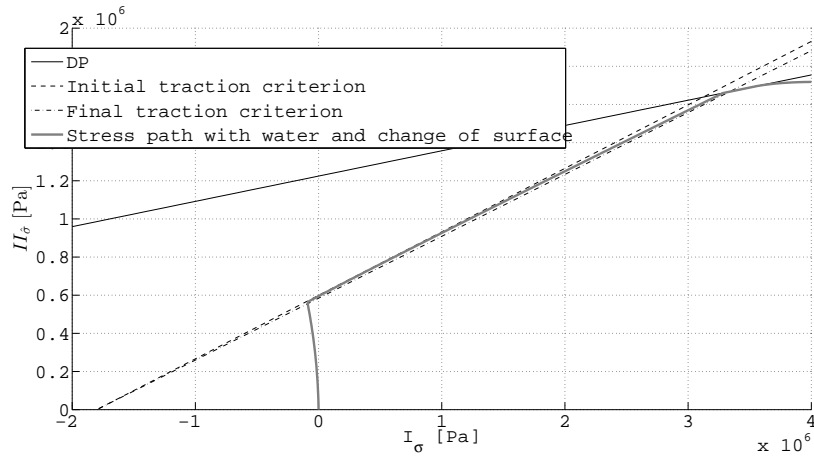Table 7.6: Mechanical law parameters

Figure 7.15: Stress path followed during a plane strain undrained uniaxial tension test on a dilatant material when both criteria are active
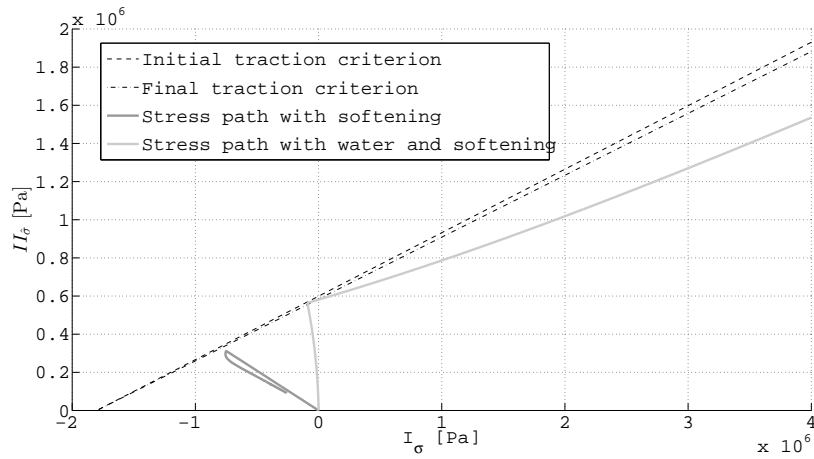

Figure 7.16: Stress path followed during a plane strain undrained uniaxial tension test on a dilatant material

Strain per time step	Total axial strain		
	1%	5%	10%
10^{-3} %/s	$1.153 \ 10^{-5}$	$2.833 \ 10^{-4}$	$5.216 \ 10^{-4}$
0.01 %/s	0.002	0.062	0.014
0.1 %/s	0.002	0.062	0.014

Table 7.7: Error related to a change in strain per step for an uniaxial tension test with water and softening

exhibits the influence of β_{σ_t} (cf. Fig. 7.19). The smaller the value of β_{σ_t} the faster the softening as expected from Eq. 7.32 and Eq. 7.33. Smaller values are not available because they lead to a loss of the homogeneity over the element as visible for the curve corresponding to $\beta_{\sigma_t} = 0.005$ in Fig. 7.19.
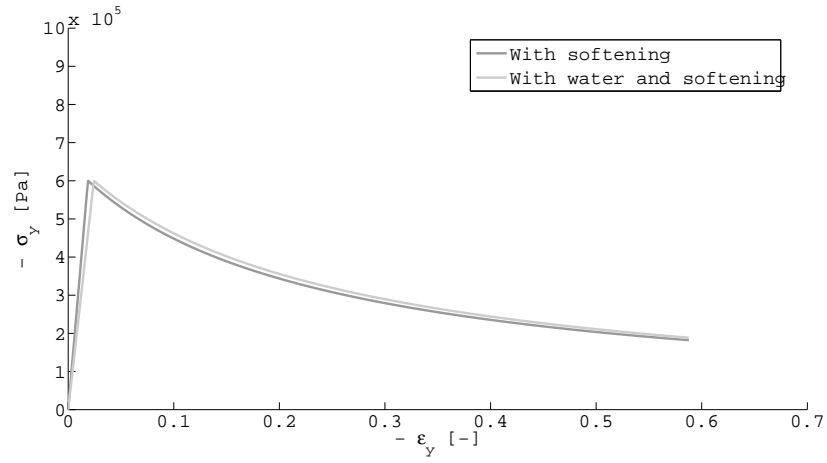
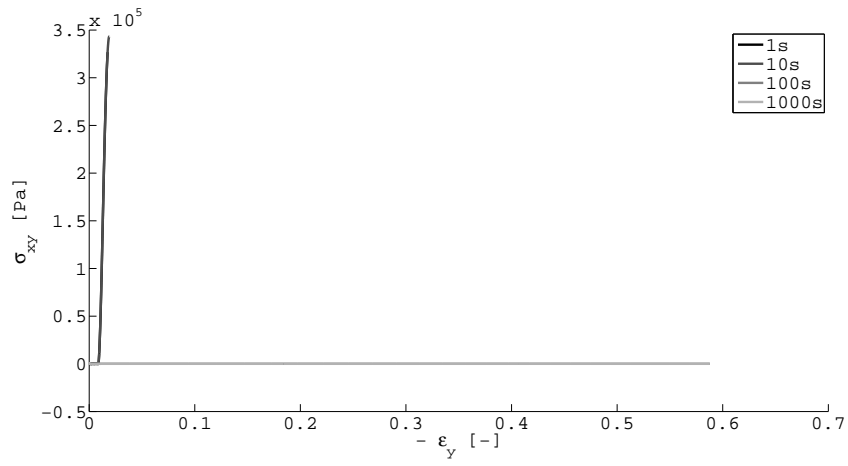Figure 7.17: Evolution of the vertical stress with the vertical strain

Figure 7.18: Evolution of the shear stress with the axial strain for the different "strain steps" in the case with softening
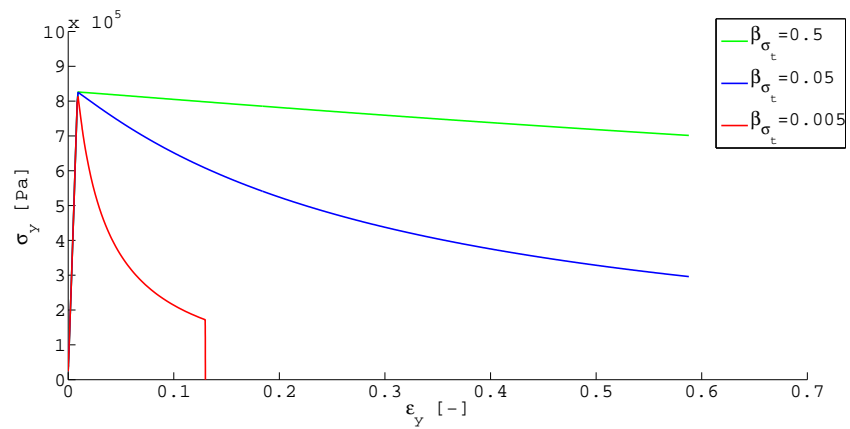

Figure 7.19: Influence of β_{σ_t} on the softening rate

7.4.2 Triaxial traction test

The same uniaxial traction test was conducted in axisymmetric conditions to ensure that the law was compatible with those conditions. The stress path is visible at Fig. 7.20 and the evolution of the vertical stress with the vertical strain at Fig. 7.21. The stress path is a bit different because in this case $\sigma_2 = \sigma_3$. Also in this case, Lode's angle remains constant.
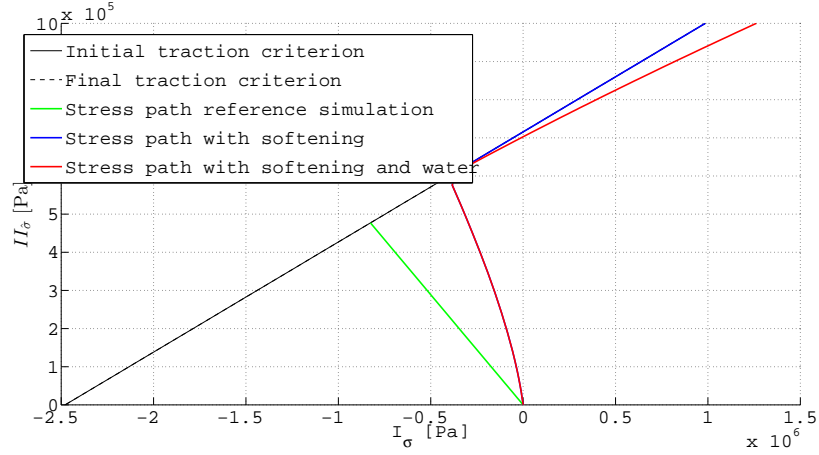

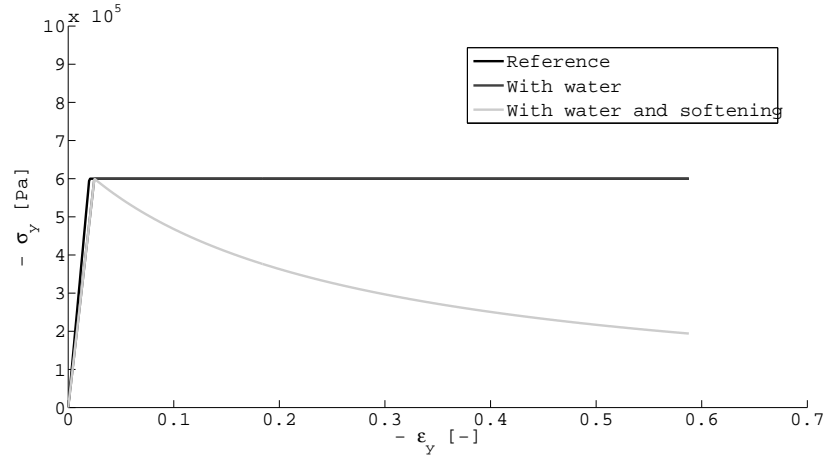Figure 7.20: Stress path followed in axisymmetric conditions

Figure 7.21: Evolution of the vertical stress with the vertical strain in axisymmetric conditions

Overall, the simulations behaved as expected and in complete accordance with previous analysis.

7.4.3 Lateral tension triaxial test

In triaxial conditions, another simulation was performed. The geometry, mesh and properties all remained unchanged but now the sample is pulled laterally. This kind of loading is chosen because it will lead to the stress path the closest to the one followed during desiccation cracking. The stress compensation mechanism resulting from prevented radial shrinkage leads to radial

tensile stresses just as in this configuration. In this configuration, Lode's angle is going to remain constant at a value of $30°$. Referring to Appendix B, the derivatives of the tensile failure yield criterion and flow rule are not defined for $\beta = \pm 30°$. Yet this is a configuration we need to be able to solve so we defined a small interval of Lode's angle, $\Delta\beta \pm 0.5°$, around the value of $30°$ and in that interval, we decided to locally remove the dependency of the yield criterion and of the flow rule to Lode's angle. Even though this leads to small oscillations around the correct solution, it allows to find the solution to an otherwise unsolvable problem.
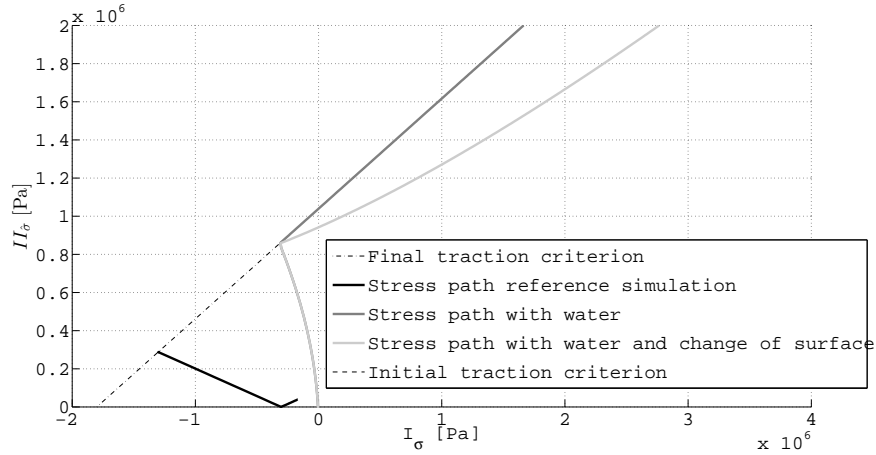

Figure 7.22: Stress path followed in axysymmetric conditions with lateral tension
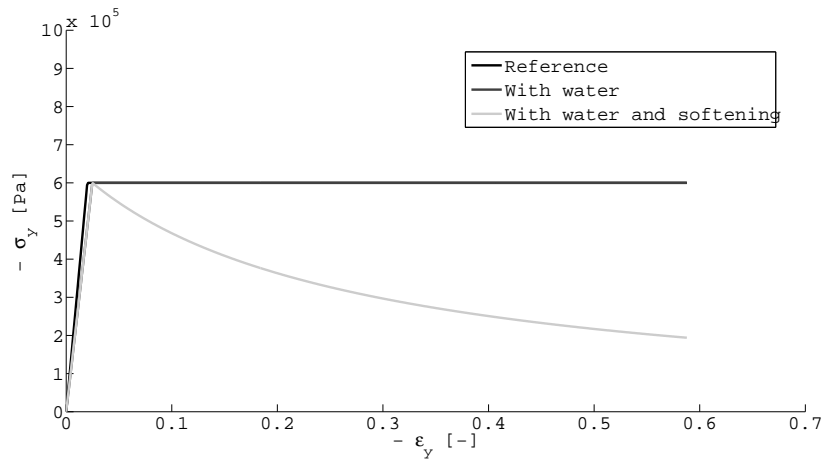

Figure 7.23: Evolution of the vertical stress with the vertical strain in axisymmetric conditions with lateral tension

As can be seen on both Fig. 7.22 and Fig. 7.23 the model behaves correctly.

7.5 Conclusion

In this chapter, we presented the mechanical constitutive model chosen. It is an elasto-plastic model with non linear elasticity. The plastic part is controlled by three yield criteria : a cohesive frictional criterion which is a Drucker-Prager yield surface, a tensile failure criterion

and its truncation at the apex. The implementation of the truncated tensile criterion in the in house-built finite element method code LAGAMINE is detailed from the calculation of the elastic predictor to the plastic corrector and the convergence conditions. A substepping procedure is also used to divide the time step into several sub-steps which can be different for each integration point. Finally a short validation of the tensile criterion is presented to make sure that it behaves as expected. A simple uniaxial tension test is performed over a 1 element mesh in different conditions to ensure that the criterion is reached for the right value of the tensile strength and that the switch from one yield criterion to the other occurs correctly. Time step related errors are also calculated to evaluate the stability of the law. In the next chapter, the model implemented is applied to convective drying simulations to try to predict desiccation cracking.

Chapter 8

Resorcinol Formaldehyde gel desiccation cracking

Contents

8.1 Introduction

In the previous two chapters, we introduced the notion of tensile strength as well as a tensile failure criterion and detailed its implementation into a finite element code. At last, the model described and implemented in previous chapter is used to predict desiccation cracking.

When we studied the drying behavior of a porous medium, we chose Boom clay as a validating material because of its potential application and well documented properties. Even though

Boom clay samples crack during convective drying experiment, cracks always occur along the bedding planes of the material (cf. Chapter 5). It is therefore not an ideal material to validate an isotropic desiccation cracking model like the one we implemented. A new material is thus required and Resorcinol (R) Formaldehyde (F) hydrogels have been chosen. They have been chosen because they are synthetic materials which properties are well controlled and as isotropic and homogeneous as possible. Also, this thesis is a part of a F.R.S. - FNRS project co-supported by teams of the geomechanical (GEO3) and chemical engineering (LGC) departments of the university of Liège. The LGC conducted previous work on RF hydrogels and is interested in being able to predict crack formation. These factors make them a suitable candidate for the validation of our model.

This chapter starts by a literature review on the new material chosen from its origin and synthesis to applications and known properties. Specifically, the experimental campaign conducted by Léonard et al. (2008) and Job et al. (2006b) are detailed as they are used as reference for material properties and drying behavior. Then, the experimental campaign we conducted to confirm the literature properties or to investigate undocumented ones is presented. Finally convective drying simulations are performed to evaluate the capacity of our model to predict desiccation cracking.

8.2   Definition

Gel   Gels are a unique class of materials, which exhibit solid-like behavior resulting from a continuous, three-dimensional framework extending throughout a liquid. This framework consists of molecules interconnected through multifunctional junctions. These junctions can be formed through covalent crosslinking, crystallization, ionic interactions, hydrogen bonding, or chain entanglements. In some cases, junction formation is reversible and the gels revert to liquid-like behaviour upon a change in temperature (Pekala (1989)).

Hydrogel   Hydrogels are materials made up of hydrophilic polymer chains held together via cross-links to form a solid, three-dimensional network and may contain large amounts of water (Warren et al. (2017)). Basically there are gels in which the dispersed phase is specifically water. Because of the inherent cross-links, the structural integrity of the hydrogels network does not dissolve from the high concentration of water.

Aerogel   Aerogels are gels in which the liquid component for the gel has been replaced by a gas (Alemán et al. (2007)). The gel is dried under supercritical conditions. In consequence, the network does not shrink and a highly porous, low-density material known as an aerogel is produced.

Xerogel   Xerogels are gels in which the liquid component has been removed by convective drying (with unhindered shrinkage). Xerogels usually retain high porosity ($15 - 50\%$) and enormous surface area ($150 - 900 m^2/g$), along with very small pore size ($1 - 10 nm$). They are similar to aerogel except that the solvent removal does not occur under supercritical conditions (Alemán et al. (2007)).

8.3   Resorcinal formaldehyde hydrogel

The resorcinol formaldehyde hydrogels have been discovered by Pekala in 1989 (Pekala (1989)). In his work, Pekala stated that the polycondensation of resorcinol with formaldehyde under alkaline conditions results in " *the formation of surface functionalized polymer clusters* ". The covalent crosslinking of these clusters creates a 3D framework filled with liquid i.e. a gel. The hydrogels are dark red in colour and consist of interconnected colloidal-like particles with diameters of approximately 10 nm. They can be produced in densities ranging from 0.035 to 0.100 g/cm^3. A schematic diagram of the RF gelation mechanism is presented at Fig. 8.1.
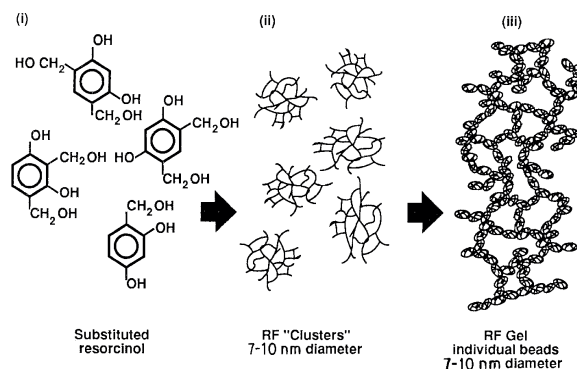

Figure 8.1: Schematic diagram of the RF gelation process (Pekala (1989))

In this case, the hydrogel is just an intermediate phase in materials processing and Pekala (1989) used supercritical drying condition to obtain low density, organic aerogels ($< 0.1 \, g/cm^3$). Supercritical drying was used because of the small cell size ($< 50nm$) of the gel. Large capillary forces at the liquid-vapour interface cause the gel to shrink or crack if the solvent was removed by evaporation. In the case of supercritical drying, no surface tension is exerted across the pores, and the dry aerogel retains the original morphology of the hydrogel. Nonetheless, Pekala (1989) also stated in his original article that even though the aerogels were obtained by supercritical drying, they still experienced some shrinkage. This was exhibited through a higher than expected density of the aerogels. He also noticed that the amount of shrinkage was dependent on the catalyst level during the synthesis process. This suggests that there exists differences in the size, distribution, interpenetration and chemical linking of the RF clusters depending on reaction conditions. That assumption was confirmed by Brunauer–Emmett–Teller (Brunauer et al. (1938)) adsorption analysis which exhibited substantial differences depending on the gel formulation. The surface area decreased with the catalyst level. The level of catalyst is evaluated through the ratio of resorcinol (R) over catalyst (C) or R/C ratio.

The material has been studied because its large mesopore volumes ($5cm^3/g$) and high specific surface areas ($500 - 1000m^2/g$) make it interesting for many potential industrial applications such as catalysts supports, adsorband material, lithium-ion batteries electrods, thermal isolant, etc [Job (2005)]. It is an interresting alternative to activated carbon because it is a synthetic material which means its structure and properties can be accurately and reliably chosen. The main limitation of the process introduced by Pekala (1989) is the supercritical drying of the hydrogel. Supercritical drying is not applicable at an industrial scale because of technical (cost) and safety reasons. Some other methods to produce an aerogel-like mesoporous texture

have been tested and it has been shown (Job et al. (2006b)) that it is possible to produce porous resorcinol–formaldehyde xerogels by using atmospheric convective drying which suppresses the main limitation of the process. Nonetheless the convective drying of the gels can, depending of the synthesis and drying conditions lead to desiccation cracking (Job (2005)).

Since crack-free monoliths are required, investigating the drying behavior of the RF hydrogels is an important issue. (Job (2005)) in her PhD thesis thoroughly studied the drying behavior of the resorcinol formaldehyde hydrogels and the following is a summary of the properties obtained throughout her thesis.

8.3.1 Mechanical properties

The R/C ratio has an influence on the polymerization mechanism (Job et al. (2004)) through the pH of the solution and thus on the mechanical of the RF hydrogels. The properties also depend on the water content of the gels.

Léonard et al. (2008) investigated a range of mechanical properties at different water content and for different R/C ratio.

Sample preparation   Hydrogels were obtained by polycondensation of resorcinol solubilized in water with formaldehyde in the presence of Na_2CO_3 acting as a catalyst (C). Cylindrical samples were obtained by casting 5ml of the solution into glass molds of 22mm of diameter and putting them for curing under saturated atmosphere in an oven for 24h. Forced convection in the oven allowed high level of heat transfer during gelation. After gelation, the water content on a dry basis, W, was determined and was, for all the samples, close to 2 kg/kg. R/C ratios of 300, 600, 750, 900, 1200, 1500 were considered.

Young modulus   The Young modulus of the gels was determined by compressive axial loading of cylindrical samples and simultaneous measurement of corresponding deformation. Since the Young modulus varies with the water content, the samples were brought to a series of desired water contents which were obtained by ambient drying of the samples in order to limit internal moisture gradients. As the gelation was totally completed, only water is removed, and the samples remain in a monolithic shape. The gels were charged up to 700 N with a loading rate of 0.5 N/s. Two replicates were used for each R/C ratio. The results (cf. Fig. 8.2) pointed that the orginal Young modulus of RF hydrogels is not dependent on the R/C ratio. The stiffening experienced by the sample as they dry is, on the other hand, strongly influenced. The final Young modulus of RF xerogel increases with decreasing R/C ratio.

Poisson ratio   Mercury porosimetry, which is usually used to determine the pore size distribution (Washburn (1921)), is affected by a peculiar behavior in the case of RF samples (Job et al. (2004); Léonard et al. (2005b)). For this material, the pore size distribution cannot be obtained in a straightforward manner due to the collapse of the sample under mercury pressure (Job et al. (2006a)). Nevertheless the data allow to determine the compression modulus of the network according to Scherer's methodology (Scherer et al. (1995)). Combination of the results obtained from the axial compression tests, on the dried samples, and the mercury porosimetry
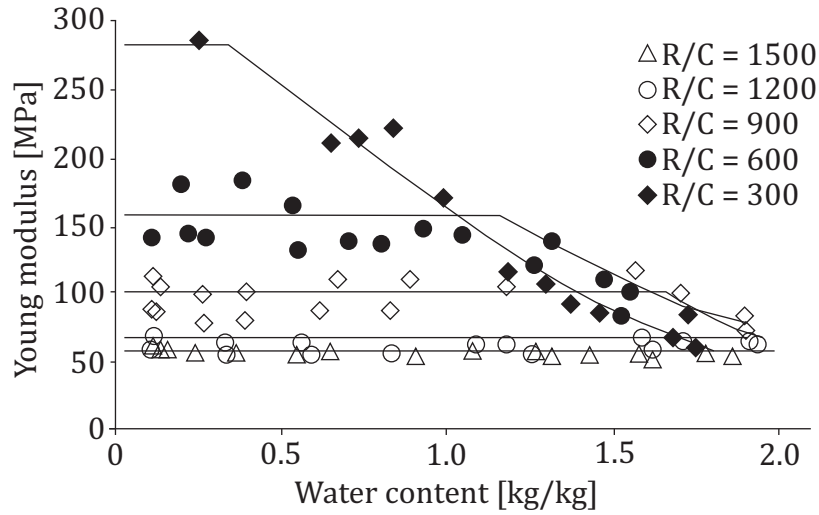
Figure 8.2: Evolution of Young modulus with water content for different R/C ratios (Léonard et al. (2008))

measurements allows to determine the Poisson ratio, ν, according to :

$$K = \frac{E}{3(1 - 2\nu)}$$ (8.1)

The results obtained for the different R/C tested are presented in Table 8.1.

R/C	300	600	750	900	1200	1500
$\nu\,[-]$	0.48	0.47	0.45	0.44	0.42	0.42

Table 8.1: Poisson ratio for different R/C ratio

Given the results obtained, our understanding is that the procedure most probably lead to the measurement of the undrained Poisson's ratio which is logically around 0.5. Consequently, these results will not be used later on.

Density The apparent dried density, ρ_d and the intrinsic density of the resin, ρ_s, are measured by mercury and helium pycnometry, respectively. The results are presented in Table 8.2.

R/C	300	600	750	900	1200	1500
$\rho_d\,[kg/m^3]$	870	510	470	420	370	360
$\rho_s\,[kg/m^3]$	1480	1500	1480	1480	1450	1490

Table 8.2: Density characterization

Based on the dry and intrinsic densities it is possible to determine the total porosity, n, of the sample based on :

$$\rho_d = (1 - n)\rho_s$$ (8.2)

The value obtained are visible in Table 8.3. The total porosity increases with increasing R/C ratio.

R/C	300	600	750	900	1200	1500
Total porosity [%]	41	66	68	72	75	76

Table 8.3: Textural characterization

Textural characterization   Nitrogen adsorption–desorption test were carried out on dried gels to determine the porous texture of the material. As R/C increases, xerogels evolve from micro-mesoporous texture for R/C =300, to a micro-macroporous texture for higher R/C. Generally, the mean pore size increases with R/C.

8.3.2   Drying behavior

In this work, we did not perform any convective drying experiment on the resorcinol formaldehyde hydrogels because the chemical engineering team from the University of Liège, especially Job (2005), thoroughly studied the production and drying behavior of RF hydrogels. In this section, a brief summary of their conclusion is presented.

Sample preparation   The samples preparation is analog to the one described in section 8.3.1 except that for the gelation part, the solutions were placed in a water bath for 24 h at 70°C and that a second cylindrical mold, slightly smaller in diameter, was slipped into the first one until it touched the solution to avoid any contact between air and the solution. Moreover, evaporation was prevented by a paraffin film covering both cylinders. This procedure aimed at avoiding thermal inertia and temperature gradients during the gelation phase.

Convective drying experiment   The RF hydrogel samples were dried in a classical convective dryer controlled in air relative humidity, temperature and velocity (cf. Chapter 3). The samples were weighed every 10 seconds during the test. As already explained, based on the variation of the mass with time, it is possible to express the Krischer curve, representing the drying rate versus the water content. The influence of the air velocity, air temperature and R/C ratio was tested. Preliminary tests were carried out at 115 $°C$ and with an air velocity of 2 m/s to determine whether the sample experienced desiccation cracking or not. Based on those results, experimental program were designed for each R/C ratio. R/C ratio of 300, 500 and 1000 were tested (cf Fig. 8.3). The R/C 300 presented desiccation cracks after drying at 115 $°C$. Consequently, the temperature was progressively reduced to 70°C, 50°C and finally 30 $°C$) to find conditions preventing cracking. R/C 500 also cracked and the same procedure was applied except it didn't crack for a temperature of 70°C and thus and intermediate temperature of 92.5 $°C$ was tested (Fig. 8.4(a)). R/C 1000 didn't crack at 115 $°C$. Three temperatures were thus tested : 70 $°C$, 115 $°C$, 160 $°C$. The influence of air velocity was studied at a temperature of 50 $°C$ and three velocities of $1[m/s]$, $2[m/s]$ and $3[m/s]$ were considered (cf Fig. 8.4(b)).
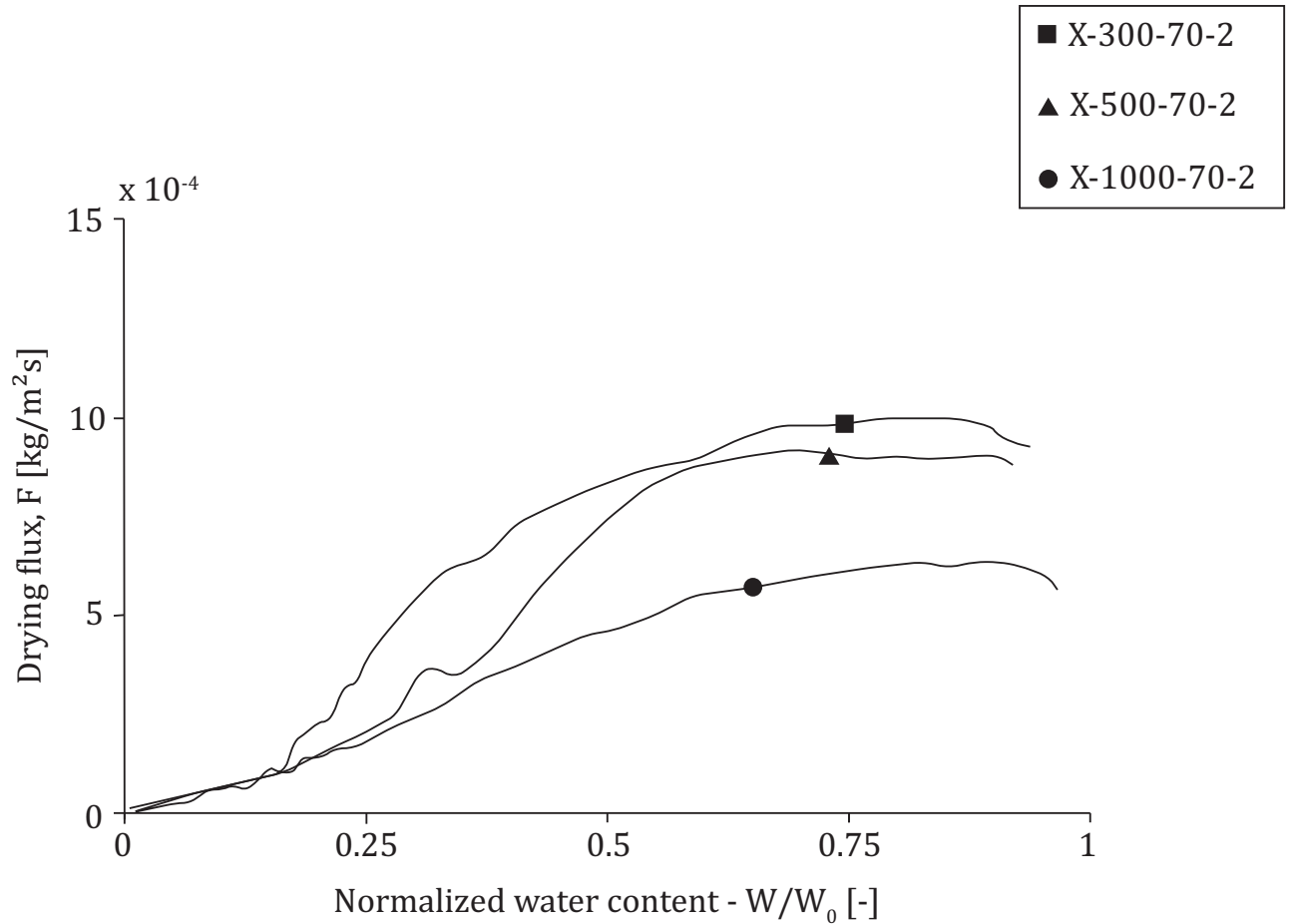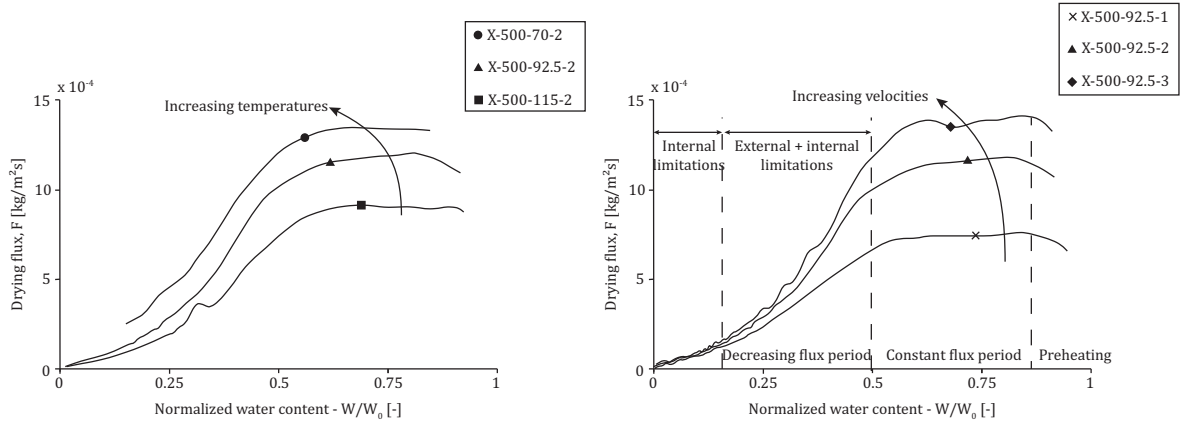
Figure 8.3: Krischer curve for different R/C ratios with a temperature of 70 $^\circ C$ and an air velocity of 2 m/s (Job et al. (2006b))

Drying kinetics   The drying kinetics results are presented in the form of Krischer curves :

8.3 exhibits very similar results (almost similar drying rate during the CRP and similar CRP length) for R/C 300 and R/C 500 but much lower drying rate for R/C 1000. The curve for R/C 1000 also does not present a clear CRP.

Fig. 8.4(a) and Fig. 8.4(b) show a clear increase of the drying flux with both the temperature and the air velocity.

Shrinkage   X-ray microtomography was used to monitor the samples shrinkage as well as to detect crack initiation. The samples were taken out of the drier at regular interval and put inside the microtomograph for 2 minutes (to limit potential drying in the microtomograph) then replaced in the convective dryer. Image analysis procedure are used to determine the diameter and height of the sample based on the scans. From those results, the shrinkage can be determined (Fig. 8.4).

169

(a) Krischer curve for different drying temperatures on samples with a R/C ratio of 500 and and air velocity of 2 m/s (Job et al. 2006b))

(b) Krischer curve for different drying air velocities on samples with a R/C ratio of 500 of 50 °C (Job et al. (2006b))
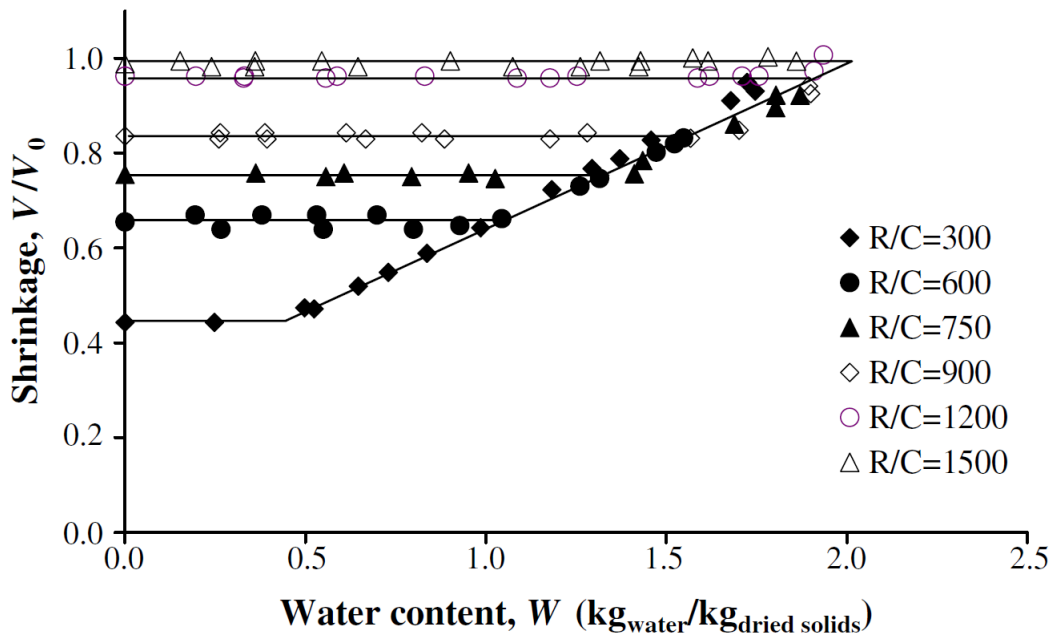

Figure 8.4: Evolution of the shrinkage with water content for different R/C ratios (Léonard et al. (2008))

Fig. 8.4 shows the evolution of the volumic shrinkage with the normalized water content. Note that since the shrinkage is mostly isotropic, directionnal (axial and radial) value of the shrinkage can easily be extrapolated from these measurements. The results clearly exhibit a significant dependence of the volume variation to the R/C ratio. All the curves (except R/C = 1500) follow the same trend during the linear part of the graph which is assumed to correspond to ideal shrinkage. Then the shrinkage curve reaches a plateau which value depends on the R/C ratio. The lower the R/C ratio, the higher the shrinkage. It is noteworthy that the sample experiencing the most important shrinkage also present the most important stiffening. The two curves on Fig. 8.4 and Fig. 8.2 are very similar which indicates that the stiffening of the material is due

to a densification mechanism provoked by the shrinkage. It has also been proven (Job et al. (2006b)) that there is no influence of the drying air temperature or velocity on the shrinkage.

Cracking   During the experimental campaign, a series of samples exhibited desiccation cracks (see Fig.8.5).
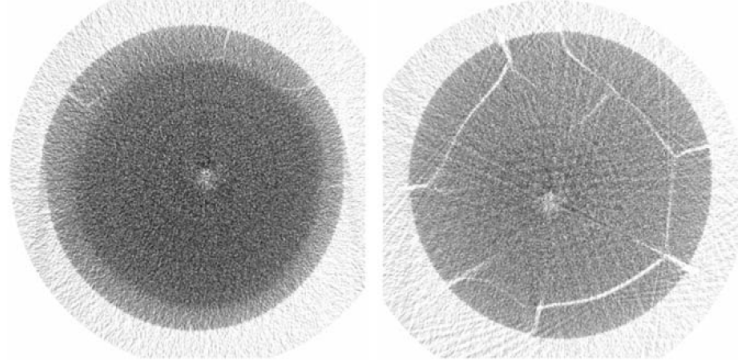

Figure 8.5: Evolution of the desiccation cracking ($W/W_0 = 0.23$ on the left and $W/W_0 = 0.10$ on the right) (Job et al. (2006b))

On the scans, we see that cracking first occurs radially and then orthoradially. The samples crack radially for a length corresponding to around a quarter of their radius. The factor influencing cracking are the R/C ratio and the drying air temperature. Sample with R/C ratio over 1000 didn't experience any cracking but for samples with R/C lower than 1000, the lower the R/C ratio the lower the temperature required for the sample to crack. For scale, samples with R/C 500 cracked for temperatures over 90 $°C$ whereas samples with R/C 300 cracked for temperatures over 30 $°C$.

8.4   Experimental campaign

In the previous section, the documented mechanical properties of the RF hydrogels were presented. Those are, however, insufficient to predict desiccation cracking or even to simulate a drying experiment. To further characterize the RF hydrogels, an experimental campaign is conducted. Particularly, the hydraulic properties of the material are investigated. Constant head permeameter experiments are conducted to determine the hydraulic conductivity of the material. The water retention curve is obtain using dynamic vapor sorption. The tensile stress of the material is obviously required and it measured using a Brazilan test appartus. Since, we know from the literature that RF hydrogels properties depend on the water content their evolution with it will be investigated. The section starts with a brief description of the sample preparation and is followed by the different tests performed.

8.4.1   Samples preparation

Hydrogels are prepared by polycondensation of resorcinol, solubilized in water, with formaldehyde, in the presence of Na_2CO_3. The pH of the precursors solution is achieved by changing the resorcinol/catalyst (in this case sodium carbonate) molar ratio, R/C. The R/C ratio was

fixed at 600. The resorcinol–formaldehyde molar ratio, R/F, and the dilution ratio (the solvent on resorcinol plus formaldehyde molar ratio) are fixed at 0.5 (stochiometric ratio) and 5.7, respectively. The total amount of solvent takes into account the deionised water added but also water and methanol (stabilizer) included in the formaldehyde solution. 9.91 g resorcinol were first mixed with 18.8 ml deionised water with the required amount of Na_2CO_3 in 250 ml sealable flasks under magnetic stirring. The formaldehyde solution was poured into a separated flask. All the solutions were then placed in a thermostated bath at 70°C. After temperature stabilization, 13.5 ml formaldehyde were added to the resorcinol solution. Cylindrical samples were obtained by casting solution into glass molds and putting them back in the water bath for gelation and aging during 24 h at 70°C. A second cylindrical mold, slightly smaller in diameter, was slipped into the first one and put in touch with the solution so that the contact between air and liquid was avoided. Evaporation was prevented by a paraffin film covering both cylinders. This procedure aims at avoiding thermal inertia and temperature gradients during the gelation phase. Moreover, the size of the samples was adapted to have a slenderness of around two for uniaxial compression test.

8.4.2 Saturated Hydraulic conductivity

Constant-head permeability experiments (cf. Fig. 8.6) were used to determine the saturated permeability, K_{sat}, of cylindrical resorcinol formaldehyde samples. The flow through the sample
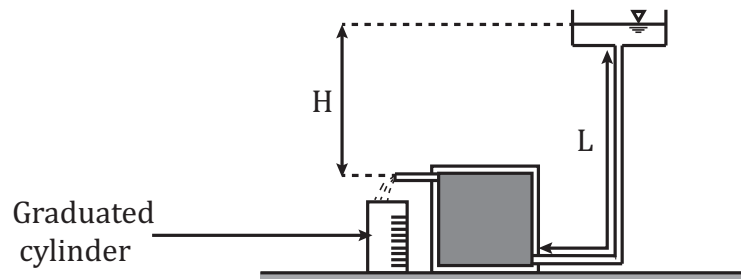

Figure 8.6: Constant head permeameter

is measured at a steady rate under a constant pressure difference. The hydraulic conductivity can thus be assessed using the relationship :

$$K_{sat} = \frac{QL}{A\Delta H} \tag{8.3}$$

where Q is the water flow, A is the cross sectional area of the permeameter, ΔH is the head difference, L is the length of the tube. Three samples were tested for reproducibility and the results are visible at Fig. 8.7. The three tests performed gave very consistent results. Based on the collected volume measure and using Eq. 8.3, it is possible to calculate the hydraulic conductivity of the sample (Table 8.4) :

8.4.3 Water retention curve

A very small sample (a few grams chip of a sample actually) was used to determine the water retention curve of the material. The sample was initially fully saturated and placed in a chamber
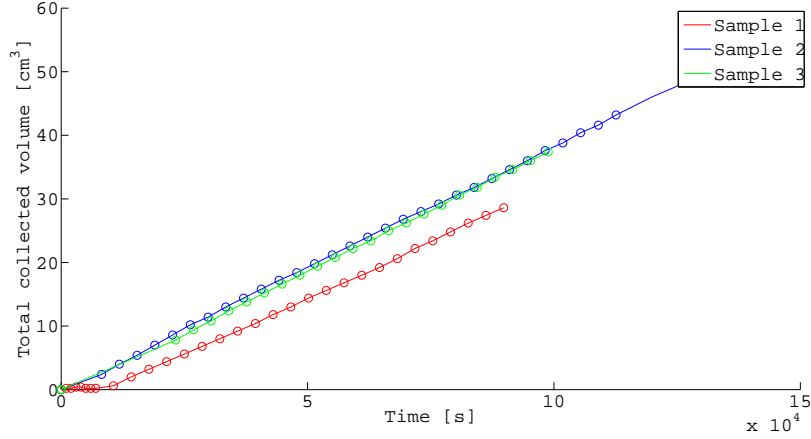
Figure 8.7: Total volume of water collected

Sample	1	2	3
Hydraulic conductivity $[m/s]$	$5.04\ 10^{-10}$	$5.007\ 10^{-10}$	$5.47\ 10^{-10}$

Table 8.4: Hydraulic conductivity for the different samples tested

whose relative humidity and temperature can be imposed. The relative humidity varied from 90 % to 0 % in about two days and the temperature was fixed at 40 °C. The evolution of the sample mass was recorded every two minutes until the end. Each relative humidity "step" (i.e. from 90 % to 80 %) was maintained until the sample mass stabilized. Using Kelvin law and knowing the imposed temperature and relative humidity in the chamber, it is possible to determine the suction in the sample. Given the sample dimensions and the length of each relative humidity step, the suction is assumed to be homogeneous over the whole sample. The assumption that the sample is initially saturated means that the saturation degree of the sample at any given time is the ratio of the mass of water at that mass measured at that instant and the dry mass) to the initial mass of water. We now have the evolution of the sample saturation degree with time and of the suction with time. Combining those, we obtain the water retention curve of the sample (see Fig. 8.8). It is possible to fit a van Genuchten's curve to the data obtained. As a remider, van Genucthen's formulation Van Genuchten (1980) is :

$$S_{r,w} = S_{res} + (S_{sat} - S_{res})(1 + (\frac{s}{\alpha_{vG}})^{n_{vG}})^{-m_{vG}} \tag{8.4}$$

in which $n_{vG}\ [-]$, $m_{vG}\ [-]$ are model parameters. n_{vG} is associated with the rate of desaturation of the soil while m_{vG} is linked to the curvature of the water retention curve for high suctions. $\alpha_{vG}\ [Pa]$ is a model parameter related to the air entry pressure, $S_{res}\ [-]$ is the water residual saturation, $S_{sat}\ [-]$ is the water maximum saturation and $s\ [Pa]$ is the suction. The parameters obtained are presented in Table 8.5.

This experiment also allows us to determine the porosity of the material and see if the sample we produced are in the same range as the one documented by Léonard et al. (2008). Considering the sample initially saturated and knowing its initial volume, initial and dry mass, the porosity
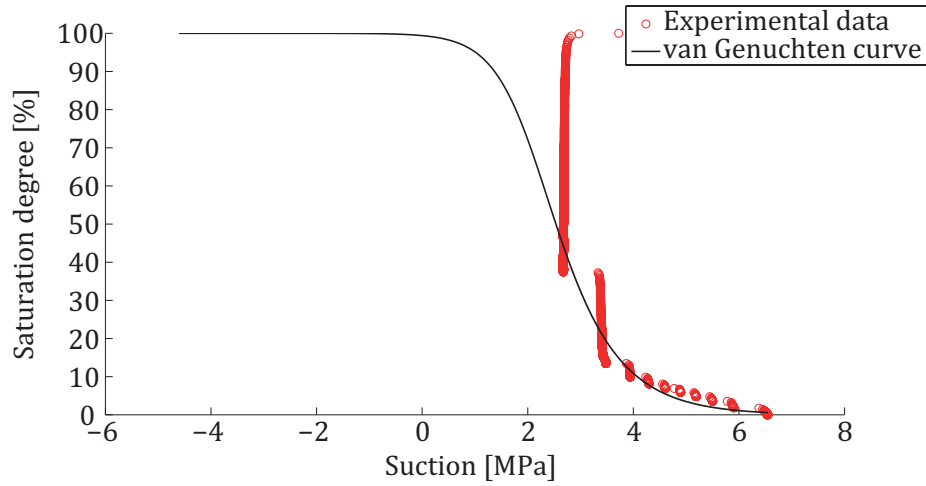
173

Figure 8.8: Water retention curve for the resorcinol formaldehyde gel with a R/C ratio of 600

van Genuchten parameters		
α_{vG}	6	$[MPa]$
n_{vG}	2	$[-]$
S_{sat}	1	$[-]$
S_{res}	0	$[-]$

Table 8.5: van Genuchten's formulation parameter for the resorcinol formaldehyde gel with a R/C ratio of 600

is easily obtained as :

$$n = \frac{\frac{m_i - m_f}{\rho_w}}{V_i} \tag{8.5}$$

where m_i and m_f are respectively the saturated and dry mass, ρ_w is the water density and V_i is the initial volume of the sample. In this case, the porosity is of $n = 75.76\%$ which is a bit higher but still concordant with values measured by Léonard et al. (2008).

8.4.4   Different water contents for the mechanical characterization

Since the mechanical parameters have been shown to be significantly influenced by the water content of the sample, sample at different water content were prepared.

Some samples were put into saline solutions (see Fig. 3.2 in Chapter 3 section 3.3.1) to achieve a chosen suction. These solutions were chosen because their relative humidity correspond to saturation degrees all along the water retention curve of the material. The relative humidity of the saline solution combined with the temperature of the saline solution (room temperature of around 25 $°C$) gives us the suction of the solution using Kelvin's law :

$$p_c = p_g - p_w = -\frac{\rho_w RT}{M} ln(RH) \tag{8.6}$$

174

where ρ_w is the water density, R is the gas constant, M is the water molar mass and T and RH are the temperature and relative humidity of saline solution. Since we know the water retention curve of the material, we can determine the corresponding saturation degree. The different solutions chosen are presented in table 8.6 as well as the saturation degree they lead to.

Solution	NH_4NO_3	KCl	$ZnSO_4$	K_2SO_4
Relative humidity [%]	65	76	91	97
Corresponding saturation degree [%]	10	16	42	82

Table 8.6: Different saline solutions prepared

The samples were weighed every day and were left into the saline solutions until complete stabilization of their mass.

Other samples were dried in a stove for 24h in a stove at 105 $°C$) to obtain completely dried samples.

8.4.5 Elastic modulus

Even though the elastic modulus of RF hydrogels is documented as well as its variation with suction, we still performed uniaxial compression tests (cf. Fig. 8.9) to ensure that the modulus of the sample we produced would be in the expected range. The applied load and the displacements were measured.
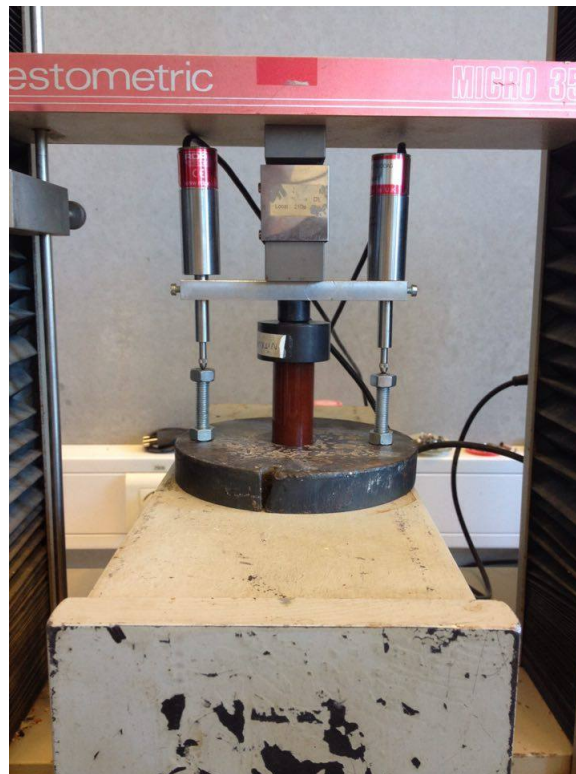

Figure 8.9: Uniaxial compression test on resorcinol formaldehyde sample

175

Stress is obtained by dividing the compressive load by the initial cross-sectional area, determined from the measurement of the diameter before each test. Strain is the change per unit length of the height of the sample. The loading rate was fixed at 0.4 mm/min. The tests were performed on samples at different water content. The results of the uniaxial compression test are presented on Fig. 8.10. Note that the dried samples (w = 0) tested could not be broken
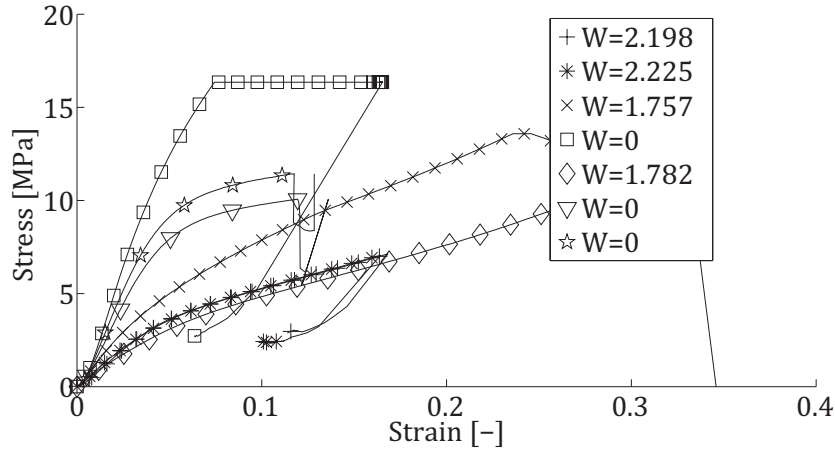

Figure 8.10: Stress-strain curves

using our loading cell explaining the constant stress observed one some experimental curves.
The elastic modulus is the slope of the linear part of the graph of compressive stress versus strain. As can be seen on Fig. 8.10, the slope of the elastic part of the curves increases with decreasing water content. This clearly exhibits the stiffening effect with decreasing water content documented by [Léonard et al. (2008)]. Fig. 8.11 shows the variation of the Young modulus determined with water content. The trend observed on Fig. 8.10 is, here, clearly confirmed by the trendline. The mean value of the elastic modulus for saturated samples is around $90 \, [MPa]$ and the mean value for dried samples is around $250 \, [MPa]$. The range of Elastic modulus measured is a bit higher than those measure by Léonard et al. (2008) for samples with R/C ratio of 600 but concordant enough to not require any additional measurement.

8.4.6 Tensile strength

Brazilian tests (Fig. 8.12 and Fig. 8.13) were performed to determine the tensile strength of the resorcinol formaldehyde gels. The loading rate was fixed at 0.2 mm/min. The evolution of the load with time is visible in Fig. 8.14. As can been seen, there is an increase of the maximum admissible load with decreasing water content. Some samples present maximum strength much lower than others with comparable water content. This is due to local defaults such as air bubbles, trapped during molding, leading to stress concentration and premature failure of the sample. Based on the maximum load, F_{max}, the tensile strength, σ_t, is determined using :

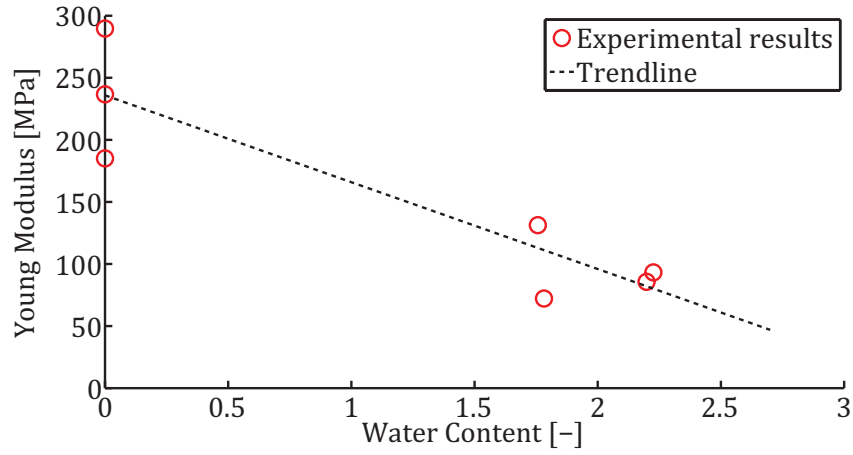$$\sigma_t = \frac{2F_{max}}{\pi D l} \tag{8.7}$$

176

Figure 8.11: Evolution of the elastic modulus with water content

Figure 8.12: Brazilian test on resorcinol formaldehyde sample

where D and l are the diameter and the length of the sample, respectively. The evolution of the tensile strength as a function of the water content is presented on Fig. 8.15. We start by pointing out that the two points corresponding to value of the tensile strength over $6\ MPa$ are way above the rest of the field and are not considered pertinent. They have not been considered for mean value nor trendline. On Fig. 8.15, the trendline also shows an increase of the material tensile strength with decreasing water content and the mean value for saturated samples is around $0.6\ MPa$ while the value for dried sample is around $2.5\ MPa$. Based on these results, it is possible to calibrate a Peron law (cf. Chapter 7.5) :

$$\sigma'_t = \sigma'^{sat}_t - k_2 \left[1 - exp\left(- \frac{k_1 s}{k_{2,0}} \right) \right] \tag{8.8}$$

177

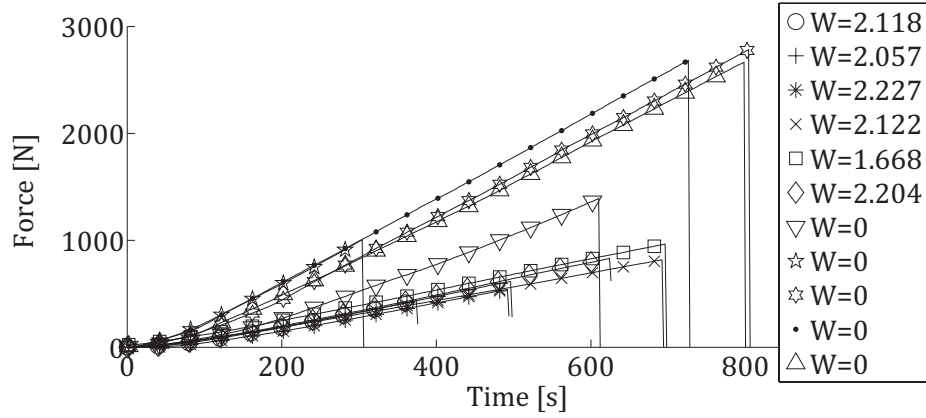Figure 8.13: Sample at the end of the brazilian test

Figure 8.14: Applied load vs. Time curves

where σ'_t is the effective tensile stress, σ'^{sat}_t is the effective tensile strength at the saturated state (s = 0), k_1 and k_2 are material parameters accounting for the increase in tensile strength as suction increases. k_2 has the dimension of a stress, and k_1 has no dimension and is actually the variation of tensile strength from the saturated to the dried state ($s = \infty$) :

$$k_2 = \sigma'^{sat}_t - \sigma'^f_t \tag{8.9}$$

Peron's formulation expresses the variation of the *effective* tensile strength as a function of suction. The first step is thus to determine the saturation degrees corresponding to the water contents of the tested samples (this is possible because we know the porosity the material). These saturation degrees can be used to calculate the suction level of each sample using the water retention curve of the material. Now that we know the saturation degree and suction level corresponding to each test, it is possible to calculate the effective tensile strength for
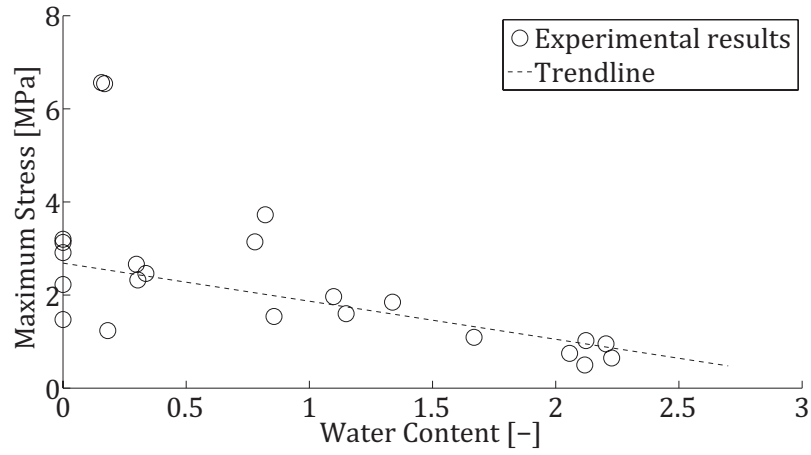
178

Figure 8.15: Evolution of the tensile strength with water content

every sample tested (see Fig. 8.4.6) using Bishop's effective stress :

$$\sigma'_{ij} = \sigma_{ij} - p_g \delta_{ij} + S_{r,w}(p_g - p_w)\delta_{ij} \tag{8.10}$$

The fitting of Peron's formulation to the effective tensile strength measured is visible on Fig. 8.4.6 and the obtained parameters are given in Table 8.7.
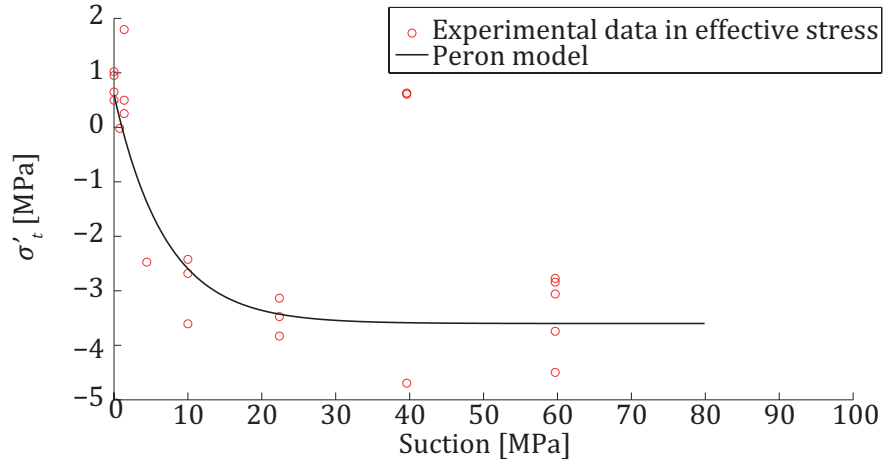

Figure 8.16: Evolution of the effective tensile strength in function of suction

$\sigma'^{sat}_{t,0}[MPa]$	$k_1[-]$	$k_2[MPa]$
0.6	0.6	4.2

Table 8.7: Parameter of the Peron model

8.5 Numerical modeling

In this section, simulations are performed to predict desiccation cracking of resorcinol formaldehyde hydrogel samples. We try to reproduce the behavior of one of the samples dried by Job et al. (2006b). The sample is a cylinder of height 10 mm and of radius 12.5 mm . The sample was dried laterally in a classical convective drier.

8.5.1 Mesh, initial and boundary conditions

The simulations are performed in axisymmetric conditions given the cylindrical shape of the sample (Fig. 8.17).
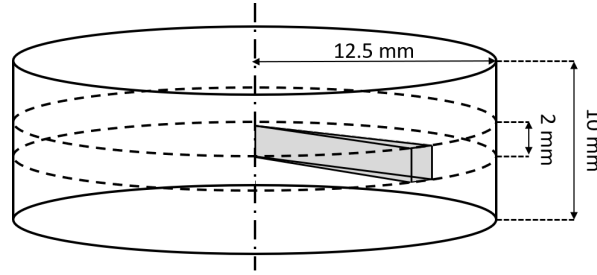

Figure 8.17: Simulated geometry

Mesh We decided to consider a 2 mm high band in the middle of the sample as represented on Fig. 8.17. This possible because the material is homogeneous and istropic allowing us to use the symmetry of the geometry to reduce the problem to a 1D axisymmetric configuration. The mesh and boundary conditions are visible on Fig. 8.18. The number of elements is progressively increased towards the drying surface since this is where all the stress and water content gradients will occur.

Boundary conditions The vertical displacements at the bottom of the sample are prevented as well as horizontal displacements along the symmetry axis. The atmospheric pressure is applied at all the external boundaries. The boundary layer boundary condition is implemented through a water pressure and a temperature at the environmental node (cf. section 4.2.1) and is imposed on the lateral surface of the sample. The temperature imposed corresponds to the temperature of the drying air (i.e. 92.5 $°C$) and the water pressure is calculated based on the temperature and relative humidity (1.5%) using Kelvin's Law :

$$p_c = -\frac{\rho_w RT}{M} ln(RH) = 711.9 \, [MPa] \tag{8.11}$$

where ρ_w is the water density, R is the gas constant, M is the water molar mass and T and RH are the temperature and relative humidity of the drying air.

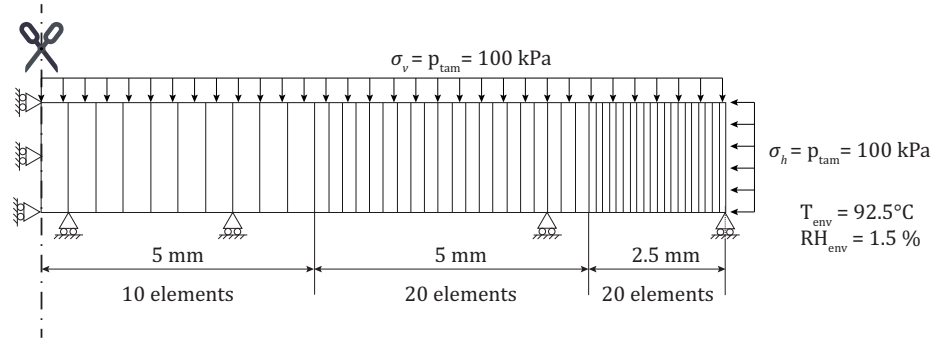**Initial conditions** The sample is initially at rest ($\sigma' = 0 \, [MPa]$), saturated and at room temperature :

180

Figure 8.18: 50 elements axisymmetric mesh

Degree of Freedom	Values	Units
$p_{w,ini}$	100	[kPa]
$p_{g,ini}$	100	[kPa]
T_{ini}	20	[° C]

Table 8.8: Initial conditions

8.5.2 Numerical results

In this section, the results obtained for the different simulations performed are presented. A step by step approach similar to the one applied to present the numerical results of the simulations performed on Boom clay is chosen. The goal is to highlight the influence of each mechanism on both the drying behavior and tensile stresses generation. Krischer curves will be presented for each simulation to compare the numerical and experimental drying kinetics. Depending on the simulation performed, other key results will be presented. Most of the time, the results presented will account for the first 2h of the drying experiments since most of the drying occurs during the first two hours.

8.5.2.1 Preliminary simulation

Even though we proved in Chapter 5 that to reproduce the drying kinetic of a porous medium, Thermo(T)-Hydro(H)-Mechanical(M) couplings are required, the preliminary simulation is a thermo-hydraulic one. All the displacements are prevented. The goal of the simulation is to assess how the mass transfer occurs. This will show if our hydraulic parameters and the transfer coefficients of the boundary layer have been correctly calibrated. This will be the case if the drying rate during the constant rate period reaches the right order of magnitude. The mass and heat transfer coefficients, α and β, are calculated using the following expressions :

$$q = \alpha(\rho_{v,surf} - \rho_{v,air}) \tag{8.12}$$

$$f = Lq - \beta(T_{air} - T_{surf}) \tag{8.13}$$

where q is the drying rate during the CRP, $\rho_{v,air}$ is vapor density of the drying air, $\rho_{v,surf}$ is the vapor density at the surface of the sample, T_{air} is the temperature of the drying air, T_{surf} is the temperature at the surface of the sample and L is the water evaporation latent heat (2500 kJ/kg). Since we know, from the experiments, the drying rate during the CRP and that all the other parameters are known since we impose the boundary conditions, α and β can be determined. The following values are obtained for the sample considered (Table 8.9)

Parameters	Values	Units
α	0.061	$[m/s]$
β	50.70	$[W/m^2/K]$

Table 8.9: Transfer coefficient for the considered sample

The hydraulic parameters used are presented in Table 8.10 as well as the van Genuchten formulation for saturation degree and relative permeability. The parameters of the thermal law

Reference	Parameters	Values	Units
Hydraulic parameters			
Expe	k	5.10^{-17}	$[m^2]$
Expe	n	0.7576	$[-]$
	τ	0.1	$[-]$
van Genuchten parameters			
Expe	α_{vG}	12.5	$[MPa]$
Expe	n_{vG}	1.7	$[-]$
Expe	S_{sat}	1	$[-]$
Expe	S_{res}	0.01	$[-]$
	$k_{r,min}$	10^{-7}	[-]

Table 8.10: Hydraulic model parameters

are given in Table 8.11 : The values used were determined during our experimental campaign (designated by "Expe" in the Table 8.10 and Table 8.11) or the literature. Parameters without references (τ,$k_{r,min}$ and α_s) were arbitrarily chosen. The value of $k_{r,min}$ is chosen based on the results of the sensitivity study in Chapter 5.
The drying kinetics obtained for the preliminary simulation is visible on Fig. 8.19 : The first observation that can be made based on Fig. 8.19 is that as first approximation, the numerical results are quite close to the experimental ones. The general order of magnitude is correct but the constant rate period is too long.

The evolution of the water pressure along the radius of the sample is visible on Fig. 8.20. As can be seen an important water pressure gradient develops near the drying surface. This gradient is so important that it leads to numerical convergence problems. These problems lead to a significant decrease of the time steps of the simulation (around $10^{-3}s$ per step). These very

| References	Parameters	Values	Units
Collin (2003)	ρ_w	1000	$[kg/m^3]$
Collin (2003)	$c_{p,w}$	4185	$[J/kg/K]$
Collin (2003)	Γ_w	0.6	$[W/m/K]$
Collin (2003)	α_w	7.10^{-6}	$[1/K]$
Collin (2003)	ρ_a	1.2	$[kg/m^3]$
Collin (2003)	$c_{p,a}$	1004	$[J/kg/K]$
Collin (2003)	Γ_a	0.025	$[W/m/K]$
Collin (2003)	ρ_v	0.59	$[kg/m^3]$
Collin (2003)	$c_{p,v}$	1864	$[J/kg/K]$
Collin (2003)	Γ_v	0.02	$[W/m/K]$
Léonard et al. (2008)	ρ_s	1500	$[kg/m^3]$
Hrubesh and Pekala (1994)	$c_{p,s}$	896.4	$[J/kg/K]$
Hrubesh and Pekala (1994)	Γ_s	0.35	$[W/m/K]$
	α_s	10^{-5}	$[1/K]$

Table 8.11: Thermal model parameters
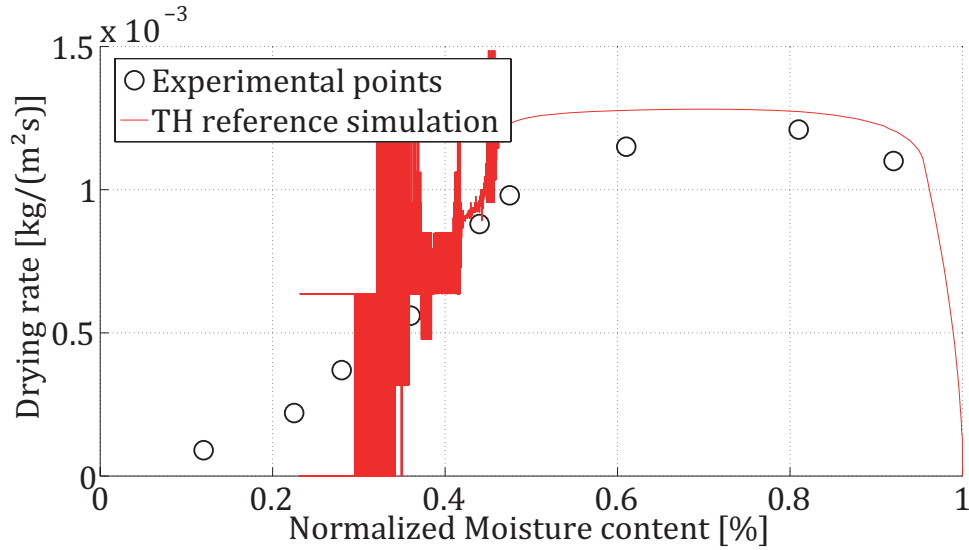
Figure 8.19: Comparison of experimental and numerical Krisher's curve for the preliminary simulation

little time steps are responsible for the oscillations visible on Fig. 8.19 because the drying rate, q, is the ratio of the derivative of the mass, δm, over the derivative of the time, δt :

$$q = \frac{\delta m}{\delta t} \frac{1}{S} \tag{8.14}$$

where S is the drying surface. Therefore, when the time steps become very small the drying rate take very variable values because both the mass and time variation are very small. Hence
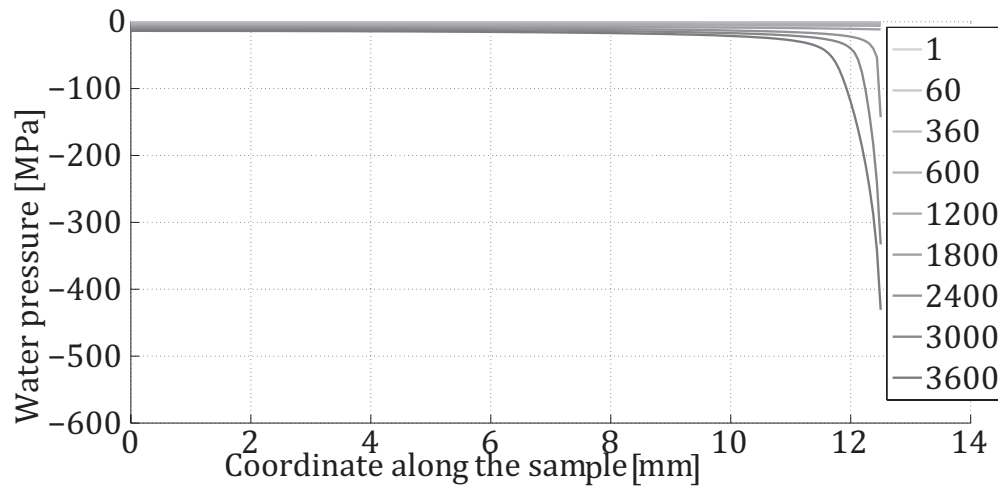
Figure 8.20: Evolution of the water pressure along the radius of the sample

the oscillations.

Mesh dependency of the results   We studied a less refined mesh to see the influence of the mesh on the results. A less refined mesh composed of 25 elements (rather than 50) was used. Bigger elements means lower water pressure gradient over the element which helped the numerical convergence as attested by the almost disappearance of the oscillation on the Krischer curve (see Fig. 8.21). But this is done at the cost of results accuracy. Indeed, on Fig. 8.21, a "rebound" of the drying rate can be observed. It is provoked by an incorrect numerical
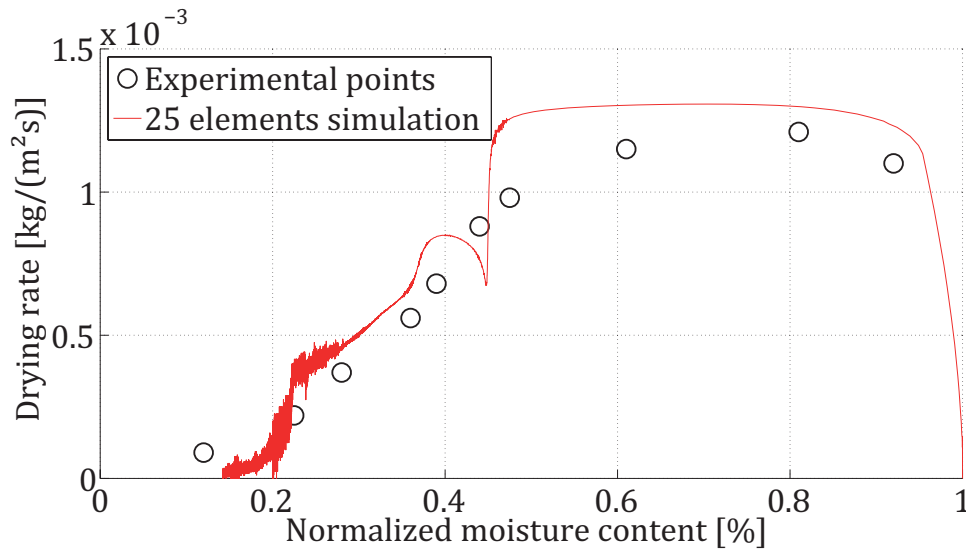

Figure 8.21: Comparison of experimental and numerical Krisher's curve for a 25 elements mesh

solution at the level of the integration points. Fig. 8.22 shows the evolution of the suction in the sample and in the red square, it can be observed that the suction decreases at the surface of the sample. Note that this behavior is not observed on the water pressure at the level of the element nodes which means it is most probably linked to the interpolation function. This decrease in suction is followed by an increase in saturation degree and in relative permeability which leads to an increase of the drying rate and the observed "rebound". Smaller mesh helps the convergence but only artificially since they lead to false results and cannot therefore be considered.
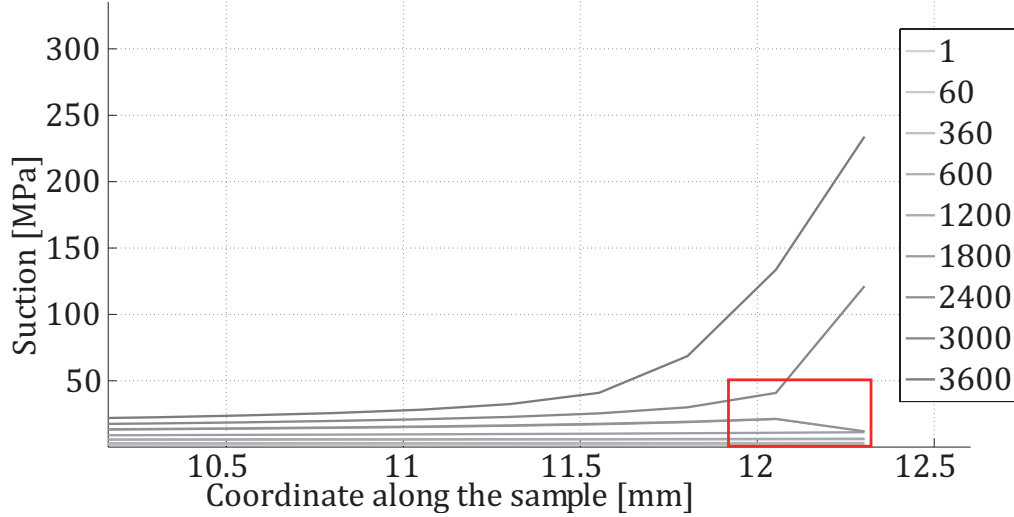

Figure 8.22: Comparison of experimental and numerical Krischer's curve for

Saturation degree of the boundary layer A solution to solve the convergence problems created by the important water pressure gradient during drying has been suggested by Gerard (2011). It consists in assuming that the saturation degree of the boundary layer is equivalent to the one at the surface of the sample. This is done by implementing a water retention curve (of the van Genuchten's type) in the boundary layer element to be able to calculate a saturation degree based on the evolution of the suction. As the saturation of the boundary layer decreases the transfer coefficient decreases too. The drying rate is thus calculated based on :

$$q = \alpha(S_{r,w})(\rho_{v,surf} - \rho_{v,air}) \tag{8.15}$$

where $\alpha(S_{r,w}) = \alpha_0 \, S_{r,w}$ in which α_0 is the initial water transfer coefficient.
The major drawback of this approach is that the mass transfer during the falling rate period is partially controlled by the boundary layer (i.e. drying conditions) and not only the internal transfer which is not in accordance with the theory of convective drying. Nonetheless, it is a efficient to be able to perform our simulations without too many convergence problems, we decided to use this formulation. The results obtained can be seen in Fig. 8.23. Using this formulation, we can obtain the following Krischer curve (Fig. 8.23) Adopting this formulation
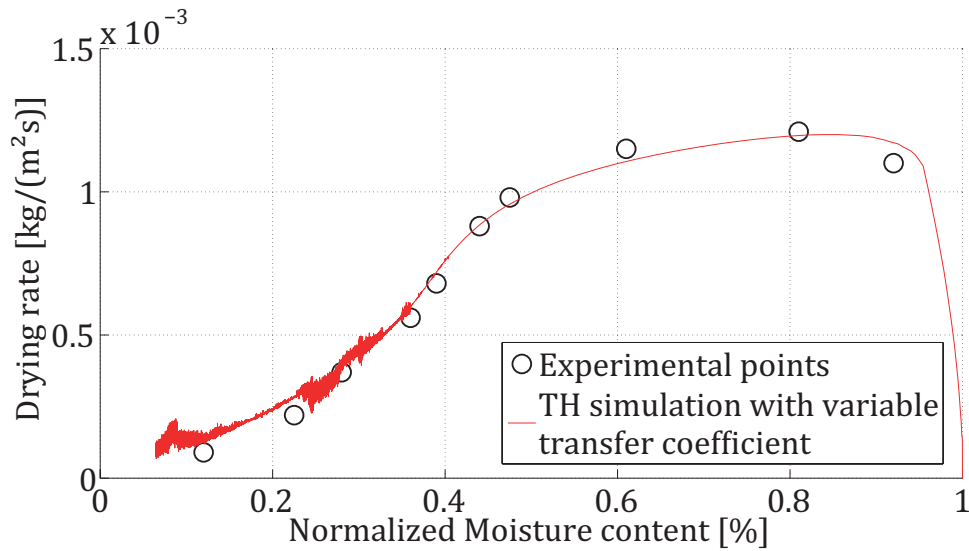
Figure 8.23: Comparison of experimental and numerical Krischer's curve for the simulation with variable mass transfer coefficient

helps to reduce the water gradient by decreasing the "demand" in water of the boundary condition (cf. Fig. 8.24 and Fig. 8.20). As can be seen on Fig. 8.23, this helps the convergence of the problem and leads to a much smoother curve even if oscillations persist. An undesired effect of the method is that we do not observe a true constant rate period anymore. Because even during the CRP, the saturation changes a little which change the mass transfer coefficient a little and leads to a slowly decreasing drying rate during the CRP.
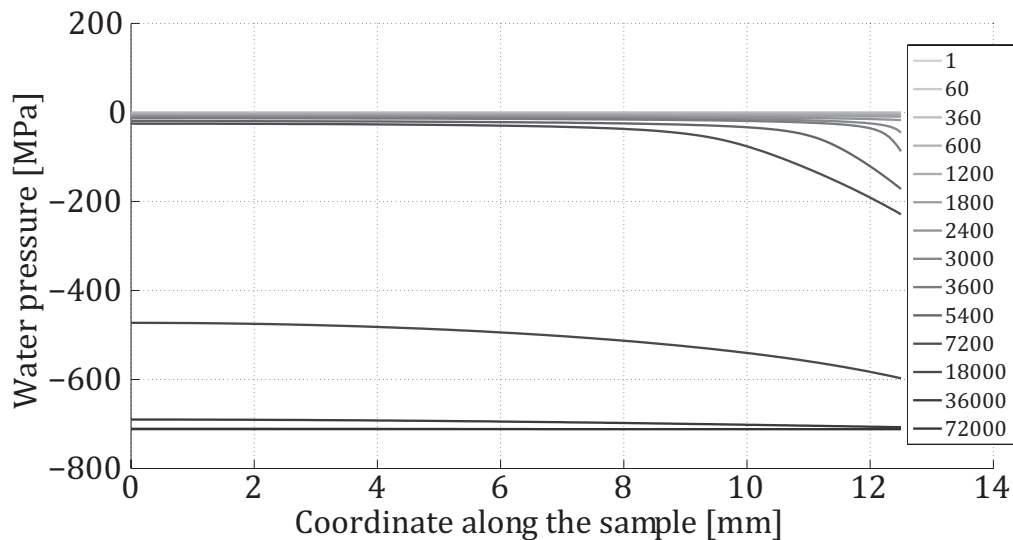

Figure 8.24: Evolution of the water pressure along the radius of the sample

8.5.2.2 Thermo-hydro-mechanical simulation

Now that we have an acceptable hydraulic solution, it is time to add the mechanical aspect of the problem and see what is changes to the drying kinetics. The mechanical law used is a linear isotropic elastic one with a tensile failure mechanism. The parameters are given in Table 8.12 and Table 8.13. Logically, the drying rate should be a bit higher due to the reduction of the drying surface and the CRP should be longer because the porous medium will remain saturated longer because of pore size reduction due to the shrinkaghe. Krischer curve for the THM simulation is visible on Fig. 8.25.

References	Parameters	Values	Units
Expe and Léonard et al. (2008)	E	300	$[MPa]$
	ν	0.25	$[-]$
	G	150	$[MPa]$

Table 8.12: Linear elasticity mechanical law parameters

References	Parameters	Values	Units
Expe and Léonard et al. (2008)	$\sigma_t'^{sat}$	0.6	$[MPa]$
	k_1	0.6	$[-]$
	$k_{2,0}$	4.2	$[MPa]$

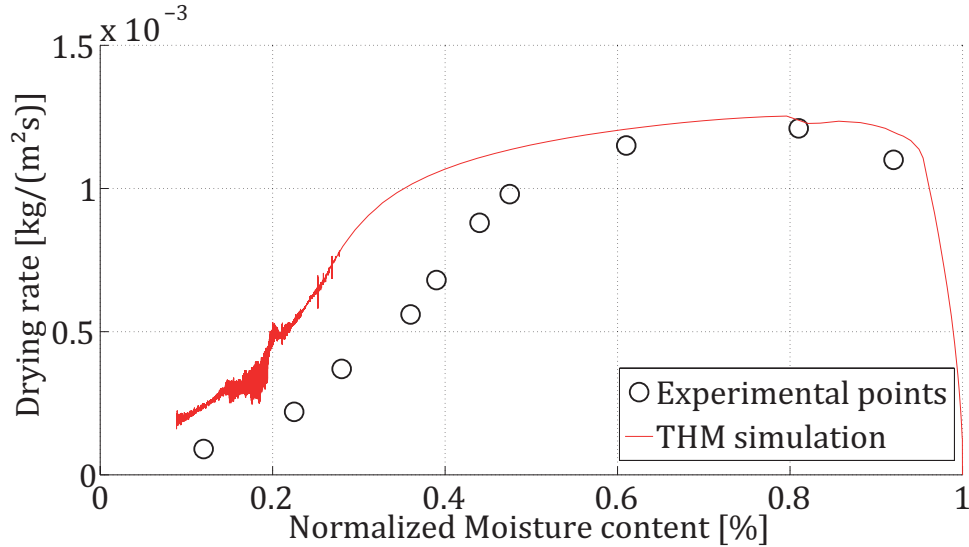Table 8.13: Tensile failure criterion parameters

Figure 8.25: Comparison of experimental and numerical Krischer's curve for the THM simulation with linear elasticity

Adding the mechanical aspect add the expected effect and the CRP is now too long. The solution suggested to solved that problem is to take into account the variation of the hydraulic conductivity with the porosity.

Variation of the hydraulic conductivity with the porosity One of the possible coupling that we did not consider before was the decrease in permeability due a reduction of the porosity. Boom clay presented volume shrinkage of around maximum 10% whereas the hydrogel can shrink to up to a 35% reduction in volume for a R/C of 600. This means that the decrease in porosity is much more important (cf. Fig. 8.26). We can see that after 2 hours, the porosity has decreased from 76% to a value of around 68%. It is thus reasonable to assume that such a decrease in porosity will have a significant impact on the hydraulic properties. To take this
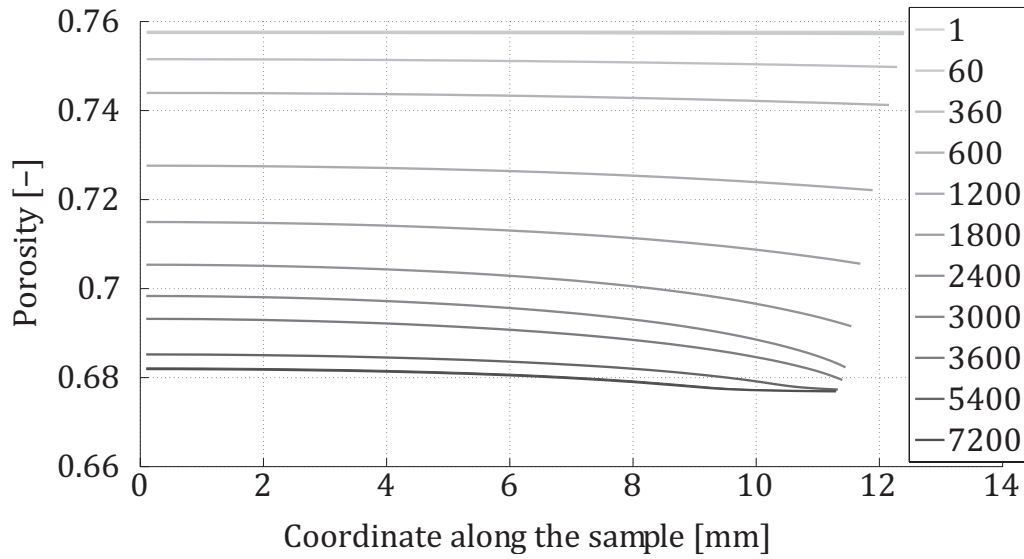

Figure 8.26: Evolution of the porosity along the radius of the sample for different time steps

effect into account we use the Kozeny-Carman formulation (Kozeny (1927)) :

$$k = k_0 \frac{(1 - n_0)^{k_m}}{n_0^{k_n}} \frac{n^{k_n}}{(1 - n)^{k_m}}$$ (8.16)

where k is the saturated hydraulic conductivity, k_0 the initial saturated hydraulic conductivity, n_0 the initial porosity and k_n, k_m are model parameters. In this case, $k_n = 3$ and $k_m = 4$. Using this formulation, the following Krischer curve is obtained (Fig. 8.27) :
The numerical results now fit very well the experimental data. We have found a formulation that allows us to accurately reproduce the drying kinetics of the RF hydrogels but the shrinkage has not been addressed yet. Based on our numerical results, we see that the radius of the sample decreased from 12.5 mm to around 11.5 mm which means a volumic shrinkage of around 23% which is much lower than the range suggested by the experimental data of Léonard et al. (2008). This is due to an initially too important Young's modulus. To solve this problem, we suggest, once again, to use non linear elasticity.
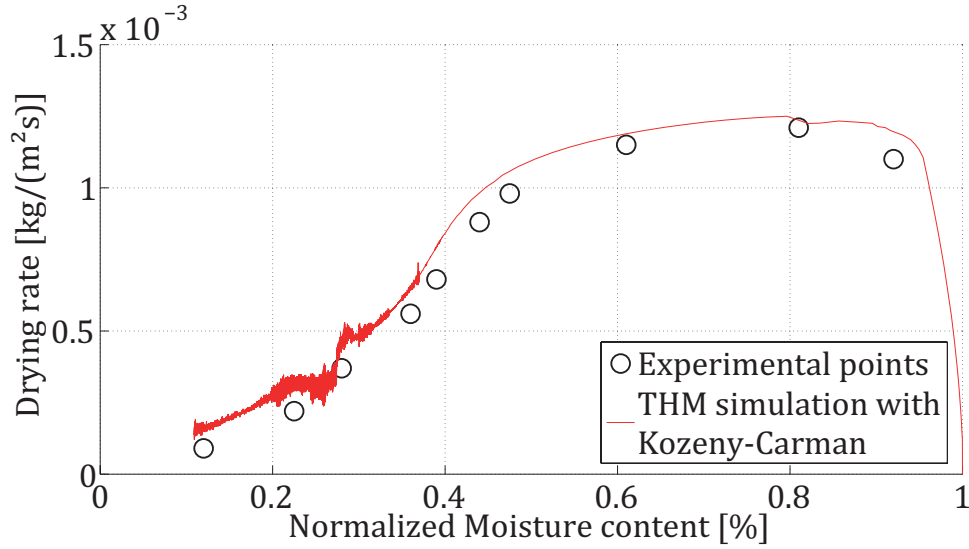
Figure 8.27: Evolution of the drying rate in function of the normalized water content for the THM simulation with Kozeny-Carman formulation

Non linear elasticity   Based on the experimental data of Léonard et al. (2008) and the experimental campaign that we conducted (cf. Fig. 8.11 and 8.2), we know that the RF hydrogels Young's modulus varies significantly with water content. The formulation of Modaressi and Laloui (1997) introduced in chapter 5 is once again used to account for the stiffening of the material:

$$E = E_0 + E_{ref}(\frac{p'}{p_{ref}})^b \tag{8.17}$$

where E_{ref} is the Young modulus at the reference mean effective stress, p_{ref}, and b is a model parameter. E_0 is used to avoid null Young's modulus when the effective stress state vanishes. The dependence on the stress state means, through the use of Bishop's effective stress, that the moduli are dependent on the suction thus on the water content. The parameters of the non linear elasticity law are given in Table 8.14

Parameters	Values	Units
E_{ref}	270	$[MPa]$
p_{ref}	6.5	$[MPa]$
E_0	30	$[MPa]$
b	2.5	$[-]$

Table 8.14: Non Linear elasticity mechanical law parameters for the resorcinol formaldehyde hydrogels

The parameters of the Modaressi and Laloui (1997) law are obtained by fitting (Fig. 8.28) the law to the experimental data collected by Léonard et al. (2008) and during our experiments.
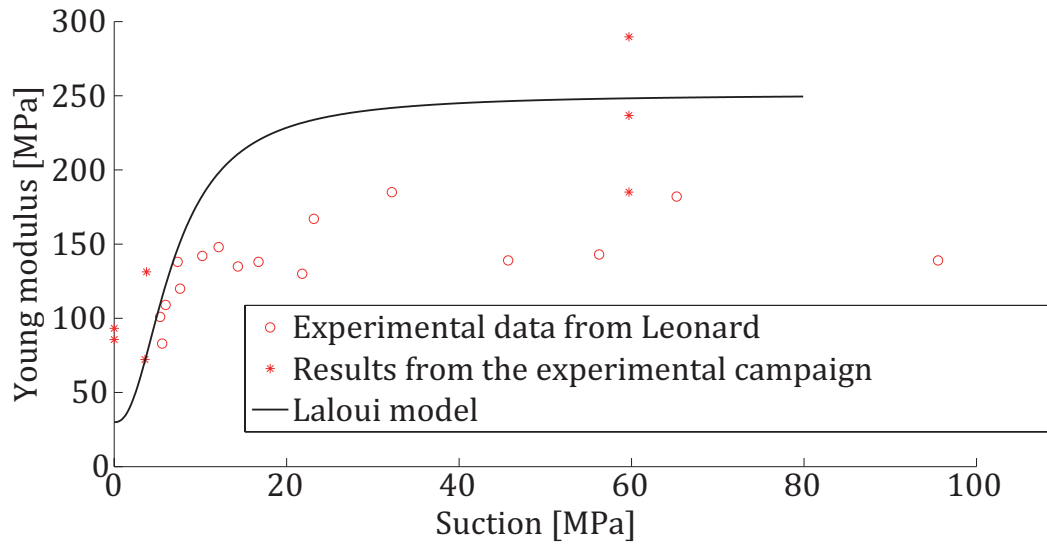
Figure 8.28: Evolution of the water pressure along the radius of the sample

Using this formulation does not have much impact of the drying kinetics as can be seen on Fig. 8.29.
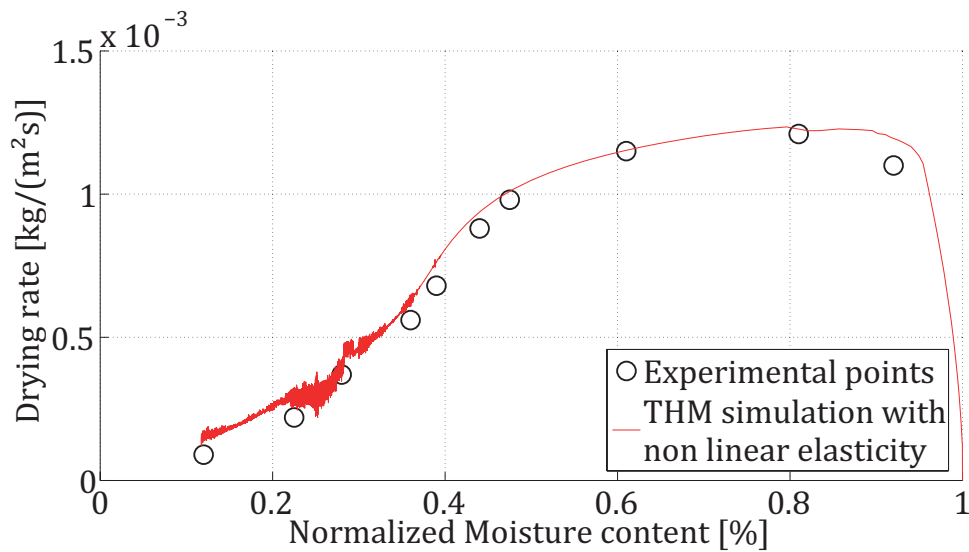

Figure 8.29: Evolution of the drying rate in function of the normalized water content for the THM simulation with Kozeny-Carman formulation and non linear elasticity

The Young modulus evolution along the radius of the sample is visible on Fig. 8.30. Young's modulus evolves from its initial value of 30 MPa toward its final value of 300 MPa but never reaches it. The reason behind it comes from the formulation of the elastic modulus in function
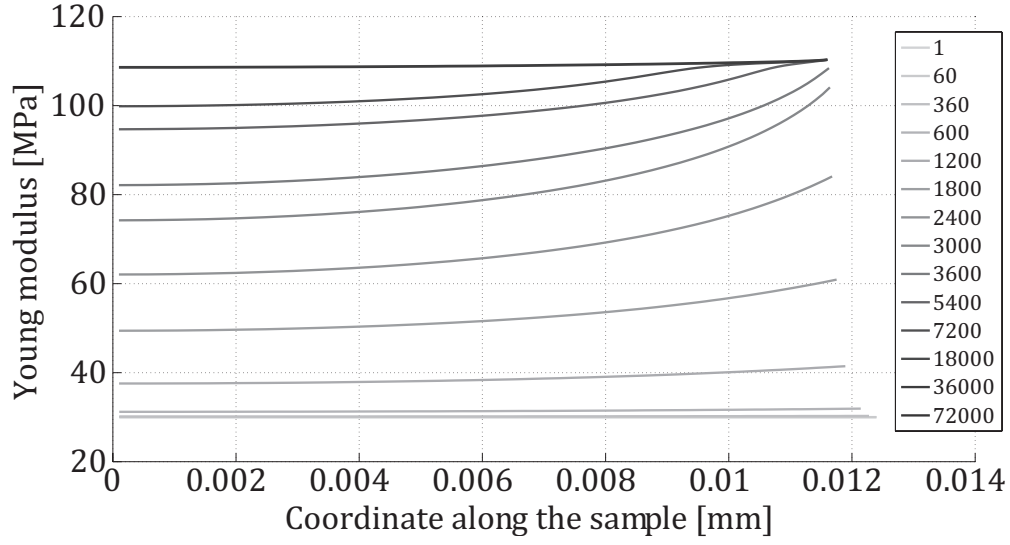
Figure 8.30: Evolution of Young's modulus for the THM simulation using Modaressi and Laloui (1997) for non linear elasticity

of the mean effective stress. Based on Bishop formulation of the effective stress we know that :

$$\Delta\sigma^{'} = \Delta\sigma - \Delta p_g + \Delta(S_{r,w}\ s) \tag{8.18}$$

Given that the gas pressure remains constant during our simulations and that the external total stress applied does not vary either, this reduces to :

$$\Delta\sigma' = \Delta(S_{r,w}\ s) \tag{8.19}$$

This means that the variation of the elastic modulus is directly dependent on the variation of the $S_{r,w}\ s$ term which reaches a maximum value of around 6 MPa (cf. Fig. 8.31).
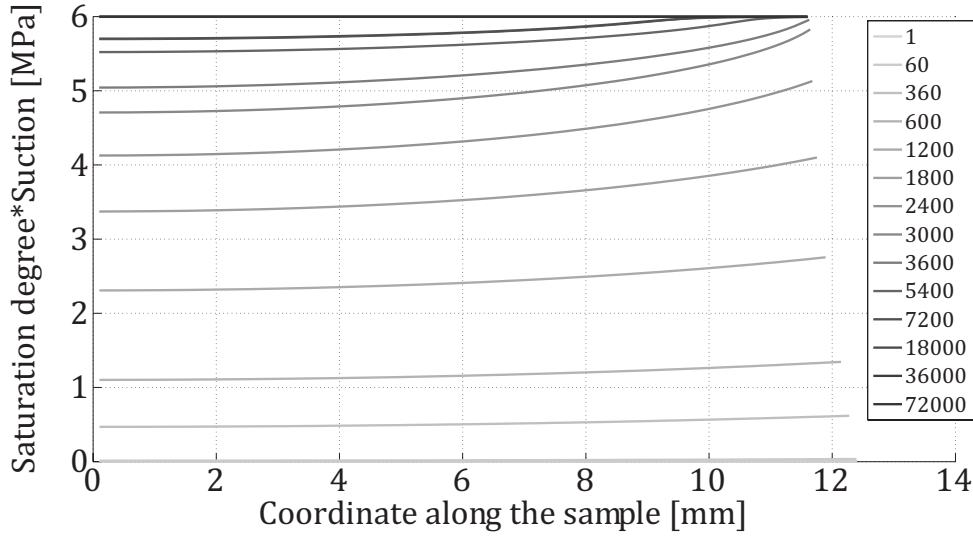
191

Figure 8.31: Evolution of the $S_{r,w}.s$ along the radius of the sample for different time steps. Those results are obtained for the THM simulation using Modaressi and Laloui (1997) for non linear elasticity

This means that the material does not perceive any ulterior modification and that the stiffening is limited. It would be possible to calibrate the Modaressi and Laloui (1997) to reach the correct final value of Young's modulus but in this case it would diverge from our experimental data. Nonetheless, volumetric shrinkage increased from 23% to 30% which is much closer to the experimental range. The evolution of the elastic modulus is not perfect but drying kinetics and shrinkage give very good results. The last step is thus to check if the tensile failure criterion is met at any point during this simulation. The different effective stresses are visible Fig. 8.32 to Fig. 8.34 and the total stresses are visible on Fig. 8.35 to Fig. 8.37.

As expected, the effective stress are all in compression and take values close to $S_{r,w}.s$ which is logical given Bishop's effective stress formulation and the fact that no external forces are applied. Total stress are thus easier to analyze since any divergence from their initial value indicates the generation of a stress induced by a strain compensation mechanism. On Fig. 8.37, we can see that total tensile stresses are generated in the orthoradial direction but could never reach the tensile failure criterion since the maximum tensile stress generated is of less then $600kPa$ which is the initial value of the material tensile strength. It is still remarkable that tensile stresses are generated. When the material dries, important water gradient develops near the drying surface. This water gradient also means - since the gas pressure is fixed - suction gradient. Following Bishop's effective stress formulation, this means that there exists an effective stress gradient. The external zone (near the drying surface) is thus submitted to much higher compressive strains than the inner part. Because of material continuity, this differential shrinkage between the dried external zone and the insided of the sample is limited (it cannot be discontinuous). The external zone therefore has to generate total tensile stresses to equilibrate the effective tensile stress to the admissible strain. When the external zone stiffens because of non linear elasticity, this strain compensation mechanisms is increased because more tensile stress are required to equilibrate the admissible strain state. Finally, when the external zone
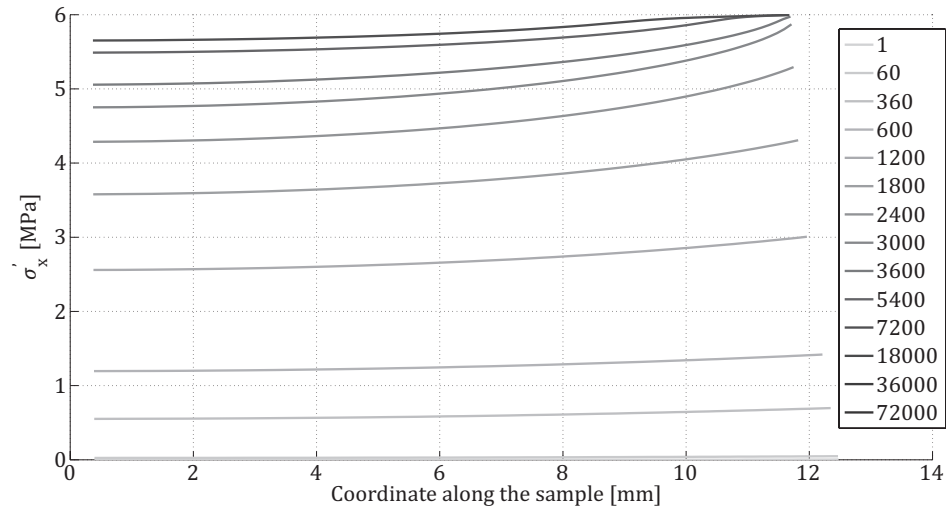
192

Figure 8.32: Evolution of effective radial stress along the radius of the sample.
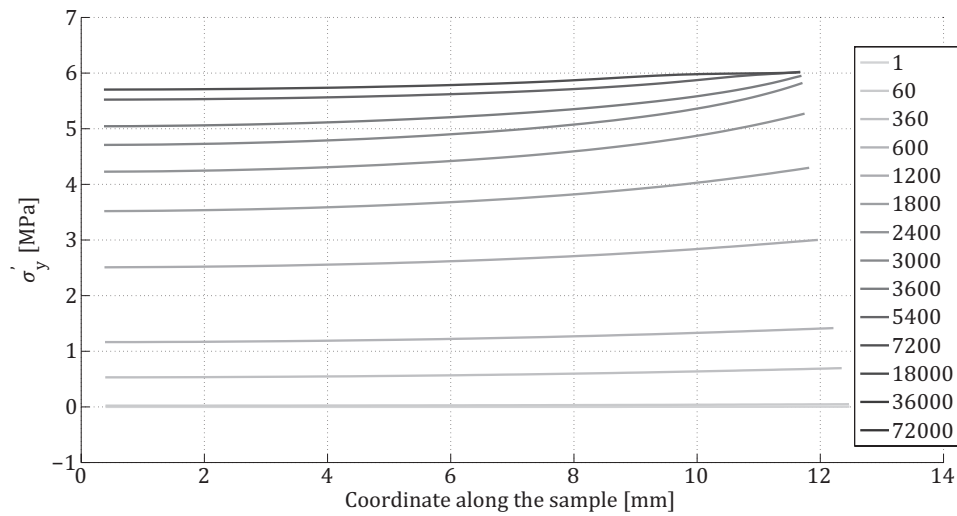
Figure 8.33: Evolution of effective axial stress along the radius of the sample.

becomes really stiff and rigid, it tends to deforms less and less and it ends up restraining the shrinkage of the inner zone. This rigid "ring" around the sample is thus "pulled" at the interface between the stiffened zone and the still more deformable zone. This explains the generation of total radial tensial stresses. When a ring (or tube) is pulled radially from the inside, it also generates compressive orthoradial stresses. This explains why the othoradial total stress now goes towards the compression range.

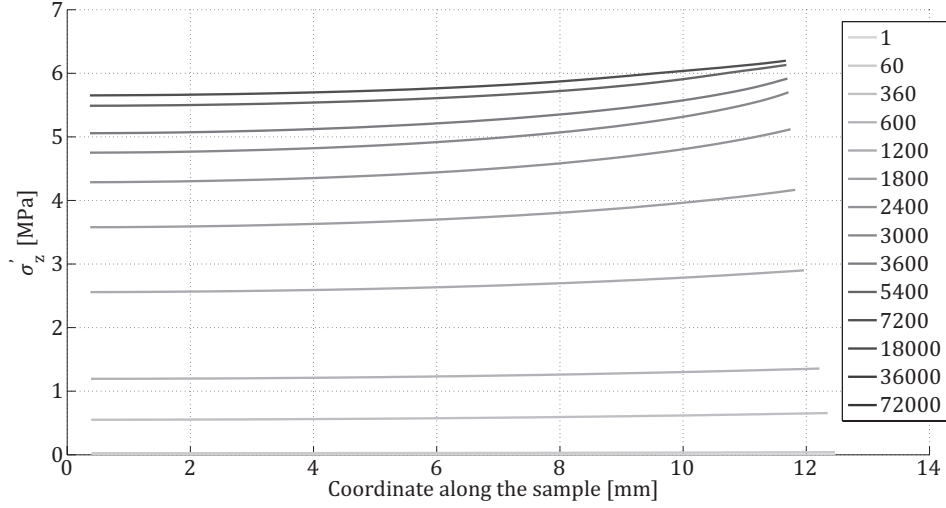Figure 8.34: Evolution of effective orthoradial stress along the radius of the sample.
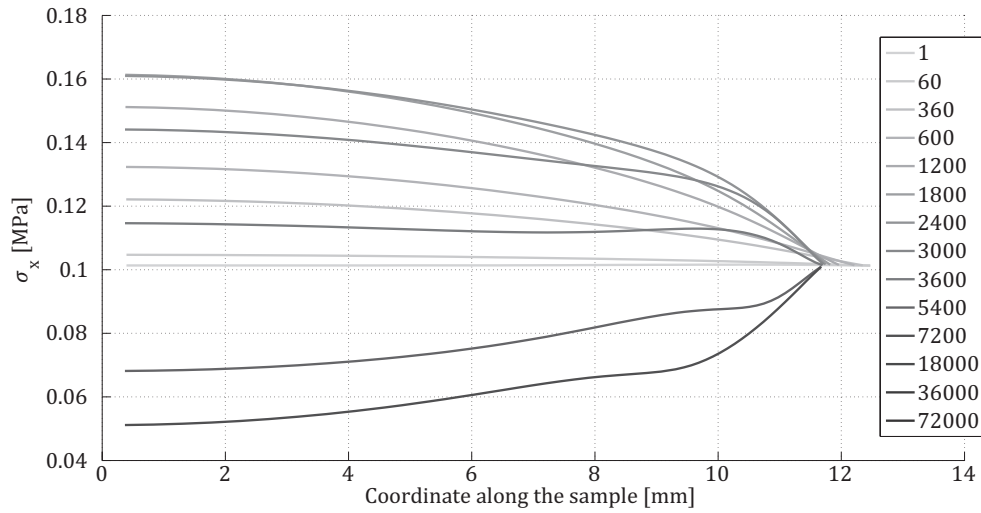
Figure 8.35: Evolution of the total radial stress along the radius of the sample.

8.5.2.3 Reference simulation

In this last step, we use a new formulation for the non linear elasticity which writes :

$$E = E_0 + \Delta E_{max}(1 - (1 + (\frac{s}{a})^b)^{-(1-\frac{1}{b})}$$

(8.20)

where E_0 is the initial value of the Young modulus, ΔE_{max} is the maximum increase in Young modulus, s is the suction and a and b are model parameters. The formulation suggested has been arbitrarily chosen but is similar is principle to the one used by other authors working on desiccation cracking (Cajuhi et al. (2018)). The formulation is also calibrated (see Fig. 8.38) based on the data gathered by Léonard et al. (2008) combined with ours. The following

194
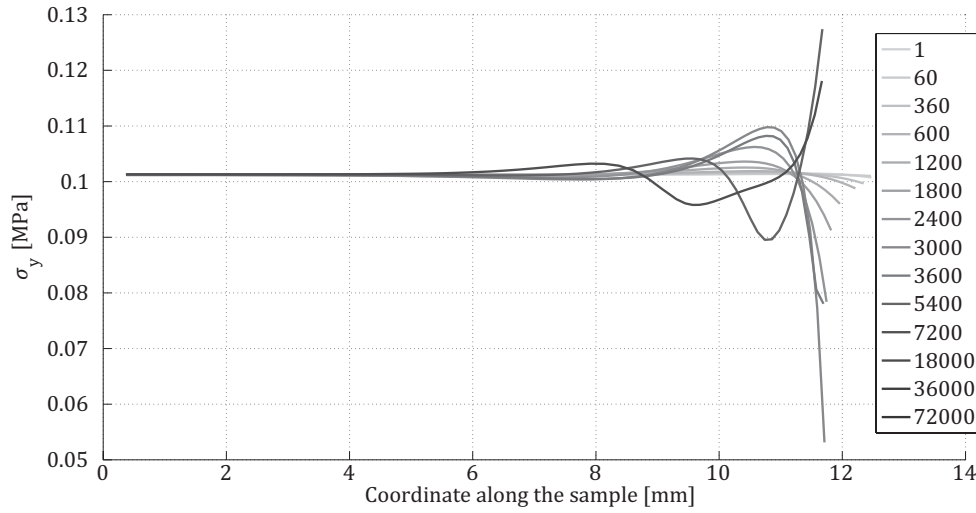
Figure 8.36: Evolution of the total axial stress along the radius of the sample.
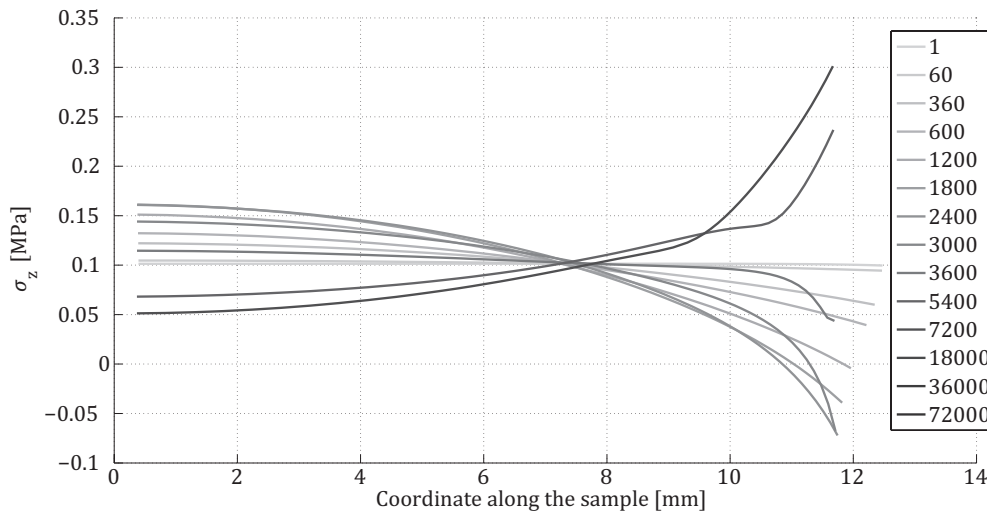
Figure 8.37: Evolution of the total orthoradial stress along the radius of the sample.

parameters are obtained (cf. Table 8.15) :

This new law allows for faster stiffening and even though it does not fit perfectly our experimental data, it stays within acceptable range. Using this new formulation, the simulation we will call the "reference" simulation is performed. This new formulation does not have any significant impact on the Krischer curve (see Fig. 8.39).

The evolution of the water pressure and of the temperature for the reference simulation are presented in Fig. 8.39 and Fig. 8.40 respectively. Temperature was not presented earlier because we do not have any data to calibrate its evolution. Still, for the sake of completeness, it is presented to give the reader insight on all the processes happening during the simulation. The water pressure distribution is still the same since the introduction of the Kozeny-Carman

Figure 8.38: Evolution of the water pressure along the radius of the sample

Parameters	Values	Units
ΔE_{max}	270	$[MPa]$
E_0	30	$[MPa]$
a	12	$[MPa]$
b	10	$[-]$

Table 8.15: Non Linear elasticity mechanical law parameters for the resorcinol formaldehyde hydrogels

formulation which was the last significant change to the hydraulic part of the problem. The evolution of elastic modulus obtained with the new formulation is presented don Fig. 8.41. It is clear that the new formulation allow for much more important Young's modulus gradient which is logical since it is now directly related to the suction and thus to the water pressure which presents a strong gradient near the drying surface. This elastic modulus distribution means that the external zone of the sample is much stiffer than is was before for the same effective stress. This means that the strain-compensation effect described earlier will be amplified. Moreover, when the external zone will be dried it will form a rigid ring with low deformability. So later in the simulation, tensile stresses are going to be generated radially by the prevented shrinkage of the inside zone of the material because of material continuity. These observations are visible on Fig. 8.42 and Fig. 8.43 describing the evolution of the radial and orthoradial total stress, respectively.

The value of the tensile stress reached orthoradially exceeds 1 MPa which could be enough to meet the tensile strength criterion. To verify it, we draw the evolution of the effective principal stresses with time as well as the evolution of the effective tensile strength of the material with time. This result is visible, at the surface of the sample, on Fig. 8.44. On this graph, it is clearly seen that the tensile failure criterion is verified. The effective orthoradial principal stress, σ'_3,
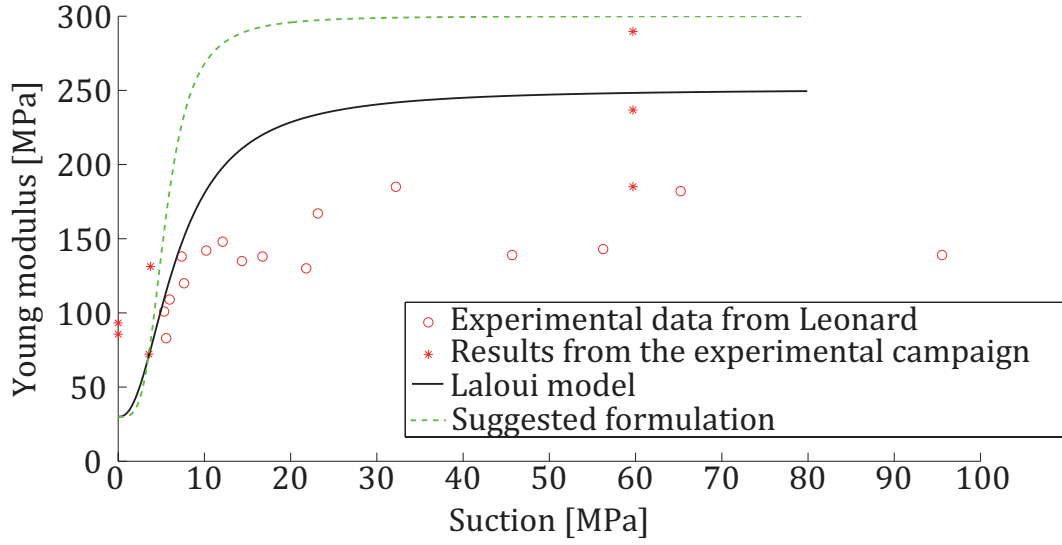
Figure 8.39: Evolution of the water pressure along the radius of the sample for the final simulation.
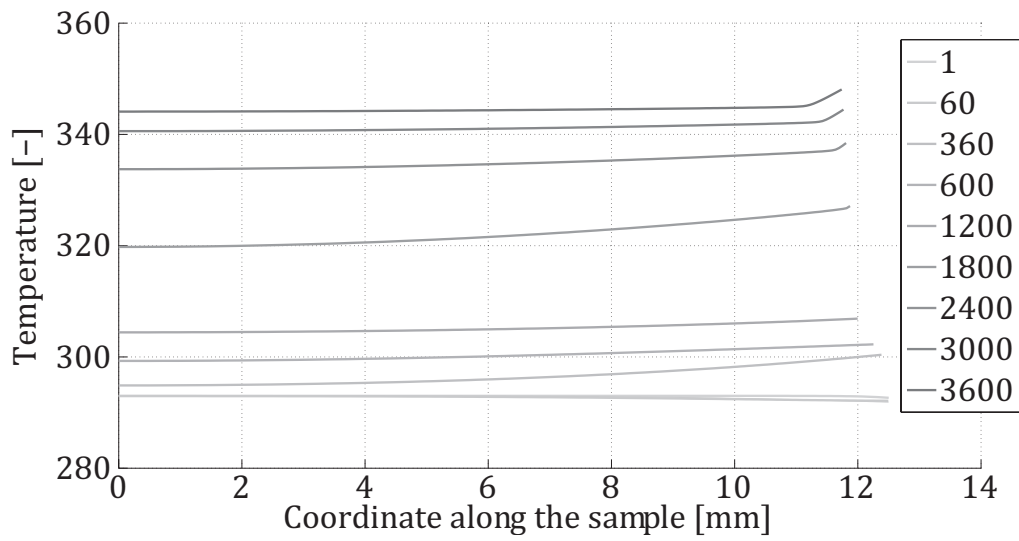
Figure 8.40: Evolution of the temperature along the radius of the sample for the final simulation.

verifies the tensile failure criterion leading to the onset of a radial crack starting at the surface of the sample. On Fig. 8.44, it is also possible to see that σ'_1, the effective principal radial stress, is coming closer to the criterion but will not reach it. This means that in this configuration orthoradial cracking is not possible in surface. This is logical because the total radial stress at the surface of the sample must be equal to the applied atmospheric pressure and thus cannot be in tension. Looking at the evolution of σ'_1, we can see that the maximum tensile value is reached
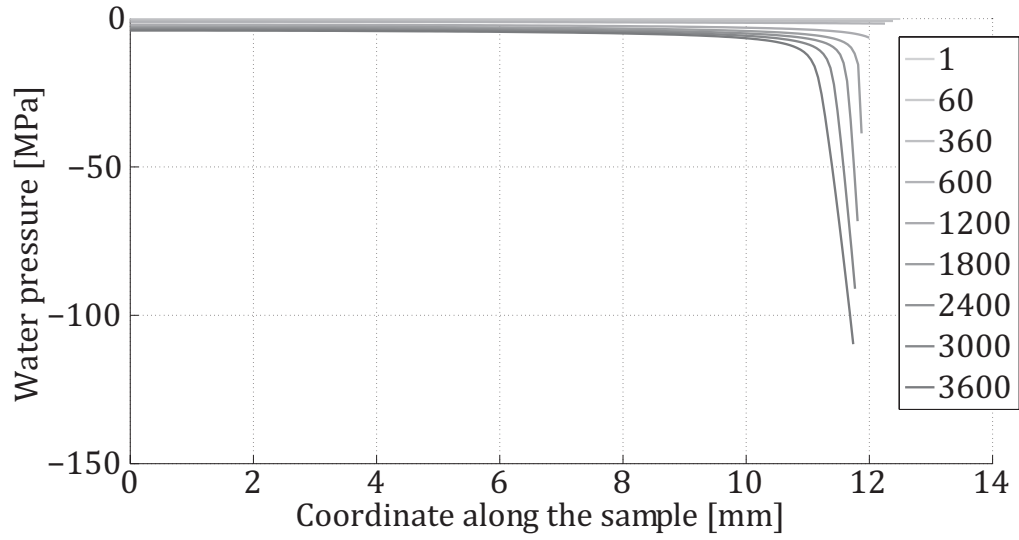
197
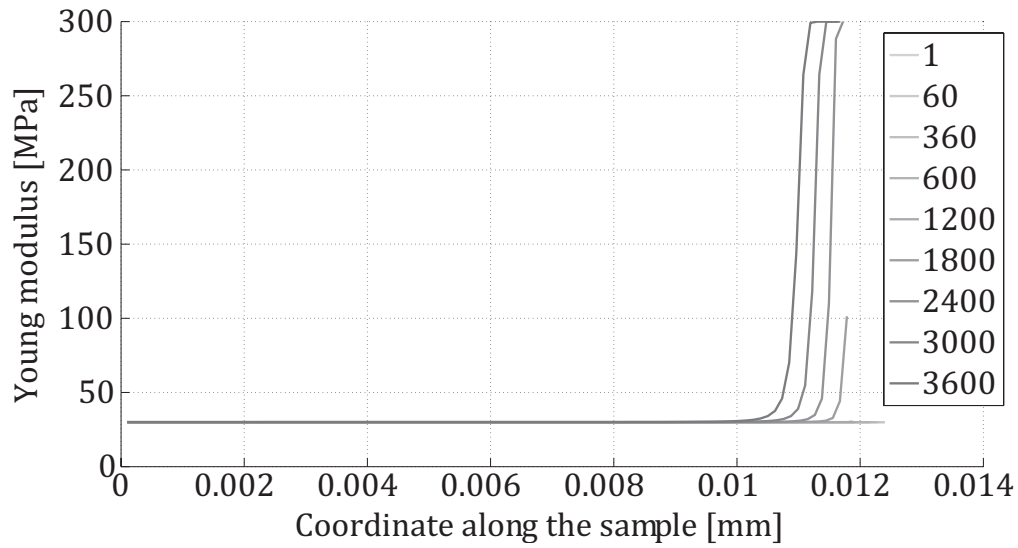
Figure 8.41: Evolution of the elastic modulus along the radius of the sample for the final simulation.
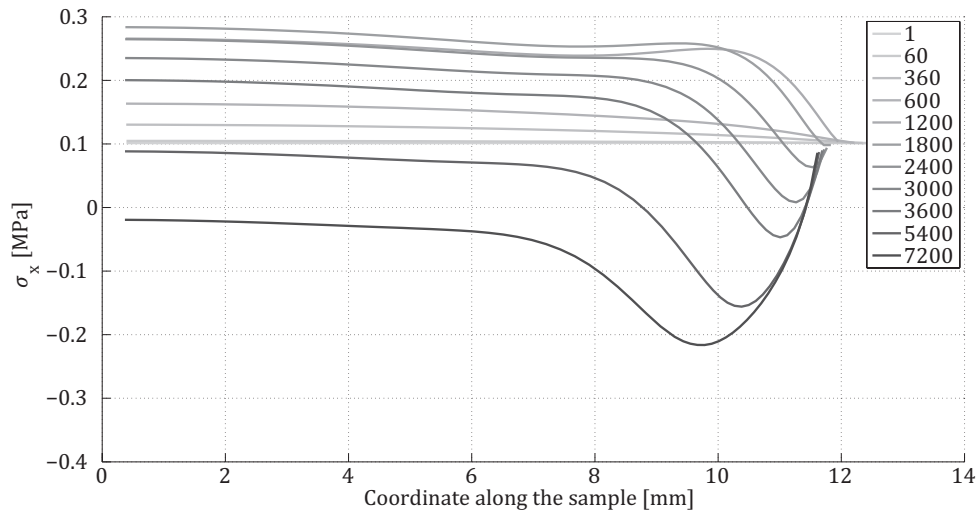
Figure 8.42: Evolution of the total radial stress along the radius of the sample.

further inside the sample and is of around 200 kPa after 2 hours. This means that orthoradial cracking will not occur in this configuration. An hypothesis is that the stiffness of the inside zone is too low and the strain compensation mechanism does not generate sufficient tensile stress. Looking further inside will also allow us to determine the crack propagation length. For the next graph we look 1 mm inside the sample and the results are visible on Fig. 8.45.

We can see that the effective orthoradial principal stress verifies once again the tensile failure criterion which means the crack is at least 1 mm long. If we go further inside, near the half
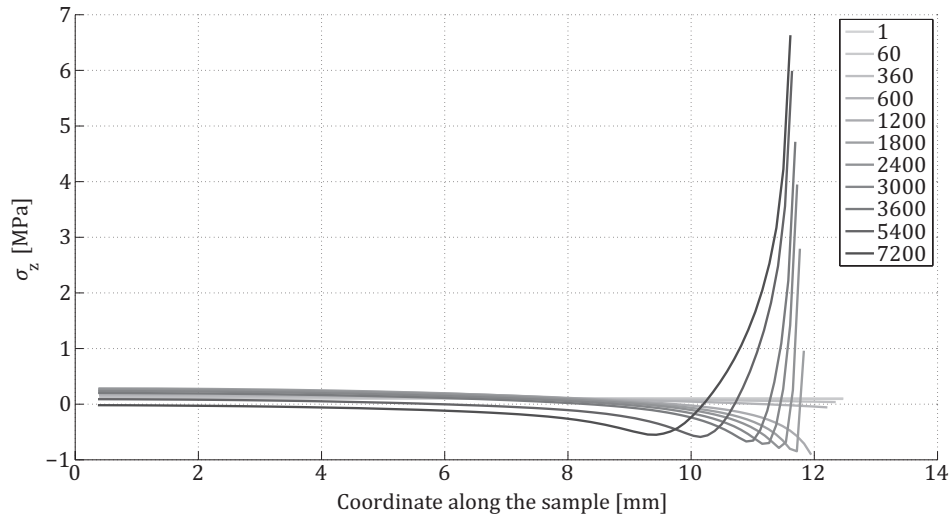
Figure 8.43: Evolution of the total orthoradial stress along the radius of the sample.
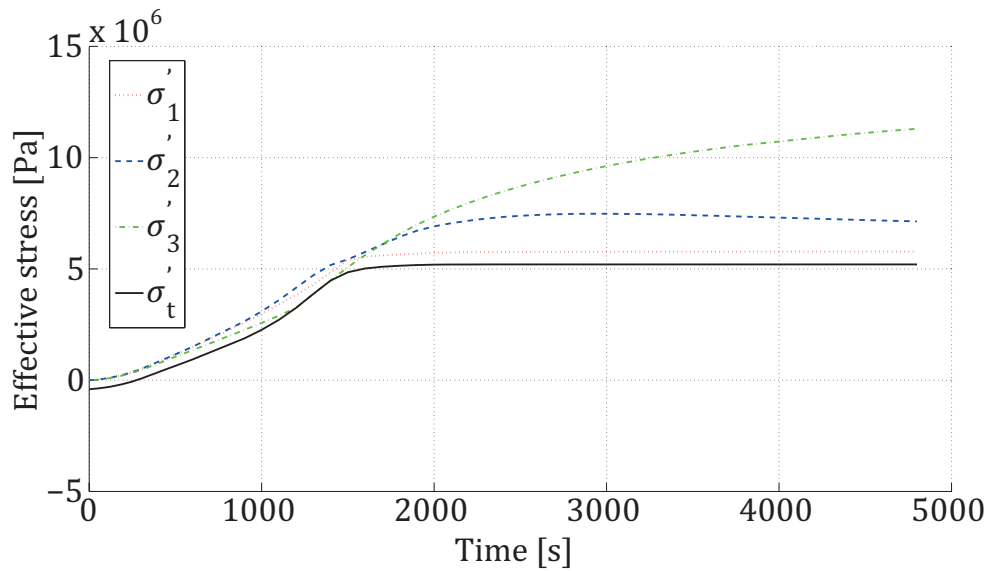
Figure 8.44: Evolution of the effective principal stresses and of the tensile failure criterion with time at the drying surface.

radius (6.25 mm from the drying surface) we obtain the following graph (Fig. 8.46). Here, the sample is still mostly undisturbed and the tensile failure criterion is not verified which means the radial crack did not propagate until there. To get a better assessment of the crack length we look at the evolution of the plastic strain along the radius of the sample (see Fig. 8.46). On this graph, is it clear that the crack propagated for a length of a bit less than a 1mm but not more than that. This cracking means that the sample cracks for around 8% of its radius which is lower than what was experimentally observed.
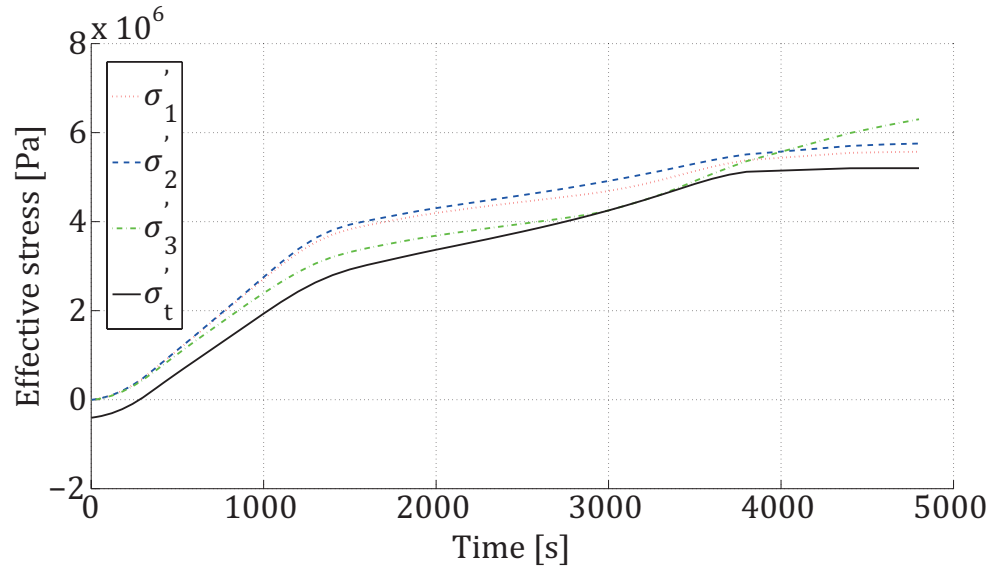
Figure 8.45: Evolution of the effective principal stresses and of the tensile failure criterion with time at 1 mm of the drying surface.
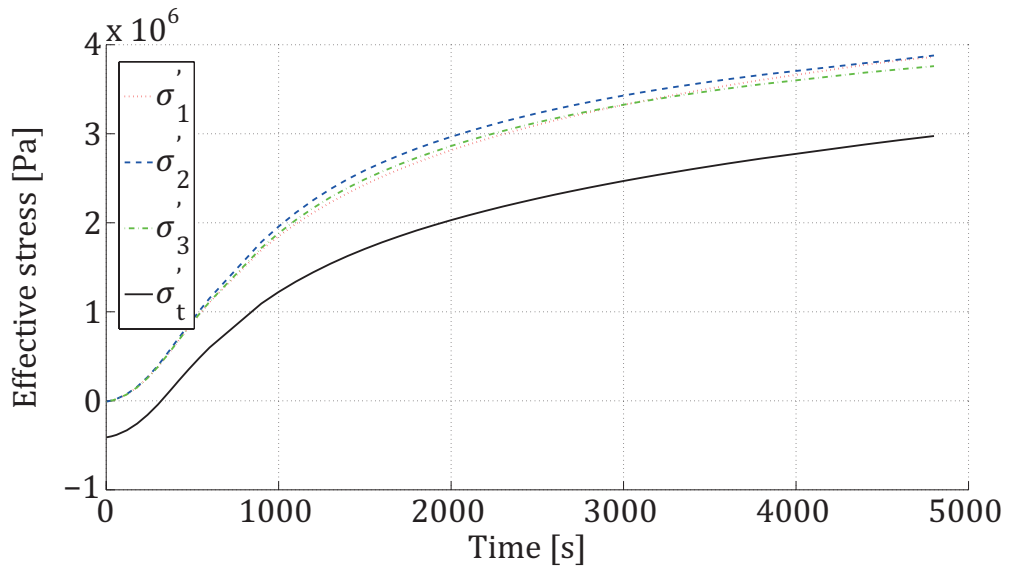
Figure 8.46: Evolution of the effective principal stresses and of the tensile failure criterion with time at 6.25 mm of the drying surface.

Sensitivity study   Our reference configuration did not allow us to closely reproduce the experimental cracking. The crack obtained does not propagate as far the experimental one and orthoradial cracking is never met. A sensitivity study is conducted to determine the parameter influencing the crack propagation length and the orthoradial cracking.
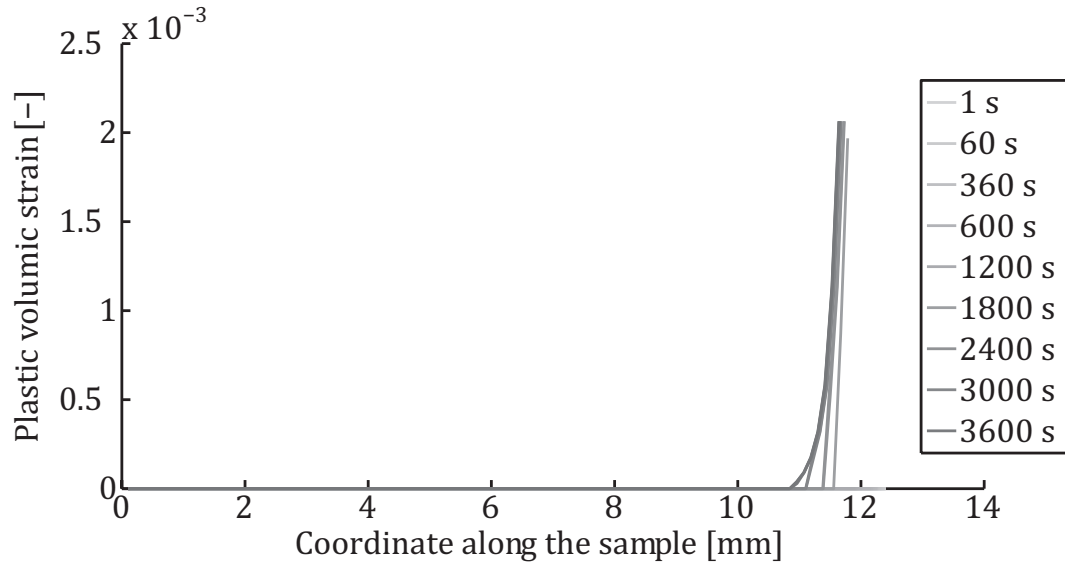
Figure 8.47: Evolution the plastic strain along the radius of the sample

Tensile strength   We tested different value of the saturated effective tensile strength, $\sigma'_{t,0}$ while keeping the same evolution in function of the suction. Value of 100 kPa, 200 kPa, 300 kPa, 500 kPa, 600 kPa (reference), 700 kPa, 1000 kPa and 1100 kPa were tested. The results are presented in the form of the crack propagation length versus the saturated effective tensile strength (cf. Fig. 8.49). Crack propagation was determined based on the evolution of the plastic strain along the radius of the sample. An example is given for $\sigma'_{t,0} = 100\ kPa$ at Fig. 8.48.
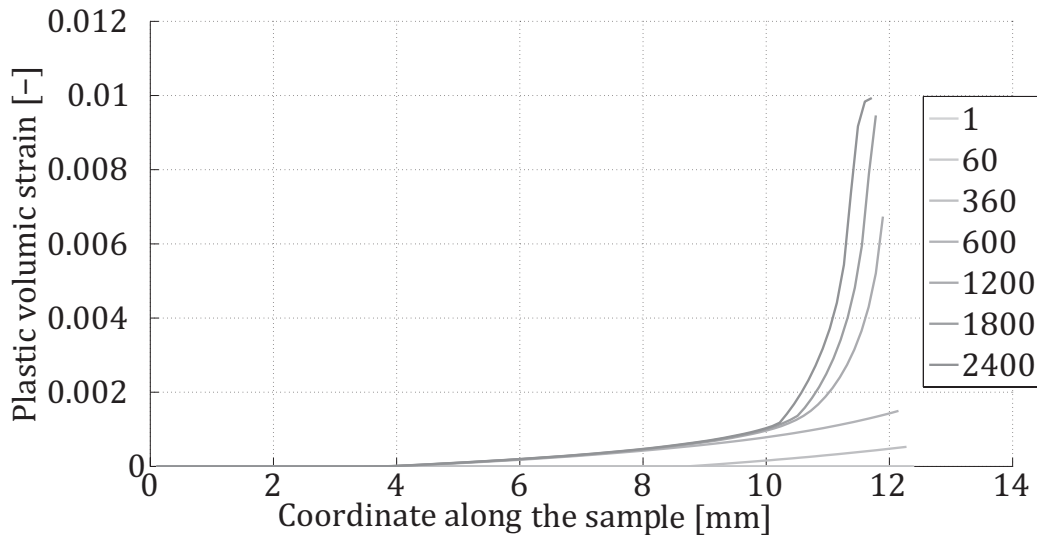
Figure 8.48: Evolution the plastic strain along the radius of the sample for $\sigma'_{t,0} = 100\ kPa$

We can see that the lower the initial tensile strength, the longer the crack will propagate. Another information obtained during the sensitivity study on the tensile strength is that for none of the values tested did orthoradial cracking occurred. It is thus not influence by the tensile strength of the material.
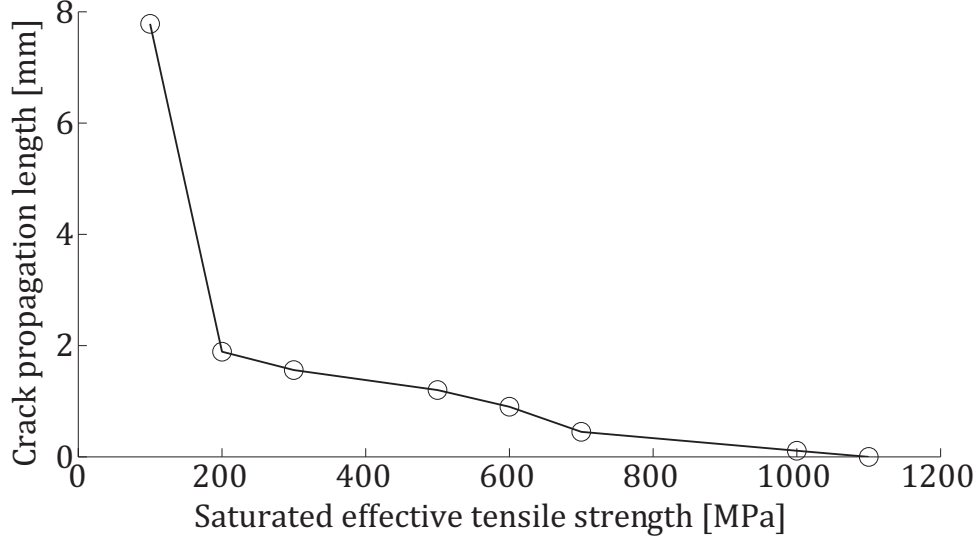
Figure 8.49: Evolution the crack propagation length in function of the saturated effective tensile stength

Orthoradial cracking Our main hypothesis concerning the development of orthoradial cracking is that the external rigid "ring", because of its much more important elastic modulus, prevents the displacement of the inside zone of the cylinder. Logically, the stiffer the rigid ring the more total tensile radial stress should be generated. We tested variation of the Young's modulus final value of 400 and 600 MPa. None of these simulations allowed the radial stress to reach the tensile criterion.

The use of the Kozeny-Carman formulation has been a meaningful addition to be able to both fit to the experimental Krischer curve but also to generate enough tensile stresses to reach the tensile criterion. Indeed the decrease in permeability due to the decrease in porosity means that a more important water pressure gradient is locally created leading to a more important local Young's modulus gradient which increases the stress compensation mechanisms. Keeping the final value of the elastic modulus at 600 MPa, we tested values of the parameters k_n and k_m of the Kozeny-Carman formulation :

$$k = k_0 \frac{(1-n_0)^{k_m}}{n_0^{k_n}} \frac{n^{k_n}}{(1-n)^{k_m}} \tag{8.21}$$

Value of $k_n = 7$, $k_m = 6$ and $k_n = 14$, $k_m = 13$ were considered because they correspond to a decrease in hydraulic conductivity of respectively 1 and 2 order of magnitude. The first simulation did not give any positive conclusive results but the second one allowed the radial

total stress to reach the tensile criterion as visible on Fig. 8.50. Fig. 8.50 describes the evolution of the effective principal stresses with time 1 mm away from the drying surface.
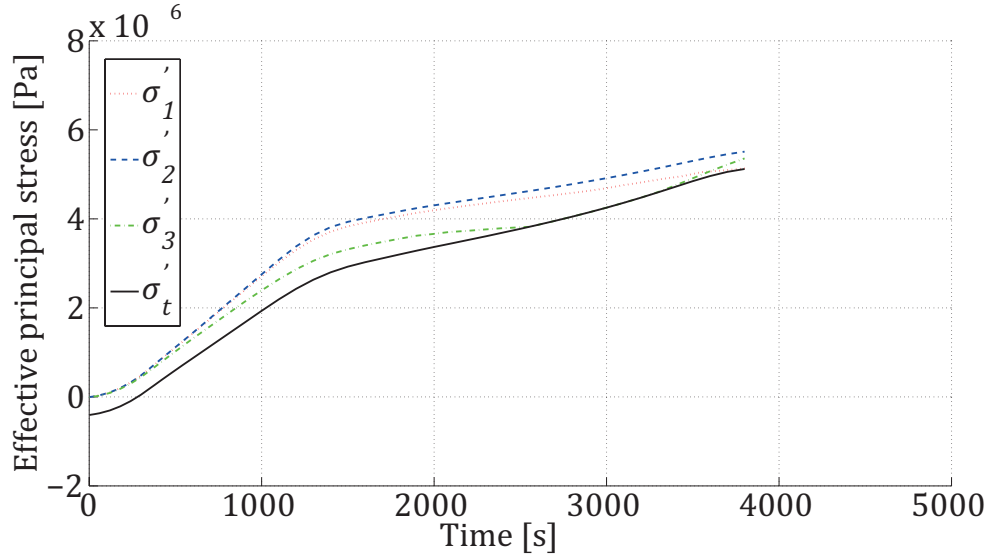
Figure 8.50: Evolution of the effective principal stresses with time at a distance of 1 mm from the drying surface

The simulation stopped converging after touching the criterion in that direction. It is assumed this is a logical behavior induced by the axisymmetric condition imposed which does not allow for the propagation of an orthoradial cracks. The cracks length cannot be determined in this configuration either. Depending on the conditions, it is thus possible for the sample to crack orthoradialy but the parameters required for this result are far from our experimental and bibliographic ones. The main problem with the variation of the parameters imposed is the value of the Kozeny-Carman parameters because they significantly modify the drying kinetics as visible on Fig. 8.51 which is not concordant with experimental data.

8.6 Conclusion

In this chapter, we combined all the tools presented throughout this PhD thesis to try to predict desiccation cracking. This part of the thesis was done on a second material because Boom clay due to its geological history always cracks along predefined planes. It was thus not appropriate to validate the tensile failure criterion implemented. Resorcinol Formaldehyde hydrogels were chosen because of previous interest of the team from the chemical engineering department (LGC) in its drying behavior and cracking conditions. The LGC is interested in the drying behavior of this material because, after cure, it can be submitted to pyrolysis to obtain high specific surface carbonate porous structures which have many industrial applications Job (2005). But depending on the curing conditions, the material may suffer desiccation cracking which is detrimental to the end goal where a monolithic structure is required. The chapter start by introducing the RF-hydrogels as well as presenting their documented properties. Then
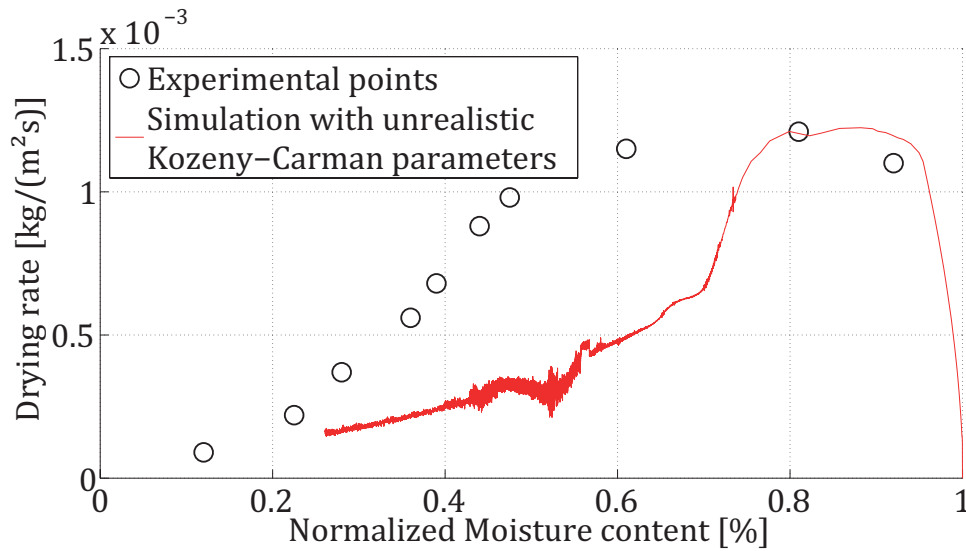
Figure 8.51: Krischer curve for the unrealistic values of the Kozeny-Carman parameters.

the experimental campaign conducted to investigate undocumented properties is detailed. Finally, numerical simulations are performed to simulate convective drying experiment on RF-hydrogels. A step by step approach is used to highlight the different mechanisms taken into account and their influence on the drying kinetic and tensile stress generation. More specifically, Kozeny-Carman formulation is used to account for account for the reduced hydraulic conductivity due to a decrease in porosity. This is an effect that had not been taken into account before due to low variation of the porosity of Boom clay during our previous simulations. A new non-linear elasticity, directly accounting for suction, is also suggested. Finally, using all these features, the tensile criterion can be met and desiccation cracking predicted. The model is able to predict desiccation cracking but not to perfectly reproduce the experimental behavior. The length of the crack is not the same and orthoradial cracking could not be reproduced. To assess the parameters controlling these behavior a small sensitivity study is conducted and show that the length of the crack is directly dependent on the tensile strength of the material while orthoradial cracking may be related to elastic modulus gradient. This is thus the end of the first step in desiccation cracking modeling with the implementation of a tensile failure criterion and the validation of its capacity to predict desiccation cracking. More work is still required, though, to upgrade the model and allow for more accurate predictions.

The last chapter of this PhD work will conclude with a summary of the work produced as well as outlooks for future developments.

Chapter 9

Conclusion

9.1 Summary

Porous material drying is a process used in many engineering fields such as food (conversation), plastic (polymer), chemical, pharmaceutical and wood (paper paste, composite beam for construction) industries as well as any manufactured process based on paste or powder. It is also of importance in civil engineering because of its impact on soil properties and soil-structure interaction.

This PhD work is part of a F.R.S-FNRS project revolving around unsaturated porous material desiccation cracking and supported by the collaboration of research groups from the geomechanical team (GEO3) and the chemical engineering team (LGC) of the University of Liège. As such this work is separated in two main parts related to materials of interest in the scope of each research group ongoing works. These parts, though studying different materials, share the same general goal of predicting desiccation cracks onset. To do so, one must first have a good understanding of the drying behavior of unsaturated porous medium. Therefore, the first chapters of this work focused on establishing all the notions required to study and model drying phenomena. It starts by introducing the notion of porous medium and the mathematical tools used to describe it. Then the drying phenomenon itself is considered from the different means of drying to the methods used to analyze it as well as the existing models. Its most direct consequence - shrinkage - is also described. Finally, the finite element method is presented as the framework used to conduct numerical simulations.

For the geomechanical research group of the University of Liège, the study of the drying behavior is conducted under the scope of deep geological storage of nuclear wastes. This follows previous works of the team carried on nuclear wastes disposal. This concept aims at sealing the wastes away for a period long enough to ensure that radionucleides reaching the biosphere are under the natural activity level. Wastes isolation is guaranteed by the combination of natural and engineered barriers, referred to as the multi-barriers principle. The natural barrier is the geological layer. The wastes are placed in super-containers formed of different layers that all have a specific role with the goal of decreasing the *risk* of biosphere contamination. The geological barrier is the last rampart protecting the environment. Its study is thus of the utmost importance to be sure that it can withstand the thermo-hydro-mechanical loading induced by the nuclear wastes storage.

The excavation of the galleries generates stress modifications and eventually fractures in the surrounding medium leading to the creation of an excavated damage zone. The properties of

this zone can be further degraded by desiccation cracks resulting from the ventilation needed to allow for people circulation during the operation period of the galleries. This may lead to a zone with important properties modifications such as important hydraulic permeability increase which could prevent the geological barrier from playing its containment role.

Given the importance of ensuring good sealing conditions, understanding the drying behavior of the host rock is essential. In Belgium, the considered potential host rock is Boom clay which is thus the material studied throughout the first part of this PhD work. In view of the general significance and environmental and sociological implications of finding a reliable solution to the nuclear wastes problem, Boom clay is abundantly studied and documented. A short summary of its geology is given and its thermo-hydro-mechanical properties are presented. An experimental convective drying campaign was conducted to gather the data required for the validation of our numerical model. The results of the experimental campaign are presented and analyzed in the light of the latest development in drying science. Thermo-hydro-mechanical simulations are then conducted to reproduce the experimental observations. A comprehensive step by step approach is followed to highlight the influence of each mechanism on the overall process. This approach clearly shows the importance of including the thermal and mechanical aspects of the problem. Indeed, even the water output (i.e. drying rate) which is a mostly hydraulic problem cannot be accurately estimated if these couplings are neglected. Non linear elasticity is also included to improve the accuracy of the numerical shrinkage rate. By combining all these features, the simulations performed reproduce very accurately the experimental results. Nonetheless, Boom clay because of its geological history presents a strong anisotropy and even though desiccation cracking was observed during the experiments, it always occured along the bedding planes of the material. It was decided that a material not presenting pre-existing failure planes would be more adequate for desiccation cracking modeling.

The second part of this PhD thesis uses the expertise acquired during the first one as a stepping stone to go further and focuses on the modeling of desiccation cracking. It starts with a literature review of the desiccation cracking phenomenon from its possible causes to the notion of material tensile strength as well as the different means to measure it. Existing numerical models are also presented. Then, the chosen model - the one suggested by Péron (2008) in his PhD thesis - is implemented in Liège finite element code LAGAMINE. Several material point simulations are performed to test the behavior of the implemented constitutive law. Finally, convective drying experiments are simulated using the described framework. The new material chosen for the numerical validation is a Resorcinol Formaldehyde hydrogel. It was chosen because of previous interest of the team from the chemical engineering department (LGC) in its drying behavior and cracking conditions. The LGC is interested in the drying behavior of this material because, after cure, it can be submitted to pyrolysis to obtain high specific surface carbonate porous structures which have many industrial applications Job (2005). But depending on the curing conditions, the material may suffer desiccation cracking which is detrimental to the end goal where a monolithic structure is required. The simulations performed using the implemented tensile failure criterion in combination with the pre-existent thermo-hydro-mechanical framework allowed to successfully predict crack initiation. The crack obtained does not accurately reproduce the experimental behavior as its length is a bit shorter than the propagation experimentally observed. Orthoradial cracking could not be reproduced either in the case of the reference simulation. To get a better insight on the parameters controlling those mechanisms, a sensitivity study is conducted.

9.2   Original contributions

The aim of this PhD thesis was to extend the existing framework by implementing a tensile failure criterion in order to predict desiccation cracking. It is based on previous developments from the geomechanics and chemical engineering teams of the University of Liège and more specifically on the work of Gerard (2011) for the atmosphere-material fluids transfer, the work of Collin (2003) for thermo-hydro-mechanical couplings, the work of Barnichon (1990) for constitutive law implementation and the work of Job (2005) for RF hydrogels properties and drying behavior.

Hence, several aspects presented throughout this thesis had already been discussed in previous works.

The main original contribution of the first part of this work was to perform highly coupled simulations putting together, for the first time in drying experiment simulations, thermal, hydraulic and mechanical aspects. The results obtained using these couplings are themselves of real interest because it is believed that few codes are able to reproduce, with this level of accuracy, the drying behavior of unsaturated porous media. These results highlighted the importance of accounting for all the couplings even if mainly thermal and or hydraulic aspects are of interest. Non-linear orthotropic elasticity was also added to the existing framework to better reproduce the shrinkage and shrinkage rate observed. The incremental approach followed to present the results is also of interest because it emphasizes the influence of each coupling and/or added level of complexity, furthering our understanding of the drying phenomenon.

In the second part, the main contribution was the implementation of a tensile failure criterion in the existing thermo-hydro-mechanical framework of the finite element code LAGAMIME and its validation on simple material point problems. Convective drying experiments on RF hydrogels were also conducted. The results are presented following a similar step by step approach to put the emphasis on each of the mechanisms influence on the drying kinetic as well as on tensile strength generation. Finally, desiccation cracking was successfully predicted but the crack length does not perfectly fit the experimental observations. A sensitivity study is also conducted to get a better understanding of the parameters influencing crack length and occurrence.

9.3   Outlook

Drying behavior   Even though the model as shown the capacity to reproduce the drying kinetics of unsaturated porous medium, the very important water pressure gradient appearing near the drying surface of the material causes numerical convergence problems drastically increasing modeling computational time. This may either be due to an inability of the interpolation function to cope with the important gradient or be a conceptual flaw of the boundary layer model. Indeed, the boundary condition demand in water is constant but as the material desaturates, its permeability decreases to a point where it is very difficult to produce a water flow answering the demand of the boundary condition. This problem should be investigated as solving it would open up the door to further developments by importantly reducing calculation time which was a limiting factor during this work.

Resorcinol Formaldehyde hydrogels   Experiments were conducted to characterize the mechanical properties of the hydrogels but more tests are required :

- to study the evolution of the hydraulic permeability with decreasing water content. It was assumed to follow the same trend as the water retention curve in this work ;

- to study the evolution of hydraulic conductivity with the decrease of porosity due to shrinkage. A Kozeny-Carman (Kozeny (1927)) formulation was used but its parameters are not based on experimental observations ;

- to study the evolution of evolution of the water retention curve as a function of porosity. This could be done by performing dynamic vapor sorption experiments on mechanically pre-compacted samples ;

- to investigate the thermal properties of the material which are mostly undocumented ;

- to perform more tensile strength measurements. It appears necessary to perform more Brazilian tests to get a clearer tendency of the evolution of the tensile strength with water content. It would also be interesting to measure it with different devices to confront those results to the one obtained with the Brazilian tests.

Desiccation cracking modeling   The model implemented was used to predict desiccation cracking but only on simple geometries. It would be interesting to apply it to more complex geometries and to extend it to 3D problems. It would also be interesting to confront it further to experimental data. The validation performed in this thesis is based on a single sample which was arbitrarily chosen. Also, the post failure behavior is not addressed in this work. We tried to account for material damage using softening but the plastic zones never stay plastic for long because of recompression due to ulterior shrinkage of the zone where the tensile strength criterion was met. This means that plastic strain accumulation is low and that a very brutal softening function would be required to lead to localization and overall failure of the sample. This is not numerically supported and leads to convergence problems or to a snap back phenomenon. Other options have to be considered to account for the post cracking behavior such as cohesive interface opening or X-FEM for remeshing with a potential function for crack propagation.

Appendix A

Tensile strength consitutive law implementation

Contents

e

A.1   Principal stress tensor and deviatoric stress tensor

There exists three orthogonal direction at a point P of a body such that area normal to these directions only experiences normal stresses (no shear). These three directions are called principal directions at P and the corresponding normal stresses are called principal stresses. Referring to the principal axis referential, the non-diagonal terms of the stress tensor must vanish. The principal stress tensor is thus defined as :

$$\sigma_{ij} = \begin{bmatrix} \sigma_1 & 0 & 0 \\ 0 & \sigma_2 & 0 \\ 0 & 0 & \sigma_3 \end{bmatrix} \tag{A.1}$$

And the deviatoric stress tensor is given by :

$$\hat{\sigma}_{ij} = \begin{bmatrix} \sigma_1 - \frac{I_\sigma}{3} & 0 & 0 \\ 0 & \sigma_2 - \frac{I_\sigma}{3} & 0 \\ 0 & 0 & \sigma_3 - \frac{I_\sigma}{3} \end{bmatrix} \tag{A.2}$$

A.2   From the principal stresses to the stress invariants

Let us consider a given stress state, $P(\sigma_1, \sigma_2, \sigma_3)$ represented in the principle stress space on Fig. A.1.
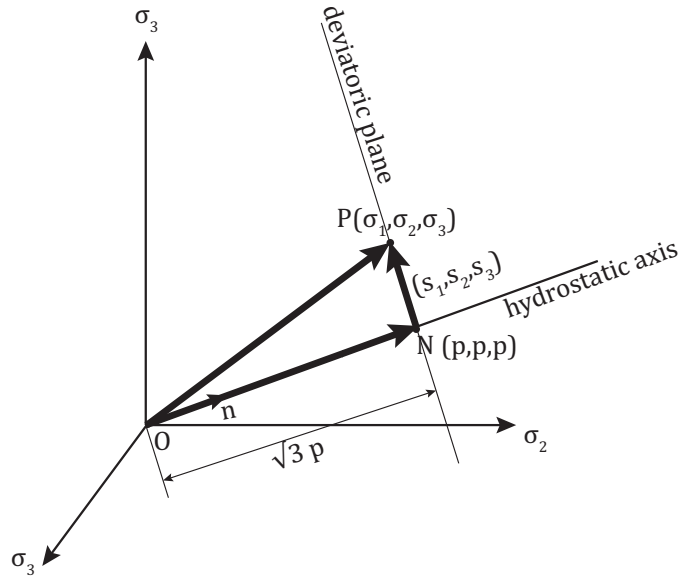
Figure A.1: Principal stress space

If we consider the hydrostatic axis ($\sigma_1 = \sigma_2 = \sigma_3$) of normal $\mathbf{n}(\frac{1}{\sqrt{3}}, \frac{1}{\sqrt{3}}, \frac{1}{\sqrt{3}})$, then the stress vector $\mathbf{OP}$ can be expressed as a combination of a vector $\mathbf{ON}$ on the hydrostatic axis and a $\mathbf{NP}$ vector perpendicular to $\mathbf{ON}$. Basically, it writes :

$$\mathbf{OP} = \mathbf{ON} + \mathbf{NP} \tag{A.3}$$

We know that

$$|\mathbf{ON}| = \mathbf{OP} \cdot \mathbf{n} = \frac{1}{\sqrt{3}}(\sigma_1 + \sigma_2 + \sigma_3) = \sqrt{3}\, p. \tag{A.4}$$

And thus

$$\mathbf{ON} = |\mathbf{ON}|\, |\mathbf{n}| = (p, p, p) = (\frac{I_\sigma}{3}, \frac{I_\sigma}{3}, \frac{I_\sigma}{3}) \tag{A.5}$$

From these we can deduce

$$\mathbf{NP} = (\sigma_1, \sigma_2, \sigma_3) - (p, p, p) = (\sigma_1 - p, \sigma_2 - p, \sigma_3 - p) = (s_1, s_2, s_3) \tag{A.6}$$

where s_1, s_2 and s_3 are the diagonal terms of the deviatoric stress tensor. The vector $\mathbf{ON}$ and $\mathbf{NP}$ represent the hydrostatic and deviatoric stress component of the stress state. Using projection in the deviatoric plane it is possible to express the components of the deviatoric stress tensor in function of the second invariant of the deviatoric stress tensor, $II_{\hat{\sigma}}$, and the similitude angle, θ :

$$s_1 = \frac{2II_{\hat{\sigma}}}{\sqrt{3}}\, cos\theta \tag{A.7}$$

$$s_2 = \frac{2II_{\hat{\sigma}}}{\sqrt{3}}\, cos(\frac{2\pi}{3} - \theta) \tag{A.8}$$

$$s_3 = \frac{2II_{\hat{\sigma}}}{\sqrt{3}}\, cos(\frac{2\pi}{3} + \theta) \tag{A.9}$$

210

The principal stresses can thus be expressed as :

$$\begin{pmatrix} \sigma_1 \\ \sigma_2 \\ \sigma_3 \end{pmatrix} = \begin{pmatrix} \frac{I_\sigma}{3} \\ \frac{I_\sigma}{3} \\ \frac{I_\sigma}{3} \end{pmatrix} + \frac{2II_{\hat\sigma}}{\sqrt3} \begin{pmatrix} cos\theta \\ cos\left(\theta - \frac{2\pi}{3}\right) \\ cos\left(\theta + \frac{2\pi}{3}\right) \end{pmatrix} \tag{A.10}$$

with θ defined as $cos3\theta = \frac{3\sqrt3}{2}\frac{III_{\hat\sigma}}{II_{\hat\sigma}^3}$.

Still, the stress invariants are linked to Lode's angle rather than the similitude angle. It is possible to pass from one to the other using the following relationship :

$$cos3\theta = \frac{3\sqrt3}{2}\frac{III_{\hat\sigma}}{II_{\hat\sigma}^3} = sin(-3\beta) \tag{A.11}$$

where β is Lode's angle. It thus writes :

$$cos3\theta = sin(-3\beta) \tag{A.12}$$

$$\Longleftrightarrow cos2\theta cos\theta - 2sin\theta sin\theta = -sin2\beta cos\beta - cos2\beta sin\beta \tag{A.13}$$

$$\Longleftrightarrow (1 - 2sin^2\theta)cos\theta - 2sin\theta cos\theta sin\theta = -2sin\beta cos^2\beta - (1 - 2sin^2\beta)sin\beta \tag{A.14}$$

$$\Longleftrightarrow cos\theta - 4(1 - cos^2\theta)cos\theta = -2sin\beta(1 - sin^2\beta) - sin\beta + 2sin^3\beta \tag{A.15}$$

$$\Longleftrightarrow 4cos^3\theta - 3cos\theta = 4sin^3\beta - 3\sin\beta \tag{A.16}$$

$$\Longleftrightarrow 4(cos^3\theta - sin^3\beta) - 3(cos\theta - sin\beta) = 0 \tag{A.17}$$

$$\Longleftrightarrow 4(cos\theta - sin\beta)(cos^2\theta + cos\theta sin\beta + sin^2\beta) - 3(cos\theta - sin\beta) = 0 \tag{A.18}$$

$$\Longleftrightarrow (cos\theta - sin\beta)(4cos^2\theta + 4cos\theta sin\beta + 4sin^2\beta - 3) = 0 \tag{A.19}$$

This equation has 3 solutions which are :

$$cos\theta = sin\beta \tag{A.20}$$

$$cos\theta = sin(\frac{\pi}{3} - \beta) \tag{A.21}$$

$$cos\theta = sin(-\frac{\pi}{3} - \beta) \tag{A.22}$$

By solving these three new trigonometric equations, it comes :

$$\theta = \beta - \frac{\pi}{2} \tag{A.23}$$

$$\theta = \frac{\pi}{2} - \beta \tag{A.24}$$

$$\theta = \frac{\pi}{3} - \beta - \frac{\pi}{2} = -\frac{\pi}{6} - \beta \tag{A.25}$$

$$\theta = -\frac{\pi}{3} + \beta + \frac{\pi}{2} = \frac{\pi}{6} + \beta \tag{A.26}$$

$$\theta = -\frac{\pi}{3} - \beta - \frac{\pi}{2} = -\frac{5\pi}{6} - \beta \tag{A.27}$$

$$\theta = \frac{\pi}{3} + \beta + \frac{\pi}{2} = \frac{5\pi}{6} + \beta \tag{A.28}$$

The existence conditions on θ and β are:

$$\theta \in [0; \frac{\pi}{3}] \qquad\qquad \beta \in [-\frac{\pi}{6}; \frac{\pi}{6}]$$

From it, we can conclude that the first, fifth and sixth solutions are never possible. The second solution is only possible if $\beta = \frac{\pi}{6}$ and the third one is only possible for $\beta = -\frac{\pi}{6}$. This leaves us with the fourth solution which is possible for all values of β.

A.3 Mohr-Coulomb criterion from principal stresses to stress invariants

The Mohr-Coulomb criterion is characterized in the principal stress plane by the following yield criterion :

$$f^1 \equiv \sigma_1 - \sigma_3 + (\sigma_1 + \sigma_3)sin\phi + 2c\,cos\phi = 0 \tag{A.29}$$

where c is the cohesion and ϕ is the friction angle. Using Eq. A.10, the criterion writes :

$$\frac{I_\sigma}{3}sin\phi + II_{\hat{\sigma}}\left(sin(\theta + \frac{\pi}{3}) + \frac{sin\phi cos(\theta + \frac{\pi}{3})}{\sqrt{3}}\right) - c\,cos\phi = 0 \tag{A.30}$$

Now using the solution (Eq. A.26) of the previous development, the criterion writes :

$$f^1 \equiv \frac{I_\sigma}{3}sin\phi + II_{\hat{\sigma}}\left(cos\beta - \frac{sin\phi sin\beta}{\sqrt{3}}\right) - c\,cos\phi = 0 \tag{A.31}$$

$$f^1 \equiv II_{\hat{\sigma}} - M_{MC}(I_\sigma + C) = 0 \tag{A.32}$$

where $M_{MC} = \dfrac{sin\phi}{3cos\beta - \sqrt{3}sin\beta sin\phi}$ and $C = \dfrac{3c}{\tan\phi}$.

A.4 Tension cut-off from principal stresses to stress invariants

The tension cut off is defined by the following three surfaces :

$$f^2 \equiv \sigma_3 = -\sigma_t \tag{A.33}$$

$$f^3 \equiv \sigma_2 = -\sigma_t \tag{A.34}$$

$$f^4 \equiv \sigma_1 = -\sigma_t \tag{A.35}$$

where σ_t is the uniaxial tensile strength of the material. Using Eq.A.10, the three surfaces writes :

$$f^2 \equiv \frac{I_\sigma}{3} + \frac{2}{\sqrt{3}}II_{\hat{\sigma}}cos(\theta + \frac{2\pi}{3}) + \sigma_t = 0 \tag{A.36}$$

$$f^3 \equiv \frac{I_\sigma}{3} + \frac{2}{\sqrt{3}}II_{\hat{\sigma}}cos(\theta) + \sigma_t = 0 \tag{A.37}$$

$$f^4 \equiv \frac{I_\sigma}{3} + \frac{2}{\sqrt{3}}II_{\hat{\sigma}}cos(\theta - \frac{2\pi}{3}) + \sigma_t = 0 \tag{A.38}$$

In the same manner as for the Mohr-Coulomb criterion, using Eq. A.26, the criterion writes :

$$f^2 \equiv II_{\hat{\sigma}} + \frac{1}{-3cos\beta - \sqrt{3}sin\beta}(I_\sigma + 3\sigma_t) = 0 \tag{A.39}$$

$$f^3 \equiv II_{\hat{\sigma}} + \frac{1}{2\sqrt{3}sin\beta}(I_\sigma + 3\sigma_t) = 0 \tag{A.40}$$

$$f^4 \equiv II_{\hat{\sigma}} + \frac{1}{3cos\beta - \sqrt{3}sin\beta}(I_\sigma + 3\sigma_t) = 0 \tag{A.41}$$

Appendix B

Analytical formulation of the derivative for the implementation of the yield surfaces into LAGAMINE

Contents

B.1   Cohesive frictional failure mechanism

The cohesive frictional failure yield surface expressed in the stress invariants plane reads :

$$f^1 \equiv II_{\hat{\sigma}} - M_1(I_\sigma + C) = 0 \tag{B.1}$$

where $M_1 = \frac{2sin\phi}{\sqrt{3}(3-sin\phi)}$ is the slope of the criterion and $C = \frac{3c}{\tan\phi}$ is its intersection with the horizontal axis and are dependent on the cohesion, c, and the frictional angle, ϕ. The consistency equation at the kth iteration at point E (after the elastic predictor) writes:

$$f^1(\sigma_{E,ij}^{'(k+1)}, \kappa_{E,m}^{(k+1)}) + \frac{\partial f^1}{\partial \sigma_{E,ij}^{'(k+1)}}\Delta\sigma_{ij}^{'p\,(k+1)} + \frac{\partial f^1}{\partial \kappa_{E,m}^{(k+1)}}\Delta\lambda^{p\,1}\frac{d\kappa_m^1}{d\varepsilon_d^{p\,(k+1)}}val^1 = 0 \tag{B.2}$$

where κ_m is a vector of internal plastic variables and ε_d^p is the Von Mises equivalent plastic strain given by :

$$\varepsilon_d^p = \int_0^t \sqrt{\frac{2}{3}\dot{\hat{\varepsilon}}_{ij}^p \dot{\hat{\varepsilon}}_{ij}^p} dt \tag{B.3}$$

and val^1 is the relation between the plastic multiplier and the Von mises equivalent strain rate :

$$val^1 = \sqrt{\frac{2}{3}\left(\frac{\partial g^1}{\partial \sigma'_{ij}}\frac{\partial g^1}{\partial \sigma'_{ji}} - \frac{1}{3}\frac{\partial g^1}{\partial \sigma'_{kk}}\frac{\partial g^1}{\partial \sigma'_{ll}}\right)} \tag{B.4}$$

In order to implement the criterion in LAGAMINE, the different derivatives of the previous equations need to be defined.

B.1.1 Derivative with respect to stress

The derivatives of the yield surface with respect to the effective stress are obtained by the chain rule:

$$\frac{\partial f^1}{\partial \sigma'_{ij}} = \frac{\partial f^1}{\partial I_\sigma}\frac{\partial I_\sigma}{\partial \sigma'_{ij}} + \frac{\partial f^1}{\partial II_{\hat{\sigma}}}\frac{\partial II_{\hat{\sigma}}}{\partial \sigma'_{ij}} \tag{B.5}$$

with

$$\frac{\partial f^1}{\partial I_\sigma} = -M_1 \qquad\qquad \frac{\partial I_\sigma}{\partial \sigma'_{ij}} = \delta_{ij}$$

$$\frac{\partial f^1}{\partial II_{\hat{\sigma}}} = 1 \qquad\qquad \frac{\partial II_{\hat{\sigma}}}{\partial \sigma'_{ij}} = \frac{\hat{\sigma}'_{ij}}{2II_{\hat{\sigma}}}$$

B.1.2 Derivative with respect to plastic variables

The derivative of the yield surface with respect to the plastic variable is given by:

$$\frac{\partial f^1}{\partial \kappa_m} = \frac{\partial f^1}{\partial c} + \frac{\partial f^1}{\partial \phi} \tag{B.6}$$

with

$$\frac{\partial f^1}{\partial c} = -\frac{3M_1}{tg\phi} \tag{B.7}$$

$$\frac{\partial f^1}{\partial \phi} = \frac{2I_\sigma}{\sqrt{3}}\left(\frac{cos\phi}{3-sin\phi} + \frac{cos\phi\,sin\phi}{(3-sin\phi)^2}\right) - \frac{6c}{\sqrt{3}}\left(\frac{sin\phi}{3-sin\phi} + \frac{cos^2\phi}{(3-sin\phi)^2}\right) \tag{B.8}$$

The terms $\frac{d\kappa_m^1}{d\varepsilon_d^p}$ becomes :

$$\frac{d\kappa_m^1}{d\varepsilon_d^p} = \frac{dc}{d\varepsilon_d^p} + \frac{d\phi}{d\varepsilon_d^p} \tag{B.9}$$

Given the hardening rules :

$$\phi = \phi_0 + \frac{(\phi_f - \phi_0)\varepsilon_d^p}{B_\phi + \varepsilon_d^p} \tag{B.10}$$

$$c = c_0 + \frac{(c_f - c_0)\varepsilon_d^p}{B_c + \varepsilon_d^p} \tag{B.11}$$

where ϕ_0 and c_0 are respectively the initial values of the friction angle and of the cohesion and ϕ_f and c_f are the final values. The coefficient B_{phi} and B_c correspond to the deviatoric plastic strain at half the variation between the initial and final values of the friction angle and the cohesion respectively. The derivatives thus writes :

$$\frac{d\phi}{d\varepsilon_d^{p\,(k+1)}} = \frac{\phi_f - \phi_0}{B_\phi + \varepsilon_d^p} - \varepsilon_d^p \frac{\phi_f - \phi_0}{(B_\phi + \varepsilon_d^p)^2} \tag{B.12}$$

$$\frac{dc}{d\varepsilon_d^{p\,(k+1)}} = \frac{c_f - c_0}{B_c + \varepsilon_d^p} - \varepsilon_d^p \frac{c_f - c_0}{(B_c + \varepsilon_d^p)^2} \tag{B.13}$$

B.2 Tensile failure mechanism

The yield criterion in the stress invariants plane is given by (only the surface f^2 is considered as explained in chapter 7) :

$$f^2 \equiv II_{\hat{\sigma}} + \frac{1}{-3cos\beta - \sqrt{3}sin\beta}(I_\sigma + 3\sigma_t') = 0 \tag{B.14}$$

$$\tag{B.15}$$

where σ_t is the uniaxial tensile strength of the material and β is Lode's angle. The consistency equation writes :

$$f^2(\sigma_{E,ij}^{'(k+1)}, \kappa_{E,m}^{(k+1)}) + \frac{\partial f^2}{\partial \sigma_{E,ij}^{'(k+1)}}\Delta\sigma_{ij}^{'p\,(k+1)} + \frac{\partial f^2}{\partial \kappa_{E,m}^{2\,(k+1)}}\Delta\lambda^{p\,2}\frac{d\kappa_m^2}{d\varepsilon_v^{p\,(k+1)}}\frac{\partial g^2}{\partial \sigma_{E,ii}^{'(k+1)}} = 0 \tag{B.16}$$

$$\tag{B.17}$$

where ε_v^p is the volumetric plastic strain given by :

$$\varepsilon_v^p = \varepsilon_1^p + \varepsilon_2^p + \varepsilon_3^p \tag{B.18}$$

B.2.1 Derivative with respect to stress

The derivatives of the yield surface with respect to the effective stress are obtained by the chain rule:

$$\frac{\partial f^2}{\partial \sigma_{ij}'} = \frac{\partial f^2}{\partial I_\sigma}\frac{\partial I_\sigma}{\partial \sigma_{ij}'} + \frac{\partial f^2}{\partial II_{\hat{\sigma}}}\frac{\partial II_{\hat{\sigma}}}{\partial \sigma_{ij}'} + \frac{\partial f^2}{\partial \beta}\frac{\beta}{\partial \sigma_{ij}'} \tag{B.19}$$

$$\tag{B.20}$$

with

$$\frac{\partial f^2}{\partial I_\sigma} = \frac{1}{-3cos\beta - \sqrt{3}sin\beta} \qquad \frac{\partial I_\sigma}{\partial \sigma_{ij}'} = \delta_{ij} \tag{B.21}$$

$$\frac{\partial f^2}{\partial II_{\hat{\sigma}}} = 1 \qquad \frac{\partial II_{\hat{\sigma}}}{\partial \sigma_{ij}'} = \frac{\hat{\sigma}_{ij}}{2II_{\hat{\sigma}}} \tag{B.22}$$

$$\frac{\partial f^2}{\partial \beta} = \frac{-3sin\beta + \sqrt{3}cos\beta}{(-3cos\beta - \sqrt{3}sin\beta)^2}(I_\sigma + 3\sigma'_t) \tag{B.23}$$

$$\frac{\partial \beta}{\partial \sigma'_{ij}} = -\frac{1}{3}\frac{3\sqrt{3}}{2II_{\hat{\sigma}}^3}\frac{\left(\hat{\sigma}_{ik}\hat{\sigma}_{kj} - \frac{2}{3}II_{\hat{\sigma}}^2 \delta_{ij} - \frac{3III_{\hat{\sigma}}\hat{\sigma}'_{ij}}{2II_{\hat{\sigma}}^2}\right)}{\sqrt{1 - \left(\frac{3\sqrt{3}}{2}\frac{III_{\hat{\sigma}}}{II_{\hat{\sigma}}^3}\right)^2}} \tag{B.24}$$

B.2.2   Derivative with respect to plastic variables

The derivative of the yield surface with respect to the plastic variable is given by:

$$\frac{\partial f^2}{\partial \kappa_m} = \frac{\partial f^2}{\partial \sigma'_t} \tag{B.25}$$

$$\tag{B.26}$$

where:

$$\frac{\partial f^2}{\partial \sigma'_t} = \frac{3}{-3cos\beta - \sqrt{3}sin\beta} \tag{B.27}$$

$$\tag{B.28}$$

We know

$$\sigma'_t = -\sigma_t'^{sat} + k_2\left[1 - exp\left(-\frac{k_1 s}{k_{2,0}}\right)\right] \tag{B.29}$$

and given the hardening rule :

$$\sigma_t'^{sat} = \sigma_{t,0}'^{sat} + \frac{(\sigma_{t,f}'^{sat} - \sigma_{t,0}'^{sat})\varepsilon_v^p}{B_{\sigma_t} + \varepsilon_v^p} \tag{B.30}$$

$$k_2 = k_{2,0} + \frac{(k_{2,f} - k_{2,0})\varepsilon_v^p}{B_{\sigma_t} + \varepsilon_v^p} \tag{B.31}$$

where $\sigma_{t,0}^{sat}$ is the initial value of the saturated uniaxial tensile strength and $\sigma_{t,f}^{sat}$ the final value and where $k_{2,0}$ and $k_{2,f}$ are respectively the initial and final values of final increment of effective tensile strength. The coefficient B_{σ_t} corresponds to the volumetric plastic strain at half the variation between the initial and final values. The derivatives thus writes :

$$\frac{d\sigma_t'^{sat}}{d\varepsilon_v^{p\,(k+1)}} = \frac{(\sigma_{t,f}'^{sat} - \sigma_{t,0})'^{sat}B_{\sigma_t}}{(B_{\sigma_t} + \varepsilon_v^p)^2} - (1 - e^{(\frac{-k_1 s}{k_{2,0}}}\frac{(k_{2,f} - k_{2,0})'^{sat}B_{\sigma_t}}{(B_{\sigma_t} + \varepsilon_v^p)^2} \tag{B.32}$$

B.3   Truncation of the tensile failure criterion

The yield criterion in the stress invariants plane is given by :

$$f^5 \equiv I_\sigma - 3(\sigma'_t - TRUNC) = 0 \tag{B.33}$$

where $TRUNC$ is arbitrarily fixed at :

$$TRUNC = \frac{\sigma_{t,0}^{'sat} * 10^{-4}}{\frac{3}{-3cos\beta - \sqrt{3}sin\beta}} \tag{B.34}$$

The consistency equation writes :

$$f^5(\sigma_{E,ij}^{'(k+1)}, \kappa_{E,m}^{(k+1)}) + \frac{\partial f^5}{\partial \sigma_{E,ij}^{'(k+1)}} \Delta \sigma_{ij}^{p\,(k+1)} + \frac{\partial f^5}{\partial \kappa_{E,m}^{2\,(k+1)}} \Delta \lambda^{p\,5} \frac{d\kappa_m^2}{d\varepsilon_v^{p\,(k+1)}} \frac{\partial g^5}{\partial \sigma_{E,ii}^{'(k+1)}} = 0 \tag{B.35}$$

$$\tag{B.36}$$

B.3.1 Derivative with respect to stress

The derivatives of the yield surface with respect to the effective stress are obtained by the chain rule:

$$\frac{\partial f^5}{\partial \sigma_{ij}'} = \frac{\partial f^5}{\partial I_\sigma} \frac{\partial I_\sigma}{\partial \sigma_{ij}'} \tag{B.37}$$

$$= 1\, \delta_{ij} \tag{B.38}$$

B.3.2 Derivative with respect to plastic variables

The derivative of the yield surface with respect to the plastic variable is given by:

$$\frac{\partial f^5}{\partial \kappa_m} = \frac{\partial f^5}{\partial \sigma_t'} \tag{B.39}$$

where:

$$\frac{\partial f^2}{\partial \sigma_t'} = 3 \tag{B.40}$$

We know

$$\sigma_t' = -\sigma_t^{'sat} + k_2 \left[1 - exp\left(-\frac{k_1 s}{k_{2,0}} \right) \right] \tag{B.41}$$

and given the hardening rule :

$$\sigma_t^{'sat} = \sigma_{t,0}^{'sat} + \frac{(\sigma_{t,f}^{'sat} - \sigma_{t,0}^{sat})\varepsilon_v^p}{B_{\sigma_t} + \varepsilon_v^p} \tag{B.42}$$

$$k_2 = k_{2,0} + \frac{(k_{2,f} - k_{2,0})\varepsilon_v^p}{B_{\sigma_t} + \varepsilon_v^p} \tag{B.43}$$

where $\sigma_{t,0}^{sat}$ is the initial value of the saturated uniaxial tensile strength and $\sigma_{t,f}^{sat}$ the final value and where $k_{2,0}$ and $k_{2,f}$ are respectively the initial and final values of final increment of effective tensile strength. The coefficient B_{σ_t} corresponds to the volumetric plastic strain at half the variation between the initial and final values. The derivatives thus writes :

$$\frac{d\sigma_t^{'sat}}{d\varepsilon_v^{p\,(k+1)}} = \frac{(\sigma_{t,f}^{'sat} - \sigma_{t,0})^{'sat} B_{\sigma_t}}{(B_{\sigma_t} + \varepsilon_v^p)^2} - (1 - e^{(\frac{-k_1 s}{k_{2,0}}} \frac{(k_{2,f} - k_{2,0})^{'sat} B_{\sigma_t}}{(B_{\sigma_t} + \varepsilon_v^p)^2} \tag{B.44}$$

219

Bibliography

, 2006. Testing evapotranspiration equations using lysimeter observations in a semiarid climate. Agricultural Water Management 85 (1), 15 – 26.

Aertsens, M., Wemaere, I., Wouters, L., 2004. Spatial variability of transport parameters in the boom clay. Applied Clay Science 26 (1), 37–45.

Al-Hussaini, M., 1981. Tensile properties of compacted soils. In: Laboratory Shear Strength of Soil. ASTM International.

Al-Mukhtar, M., Belanteur, N., Tessier, D., Vanapalli, S., 1996. The fabric of a clay soil under controlled mechanical and hydraulic stress states. Applied Clay Science 11 (2-4), 99–115.

Alemán, J., Chadwick, A. V., He, J., Hess, M., Horie, K., Jones, R. G., Kratochvíl, P., Meisel, I., Mita, I., Moad, G., et al., 2007. Definitions of terms relating to the structure and processing of sols, gels, networks, and inorganic-organic hybrid materials (iupac recommendations 2007). Pure and Applied Chemistry 79 (10), 1801–1829.

Alonso, E., Oldecop, L., 2003. Comportement des remblais en enrochement. Revue française de géotechnique (102), 3–19.

Alonso, E. E., Gens, A., Josa, A., 1990. A constitutive model for partially saturated soils. Géotechnique 40 (3), 405–430.

Bachmat, Y., Bear, J., 1986. Macroscopic modelling of transport phenomena in porous media. 1: The continuum approach. Transport in porous media 1 (3), 213–240.

Baldi, G., Borsetto, M., Hueckel, T., 1987. Calibration of mathematical models for simulation of thermal, seepage and mechanical behaviour of boom clay. Tech. rep., Commission of the European Communities.

Baldi, G., Hueckel, T., Peano, A., Pellegrini, R., 1991. Developments in modelling of thermohydro-geomechanical behaviour of boom clay and clay-based buffer materials (volume 2). Tech. rep., Commission of the European Communities.

Barnichon, D., 1990. Modélisation et simulation de systèmes de production: problèmes de spécification et d'ordonnancement. Ph.D. thesis, Clermont-Ferrand 2.

Barnichon, J.-D., Volckaert, G., 2003. Observations and predictions of hydromechanical coupling effects in the boom clay, mol underground research laboratory, belgium. Hydrogeology Journal 11 (1), 193–202.

Bastiaens, W., Bernier, F., Li, X. L., 2006. An overview of long-term hm measurements around hades urf. In: Proceedings of International Symposium on multiphysics coupling and long-term behaviour in rock mechanics, Lieege. pp. 15–26.

Bear, J., 2013. Dynamics of fluids in porous media. Courier Corporation.

Bear, J., Verruijt, A., 1987. Theory and applications of transport in porous media. Modeling of groundwater flow and pollution, Dordrecht: Reidel.

Belanteur, N., Tacherifet, S., Pakzad, M., 1997. Etude des comportements mécanique, thermo-mécanique et hydro-mécanique des argiles gonflantes et non gonflantes fortement compactées. Revue française de géotechnique (78), 31–50.

Belgium Profile, 2013. Radioactive waste management programms in oecd/nea member countries. Tech. rep., Nuclear energy agency.

Bernier, F., Li, X. L., Bastiaens, W., 2007. Twenty-five years' geotechnical observation and testing in the tertiary boom clay formation. Géotechnique 57 (2), 229–237.

Biot, M. A., 1941. General theory of three-dimensional consolidation. Journal of applied physics 12 (2), 155–164.

Biot, M. A., 1956. Theory of propagation of elastic waves in a fluid-saturated porous solid. ii. higher frequency range. The Journal of the acoustical Society of america 28 (2), 179–191.

Biot, M. A., 1962. Mechanics of deformation and acoustic propagation in porous media. Journal of applied physics 33 (4), 1482–1498.

Biot, M. A., Temple, G., 1972. Theory of finite deformations of porous solids. Indiana University Mathematics Journal 21 (7), 597–620.

Bishop, A., Garga, V., Kodikara, J., 1969. Drained tension tests on london clay. Géotechnique 19, 309–313.

Bishop, A. W., 1959. The principle of effective stress. Teknisk ukeblad 39, 859–863.

Bishop, A. W., Blight, G., 1963. Some aspects of effective stress in saturated and partly saturated soils. Geotechnique 13 (3), 177–197.

Blümling, P., Bernier, F., Lebon, P., Martin, C. D., 2007. The excavation damaged zone in clay formations time-dependent behaviour and influence on performance assessment. Physics and Chemistry of the Earth, Parts A/B/C 32 (8), 588–599.

Bossart, P., Meier, P. M., Moeri, A., Trick, T., Mayor, J.-C., 2002. Geological and hydraulic characterisation of the excavation disturbed zone in the opalinus clay of the mont terri rock laboratory. Engineering Geology 66 (1-2), 19–38.

Bouazza, A., Van Impe, W., Haegeman, W., 1996. Some mechanical properties of reconstituted boom clay. Geotechnical & Geological Engineering 14 (4), 341–352.

Bowen, R. M., 1980. Incompressible porous media models by use of the theory of mixtures. International Journal of Engineering Science 18 (9), 1129–1148.

Brunauer, S., Emmett, P. H., Teller, E., 1938. Adsorption of gases in multimolecular layers. Journal of the American chemical society 60 (2), 309–319.

Cajuhi, T., Sanavia, L., De Lorenzis, L., 2018. Phase-field modeling of fracture in variably saturated porous media. Computational Mechanics 61 (3), 299–318.

Ceaglske, N. H., Hougen, O., 1937. Drying granular solids. Industrial & Engineering Chemistry 29 (7), 805–813.

Cerfontaine, B., Dieudonné, A.-C., Radu, J.-P., Collin, F., Charlier, R., 2015. 3d zero-thickness coupled interface finite element: formulation and application. Computers and Geotechnics 69, 124–140.

Charlier, R., 1987. Approche unifiée de quelques problèmes non linéaires de mécanique des milieux continus par la méthode des éléments finis. Ph.D. thesis, Université de Liège, Liège, Belgique.

Chen, G., Sillen, X., Verstricht, J., Li, X. L., 2011. Atlas iii in situ heating test in boom clay: Field data, observation and interpretation. Computers and Geotechnics 38 (5), 683–696.

Chen, X. D., Mujumdar, A. S., 2009. Drying technologies in food processing. John Wiley & Sons.

Colina, H., Roux, S., 2000. Experimental model of cracking induced by drying shrinkage. The European Physical Journal E 1 (2-3), 189–194.

Coll, C., 2005. Endommagement des roches argileuses et perméabilité induite au voisinage d'ouvrages souterrains. Ph.D. thesis, Université Joseph-Fourier-Grenoble I.

Collin, F., 2003. Couplages thermo-hydro-mécaniques dans les sols et les roches tendres partiellement saturés. Ph.D. thesis, Université de Liège, Liège, Belgique.

Collin, F., Cui, Y. J., Schroeder, C., Charlier, R., 2002a. Mechanical behaviour of lixhe chalk partly saturated by oil and water: experiment and modelling. International journal for numerical and analytical methods in geomechanics 26 (9), 897–924.

Collin, F., Li, X.-L., Radu, J.-P., Charlier, R., 2002b. Thermo-hydro-mechanical coupling in clay barriers. Engineering Geology 64 (2), 179–193.

Comings, E. W., Sherwood, T., 1934. The drying of solids. vii moisture movement by capillarity in drying granular materials. Industrial & Engineering Chemistry 26 (10), 1096–1098.

Coussy, O., 1995. Mechanics of porous continua. Wiley.

Coussy, O., 2004. Poromechanics. John Wiley & Sons.

Coviello, A., Lagioia, R., Nova, R., 2005. On the measurement of the tensile strength of soft rocks. Rock Mechanics and Rock Engineering 38 (4), 251–273.

Craeye, B., De Schutter, G., Van Humbeeck, H., Van Cotthem, A., 2009. Early age behaviour of concrete supercontainers for radioactive waste disposal. Nuclear Engineering and Design 239 (1), 23–35.

Crochepeyre, S., 1998. Contribution à la modélisation numérique et théorique de la localisation et de la post-localisation dans les géomatériaux. Ph.D. thesis, Université Joseph Fourier (Grenoble).

Cui, Y., Delage, P., 1996. Yeilding and plastic behaviour of an unsaturated compacted silt. Géotechnique 46 (2), 291–311.

De Marsily, G., 1986. Quantitative hydrogeology. Tech. rep., Paris School of Mines, Fontainebleau.

Decleer, J., Viaene, W., Vandenberghe, N., 1983. Relationships between chemical, physical and mineralogical characteristics of the rupelian boom clay, belgium. CLAY MINER. Clay Miner. 18 (1), 1.

Dehandschutter, B., Vandycke, S., Sintubin, M., Vandenberghe, N., Wouters, L., 2005. Brittle fractures and ductile shear bands in argillaceous sediments: inferences from oligocene boom clay (belgium). Journal of Structural Geology 27 (6), 1095–1112.

Delage, P., 1987. Aspects du comportement des sols non saturés. Revue française de géotechnique (40), 33–43.

Delage, P., Howat, M., Cui, Y., 1998. The relationship between suction and swelling properties in a heavily compacted unsaturated clay. Engineering geology 50 (1-2), 31–48.

Delage, P., Sultan, N., Cui, Y. J., 2000. On the thermal consolidation of boom clay. Canadian Geotechnical Journal 37 (2), 343–354.

Delage, P., et al., 2001. L'eau dans les sols non saturés. Techniques de l'ingénieur-construction (C 301).

Dieudonné, A.-C., 2016. Hydromechanical behaviour of compacted bentonite: from micro-scale analysis to macro-scale modelling. Ph.D. thesis, Université de Liège, Liège, Belgique.

Dincer, I., 1998. Moisture loss from wood products during drying—part i: Moisture diffusivities and moisture transfer coefficients. Energy Sources 20 (1), 67–75.

Dizier, A., 2011. Caractérisation des effets de température dans la zone endommagée autour de tunnels de stockage de déchets nucléaires dans des roches argileuses. Ph.D. thesis, Université de Liège, Belgique.

Dormieux, L., Barboux, P., Coussy, O., Dangla, P., 1995. A macroscopic model of the swelling phenomenon of a saturated clay. European journal of mechanics. A. Solids 14 (6), 981–1004.

Drucker, D. C., Prager, W., 1952. Soil mechanics and plastic analysis or limit design. Quarterly of applied mathematics 10 (2), 157–165.

Dunlop, S., 2008. A dictionary of weather. OUP Oxford.

Dupré, A., Dupré, P., 1869. Théorie mécanique de la chaleur. Gauthier-Villars.

Ekechukwu, O. V., Norton, B., 1999. Review of solar-energy drying systems ii: an overview of solar drying technology. Energy conversion and management 40 (6), 615–655.

Elzinga, J., Hearn, D. W., 1972. Geometrical solutions for some minimax location problems. Transportation Science 6 (4), 379–394.

Ewen, J., Thomas, H., 1989. Heating unsaturated medium sand. Geotechnique 39 (3), 455–470.

Fang, H.-Y., Chaney, R. C., 1997. Introduction to environmental geotechnology. CRC press.

Farrell, D., Greacen, E., Larson, W., 1967. The effect of water content on axial strain in a loam soil under tension and compression 1. Soil Science Society of America Journal 31 (4), 445–450.

François, B., 2008. Thermo-plasticity of fine-grained soils at various saturation states: Application to nuclear waste disposal. Ph.D. thesis, Ecole Polytechnique Fédérale de Lausanne, Lausanne, Suisse.

François, B., Laloui, L., 2008. Acmeg-ts: A constitutive model for unsaturated soils under non-isothermal conditions. International journal for numerical and analytical methods in geomechanics 32 (16), 1955–1988.

Fredlund, D., Morgenstern, N., 1978. Stress state variables for unsaturated soils. Journal of Geotechnical and Geoenvironmental Engineering 104 (ASCE 14170 Proc Paper).

Fredlund, D. G., Rahardjo, H., 1993. Soil mechanics for unsaturated soils. John Wiley & Sons.

Gardner, W., Widtsoe, J., 1920. The movement of soil moisture. Soil Sci. (11), 215–232.

Garnier, J., 1973. Tassement et contraintes: influence de la rigidité de la fondation et de l'anisotropie du massif. Ph.D. thesis.

Garrels, R. M., Christ, C. L., 1965. Solutions, minerals, and equilibria.

Gatmiri, B., 1989. Réponse d'un massif sous-marin à l'action de la houle. Ph.D. thesis, Ecole Nationale des Ponts et Chaussées.

Geankoplis, C., 1993. Drying of process materials. Transport processes and unit operations, 520–583.

Gens, A., 2010. Soil–environment interactions in geotechnical engineering. Géotechnique 60 (1), 3–74.

Gens, A., Alonso, E., 1992. A framework for the behaviour of unsaturated expansive clays. Canadian Geotechnical Journal 29 (6), 1013–1032.

Gens, A., Olivella, S., 2001. Thm phenomena in saturated and unsaturated porous media: Fundamentals and formulation. Revue française de génie civil 5 (6), 693–717.

Gens, A., Vaunat, J., Garitte, B., Wileveau, Y., 2007. In situ behaviour of a stiff layered clay subject to thermal loading: observations and interpretation. Géotechnique 57 (2), 207–228.

Gerard, P., 2011. Impact des transferts de gaz sur le comportement poro-mécanique des matériaux argileux. Ph.D. thesis, Thèse de doctorat. Université de Liège, Belgium.

Gerard, P., Charlier, R., Chambon, R., Collin, F., 2008. Influence of evaporation and seepage on the convergence of a ventilated cavity. Water resources research 44 (5).

Gerard, P., Léonard, A., Masekanya, J.-P., Charlier, R., Collin, F., 2010. Study of the soil–atmosphere moisture exchanges through convective drying tests in non-isothermal conditions. International journal for numerical and analytical methods in geomechanics 34 (12), 1297–1320.

Gilliland, E., Sherwood, T., 1933. The drying of solids. vi. diffusion equations for the period of constant drying rate. Industrial & Engineering Chemistry 25 (10), 1134–1136.

Greenhill, A., 1893. A treatise on the mathematical theory of elasticity. Nature 47 (1223), 529.

Griffith, A. A., 1924. Theory of rupture. In Proceedings of the First International Conference on Applied Mechanics,Delft, Holland, 55–63.

Gross, D., Seelig, T., 2017. Fracture mechanics: with an introduction to micromechanics. Springer.

Haines, W. B., 1927. Studies in the physical properties of soils: Iv. a further contribution to the theory of capillary phenomena in soil. The Journal of Agricultural Science 17 (2), 264–290.

Haines, W. B., 1930. Studies in the physical properties of soil. v. the hysteresis effect in capillary properties, and the modes of moisture distribution associated therewith. The Journal of Agricultural Science 20 (1), 97–116.

Hassanizadeh, M., Gray, W. G., 1979a. General conservation equations for multi-phase systems: 1. averaging procedure. Advances in water resources 2, 131–144.

Hassanizadeh, M., Gray, W. G., 1979b. General conservation equations for multi-phase systems: 2. mass, momenta, energy, and entropy equations. Advances in Water Resources 2, 191–203.

Hayashi, H., 1989. Drying technologies of foods-their history and future. Drying technology 7 (2), 315–369.

Hernández-López, M. F., Gironás, J., Braud, I., Suárez, F., Muñoz, J. F., 2014. Assessment of evaporation and water fluxes in a column of dry saline soil subject to different water table levels. Hydrological processes 28 (10), 3655–3669.

Hilf, J. W., 1956. An investigation of pore water pressure in compacted cohesive soils.

Horseman, S., Winter, M., Enwistle, D., 1987. Geotechnical characterization of boom clay in relation to the disposal of radioactive waste. Tech. rep., Commission of the European Communities.

Hougen, O., McCauley, H., Marshall, W., 1940. Limitations of diffusion equations in drying. Trans. Am. Inst. Chem. Eng. (36), 183–210.

Hrubesh, L. W., Pekala, R. W., 1994. Thermal properties of organic and inorganic aerogels. Journal of Materials Research 9 (3), 731–738.

Hueckel, T., Borsetto, M., Peano, A., 1988. Modelling of coupled thermo-elastoplastic-hydraulic response of clays subjected to nuclear waste heat. ISMES publ./Inst. sperimentale modelli e strutture (Bergamo, Italia).

Hueckel, T., Mielniczuk, B., El Youssoufi, M., Hu, L., Laloui, L., 2014. A three-scale cracking criterion for drying soils. Acta Geophysica 62 (5), 1049–1059.

Hueckel, T. A., 1992. Water–mineral interaction in hygromechanics of clays exposed to environmental loads: a mixture-theory approach. Canadian Geotechnical Journal 29 (6), 1071–1086.

Idso, S., Reginato, R., Jackson, R., Kimball, B., Nakayama, F., 1974. The three stages of drying of a field soil. Soil Science Society of America Journal 38 (5), 831–837.

IEAA, 2003. Scientific and technical basis for the geological disposal of radioactive wastes. Tech. rep., International Atomic Energy Agency, Viena.

Jaeger, J. C., Cook, N. G., Zimmerman, R., 2009. Fundamentals of rock mechanics. John Wiley & Sons.

Jaumann, G., 1911. Geschlossenes system physikalischer und chemischer differentialgesetze. Sitzgsber. Akad. Wiss. Wien 120 (9), 385–530.

Jennings, J., Burland, J., 1962. Limitations to the use of effective stresses in partly saturated soils. Géotechnique 12 (2), 125–144.

Job, N., 2005. Matériaux carbonés poreux de texture contrôlée synthétisés par procédé sol–gel et leur utilisation en catalyse hétérogene. Ph.D. thesis, PhD thesis, Liege University (Belgium).

Job, N., Pirard, R., Marien, J., Pirard, J.-P., 2004. Porous carbon xerogels with texture tailored by ph control during sol–gel process. Carbon 42 (3), 619–628.

Job, N., Pirard, R., Pirard, J.-P., Alié, C., 2006a. Non intrusive mercury porosimetry: pyrolysis of resorcinol-formaldehyde xerogels. Particle & Particle Systems Characterization 23 (1), 72–81.

Job, N., Sabatier, F., Pirard, J.-P., Crine, M., Léonard, A., 2006b. Towards the production of carbon xerogel monoliths by optimizing convective drying conditions. Carbon 44 (12), 2534–2542.

Johnson, R., Williams, L., Ayars, J., Trout, T., et al., 2005. Weighing lysimeters aid study of water relations in tree and vine crops. California Agriculture 59 (2), 133–136.

Jommi, C., di Prisco, C., 1994. Un semplice approccio teorico per la modellazione del comportamento meccanico di terreni granulari parzialmente saturi. In: Il ruolo dei fluidi nei problemi di ingegneria geotecnica. pp. 167–188.

Jones, J. E., 1924a. On the determination of molecular fields.—i. from the variation of the viscosity of a gas with temperature. Proc. R. Soc. Lond. A 106 (738), 441–462.

Jones, J. E., 1924b. On the determination of molecular fields.—ii. from the equation of state of a gas. Proc. R. Soc. Lond. A 106 (738), 463–477.

Keey, V. R. B., 1979. Introduction to industrial drying operations.

Kemp, I. C., Fyhr, B. C., Laurent, S., Roques, M. A., Groenewold, C. E., Tsotsas, E., Sereno, A. A., Bonazzi, C. B., Bimbenet, J.-J., Kind, M., 2001. Methods for processing experimental drying kinetics data. Drying Technology 19 (1), 15–34.

Kingery, W., 1976. Introduction to ceramics 2nd ed. John Wiley & Sons, 449–468.

Konrad, J.-M., Ayad, R., 1997. Desiccation of a sensitive clay: field experimental observations. Canadian Geotechnical Journal 34 (6), 929–942.

Kowalski, S. J., 2012. Thermomechanics of drying processes. Vol. 8. Springer Science & Business Media.

Kozeny, J., 1927. Uber kapillare leitung der wasser in boden. Royal Academy of Science, Vienna, Proc. Class I 136, 271–306.

Krischer, O., 1938. Fundamental law of moisture movement in drying by capillary flow and vapor diffusion. VDIZ (82), 373–378.

Krischer, O., 1940. The heat, moisture, and vapor movement during drying porous materials. VDIZ (1), 17–24.

Laloui, L., 1993. Modélisation du comportement thermo-hydro-mécanique des milieux poreux anélastiques. Tech. rep., Ecole Centrale Paris.

Laloui, L., Cekerevac, C., Vulliet, L., 2002. Thermo-plasticity of clays: a simple constitutive approach. In: International Workshop on Environmental Geomechanics. Sous la direction de L. Vulliet, L. Laloui et B. Schrefler. Éditions EPFL Press. pp. 45–58.

Lanczos, C., 1988. Applied analysis. Courier Corporation.

Laurindo, J. B., Prat, M., 1998. Numerical and experimental network study of evaporation in capillary porous media. drying rates. Chemical engineering science 53 (12), 2257–2269.

Lebon, P., 2009. Lavoratoires Souterrains Pour L'etude Stockage Geologique Des Dechets a Vie longue. Ed. Techniques Ingénieur.

Lehmann, P., Assouline, S., Or, D., 2008. Characteristic lengths affecting evaporative drying of porous media. Physical Review E 77 (5), 056309.

Leonard, A., 2002. Étude du séchage convectif des boues de station d'épuration - suivi de la texture par microtomographie à rayon x. Ph.D. thesis, Université de Liège, Belgique.

Léonard, A., Blacher, S., Crine, M., Jomaa, W., 2008. Evolution of mechanical properties and final textural properties of resorcinol–formaldehyde xerogels during ambient air drying. Journal of Non-Crystalline Solids 354 (10-11), 831–838.

Léonard, A., Blacher, S., Marchot, P., Crine, M., 2002. Use of x-ray microtomography to follow the convective heat drying of wastewater sludges. Drying Technology 20 (4-5), 1053–1069.

Léonard, A., Blacher, S., Marchot, P., Pirard, J.-P., Crine, M., 2005a. Convective drying of wastewater sludges: Influence of air temperature, superficial velocity, and humidity on the kinetics. Drying technology 23 (8), 1667–1679.

Léonard, A., Job, N., Blacher, S., Pirard, J.-P., Crine, M., Jomaa, W., 2005b. Suitability of convective air drying for the production of porous resorcinol-formaldehyde and carbon xerogels. Carbon 43 (8), 1808–1811.

Lewis, R. W., Schrefler, B. A., 1987. The finite element method in the deformation and consolidation of porous media.

Lewis, W. K., 1921. The rate of drying of solid materials. Industrial & Engineering Chemistry 13 (5), 427–432.

Li, X., 2008. Timodaz-thermal impact on the damaged zone around a radioactive waste disposal in clay host rocks. Contract Number: FI6W-CT-2006-036449), Executive Summary of the activities (Mid Term) 14.

Li, X. L., Bastiaens, W., Van Marcke, P., Verstricht, J., Chen, G., Weetjens, E., Sillen, X., 2010. Design and development of large-scale in-situ praclay heater test and horizontal high-level radioactive waste disposal gallery seal test in belgian hades. Journal of Rock Mechanics and Geotechnical Engineering 2 (2), 103–110.

Liu, C., Zhang, X., Zhang, Y., 2002. Determination of daily evaporation and evapotranspiration of winter wheat and maize by large-scale weighing lysimeter and micro-lysimeter. Agricultural and Forest Meteorology 111 (2), 109–120.

Malvern, L. E., 1969. Introduction to the Mechanics of a Continuous Medium. No. Monograph.

McDonald, P., Pritchard, T., Roberts, S., 1996. Diffusion of water at low saturation levels into sandstone rock plugs measured by broad line magnetic resonance profiling. Journal of colloid and interface science 177 (2), 439–445.

Mertens, J., Bastiaens, W., Dehandschutter, B., 2004. Characterisation of induced discontinuities in the boom clay around the underground excavations (urf, mol, belgium). Applied clay science 26 (1-4), 413–428.

Mikulitsch, W., Gudehus, G., 1995. Uniaxial tension, biaxial loading and wetting tests on loess. In: PROCEEDINGS OF THE FIRST INTERNATIONAL CONFERENCE ON UNSATURATED SOILS/UNSAT'95/PARIS/FRANCE/6-8 SEPTEMBER 1995. VOLUME 1.

Millington, R., Quirk, J., 1959. Permeability of porous media. Nature 183 (4658), 387–388.

Modaressi, H., Laloui, L., 1997. A thermo-viscoplastic constitutive model for clays. International journal for numerical and analytical methods in geomechanics 21 (5), 313–335.

Morris, P. H., Graham, J., Williams, D. J., 1992. Cracking in drying soils. Canadian Geotechnical Journal 29 (2), 263–277.

Musielak, G., Jacek, B., 2007. Non-linear heat and mass transfer during convective drying of kaolin cylinder under non-steady conditions. Transport in porous media 66 (1-2), 121–134.

Nadeau, J.-P., Puiggali, J.-R., 1995. Séchage: des processus physiques aux procédés industriels.

Nahlawi, H., Chakrabarti, S., Kodikara, J., 2004. A direct tensile strength testing method for unsaturated geomaterials. Geotechnical Testing Journal 27 (4), 356–361.

NEA, 2008. Moving forward with geological disposal of radioactive waste, a collective statement by the nea radioactive waste management commitee (rwmc). Tech. rep., OECD-Nuclear Energy Agency, Paris.

Newman, A., 1931. The drying of porous solids : Diffusion calculations. Trans. Am. Inst. Chem. Eng. (27), 310–333.

Nireesha, G., Divya, L., Sowmya, C., Venkateshan, N., Babu, M. N., Lavakumar, V., 2013. Lyophilization/freeze drying-an review. International journal of novel trends in pharmaceutical sciences 3 (4), 87–98.

Nuth, M., Laloui, L., 2008. Advances in modelling hysteretic water retention curve in deformable soils. Computers and Geotechnics 35 (6), 835–844.

Olivella, S., Carrera, J., Gens, A., Alonso, E., 1994. Nonisothermal multiphase flow of brine and gas through saline media. Transport in porous media 15 (3), 271–293.

ONDRAF/NIRAS, 2001. Technical overview of the safir 2 report: Safety assessment and feasibility interim report 2. Tech. rep.

Ortiz, M., Simo, J., 1986. An analysis of a new class of integration algorithms for elastoplastic constitutive relations. International Journal for Numerical Methods in Engineering 23 (3), 353–366.

Oteo-Mazo, C., Saez Aunon, J., Esteban, F., 1995. Laboratory tests and equipment with suction control. Proceedings 1st Int. Conf. on Unsaturated Soils Unsat'95, Paris 3 (1-2), 1509–1515.

Panday, S., Corapcioglu, M. Y., 1989. Reservoir transport equations by compositional approach. Transport in Porous Media 4 (4), 369–393.

Pardoen, B., 2015. Hydro-mechanical analysis of the fracturing induced by the excavation of nuclear waste repository galleries using shear banding. Ph.D. thesis, Université de Liège, Liège, Belgique.

Pekala, R., 1989. Organic aerogels from the polycondensation of resorcinol with formaldehyde. Journal of materials science 24 (9), 3221–3227.

Pel, L., Brocken, H., Kopinga, K., 1996. Determiination of moisture diffusivity in porous media using moisture concentration profiles. International Journal of Heat and Mass Transfer 39 (6), 1273–1280.

Péron, H., 2008. Desiccation cracking of soils. Ph.D. thesis, École Polytechnique Fédérale de Lausanne, Suisse.

Philip, J., De Vries, D., 1957. Moisture movement in porous materials under temperature gradients. Eos, Transactions American Geophysical Union 38 (2), 222–232.

Plougonven, E., Bernard, D., 2006. A rigid registration method for the study of microgeometry evolution of limestone during dissolution by acidic water. In: Advances in X-ray tomography for geomaterials. pp. 349–354.

Prager, W., 1949. Recent developments in the mathematical theory of plasticity. Journal of applied physics 20 (3), 235–241.

Prime, N., Levasseur, S., Miny, L., Charlier, R., Léonard, A., Collin, F., 2015. Drying-induced shrinkage of boom clay: an experimental investigation. Canadian Geotechnical Journal 52 (999), 1–14.

Richards, L., 1941. A pressure-membrane extraction apparatus for soil solution. Soil Sci 51 (5), 377–386.

Richards, L. A., 1931. Capillary conduction of liquids through porous mediums. physics 1 (5), 318–333.

Risnes, R., Korsnes, R., Vatne, T., et al., 1999. Tensional strength of soft chalks measured in direct and brazilian tests. In: 9th ISRM Congress. International Society for Rock Mechanics.

Rowe, R., Hosney, M., 2010. A systems engineering approach to minimizing leachate leakage from landfills. In: Proceedings of the 9th International Conference on Geosynthetics, Brazil. pp. 501–506.

Salehnia, F., 2015. From some obscurity to clarity in boom clay behavior: analysis of its coupled hydro-mechanical response in the presence of strain localization. Ph.D. thesis, Université de Liège, Liège, Belgique.

Sánchez, M., Manzoli, O. L., Guimarães, L. J., 2014. Modeling 3-d desiccation soil crack networks using a mesh fragmentation technique. Computers and Geotechnics 62, 27–39.

Scherer, G. W., 1990. Theory of drying. Journal of the American Ceramic Society 73 (1), 3–14.

Scherer, G. W., 1997. Stress from re-immersion of partially dried gel. Journal of non-crystalline solids 212 (2-3), 268–280.

Scherer, G. W., Smith, D. M., Qiu, X., Anderson, J. M., 1995. Compression of aerogels. Journal of Non-Crystalline Solids 186, 316–320.

Schrefler, B., 1984. The finite element method in soil consolidation. Ph.D. thesis, University College of Swansea.

SCK-CEN, 1997. Hades tour guide. Notebook.5th edition.

Shaw, T., 1987. Drying as an immiscible displacement process with fluid counterflow. Physical Review Letters 59 (15), 1671.

Sheng, D., Sloan, S. W., Gens, A., Smith, D. W., 2003. Finite element formulation and algorithms for unsaturated soils. part i: Theory. International Journal for Numerical and Analytical Methods in Geomechanics 27 (9), 745–765.

Sherwood, T., 1929. The drying of solids—i. Industrial & Engineering Chemistry 21 (1), 12–16.

Simo, J. C., Taylor, R. L., 1985. Consistent tangent operators for rate-independent elastoplasticity. Computer methods in applied mechanics and engineering 48 (1), 101–118.

Smits, K. M., Cihan, A., Sakaki, T., Illangasekare, T. H., 2011. Evaporation from soils under thermal boundary conditions: Experimental and modeling investigation to compare equilibrium-and nonequilibrium-based approaches. Water Resources Research 47 (5).

Song, W.-K., Cui, Y.-J., Tang, A. M., Ding, W.-Q., Tran, T. D., 2013. Experimental study on water evaporation from sand using environmental chamber. Canadian Geotechnical Journal 51 (2), 115–128.

Stirling, R. A., 2014. Multiphase modelling of desiccation cracking in compacted soil.

Tang, G. X., Graham, J., 2000. A method for testing tensile strength in unsaturated soils. Geotechnical Testing Journal 23 (3), 377–382.

Tazawa, E.-i., Miyazawa, S., Kasai, T., 1995. Chemical shrinkage and autogenous shrinkage of hydrating cement paste. Cement and concrete research 25 (2), 288–292.

Terzaghi, K., 1944. Theoretical soil mechanics. Chapman And Hali, Limited John Wiler And Sons, Inc; New York.

Terzaghi, K. v., 1936. The shearing resistance of saturated soil and the angle between the planes of shear. In: Proc. of 1st Int. Conf. on SMFE, Harvard. Vol. 1. pp. 54–56.

tests catalog, I., ???? `http://www.instron.in/en-in/testing-solutions/by-test-typ` accessed: 04-2018.

Tournier, B., 2006. Transferts par capillarité et évaporation dans des roches: rôle des structures de porosité. Ph.D. thesis, Atelier national de reproduction des thèses.

Tsang, C.-F., Bernier, F., Davies, C., 2005. Geohydromechanical processes in the excavation damaged zone in crystalline rock, rock salt, and indurated and plastic clays—in the context of radioactive waste disposal. International Journal of Rock Mechanics and Mining Sciences 42 (1), 109–125.

Tuller, M., Or, D., 2001. Hydraulic conductivity of variably saturated porous media: Film and corner flow in angular pore space. Water Resources Research 37 (5), 1257–1276.

van Arsdel, W., 1947. Approximate diffusion calculations for the falling rate phase of drying. Trans. Am. Inst. Chem. Eng. (43), 13–24.

Van Brakel, J., 1980. Mass transfer in convective drying.

Van Genuchten, M. T., 1980. A closed-form equation for predicting the hydraulic conductivity of unsaturated soils. Soil science society of America journal 44 (5), 892–898.

Van Humbeeck, H., Bastiaens, W., De Bock, C., Van Cotthem, A., 2008. Experimental programme to demonstrate the viability of the supercontainer concept for hlw. dimensions 16, 18.

Verruijt, A., Van Baars, S., 2007. Soil mechanics. VSSD Delft, the Netherlands.

Verwey, E. J. W., Overbeek, J. T. G., Overbeek, J. T. G., 1948. Theory of the stability of lyophobic colloids. Courier Corporation.

Vincent, L., Soille, P., Jun. 1991. Watersheds in digital spaces: An efficient algorithm based on immersion simulations. IEEE Transactions on Pattern Analysis and Machine Intelligence 13 (6), 583–598.

Warren, D. S., Sutherland, S. P., Kao, J. Y., Weal, G. R., Mackay, S. M., 2017. The preparation and simple analysis of a clay nanoparticle composite hydrogel. Journal of Chemical Education 94 (11), 1772–1779.

Washburn, E. W., 1921. Note on a method of determining the distribution of pore sizes in a porous material. Proceedings of the National Academy of Sciences 7 (4), 115–116.

Wemaere, I., Marivoet, J., Labat, S., 2008. Hydraulic conductivity variability of the boom clay in north-east belgium based on four core drilled boreholes. Physics and Chemistry of the Earth, Parts A/B/C 33, S24–S36.

Whitaker, S., 1977. Simultaneous heat, mass, and momentum transfer in porous media: a theory of drying. In: Advances in heat transfer. Vol. 13. Elsevier, pp. 119–203.

Wilson, G., Fredlund, D., Barbour, S., 1997. The effect of soil suction on evaporative fluxes from soil surfaces. Canadian Geotechnical Journal 34 (1), 145–155.

Wilson, G. W., Fredlund, D., Barbour, S., 1994. Coupled soil-atmosphere modelling for soil evaporation. Canadian Geotechnical Journal 31 (2), 151–161.

Wouters, L., Vandenberghe, N., 1994. Géologie de la Campine: essai de synthèse. ONDRAF.

Yiotis, A., Boudouvis, A., Stubos, A., Tsimpanogiannis, I., Yortsos, Y., 2003. Effect of liquid films on the isothermal drying of porous media. Physical Review E 68 (3), 037303.

Yiotis, A., Stubos, A., Boudouvis, A., Tsimpanogiannis, N., Yortsos, Y., 2005. Pore-network modeling of isothermal drying in porous media. In: Upscaling Multiphase Flow in Porous Media. Springer, pp. 63–86.

Yiotis, A. G., Tsimpanogiannis, I. N., Stubos, A. K., Yortsos, Y. C., 2006. Pore-network study of the characteristic periods in the drying of porous materials. Journal of colloid and interface science 297 (2), 738–748.

Yortsos, Y. C., Xu, B., Salin, D., 1997. Phase diagram of fully developed drainage in porous media. Physical review letters 79 (23), 4581.